UNIVERSIDAD COMPLUTENSE DE MADRID
FACULTAD DE CIENCIAS FÍSICAS

TESIS DOCTORAL

Nanoestructuras de óxidos para espintrónica superconductora

MEMORIA PARA OPTAR AL GRADO DE DOCTOR

PRESENTADA POR

David Sánchez Manzano

Directores

Jacobo Santamaría Sánchez-Barriga
Carlos León Yebra

Madrid

UNIVERSIDAD COMPLUTENSE DE MADRID
FACULTAD DE CIENCIAS FÍSICAS

TESIS DOCTORAL

NANOESTRUCTURAS DE ÓXIDOS PARA ESPINTRÓNICA SUPERCONDUCTORA

MEMORIA PARA OPTAR AL GRADO DE DOCTOR

PRESENTADA POR

David Sánchez Manzano

DIRECTOR

Jacobo Santamaría Sánchez-Barriga
Carlos León Yebra

A mi padre, a mi madre,

a mis abuelos, a mis tios

a mis hermanos y a Julieta

“No man is an island,

Entire of itself.

Each is a piece of the continent,

A part of the main.

If a clod be washed away by the sea,

Europe is the less.

As well as if a promontory were.

As well as if a manor of thine own

Or of thine friend's were.

Each man's death diminishes me,

For I am involved in mankind.

Therefore, send not to know

For whom the bell tolls,

It tolls for thee.”

John Donne

Agradecimientos

Esta tesis no ha sido fácil, pero por fin hemos llegado al momento más fácil de este proceso: los agradecimientos. Hay tanta gente que agradecer, no solo por la tesis y su contenido, sino por todas las vivencias que ha habido entre medias, que muchas veces han ayudado a calmar el espíritu después de una larga sesión de medidas en el laboratorio. Pero empecemos por el principio.

Primero, quiero agradecer, por supuesto, a mis directores de tesis, Jacobo y Carlos. Ha pasado ya mucho tiempo desde que entre en el despacho de Carlos para preguntarles si podría hacer el trabajo de fin de máster con ellos, y mira ahora, años después, terminando la tesis. Gracias por toda la ayuda, las conversaciones hasta tarde hablando de los datos, las palmadas en la espalda y los ciclos continuos de "Profesooooooor". Por supuesto, ha habido mucho otros profesores que me han ayudado de una forma más que tangible en esta tesis. Alberto, gracias por… bueno, prácticamente todo, por salvarnos la vida (alguna vez literalmente) múltiples veces en el laboratorio y especialmente en el EBL, esa máquina del demonio. Además, por supuesto gracias por ser un amigo tanto dentro como fuera del lab. Norbert, gracias por la ayuda y la información sobre FMR cuando estaba completamente perdido, y también por las duras preguntas que siempre hacían que me cuestionara las cosas que daba por supuesto. María, gracias por el buen humor siempre, aún en los peores momentos. Rainer, gracias por esas grandes conversaciones en las comidas, y esas mejores jugadas de la noche anterior en la NBA. Juan, gracias por los chascarrillos, y por estar siempre disponible cuando había una duda (aunque fuera teórica). Gracias Zouhair por ese increíble mes en el IMA y por siempre estar disponible para ayudar en las medidas. También gracias a Neven por esas charlas durante los almuerzos nada más empezar la tesis.

También quería agradecer a mis antecesores como estudiantes de doctorado, Mariona, Ana, Mirko, Gabriel y David, que me enseñaron (a mi y a mis compañeros) todo lo que sabían y gracias a los cuales nos iniciamos en el verdadero mundo de la carrera investigadora. Todos esos días metidos en la sala blanca, con el sputtering a mil, haciendo litografías… gracias de verdad. Fue un largo camino, pero ¡aquí estamos! Gracias especialmente a todos los que están al lori. Gracias Javi por las charlas trascendentales y los abrazos, la verdad es que, aunque no lo pareciera, ayudaban mucho. Gracias Fabián por estar siempre disponible para una conversación, un té y unas galletas, y por los abrazos. Gracias Gloria por esos buenos momentos en el despacho, de risas, y por los buenos momentos fuera, aunque después ya no estuviéramos en el mismo despacho. Gracias Víctor por ser una maquina de ciencia dentro del laboratorio y una maquina de amistad fuera. Y dentro también. Gracias Andrea por ser tan inquisitiva y hacer que me cuestione cosas que daba por supuestas, vas a ser una investigadora increíble (en realidad ya lo eres). Y tranquila que, si encuentro tictacs en Paris, te llevare un cargamento. Gracias a los chicos nuevos, Emanuel y Alex, por alegrar mis últimos momentos en el lab, vais a ser unos investigadores de primer nivel, y además sois buena gente, lo tenéis todo. Gracias a Miguel, por ser un tio genial, tanto en Paris, como en Madrid. Gracias a Edu, fue una estancia corta, pero lo pasamos muy bien, y acabamos comiendo cachopo. Y hablando de cachopo, gracias Fer, por ser mi compañero durante tantos años y aun así aguantarme. Y por seguir aguantándome ahora en París. Tenemos que aprender francés para poder hacer nuevos chascarrillos.

Por supuesto, tengo que agradecer y mucho a toda la gente que me ayudó durante mis estancias en CNRS-Thales. Lo primero, gracias Javier por darme esa oportunidad, y gracias por ofrecerme el postdoc. Es un sueño hecho realidad. Además, gracias por toda la ayuda durante la tesis, no solo durante mi estancia. Gracias a Xavier y Philippe por esos buenos momentos en el despacho, a pesar de que mi inglés fuera bastante malo al principio. Gracias también a Anke, a Salvatore y a Adrian, por toda la ayuda que me han brindado en estos años y sin los cuales no podría haber terminado mi investigación. Gracias también a la gente de ESPCI, Jerome Lesueur y Nicolas Bergeal por la ayuda con las medidas para el paper. Y gracias a Alexandre Buzdin por la ayuda con la vertiente teórica cuando estábamos perdidos.

Gracias a toda la gente del ICMM, a Mar, Federico, Carmen y Felix. Gracias por siempre recibirme con los brazos abiertos y con buenas ideas.

Gracias a la gente del sincrotrón. Gracias Sergio por estar siempre disponible, por esas conversaciones a altas horas de la noche y por toda la ayuda que me has brindado. Gracias Lourdes y Ashima por salvarnos la vida en el PEEM mas de una vez y por tener siempre tiempo para charlar un rato.

Escribo esto ya desde París, lejos de mi familia y de la mayoría de mis amigos. Gracias a todos ellos estoy donde estoy, y por supuesto, no puedo hacer más que agradecerles a todos y cada uno de ellos. Gracias a esos buenos amigos con los que empecé la carrera y ahí siguen. Gracias Isma por ser uno de mis mejores amigos, compañero de piso y compañero de muchos buenos momentos, pero también de los malos. Gracias Levi, por aguantarme en mis buenos y en mis malos momentos, siempre has sido un apoyo fundamental para mí, y nunca olvidaré ese increíble viaje por Holanda que hicimos juntos. Gracias Víctor por estar siempre ahí cuando te necesitaba, por esas comidas, cenas, viajes… Por todo. Gracias Mario por ser la voz de la razón y a veces de la locura. Gracias Alberto por ser el experto en los Simpsons que siempre consigue alegrarte el día. Gracias a Rodrigo por ser ese amigo grandote que siempre esta dispuesto a ayudar o a dar un abrazo. Gracias a JM y Laura, por ser tan geniales y por esas llamadas grupales durante la cuarentena. Gracias Abel por inculcar esa pasión en la astrofísica en todos nosotros. Gracias a Sara, por estar siempre cerca y ser una amiga increíble, además de comunista. Gracias a Sergio, amigo de última incorporación, por esas partidas durante la cuarentena que nos salvaron la vida. Gracias a toda la gente de ASAAF-UCM, por ser una parte tan importante de mi vida universitaria, y por supuesto, gracias a Rugby Fisicas por hacerme amar el rosa, y esos primeros, segundos y terceros tiempos expectaculares. Gracias especialmente a Pocoyó, por ayudarme tanto en mis inicios, y a MK y Fua, por ser los mejores del equipo, aunque no sea jugando. También me gustaría no agradecer, es más, desagradecer a Willy y Eva, a pesar de que Eva sea una amiga genial. Esto no es un premio Nobel, pero espero que sirva.

Por último, la familia. Primera en el corazón, ultima en los agradecimientos. Hagámoslo por orden genealógico entonces. Gracias a mis abuelos y abuelas. Gracias abuelo Paco, por estar toda la vida conmigo, ayudándome en absolutamente todo lo que podías. Gracias yaya Maruja por cuidarme también desde pequeño, y por esos buenos momentos en Benidorm. Gracias abuelo Isidro, por saber cuando había que tener mano dura. Gracias yaya María por esas llamadas todas las semanas para conectar a pesar de la distancia, y por esos paseos por la montaña y visitas a la finca. Gracias papa y mama, por hacerme ser quien soy ahora, a pesar de todos los problemas e inconvenientes que nos pone la vida por delante. Papa, estoy seguro de que te habría encantado fardar de que tu hijo pueda ser doctor. Siempre estarás con nosotros. Mama, ya tienes casa para venir a Paris cuando quieras, estoy esperándote.

Gracias tio Paco por esos libros que me enseñaron a pensar y a imaginar. Sin ti no estaría donde estoy. Y gracias por supuesto a Pili, por estar siempre dispuesta a recibirme. Gracias tio Pepe por enseñarme lo que es la Naturaleza con mayúsculas, por todos esos otros libros de ciencia ficción que me dejaste y que también me han traído a este momento. Gracias Lola por ser la voz de la razón muchas veces y por ser tan buena persona. Gracias Raúl y Jorge por ser mis hermanos, a pesar de las peleas, los gritos y las desconexiones del router para que me dejarais dormir. Ya sois unos hombres hechos y derechos y vais a llegar lejos. Gracias a los pequeñines, Eva y Sergio, por los juegos y las risas. Por último, gracias a Julieta, por acompañarme durante el doctorado, y en esta nueva aventura que va a ser el postdoc. Gracias por compartir tu vida conmigo, y por empezar esta nueva vida en Paris juntos.

Seguramente me falte gente, pero bueno, nadie es perfecto. Si sientes que faltas en estos agradecimientos solo tienes que llamarme, y te lo agradeceré personalmente. En todo caso, gracias por leer estos agradecimientos, y esta tesis. Espero que os guste.

David.

INDEX

Chapter 1: Introduction

1.1 MOTIVATION, OBJECTIVES AND OUTLINE

The antagonism between ferromagnetism, in which the exchange field tends to spin-polarize the conduction electrons, and singlet superconductivity, in which electrons form Cooper pairs with opposite spins, makes their coexistence challenging [1]. In bulk samples, this has been observed only recently in a P-doped $EuFe_2As_2$ compound with extremely weak exchange interaction between electrons and localized moments [2]. Contrarily, equal-spin triplet superconductivity can survive in strong ferromagnets, although only rare bulk materials are considered triplet superconductors [3,4].

Seminal theoretical studies [5] showed that triplet correlations can be generated at the interface between a ferromagnet (F) and a superconductor (S). Much work has followed to identify various mechanisms that can lead to the opposite-spin singlet to equal-spin triplet conversion. Generally, these include spin-mixing, which leads to generation of opposite-spin (S_z=0) triplet component out of the singlet one, and spin-flip, which produces the equal-spin (S_z=$\pm$ 1) triplet component. At the microscopic level, those processes result from spin dependent scattering at interfaces with strong ferromagnets [6], and from the presence of an inhomogeneous magnetization [7–14] or a momentum dependent exchange field due to the spin-orbit interaction [15,16]. A number of experiments based on conventional (s-wave) low-temperature superconductors have found critical currents across S/F/S junctions for F thickness in the tens of nanometers range [17–21], which is much larger than expected for the singlet superconductor/ ferromagnet proximity effect, and therefore supports the triplet scenario. In these vertical junctions, the triplet generation was engineered through the artificial design of a magnetic inhomogeneity at the interface with the superconductor, e.g. by intercalating various ferromagnetic layers with different magnetic anisotropy or spin texture. Experiments on lateral (planar) devices, particularly based on the half-metallic ferromagnet CrO_2, found critical currents that decay over even longer distances –up to a few hundred of nm [22,23]. Because in half-metals the conduction electrons are fully spin-polarized, and consequently the penetration of opposite-spin singlet correlations is forbidden, that experimental observation was considered evidence for the generation of triplet superconductivity, which was explained [24] by the presence of strong spin dependent scattering at S/F interface combined with intrinsic magnetic inhomogeneities [25].

The generation of triplet pairs at proximity coupled interfaces between ferromagnets and superconductor opens the door to a wide category of unexplored phenomena in Josephson junctions with ferromagnetic barriers. The Josephson effect results from the coupling of two superconductors across a weak link or spacer –e.g. an insulator, a normal metal or a ferromagnet– to yield a phase coherent quantum state. In ferromagnets, singlet (opposite-spin) Cooper pairs decay over very short distances, and thus Josephson coupling usually requires a nanometric spacer. However, as theoretically demonstrated, in special conditions equal-spin triplet pairs are generated that can couple superconductors across thicker ferromagnets. Triplets allow explaining the observation of supercurrents across very thick (tens or even

hundreds of nm) ferromagnets combined with conventional low-temperature (few K) superconductors. Despite many hints of triplet superconductivity, very long-range Josephson effects have remained elusive, especially in the intriguing case of unconventional high-temperature superconductors combined with half-metal ferromagnets.

This scenario constitutes the main motivation of this thesis. We want to examine the possibility of a very long-range Josephson coupling across the half-metallic manganite $La_{0.7}Sr_{0.3}MnO_3$ (LSMO) combined with the superconducting cuprate $YBa_2Cu_3O_7$ (YBCO). The objectives result naturally of this motivation. 1) We want to show a long-range Josephson coupling across a half metallic ferromagnet which would enable fully spin polarized supercurrents of great interest in a future superconducting spintronics. 2) We want to use ferromagnetic resonance to explore the effect of spin excitations on the ferromagnet superconducting interfaces with the aim of using superconducting layers to externally manipulate the magnetization dynamics in S/F hybrids.

Because of their fundamental and technological interest, heterostructures of unconventional (d-wave) high-temperature cuprate superconductors combined with half-metallic manganites have attracted much attention, and hints for triplet proximity effect have accumulated along the years: unexpected superconducting proximity effect [26], an induced superconducting gap [27–29], Andreev reflection and coherent transport [30,31], as well as supercurrents [32] over length scales of the order few tens-of-nm have been experimentally observed in vertical junctions (although at relatively low temperatures ~10 K). Notwithstanding, the demonstration of long-range Josephson effects has remained elusive. Proving Josephson coupling requires evidencing the macroscopic phase coherent state. A first signature is the observation of flux quantization effects in the critical current: in principle, the Josephson current must vanish for integer number of flux quanta, giving rise to the well-known Fraunhofer diffraction pattern [33,34] . While realized in triplet Josephson junctions based on with low-temperature superconductors [18,19,35], flux quantization effects have been never observed in cuprate/manganite junctions. They are clearly demonstrated in the present experiments. The second signature are the so called Shapiro steps in the I(V) characteristics measured under microwave radiation [36]. These originate from the current phase relation $I = I_0 \sin\varphi$, where the phase φ difference between the electrode evolves in time under application dc voltage bias V according to $\frac{\partial\varphi}{\partial t} = \frac{2\pi}{\Phi_0}V$, with $\Phi_0 = \frac{h}{2e}$ is the flux quantum, yielding an ac current with the Josephson frequency $\nu_J = \frac{V}{\Phi_0}$. Resonant absorption of microwave radiation occurs when the Josephson frequency is a multiple of the microwave's frequency, yielding steps in the I(V) curve measured under microwave illumination at voltages given in the conventional case by $V = n\Phi_0\nu$, with $n = 0, 1, 2, \ldots$

Anticipating the conclusion, in this thesis we unambiguously demonstrate extremely long range (micrometric) high-temperature (tens of K) Josephson coupling across the half-metallic manganite $La_{0.7}Sr_{0.3}MnO_3$ (LSMO) combined with the superconducting cuprate $YBa_2Cu_3O_7$ (YBCO). This is shown in planar junctions which, in addition to large critical currents and, quite remarkably, display the hallmarks of Josephson physics: i) critical current oscillations

driven by magnetic flux quantization; and ii) quantum phase locking effects under microwave excitation (Shapiro steps). The latter, unreported in the context of induced triplet superconductivity, display here an anomalous doubling of the Josephson frequency predicted by several theories. In addition to its fundamental interest, the marriage between high temperature, dissipation-less, quantum coherent transport and full spin polarization brings unique opportunities for the practical realization of novel superconducting spintronics concepts, and signals a path for novel strategies in quantum computing

The outline of the thesis is as follows:

- Chapter 1: Introduction. In this chapter the theoretical foundations and previous experiments on the matter will be described and analyze. The two principal effects that are measured in this thesis, Josephson effect and ferromagnetic resonance, will be described in depth. The choice of ferromagnetic and superconducting materials will be justified.
- Chapter 2: Experimental techniques. The techniques used for both the growth and measurements of samples in this thesis will be explained. Of special importance is the description of the two ferromagnetic resonance systems which have been set up from scratch in this thesis, both at CNRS-Thales and at Universidad Complutense de Madrid.
- Chapter 3: Proximity effect in Half-metal/Superconductor Josephson junctions. This is the most important of results of this thesis, and in this chapter the fabrication of superconductor/ferromagnet devices are explained and their measurements analyzed. The most important result is described, namely the finding of a superconducting long-range proximity effect in a half metallic Josephson junction at high (>50 K) temperature. This is the first time such a proximity effect has been observed over such a long distance and high temperature and constitutes an important breakthrough in the field of superconducting spintronics.
- Chapter 4: Proximity effect in Superconductor/Ferromagnet structures are studied by ferromagnetic resonance. After measuring the proximity effect by the usual magnetotransport characterization, ferromagnetic resonance experiments were performed. An increase of damping below the superconducting transition has been found in ferromagnet/superconductor structures, confirming and supporting the presence of triplet Cooper pairing in our systems.
- Chapter 5: Conclusions. The main findings of this thesis will be summarized, and the significance of the achievements described. The chapter finishes with a set of outlook remarks.

1.2 HIGH Tc SUPERCONDUCTORS: YBCO

First, we will talk about the origin of superconductivity, its properties and the different types of superconductors before introducing the YBCO characteristics.

1.2.1 DISCOVERY AND PROPERTIES OF SUPERCONDUCTIVITY

Materials behave completely different as a function of variables such as temperature, pressure, presence of light… And one of the most important properties that change with these variables is electrical resistance. Depending on how their resistance behave with temperature materials are classified into conductors, semiconductors and insulators. But what would happen if we approach the lowest temperature possible? This question was a highly debated one as H. Kammerlingh Onnes reached 4.2K by liquifying He in 1911. Before this, the lowest temperature was 20K (liquified H_2) and at that temperature all materials behaved as usual, conductors decreasing its resistance and semiconductors and insulators increasing it. The liquefication of He gave room to a wider type of experiments. One of them was to measure Hg at the lowest temperature possible. And it was found that around 4.2K mercury resistance became strictly zero. This was the first observation of superconductivity [37].

This new non-dissipative state had also some interesting features, it could be destroyed by three variables: temperature, electrical current and magnetic field, then we have three critical values characteristics of superconductors.

We can say that superconductivity is a macroscopic quantum phenomenon characterized by a zero-resistance state that can be broken by increasing current density, temperature and magnetic field.

There are two distinctive properties displayed by a superconductor, zero-resistance [38], Meissner effect [39]. Other two result from the superconducting state being a macroscopic quantum state, flux quantization [40] and Josephson effect [41].

According to the BCS theory, superconductivity is originated by Cooper pairs, which are two electrons interacting via a phonon. This Cooper pairs are bosons and then they follow a Bose-Einstein distribution in which all pairs can be at the fundamental energy of the system, contrary to a Fermi distribution in which each electron has a different quantum state. *All* the Cooper pairs then form a phase-locked state that can be observed macroscopically. The fact that the state is phase-locked is which allows the previously mentioned properties.

1.2.1.1 ZERO-RESISTANCE

A simplified explanation for the zero-resistance state is as follows: if there are charge carriers moving through a material without interacting it means there is no free states in which they can relax. Then their energies must be quantized and there must be a gap of forbidden energies. Only when the system's energy is large enough (due to temperature, current density or magnetic field), this gap can be surpassed, breaking the superconductivity and giving rise a dissipative state. Cooper pairs occupy the energy range around the Fermi energy ± an energy gap. Due to the Pauli principle the electrons forming a Cooper pair have the momentum +k and -k. If the conduction is mediated by Cooper pairs there is no free states to the pairs to be scattered (to dissipate energy and show a resistance).

1.2.1.2 MEISSNER EFFECT

When a material becomes superconductor, it excludes all magnetic fields from its interior, even when the magnetic field is already applied (contrary to the perfect diamagnetism), this is called the Meissner effect. This effect then cannot be explained only by the zero-resistance state, in which if you introduce a magnetic field supercurrent loops will be generated to exactly cancel the applied field, but in the case of a magnetic field applied before the superconducting

transition, there should not appear these supercurrents. One theoretical approach to the Meissner effects using the London and Maxwell equations is as follows:

$$\boldsymbol{\nabla} \times \boldsymbol{J} = -\frac{1}{\mu_0 \lambda_L^2} \boldsymbol{B}$$
$$\boldsymbol{\nabla} \times \boldsymbol{B} = \mu_0 \boldsymbol{J}$$

If we take the curl of the second equation and substitute the first equation, we obtain:

$$\nabla^2 \boldsymbol{B} = \frac{\boldsymbol{B}}{\lambda_L^2}$$

Given that $\nabla^2 \boldsymbol{B}$ is zero by Maxwell's equations, the only possibility for a superconductor is to have an infinite penetration depth or to have an exactly zero field inside it, even when the field was applied before the superconducting transition.

1.2.1.3 FLUX QUANTIZATION

The flux quantization follows from the Meissner effect. What happens if when we are cooling a superconducting material with an applied field and *it has a hole?* This Is known as a superconducting ring. The field then remains trapped in that hole because it is surrounded by superconducting material in which it cannot penetrate. In this case, the field does not have to be zero, but it must be quantized. An easy way to look at it is as follows: If there is a charged particle (a Cooper pair) traveling around a region in which there is a trapped magnetic flux, when it has completed a loop, the particle has acquired an additional phase which can be written in terms of the trapped magnetic flux as $^{2e\phi}/_{\hbar}$ being ϕ the trapped magnetic flux and 2e the charge of our particle. But the wave function is periodic $2\pi n$, so we have a contour condition:

$$\frac{2e\phi}{\hbar} = 2\pi n, \quad \text{with } n = 0, \pm 1, \pm 2 \ldots$$

In this case we have a condition for the flux trapped: it must be quantized, with a minimum value of:

$$\phi_0 = \frac{h}{2e}$$

1.2.1.4 JOSEPHSON EFFECT

A Josephson Junction is a junction formed by an insulator separating two superconductors. It is characterized by the flow of a current, proportional to the phase difference of the Cooper pair wave functions at both superconductors, in the absence of a voltage. Also, when there is a voltage applied to the junction, it will oscillate at a characteristic frequency depending on the voltage, radiating microwaves. This effect will be described in more detail in section 1.3.

1.2.2 *TYPES OF SUPERCONDUCTORS*

As a function of the behavior of the superconductors with the magnetic field we can define two types of superconductors [42]. Type I superconductors, as Hg, only have one critical magnetic field with an abrupt transition to normal state. Type II superconductors [43] as NbSn have two critical fields, the lower one below which the material is purely superconductor, and the higher one above which the material is purely normal. In between both there is a mixture of normal

and superconducting state composed by a normal state vortex lattice. An example of a phase diagram of both types of superconductors can be seen in Figure 1.1.

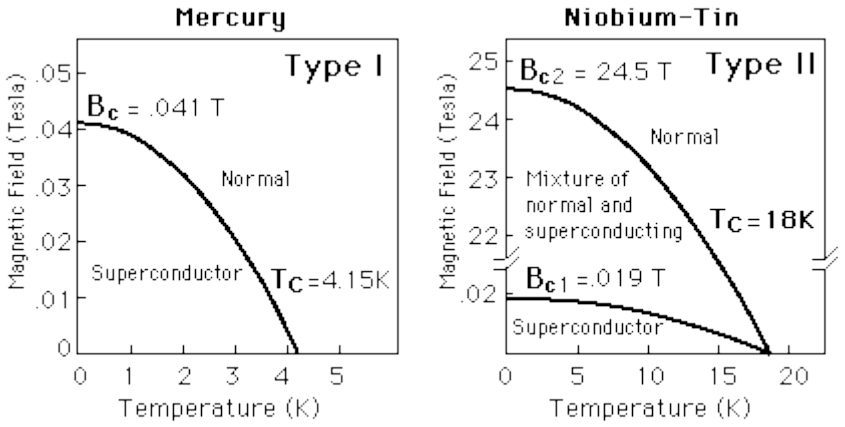

Figure 1.1: Phase diagram of different types of superconductors in function of the magnetic field. Note that the upper magnetic field of type II superconductors is orders of magnitude higher than the one for type I.

This mixed state in type II superconductors is due to the nucleation of normal vortex core, which has a radius of ξ (coherence length), surrounded by superconducting currents in a region of λ_L (London penetration depth). As was explained before, the field can penetrate through this vortex, because they are not superconducting, but the flux crossing them is going to be quantized. Also, if these vortices are not pinned, they are going to dissipate, breaking the superconducting state.

Another way to classify the two types of superconductors is using the parameter κ, which relates the magnetic penetration depth (λ_L) and the coherence length (ξ) as follows:

$$\kappa = \frac{\lambda_L}{\xi}$$

This variable defines the behavior of the superconductor in an external magnetic field. For $\kappa < {}^{1}/_{\sqrt{2}}$ we have type I superconductors and for $\kappa > {}^{1}/_{\sqrt{2}}$ type II. In Figure 1.2 we show how both variables evolve with the distance into the superconductor.

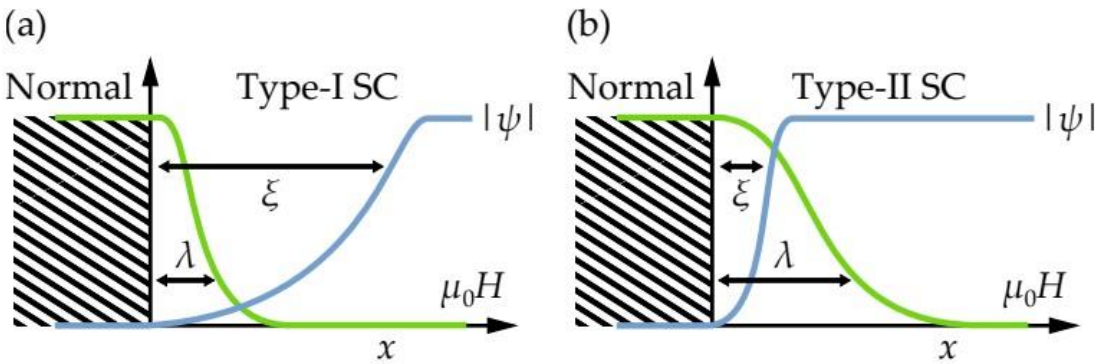

Figure 1.2: Evolution of the coherence lenght and penetration depth in function of the type of superconductors. For type I the magnetic field can penetrate less than in type II, but it has a much larger coherence length.

For the first case the system requires energy to generate a superconductor-normal interface, so the material remains in the Meissner state until the external field is above the critical field. For type II superconductors there is a critical field below which there is a perfect Meissner effect, but above it, it becomes energetically favorable for the system to let quantized magnetic flux

vortex to penetrate [44]. This is called the mixed-state or Shubnikov phase [45]. Superconductivity then is preserved until the magnetic field surpasses the upper critical magnetic field, and all material becomes normal.

The process from the mixed-state to the normal state is as follows. When the applied field is above the first critical field vortex are nucleated. When the field is increased the core of the vortex grow, until there is a field in which the core is so big that all the material is vortex core, i.e., normal material.

1.2.3 HIGH Tc SUPERCONDUCTORS. YTRIUM BARIUM CUPRATE (YBCO)

In this thesis the superconducting material used has been $YBa_2Cu_3O_7$ (YBCO). It is a high temperature superconductor with an optimal critical temperature of T_c=92K.

High temperature superconductivity (HTS) was discovered in 1986 by Bednorz and Müller [46] in $Ba_xLa_{5-x}Cu_5O_{5(3-y)}$ paving the way to a new era of superconductivity, in which non-conventional superconductivity would have a very important role. In 1987 the first compound with a superconducting transition above liquid nitrogen temperature was announced: $YBa_2Cu_3O_{7-\delta}$ with a Tc of 92 K [47]. The fact that liquid nitrogen was much cheaper than liquid helium made the research in high Tc superconductivity much more profitable than before. These HTS are type II, and BCS theory cannot explain them, so the theoretical effort to explain the origin of high Tc superconductivity is still on going.

One of the more important families of HTS are the cuprates, to which BLCO and YBCO belong. They are compounds based on copper oxides and are ceramic materials with a very rich and complex phase diagram (Figure 1.3) as a function of hole doping (or oxygen content). Its properties range from antiferromagnet to metal to superconductor to an exotic phase known as pseudogap [48]. In these types of materials, the Coulomb repulsion between electrons plays a very important role in their properties. The localization of electrons due to these interactions makes that at certain low charge doping they present a Mott insulator antiferromagnetic state. Above that state, for higher doping, a pseudogap opens in the energy spectrum of charge carriers around Fermi energy, close to a superconducting gap but without zero resistance. Above this pseudogap there is a Fermi liquid state with unusual metallic properties. Then if we keep increasing the doping, we obtain the superconducting state, which has a maximum critical temperature, and after that it starts to decrease again into a Fermi liquid.

YBCO is one of these HTS cuprates [47], and the one we have used in this thesis. It is also a strong correlated oxide, in which the oxygen content controls heavily all of its properties, as seen in figure 1.3. We use the oxygen doping for which the critical temperature is close to T=91K, $YBa_2Cu_3O_7$.

One of the main reasons why YBCO is so important is the pinning effect. In type II superconductors there are vortices, and if they are not pinned their movement generates resistance breaking the superconducting effect. In YBCO, due to the presence of defects (copper oxide precipitates, grain boundaries or oxygen vacancies) the pinning is huge, enabling the survival of superconductivity, but also artificial pinning can be used to enhance the superconducting properties [49].

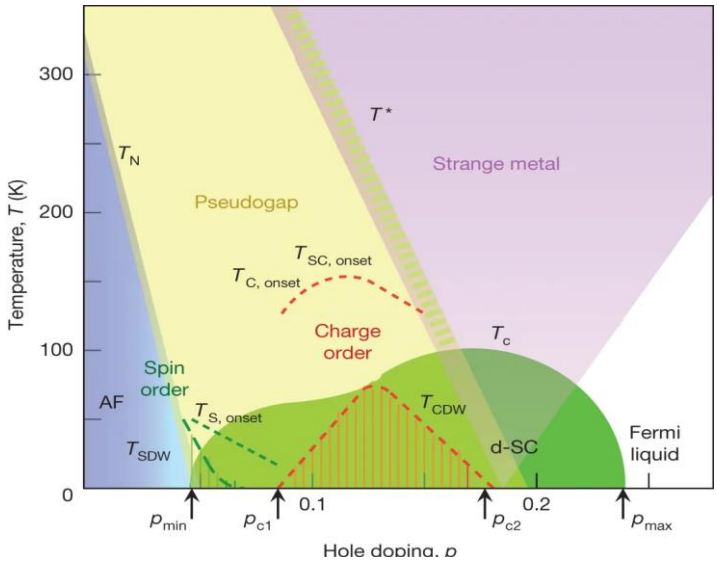

Figure 1.3: Phase diagram of cuprates in function of the hole doping (or oxygen content). Only for a small regime (from 0.05 to 0.275) there is a d-pairing superconductivity.[6]

YBCO structure consists on an oxygen deficient triple perovskite cell (orthorhombic structure) as can be seen in Figure 1.4 with lattice parameters a=3.82 A, b=3.89 A, c=11.68 A. The Y is at the center of the central unit cell, in the middle of two copper-oxide (CuO_2) planes which form two CuO_5 pyramids. After that, there is barium-oxide (BaO) plane, and finally in the direction of the b-axis, the CuO chains. Frequently there is a deficiency of oxygen in that chain, explaining why the oxygen stoichiometry is 7-δ.

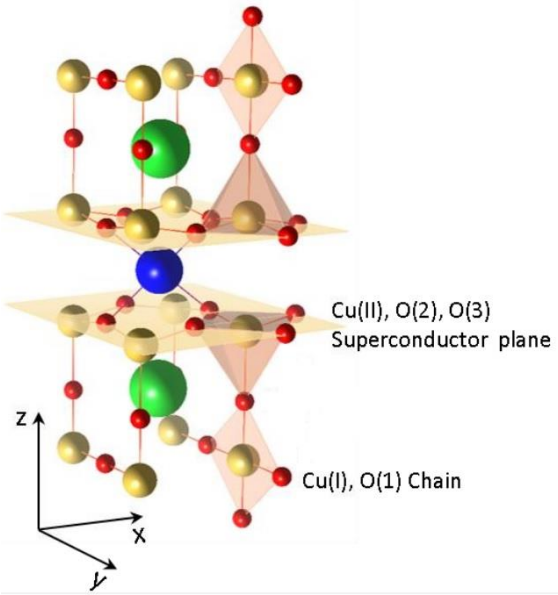

Figure 1.4: Crystalline structure of YBCO. The superconducting planes are believed to mediate the pair conduction, and the Cu chains acts as charge reservoirs to allow the correct doping in the planes

The CuO_2 planes are associated with the superconducting correlation, the pairs travel through the material by them, and this is allowed by the CuO chains, which act as charge reservoirs. Electrons are withdrawn from the CuO2 planes by interchanging electrons with the chains: there is a charge transfer from the CuO chains to the CuO_2 planes. In addition, YBCO doping can be controlled by changing the oxygen content of the CuO chain, making both components

fundamental in the superconducting state, and the main difference between YBCO and other HTS cuprates.

Also, of special importance is the fact that YBCO is a d-wave superconductor [50], i.e., its gap and order parameter is not isotropic (s-wave superconductor) in the momentum space (Figure 1.5)

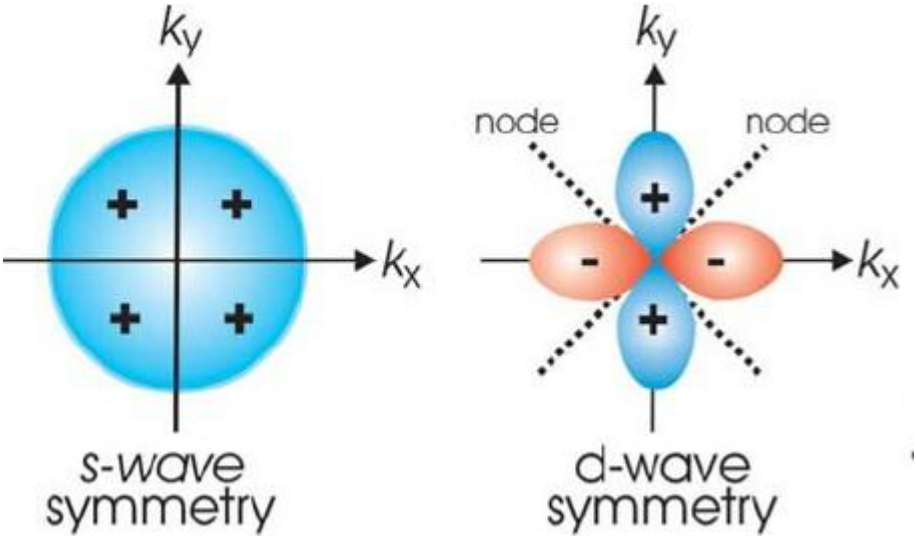

Figure 1.5: The sketch of order parameter symmetry in (a) conventional superconductors, (b) high- T C cuprates.

YBCO is a type II superconductor which in bulk presents critical fields H_{c1}= 0.024±0.002 T and H_{c2}=44±2 T [51], and a maximum critical current density [52] J_c=8 MA/cm^2 at zero field. Even presenting lower Tc than other cuprates such as BSCCO [53], YBCO is the most used superconductor in applications because of its highest irreversibility line i.e. the widest temperature and magnetic field region where this material can operate in the superconducting form.

1.3 PROXIMITY AND JOSEPHSON EFFECTS

1.3.1 SUPERCONDUCTIVITY AS A MACROSCOPIC QUANTUM STATE

Why does light from a lightbulb and light from a laser are produced in so different way? The light is composed of the same particles, photons, a quantum particle that can be both a particle and a wave. Why the production of a laser light is a “quantum” phenomenon and common light not? Why wood doesn’t behave as a quantum material even when it is composed by quantum entities (electrons, protons and neutrons)?

On the other hands, why do we have superconductivity? Why do we have SQUIDs (Superconducting Quantum Interference Device)? Why does superfluids have zero viscosity? How can we obtain laser light? Those phenomena can't be explained using classical physics. Those are inherently quantum macroscopic phenomena.

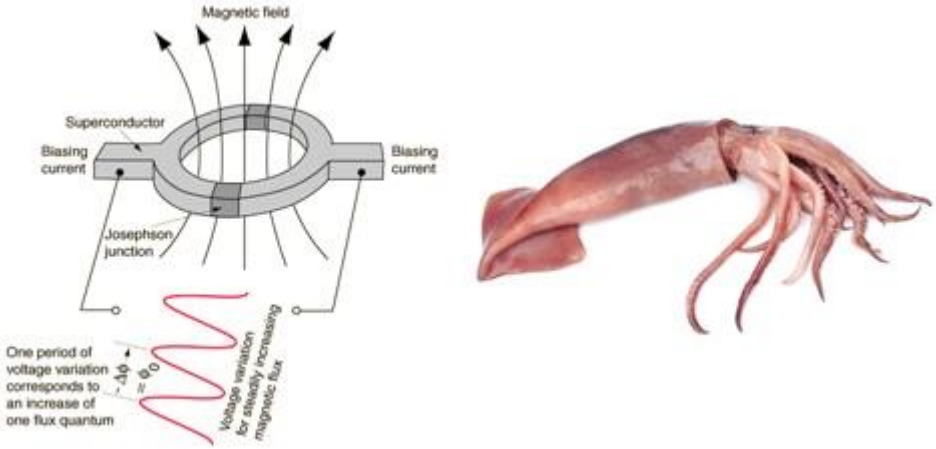

Figure 1.6. Scheme of a SQUID device composed of two Josephson junctions in a superconducting ring.

In macroscopic systems there are no quantum effects and the simple explanation is because the thermal motion masks them. If all the particles of the system can behave like waves, it means they can *interfere* and if they interfere destructively, we no longer have a quantum behavior. So, the key to have quantum effects is to avoid this destructive interference, but how? By having the particles correlated so their wave functions cannot interfere between them.

In superconductors that's exactly what happens, the particles (in this case, the Cooper pairs) are correlated which gives arise to a group of new macroscopic quantum effects, as the flux quantization. Superconductivity is a quantum phenomenon that manifests itself macroscopically.

For a better understanding of superconductivity, we have to look at the microscopic BCS Theory (J. Bardeen, L. N. Cooper and J.R. Schrieffer) [39]. This theory comes from the idea that in superconducting metals there is an attractive force between the electrons near the Fermi level (conducting electrons). This attractive force becomes so strong that below a certain temperature it can bind two electrons together, forming a new quantum state called Cooper pair, in which two electrons of opposite spins are coupled by a phonon. The radius (or distance between the two electrons) of this new Cooper pair is usually in the range between 10nm and 1 micron, while the lattice spacing is usually below the nanometer; this means that the individual pairs overlap strongly in space, its wave functions are always interacting which turns all process related to Cooper pairs in *Cooperative Effects*. The fact that the binding energy between the pairs depends on the number of pairs, and that the center of mass motion of them is strongly correlated allow us to describe the system by using only one macroscopic wave function $\Psi\,(\mathrm{r},\mathrm{t}) = \Psi_0(r,t)e^{i(\theta\,(r,t))}$.

This wave function describes the behavior of ALL Cooper pairs in a superconductor, and it also has its normalization conditions, which are:

$$|\Psi(\boldsymbol{r},t)|^2 = \Psi^*(\boldsymbol{r},t)\cdot\Psi(\boldsymbol{r},t) = n_s$$

$$\int \Psi^*(\boldsymbol{r},t)\cdot\Psi(\boldsymbol{r},t)\,dV = N_s$$

The first one meaning that the square root of the amplitude of the wave function is equal to the density of Cooper pairs and the second one that if we integrate over the space, we have to found N_s being the total number of Cooper pairs.

Now, when we have a normal metal, each electron has its wave function, and if we introduce their wave function in the Schrödinger equation (in the approximation of weakly or non-interacting particles) we obtain as follows:

$$\Psi(\boldsymbol{r},t) = \Psi_0(\boldsymbol{r},t)e^{i\theta\prime(\boldsymbol{r},t)} \qquad \hat{H}\Psi(\boldsymbol{r},t) = i\hbar\frac{\partial\Psi(\boldsymbol{r},t)}{\partial t} \qquad \hbar\frac{\partial\theta'(t)}{\partial t} = -E$$

Which means that the quantum behavior of these electrons is reduced to that of the wave function phase, θ. But this does not result in quantum correlations in normal metals. Electrons follow the Fermi-Dirac statistics, i.e., any two electrons can't be in the same quantum state, which means that these electrons can't have the same energy. If all of them have different energies, that means they have different phases. The temporal evolution of phases of the particle wave functions differs for all particles, which drops out when we sum over all particles. This way, there is no quantum correlations between particles, and hence, no macroscopic quantum behavior.

When we look at the same case in a superconductor, the scenario is completely different. Instead of electrons, we have Cooper pairs, which are particles with zero net spin (S=0), bosons. This means they follow Bose-Einstein statistics. In this case, particles can have the same energy, and they all can be at the lowest energy state at low temperatures. Because of that, their rates $\frac{\partial\boldsymbol{\theta}(\boldsymbol{t})}{\partial\boldsymbol{t}}$ are in fact identical. If we consider that the wave functions of the pairs are strongly overlapping because of the large size of pairs compared to the distance between them, we can affirm that all the pairs are forming a phase-locked state which can be described by a single wave function Ψ. Now the sum over all particles of the phase does not drop out and therefore macroscopic variables can depend on the phase θ. This phase in superconductors can change for different reasons, for example under the action of an electromagnetic field or by the presence of a discontinuity. The quantum dependence on phase leads to some of the most important superconducting properties, as the zero-resistance state, the Meissner-Ochsenfeld effect, the flux quantization and the Josephson effect, which is the leitmotiv of this thesis and which we will discuss in the next subsection.

1.3.2 THE JOSEPHSON EFFECT

The Josephson effect is the effect we observe when two superconductors are weakly connected by an electrical contact (usually a thin insulator). This effect was studied by Brian David Josephson, and his work lead him to win the Nobel prize of Physics in 1973 [54].

For a better understanding of this effect we can start with the classic non superconducting tunnel junction. A tunnel junction [55] composed of a normal metal (or semiconductor), an

insulator and a normal metal (or semiconductor) will have conduction electrons flowing through the insulating barrier when the applied voltage to the junction is above a threshold determined by the barrier, but also, due to the tunneling effect, there will be tunneling electrons flowing

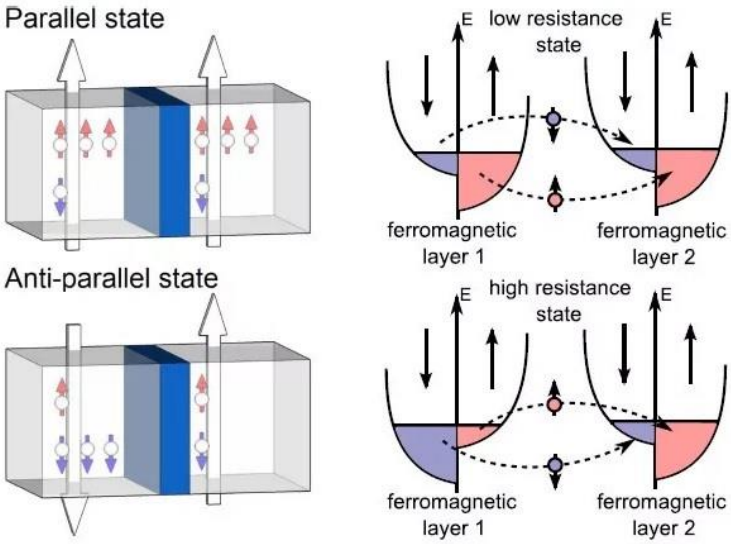

Figure 1.7: Depending on the alignment of the ferromagnetic tunnel junction there will be different states of resistance.

even when the applied voltage is lower than the barrier height. When we have a magnetic tunnel junction [56], the tunneling probability can be even less, due to the misalignment of the magnetization of the layers, which causes more resistance difference between the conductive (high applied voltage) and the tunneling (voltage below barrier voltage threshold) (Figure 1.7).

For superconducting tunnel junctions [57–59], the case is completely different. Now at T=0 at the Fermi level we only have Cooper pairs, which are composed of two electrons, and also we have a superconducting gap of 2Δ, so if the voltage applied to the junction is below 2Δ/e, there shouldn't be any current. Thinking classically, if two electrons have to tunnel, the probability would be the square of the probability of an electron. Luckily, this process is dominated by the quantum character of the Cooper pairs. The probability of a Cooper pair tunneling through the barrier is the same as that for a single electron because it is a coherent process, the Cooper pair behaves as a particle. It is the macroscopic wave function describing the entire group of pairs that is tunneling through the barrier. This wave function overlaps on both sides of the junction (if the barrier is small enough) and results in a binding energy. Apart from the tunneling of Cooper pairs, there is also quasiparticle (particles above the superconducting gap) tunneling, when the applied voltage is above 2Δ/e (Figure 1.8).

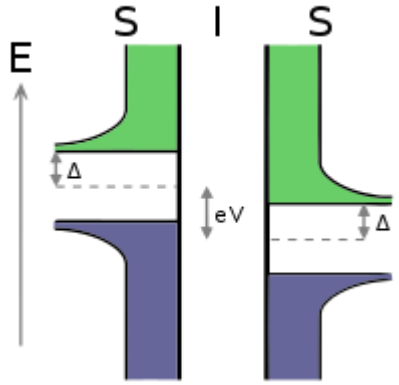

Figure 1.8.: Energy structure of SIS junction showing the superconducting gap when an energy is applied to the system

The Josephson equations then explain what happens to the supercurrent when the Cooper pairs tunnel through the junction and show theoretically interesting properties that can be used for numerous applications.

1.3.3 FIRST JOSEPHSON EQUATION: CURRENT PHASE RELATION

The first Josephson equation [60] links the current that cross the junction (Figure 1.9) with the phase across it.

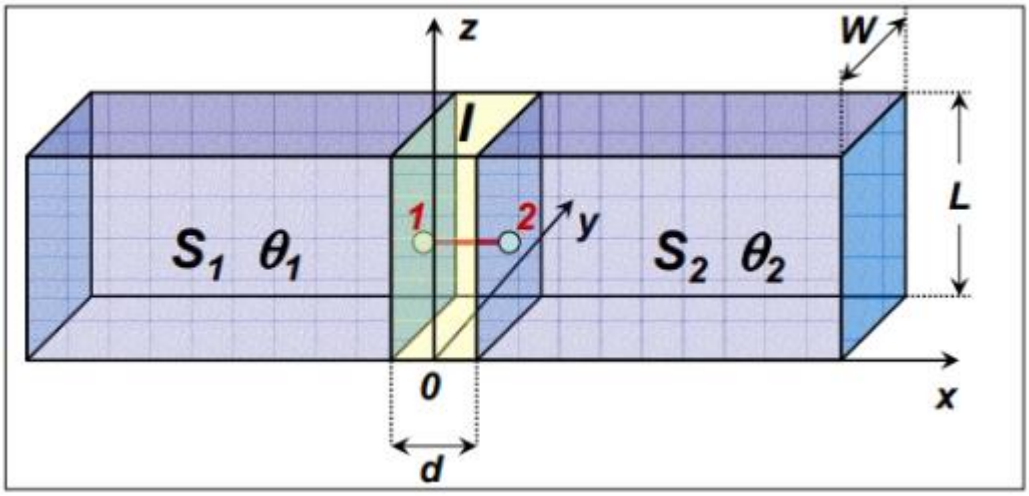

Figure 1.9: Josephson junction SIS. For the calculations we assume that the system is unidimensional and the supercurrent flows between 1 and 2.

First, we start with the supercurrent density in bulk superconductors, which depends on the gauge invariant phase gradient γ:

$$J_s(r,t) = \frac{q^* {n_s}^* \hbar}{m^*}\left[\nabla\theta(r,t) - \frac{2\pi}{\phi_0}A(r,t)\right] = \frac{q^* {n_s}^* \hbar}{m^*}\gamma(r,t)$$

Where q^* is the charge of a Cooper pair (2e), $n_s{}^*$is the density of Cooper pairs and m^* is the mass of the Cooper pair. If we look at this equation, the two factors that can change the current density are the phase and the vector potential, i.e., the magnetic field. If these values change through the barrier, there will be a change in the current density. And, in fact, without any external perturbation, there will always be a change in the phase, simply because the two superconductors are not connected.

Now, we integrate the gauge invariant phase gradient to see how it changes across the barrier:

$$\varphi(r,t) = \int_1^2 \gamma(r,t) = \int_1^2 \left[\nabla\theta(r,t) - \frac{2\pi}{\phi_0}A(r,t)\right] dx = \theta_2(r,t) - \theta_1(r,t) - \frac{2\pi}{\phi_0}\int_1^2 A(r,t)\, dx$$

If there is no field across the junction (we will explain this case in the Fraunhofer diffraction pattern), the only parameter that changes is the phase. Also, we must consider that any phase change of 2π in the wave functions of the electrodes have to result in the same wave function and that when $\varphi(r,t) = 0$, the critical current density is zero:

$$J_s(\varphi) = J_s(\varphi + n2\pi) \text{ and } J_s(0) = J_s(n2\pi) = 0$$

With these boundary conditions the only solution possible is a sinusoidal function with the argument being φ:

$$J_s(\varphi) = J_c\, sin(\varphi)$$

This means that the supercurrent density through a Josephson junction varies sinusoidally with the phase difference $\varphi = \theta_2 - \theta_1$ across the junction in the absence of any scalar and vector potentials.

1.3.4 SECOND JOSEPHSON EQUATION: VOLTAGE PHASE RELATION

The second Josephson equation [60] links the phase difference in the junction with the voltage drop across the junction (Figure 1.9). To obtain the second Josephson equation we use the time derivative of the gauge invariant phase difference.

$$\frac{\partial}{\partial t}\varphi(r,t) = \frac{\partial}{\partial t}\left[\theta_2(r,t) - \theta_1(r,t) - \frac{2\pi}{\phi_0}\int_1^2 A(r,t)\, dx\right]$$

Which lead us to the equation:

$$\frac{\partial\varphi}{\partial t} = \frac{2\pi}{\phi_0}\int_1^2 E(r,t)dx = \frac{2\pi}{\phi_0}\mathrm{V}$$

Where we can see that the phase depends on the voltage applied to the junction. In the case V=0 we recover the first Josephson equation in which the phase is constant. The fact that the phase is proportional to the applied voltage is a proof of the quantum interference effect of the macroscopic wave function of two superconductors in a Josephson junction.

When we apply a constant voltage to the junction, we obtain the voltage-phase relation, and we can introduce this value in the critical current:

$$\varphi(t) = \varphi_0 + \frac{2\pi}{\phi_0} V \cdot t \qquad\qquad J_s(t) = J_c \, sin\varphi(t)$$

This way, the Josephson current is oscillating at a frequency proportional to universal constants and the applied voltage. This fact is used as the more exact form of defining the standard volt, by applying a microwave of 0.4835979 GHz to a Josephson junction we measure exactly 1 nV.

The other way, the Josephson junction can be used to generate high frequencies using voltage to control it (0.5GHz with only 1 nV). Also, as can be seen in the equations, this effect doesn't depend on the superconducting or barrier materials, it has the exact same value always.

One of the most usual confirmation of the existence of a Josephson junction is the presence of the known as Shapiro steps [61] which are related to the second Josephson equation. When a microwave signal is applied to a Josephson junction, it resonates, and this resonance can be seen in the current vs voltage characteristic of the junction as steps (Shapiro steps) in voltage. In this thesis it has been represented as a plot in function of current, differential resistance and power of the microwaves, an usual way to portrait this effect as can be seen in Figure 1.10 [62].

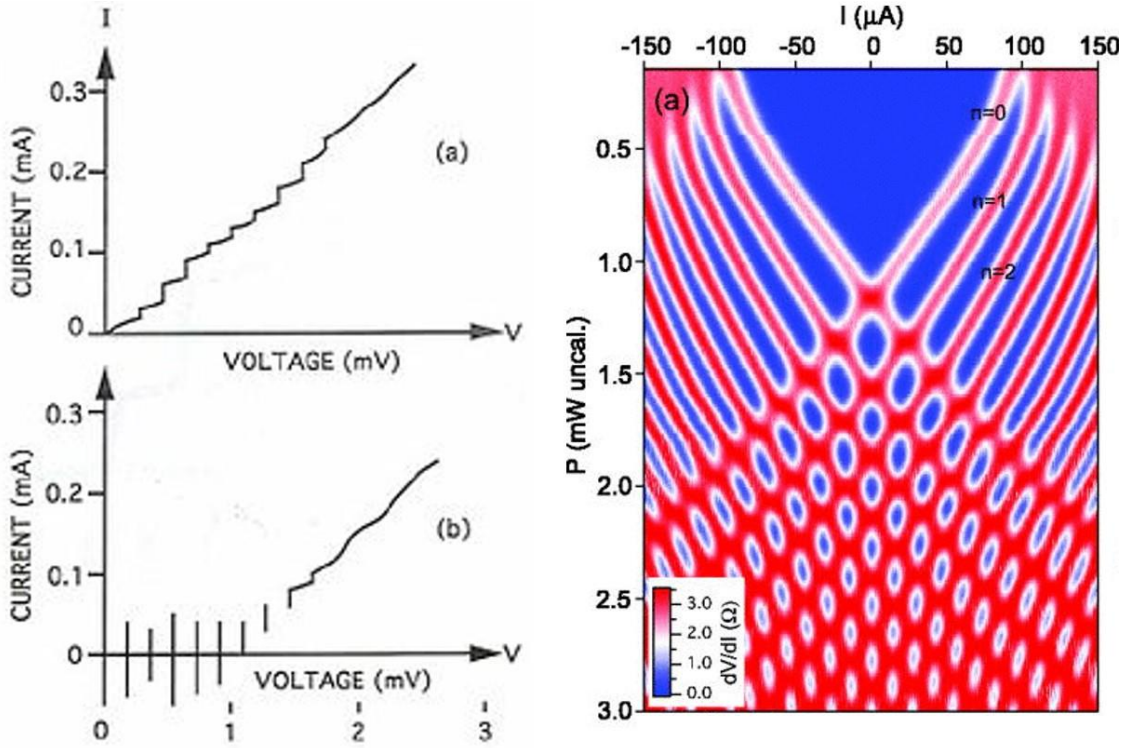

Figure 1.10.: Typical Shapiro step structure both in the IV and in the colour plot in function of the power of the microwaves.

Theoretically, it has been argued that in Josephson junctions with ferromagnetic barriers can be markedly non linear, allowing non integer Shapiro steps [63–65]. This steps could be caused by

the doubling of the Josephson frequency due to second order components (superharmonics). Half integer Shapiro steps have been experimentally observed in S/F/S vertical (tunnel) junctions with weak ferromagnets at the verge of the 0-pi transitions [66,67].

Not included in the Josephson equations, but equally important to the study of the Josephson junctions, is the appearance of the Fraunhofer pattern when a magnetic field is applied perpendicular to a junction.

1.3.5 FRAUNHOFER DIFFRACTION PATTERN

The Fraunhofer diffraction pattern [68] is observed when a magnetic field is applied perpendicular to a Josephson junction, and the critical current oscillates with a period of ϕ_0, a flux quantum. At zero field we will have the maximum of the critical current, but when the flux that crosses the junction is an integer times the flux quantum, we will have zero critical current, as can be seen in Figure 1.11.

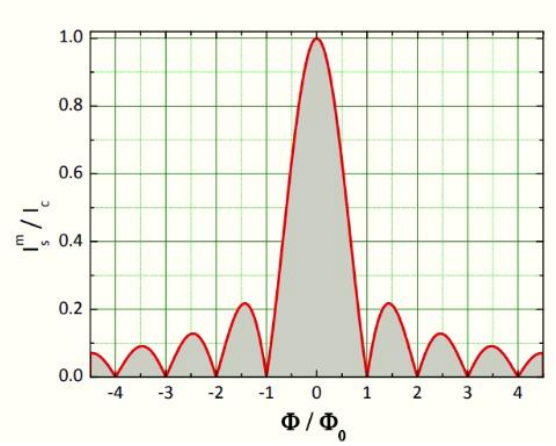

Figure 1.11: Fraunhofer pattern of a Josephson junction in function of the magnetic flux crossing it.

For previous Josephson equations we have neglected the term that goes with the potential vector A, and we have only considered the 1D problem. To understand the Fraunhofer diffraction pattern, which arises specifically from the potential vector, we have to take these two factors in consideration.

The Fraunhofer pattern is simply a spatial interference in Josephson junctions, generated by the

$$\varphi = \theta_2(\boldsymbol{r},t) - \theta_1(\boldsymbol{r},t) - \frac{2\pi}{\phi_0}\int_1^2 A(\boldsymbol{r},t)\, d\boldsymbol{r}$$

spatial changes of the gauge invariant phase difference when a magnetic field is applied:

Now that we have a 3D problem and also a magnetic field, we have to integrate over the surface that the magnetic field is crossing, as can be seen in Figure 1.12.

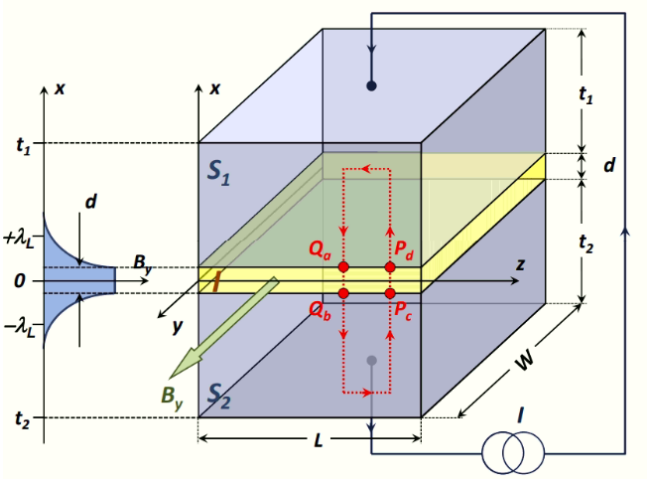

Figure 1.12: Josephson junction in which the field is applied in the y direction and current in the x direction. To calculate the gauge invariant we integrate over the closed contour between Qa, Qb, Pc and Pd, being Q and P any points of the junction at the interface with the superconducting contacts.

Being ϕ the total flux inside the junction ($B_y z d$, looking at the scheme of Figure 1.12), if we calculate the gauge invariant phase difference we obtain:

$$\varphi(P) - \varphi(Q) = \frac{2\pi\phi}{\phi_0}$$

The same way as in the Current-Phase relation, we introduce this value in the critical current density and we obtain:

$$J_s(y,z,t) = J_c(y,z) sin\left(\frac{2\pi}{\phi_0} B_y z d + \varphi_0\right)$$

But as the value we measure is the critical current, not the density, we finally can obtain the Fraunhofer diffraction pattern:

$$I_s = I_0 \left| \frac{\sin\left(\frac{\pi}{\phi_0} B_y z d\right)}{\frac{\pi}{\phi_0} B_y z d} \right|$$

As in the Voltage-Phase relation, this Fraunhofer pattern does not depend on the materials, but in the applied field and the dimension of the junction. This allows this system to be one of the best methods (when two Josephson junctions are in parallel) of measuring magnetic fields: the SQUID.

1.3.6 BASIC CONCEPTS IN PROXIMITY EFFECT

All the previous study of Josephson junctions has been carried out assuming that the barrier is an insulator, but as we mentioned the barrier can be any material that connects two superconductors via a weak link. Then the barrier can be a normal metal, a semiconductor, a lower Tc superconductor or even ferromagnetic materials (either metal or insulators).

In the case of a normal metal the maximum thickness of the barrier to have Josephson effect is given by the lifetime of the Cooper pairs in the metal (which is usually hundreds of nanometers. This allows a transport of Cooper pairs from one superconductor to the other, and it exists a phase difference [69].

For the case of a Josephson junction with a semiconductor barrier the effect is even more interesting because of the possible appearance of Majorana particles. This Majorana particles have been predicted when semiconductor wires are coupled to a superconductor, exactly what we have in a Josephson junction [70].

When the barrier is a superconductor with lower Tc that the contacts the problem is similar to that of the normal metal.

One of the most interesting cases is when the barrier is ferromagnetic [18–20,22,23,67,71]. Here we have two options, to have an insulating or metallic ferromagnet. Again, as in normal metals, there is a maximum thickness of the barrier given by the lifetime of the Cooper pairs in the material, but in the case of ferromagnetic materials this thickness is almost negligible. The spin of the electrons in the Cooper pair being antiparallel to each other makes the pair not stable under the high exchange field that exist in the ferromagnet, which tends to align parallel all the spins. This provokes a really small lifetime of the pairs in the ferromagnet. In contrast with normal metals (100 nm penetration), in metallic ferromagnets the penetration can be down to 1 nm or even zero, depending on the polarization of the ferromagnet [72] (Figure 1.13). The singlet component of the Cooper pair decays rapidly, depending on the spin-polarization of the ferromagnet, being the extreme case a half-metal in which the polarization is 100% and the singlet Cooper pairs cannot penetrate it. Even the triplet components with S=0 cannot penetrate the ferromagnet, although they are created at the interface S/FM. As we will see, even with all these problems superconductivity can exist in a ferromagnet, by achieving a triplet Cooper pair in which the spins of the electrons are aligned parallel. The process for which a non-superconducting material can exhibit superconducting properties when in contact with a superconductor is called superconducting proximity effect.

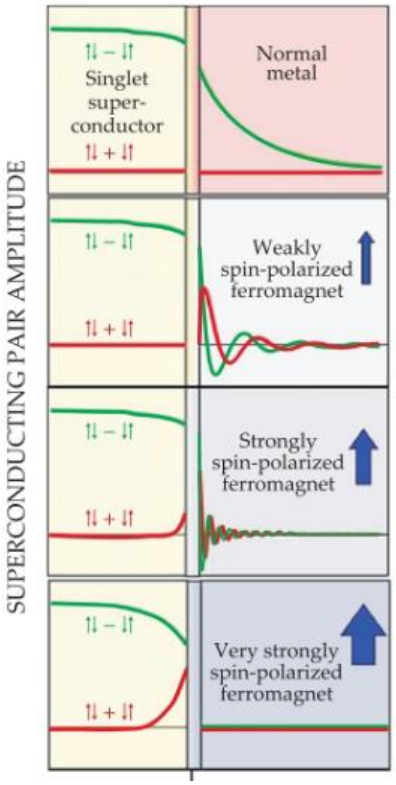

Figure 1.13: Decay of Cooper pairs (singlets and triplets S=0) depending on the polarization of the ferromagnet. The Cooper pairs will decay oscillating and exponentially, faster when the polarization is stronger.

The superconducting proximity effect happens when a superconductor is put in electrical contact with a non-superconducting material, and this one obtains superconducting properties, even in the absence of attractive electron-electron interactions. Usually this leads to a suppression of the critical temperature of the superconductor by the inverse proximity effect [73].

The mechanism that mediate this effect is called Andreev reflection [1,74,75]. It is the mechanism that converts single electron states, which are the origin of a dissipative electrical current, from a normal metal to Cooper pairs, i.e., a non-dissipative supercurrent.

To confirm the presence of Andreev reflection (or proximity effect) in a junction [73], there are some signatures we have to look for:

a) Andreev reflection is a process of two particles: to obtain a Cooper pair at the interface between a non-superconducting and a superconducting material, two electrons have to be transferred, which is equivalent to the transference of an electron and the reflection of a hole. This can be seen (for high transparency interfaces) as a sub-gap conductance twice the normal state conductance.
b) Andreev reflection also implies a perfect retro-reflection for electrons incident at the Fermi energy, which in a ballistic system results into resonance effects.
c) Andreev reflection conserves the phase coherence. The reflected hole necessary for the formation of a Cooper pair carries information both on the phase of the electron and on the macroscopic phase of the superconductor.
d) The impurities enhance Andreev reflection. These impurities do not suppress the quantum interference process and even provide a mechanism to redirect the trajectories of electrons to the interface. The presence of disorder in the metal results in a strong enhancement of the conductance of the junction.
e) The Andreev reflection of a hole is equivalent to the transfer of a Cooper pair out of the superconducting material. The proximity effect is in fact the leaking of Cooper pairs into the normal metal, and this process depends strongly on the presence of impurities and the transparency of the barrier.
f) The hole retroreflected has the same spin as the electron transmitted (because is the counterpart of the other electron that conforms the Cooper pair). But when we have a ferromagnetic material in which the energy bands are spin-dependent, this situation changes completely, as can be seen in Figure 1.14. For weak ferromagnets, the range of propagation of the holes is much shorter, and in half metals with 100% spin polarization it is strictly forbidden. This has much to do with the exchange field in the ferromagnet. The bigger the exchange field, the shorter will be the coherence length of the pair.

To sum up, for the existence of a proximity effect in normal metals, a conversion from electrons to Cooper pairs via Andreev reflection is necessary. This affects both the normal metal and the superconducting material [Figure 1.14].

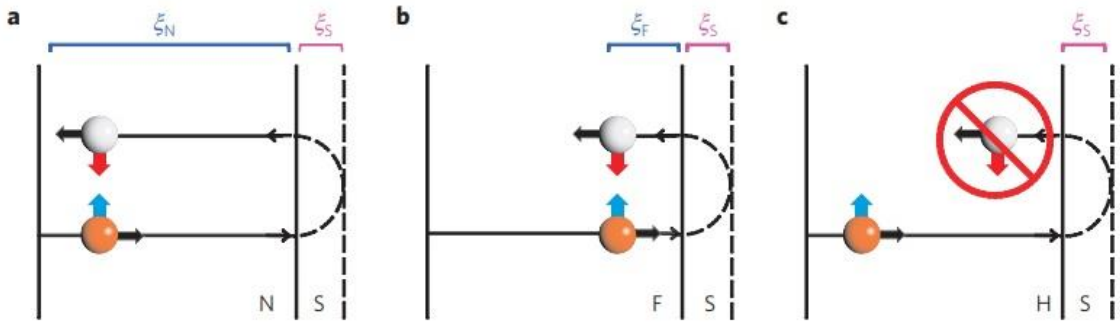

Figure 1.14: Pair electron-hole Andreev reflection. a) corresponds with a normal metal, in which there is long range phase-correlated propagation, b) in a ferromagnet, which is short-range, and c) in a half-metal in which the propagation of a hole with opposite spin is forbidden due to the 100% spin polarization at the Fermi level.

1.3.7 PROXIMITY EFFECT IN NORMAL METALS

Andreev reflection in metals is going to follow the usual properties, as there is no restriction in spin or extra exchange field that can break the correlations of Cooper pairs. In this case we will have different resonance because of the interaction of the phase correlated particles. There are two types of resonance, Tomasch resonances and McMillan-Rowell resonances.

Tomasch resonances [76] comes from the quasiparticle interferences in the superconductor side of the interface and is produced by the interference between the incident electron and the retroreflected hole. This interference happens for given energies:

$$\mathrm{V_n} = \sqrt{\Delta^2 + \left(\mathrm{nhv_F^S}/2\mathrm{d_S}\right)^2}$$

Where Δ is the energy gap of the superconductor, n is an integer number 0,1,2…, $\mathrm{v_F^S}$ is the Fermi velocity in the S and $\mathrm{d_S}$ is the thickness of the superconductor [77].

McMillan-Rowell resonance [34], on the other hand, is present in the non-superconducting part of the interface. The incident electron is reflected as a hole at the interface. In the S the mixed character of quasiparticles enables the interference between electron and hole, but in a non-superconducting material an electron and a hole cannot interfere. In order for the interference to occur in the N, the Andreev-reflected hole must maintain its phase coherence through the travel to the opposite interface and, after being normal-reflected, propagate back to the S/N interface to undergo a second Andreev reflection. This returns the hole to its original electron state. This double-reflected electron will interfere with the first incident electron, which gives rise to conductance oscillations. The voltage at which these oscillations appear is given by:

$$V_m = V_0 + mhv_F^N/4d_N$$

Where m is an integer number, v_F^N is the Fermi velocity in the normal metal, and d_N is the thickness. Notice that the McMillan-Rowell resonance requires that the electrons and holes maintain the phase coherence induced by the superconducting material a distance of $2d_N$. This implies that there has to be superconductivity order in the normal metal, which will have superconducting properties due to the proximity effect [34].

These two resonances can be better understood in Figure 1.15.

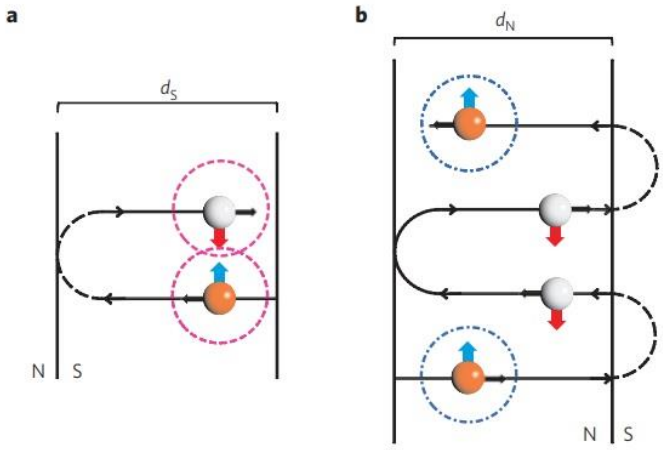

Figure 1.15: Scheme of Tomasch and McMillan-Rowell resonances in a normal metal / superconductor interface. The dashed lines denote the particles that are interfering in each case. Note that both resonances require Andreev reflection to be explained.

1.3.8 PROXIMITY EFFECT IN FERROMAGNETS

When we put a ferromagnet as barrier in a Josephson junction, or simply in contact with a superconductor there should be Andreev reflection. But for Andreev reflection to occur, there is the need of a hole with opposite spin to the incident electron. Then, the stronger our ferromagnet is (the higher spin-polarization at Fermi level), the more difficult (smaller coherence length) will be to have superconducting order in it. But even then, is it possible? Superconductivity and ferromagnetism are antagonistic mechanisms. Superconductivity is mediated by the Cooper pairs, which are two electrons of opposite spin interacting via a phonon. When this charged Cooper pairs interact with an internal magnetic field (vector potential) the superconductivity is depressed. If we add this to the fact that in ferromagnetic materials the spins of the atoms tend to align parallel, due to the exchange field present in it, the coexistence becomes even worse. These interactions lead to the paramagnetic effect of pair breaking and is similar to the situation when an external magnetic field is applied to the superconductor, in which the exchange interaction is played by the Zeeman interaction. Both when there is ferromagnetic material or an external field, the electrons are spin-polarized, so the spin up and spin down have different levels of energy excitations (Figure 1.16), and so the electrons of the Cooper pair have to travel through different energy bands. When this effect is too large the Cooper pairs became energetically unfavorable and they break into single electrons. Also, the magnetic scattering favors the breaking. Only taking this into account, the penetration of Cooper pairs into a ferromagnet would be even less than 1nm.

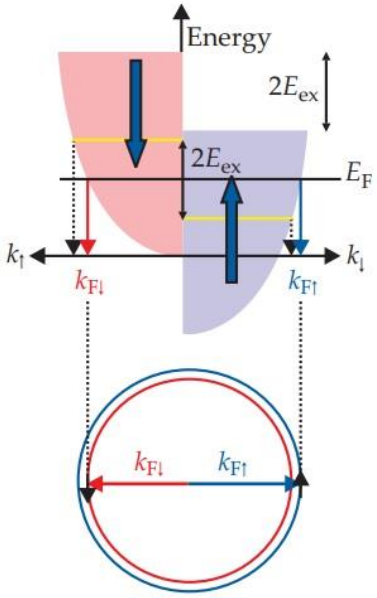

Figure 1.16: Splitting of energy bands due to spin-spin interactions in a ferromagnet. The exchange splitting shifts the momenta at the Fermi energy so two electrons with opposite spins will have different momenta given by the exchange energy. This effect leads to the modulation of the amplitude of the Cooper pair resulting in a mixed state of singlet and triplet component of zero spin.

1.3.8.1 LONG RANGE FERRO/SUPER PROXIMITY: TRIPLET CORRELATIONS

Even when the penetration depth of the Cooper pairs is so small, there have been experiments in which a proximity effect in ferromagnet has been observed, and we also have to take into account the existence of superconducting ferromagnets. Let's start with these ones.

Some crystalline materials have achieved coexisting singlet superconductivity and ferromagnetism, as rare-earth compounds $ErRh_4B_4$ [78] and $HoMo_6S_8$ [79] in which there is a coexistence in a narrow temperature region after its Curie temperature. Another way to obtain this coexistence is by introducing magnetic ions in a superconducting material. Both cases show a small effect in which the coexistence only survives a narrow temperature region.

Besides this conventional singlet superconductors, a new type of unconventional superconductors have been discovered, in which there are breaking of the spin rotational symmetry. This is the case for the spin-triplet pairing superconductors. But what is the spin-triplet pairing? When we have two paired electrons there is 4 possible combination of their spin states: singlet with spin zero, and triplet with spin 0, 1 and -1 (Figure 1.17)

This spin-triplet pairing can be observed in ferromagnetic superconductors. This are usually heavy fermion compounds, as UTe_2, UGe_2, URhGe, UCoGe and $EuFe_2(As_{0.79}P_{0.21})_2$ [3,80,81]. Even though, not many superconductors support triplet pairing, and those of them that support it are typically p-wave, which are very sensitive to pair breaking by normal impurities [82–87]. For this reason, the study of s-wave and d-wave superconductors has been growing in the last years because they are much more common in nature. The way to obtain ferromagnetic superconductors is then to use the proximity effect to induce superconductivity. The problem with this approach is that is not easy. To allow the long-range coexistence of superconductivity and ferromagnetism we need a spin triplet pairing that is not perturbed by the exchange

interaction of the ferromagnet. In a spin-singlet superconductor, there are some mechanisms to obtain different pairings between the electrons conforming the Cooper pair [1,6,82,83,88,89].

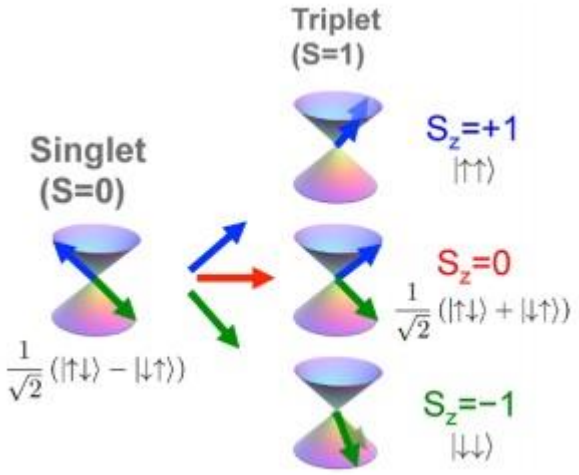

Figure 1.17: Four possible ways of combine two electrons with spin ½. There is one singlet state S=0, and three triplet states S=1. Each triplet state has a different z-proyection, 1, 0 and -1. Pairs with Sz=1,-1 are called equal-spin Cooper pairs.

If we start with a spin-singlet Cooper pair the first step is to obtain a triplet with Sz=0 [90]. When the paramagnetic effect in a superconductor is large enough or there is an external field, our Cooper pairs are going to relax into normal electrons or, the most interesting thing, change the pairing between them. There is two ways for the superconducting correlations to survive: the Cooper pair can become an equal-spin pair in which the spin of the electrons are parallel to the magnetization vector (even though obtaining this state is difficult due to the large conditions for its formation), or it can keep its spin antiparallel and acquire a nonzero center of mass momentum, which is known as the FFLO state (Fulde, Ferrell, Larkin and Ovchinnikov) [91,92]

When there is an exchange field in the superconductor the bands for spin up and down are shifted $2E_{ex}$, and this exchange shifts the momenta of the electrons at the Fermi level +Q/2 for spin up and -Q/2 for spin down, so the center of mass momentum of the Cooper pair will be ±Q. Now the two spin contributions to the pair amplitude are going to be proportional to $e^{\pm i[(k_{f\uparrow}-k_{f\downarrow})R]} = e^{\pm iQR}$ which means that the modulation of the pair amplitude will change with position R. Finally, we have a state that is a mixture of singlet and triplet spin states, both of them with zero spin projection:

$$(\uparrow\downarrow - \downarrow\uparrow) \rightarrow \left(\uparrow\downarrow e^{iQR} - \downarrow\uparrow e^{-iQR}\right) \rightarrow (\uparrow\downarrow - \downarrow\uparrow)\cos(Q\cdot R) + i(\uparrow\downarrow + \downarrow\uparrow)\sin(Q\cdot R)$$

This FFLO state can be induced in a proximity structure consisting in a ferromagnet adjacent to a superconductor, for which Q is perpendicular to the interface and proportional to the exchange splitting. This way, the stronger exchange in the ferromagnet, the faster will decrease the amplitude of the zero-spin state (superconducting pair amplitude). Also, not only the pairs that penetrate the ferromagnet will be affected, but the pairs present near the SF interface. The modification of this pairs is due to the phase shifts that electrons acquire when they penetrate the interface. If the interface is spin polarized, there will be a phase shift spin-dependent between the electron spin up and spin down of the pair, and it will acquire a phase difference during the reflection, which will lead to the same type of spin-mixing between singlet and triplet with Sz=0 as in the FFLO state [93] (Figure 1.18):

$$(\uparrow\downarrow - \downarrow\uparrow) \rightarrow \left(\uparrow\downarrow e^{i\theta} - \downarrow\uparrow e^{-i\theta}\right) \rightarrow (\uparrow\downarrow - \downarrow\uparrow)\cos(\theta) + i(\uparrow\downarrow + \downarrow\uparrow)\sin(\theta)$$

This also can be achieved by the precession of magnetization in the ferromagnetic material in a state of magnetic resonance, in which the orientation of the magnetization is precessing at high frequencies [94].

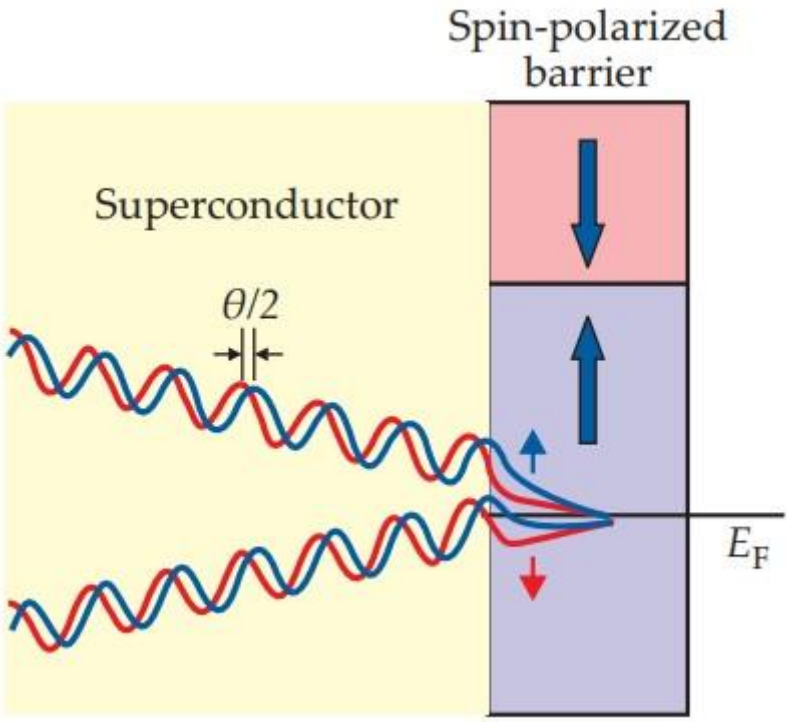

Figure 1.18: Phase acquired by electrons of a Cooper pair due to the presence of a spin-polarized interface. This allows the presence of triplets with net spin zero in the superconductor due to the reflected Cooper pairs.

Now we have a triplet state with Sz=0 whose amplitude oscillates inside the superconductor with a frequency proportional to the distance and the phase difference. This oscillatory character is which allows the formation of a π junction, in which the wavefunctions of the Cooper pairs have a phase difference of π between the two superconducting electrodes in the junction [95,96] (Figure 1.19).

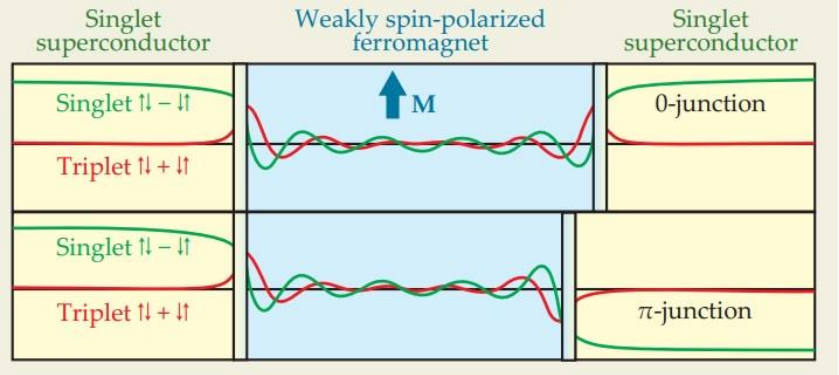

Figure 1.19: Ferromagnetic Josephson junction. Depending on the thickness of the ferromagnetic barrier there will be different type of junctions, from a 0-junction to a π junction, depending on the phase difference between the two superconductors.

Even though triplet pairing can be achieved, the fact that the ferromagnetic layer has to be weakly spin polarized and also its short range makes this coupling not very practical for future applications. The final goal to make this kind of effect more practical is to obtain long range correlations, and by using only the Sz=0 component of the triplet it is not possible. The solution: to achieve equal-spin triplet pairing [6].

This Sz=1 component of the triplet is not going to acquire a momentum when through a magnetic material, now the two electrons are in the same spin-band, and so they are not going to oscillate like the Sz=0 triplets and therefore they will be long range. This triplets will behave in a magnetic Josephson junction as singlets in a normal metal, they will not sense any exchange interaction if they are parallel to the magnetic moment of the barrier, making possible a penetration depth of the superconducting interactions in the order of microns.

On the other hand, to obtain a considerable amount of the Sz=1 component of the triplets is not easy. First, we need the Sz=0 triplet, which can be achieved by FFLO or by spin-mixing. As we have seen before, the proportion of these triplets will be much less than the one of singlets which will lead to an even less proportion of the equal-spin triplets. Then it is optimal to transform as much Sz=0 triplets to Sz=1 triplets as possible. The mechanism to obtain equal-spin triplets is quite simple, they are not rotationally invariants as the singlets are.

First, we need that the interface between the ferromagnet and the superconductor to have a magnetic moment perpendicular to the bulk magnetization of the ferromagnet. For example, we have the magnetization in the interface pointing in the z direction, then the zero spin triplets generated will have its spins pointing in the z direction, if the magnetization in the bulk is the same we will only have the zero spin component, because there is no rotation. On the contrary, if we have the magnetic moment of the interface in the y direction, the zero spin triplet will have the spins pointing in the y direction, and when the triplet crosses the interface it will be an equal spin triplet viewed respect to the magnetic moment pointing in the z axis inside the bulk ferromagnet. This can be seen as a change of basis depending on the magnetic moment of the ferromagnet. This can be better understood looking at the scheme in Figure 1.20 [6].

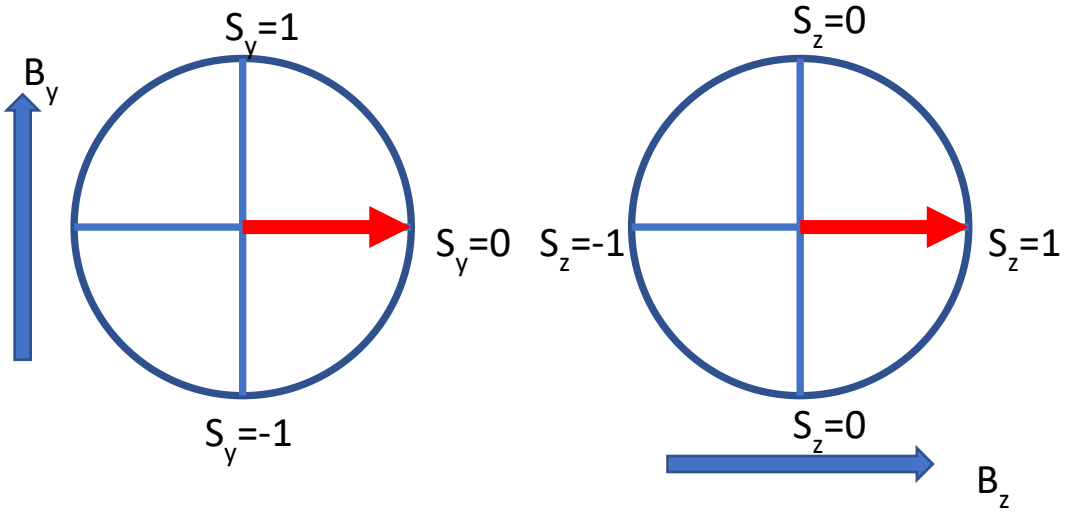

Figure 1.20: When we have a magnetic field pointing in the y direction, our spin projection is Sy=0. For the same spin if the field is applied in the z direction its projection is Sz=1. It can be seen as the first step is the formation of zero spin triplet at the interface and the second step is the projection of the triplet in the bulk. This way a zero spin triplet becomes an equal spin triplet just changing the magnetic basis. The equal spin triplet proportion will be maximized when the orientation between the magnetic moment in the interface an in the bulk is perpendicular.

Depending on the orientation between the magnetic moment in the interface and in the bulk, there will be a different proportion of zero spin and equal spin projection, being maximized the Sz=1 triplet when the magnetizations are perpendicular.

To sum up, we can obtain Sz=1 triplets by putting in contact a superconductor with a ferromagnet in which there is a region at the interface with magnetic moment perpendicular to the bulk. This perpendicular region can be an inhomogeneity in the ferromagnet that presents magnetization in the perpendicular direction with respect the bulk, as mentioned. There is a process of spin mixing (or FFLO state) in the interface and spin rotation in the bulk. Triplets are generated, but only the equal spin ones can survive more than a few nanometers in the ferromagnet. To make the equal spin survive even more, the use of half-metals (100% spin polarization at Fermi level) can reduce the magnetic scattering when the triplets have already been created. With this process we can achieve a long range superconducting proximity effect in a half-metal.

1.3.8.2 STATE OF THE ART

Even though the theoretical papers on long range proximity effect were published in the early 2000's [6,97], an experimental realization was not found until 2006 by Keizer [22].In their paper they found for the first time a long range (430 nm) spin triplet supercurrent through a half-metallic ferromagnet. They used NbTiN as superconductor contacts, separated between 310 and 430 nm depending on the device. A layer of CrO2 was below them, so when a current was injected between the superconducting contacts it had to flow through the CrO2. This can be seen in Figure 1.21.

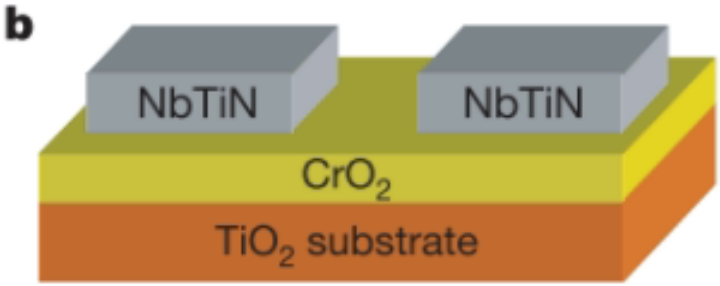

Figure 1.21.: Scheme of the device measured by Keizer. CrO_2 growth on TiO_2 with two NbTiN superconducting contacts on top of it.

They observed a critical current of the order of mA below 9K in 3 different devices, and a Fraunhofer like pattern with the magnetic field applied in plane perpendicular to the sample (FIGURE 1.22). Also they could change the critical current in function of the magnetization orientation.

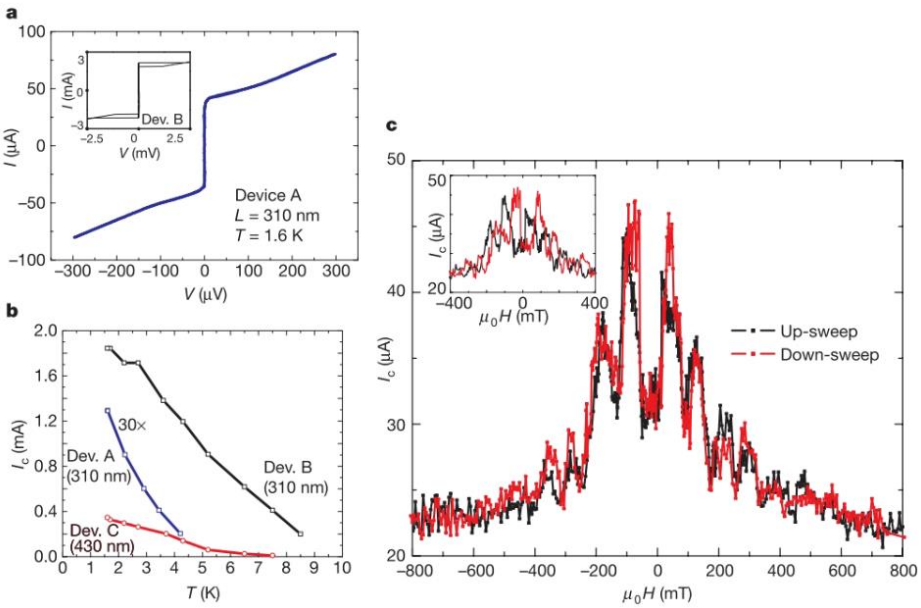

Figure 1.22: (a) Superconducting IV curve for device A and B. (b) Critical current in function of temperature for devices A,B and C. (c) Current in function of applied magnetic field

Anwar et al. [23] measured the same type of device with a CrO_2 separation and confirmed the presence of a critical current in these type of devices, but could not reproduce a Fraunhofer pattern (Figure 1.23).

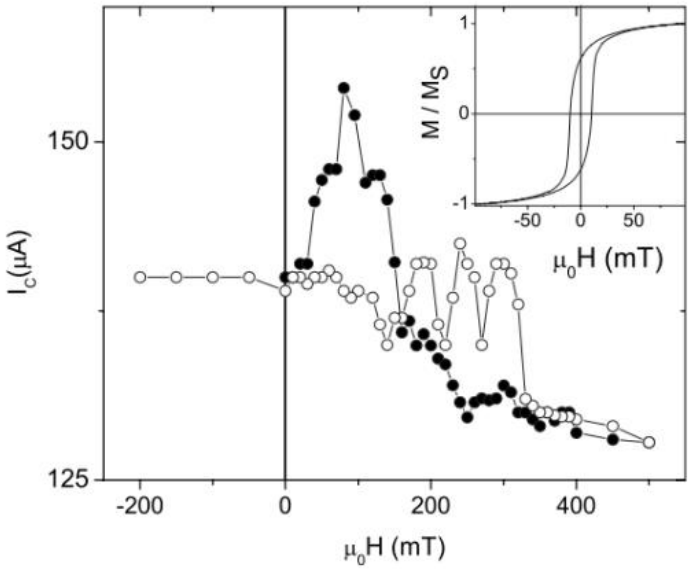

Figure 1.23: Critical current in function of applied field. There is no signature of Fraunhofer like pattern as in the previous paper by Keizer.

Wang et al. [98] measured single-crystal ferromagnetic cobalt nanowires with superconducting W contacts separated 600 nm. They found a zero resistance state below T=3.5K, and superconducting IVs whose critical current are heavely depressed under the application of magnetic fields perpendicular to the nanowire (Figure 1.24). They also measure longer nanowires (1.5um), in which there is no critical current, but a transition can be observed at similar temperatures and there is superconducting signatures in the resistance in function of applied field curves. Note that this case cannot be explained by spin triplet rotation, because of

the magnetic homogenety of the nanowire. Also, no indication of a Fraunhofer pattern is presented.

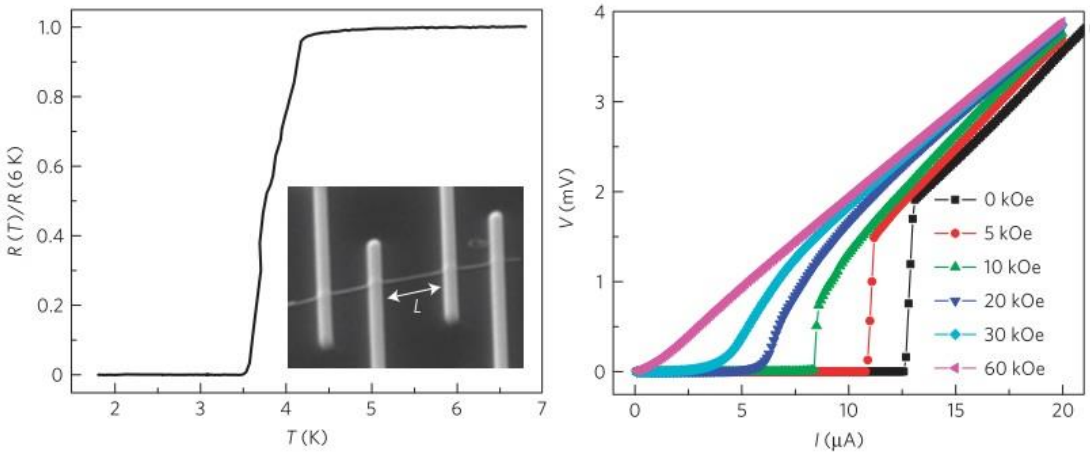

Figure 1.24: Resistance vs Temperature and IVs of a cobalt nanowire with two superconducting W contacts. A zero-resistance state was found, and critical current is depressed under application of out of plane magnetic field.

To the best of our knowledge, these three are the only papers that find a long-range proximity effect in a planar configuration. They show clear indications of proximity effect, though not a clear signature of Josephson junction. The Fraunhofer patterns are not canonical and there are no indications of Shapiro steps, which are the two ways of verifying a Josephson junction.

Apart from the in-plane configuration, also vertical Josephson junctions have been studied, with much smaller ferromagnetic separations, using conical ferromagnets or using additional ferromagnetic layers to allow the triplet formation.

The group of Norman Birge observed triplet superconductivity in junctions with Co and thin layers of weak ferromagnetic alloys that promotes the triplet formation [71]. The long range supercurrent can be then controlled by the thickness of this alloy layers. In Figure 1.25 we can see their results: a clear Fraunhofer pattern which corresponds with the junction and the different behaviour of the critical current when there is formation of triplets (red dots) due to the presence of ferromagnetic alloys interlayers.

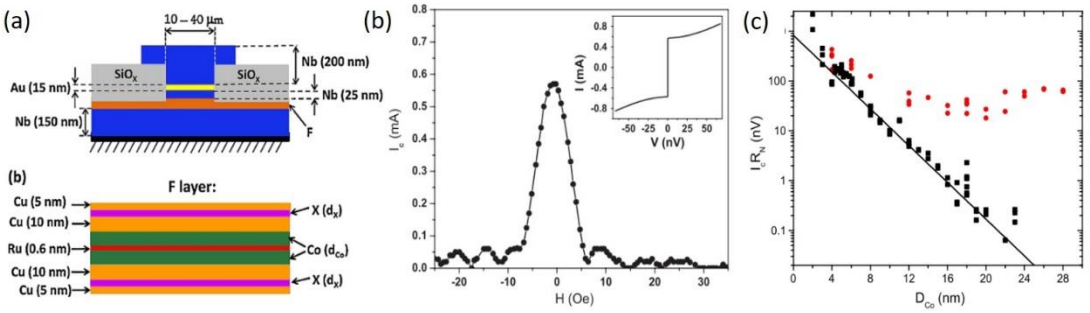

Figure 1.25.: a) Scheme of the sample, where X are the different ferromagnetic alloys. b) Fraunhofer pattern of the junction, with the IV characteristic of the system. c) Critical current times the normal resistance vs thickness of Co without weak ferromagnetic alloy (black dots) and with it (red dots). It can be seen the different behavior when the formation of triplets is allowed, in which case the critical current remains constant with the increasing of the Co layers.

Another way proposed to obtain triplet supercurrents is the use of conical ferromagnets. Because of the rotation of the magnetization the rotation from triplet S=0 to triplet S=1 becomes more probable allowing the existance of a triplet supercurrent. The group of M.G. Blamire studied this case [20]. They use again Co as ferromagnetic layer and Ho as conical ferromagnet.

In this case the central maximum of a supposed Fraunhofer pattern appears displaced from zero field depending on the thickness of Co. Also the existence of a critical current is observed in

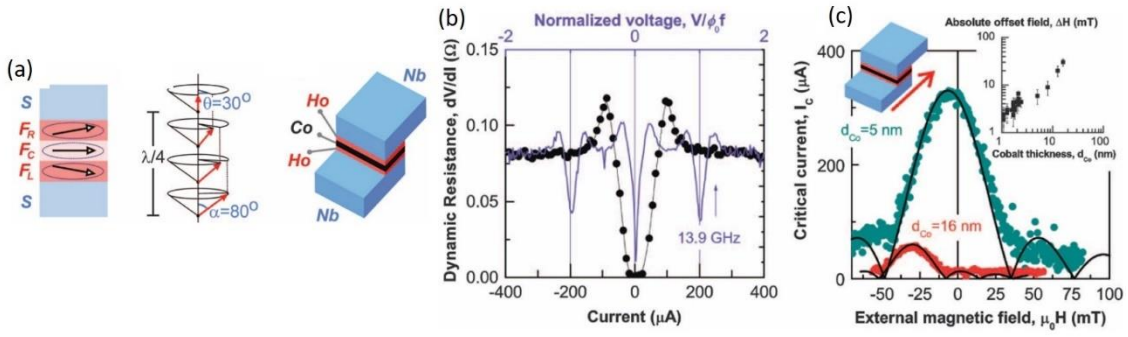

Figure 1.26.: a) Scheme of the sample, with Co between two layers of conical Ho. b) Dinamic resistance vs current, showing a critical current of tens of microampers. c) Fraunhofer patterns in function of Co thickness. The thicker the cobalt layer, the higher the center of the Fraunhofer pattern is displaced in field, due to the magnetic hysteresis.

dynamic resistance vs current measurements as can be seen in Figure 1.26

Studies, both in vertical junctions and in multilayers, have been conducted on the SC/HM YBCO/LCMO systems [99–105]. The proximity effect in vertical junctions have been studied also looking at its spectrostopic signature. In the work of C. Visani et al [106] evidence was found on the conductance vs voltage curve characteristics of McMillan-Rowell resonance on the YBCO/LCMO interfaces, which can only be caused by equal spin Andreev reflection. This proves the penetration of superconducting correlations in the LCMO. In Figure 1.27 we can see these resonances.

Still in the present day, superconducting spintronics is a very active topic in condensed matter, both theoretically [15,88,107–109] and experimentally [18,19,80,110]

1.3.9 SUPERCONDUCTING SPINTRONICS

With the new realization of equal spin triplets with superconducting correlations, the merge of superconductivity and spintronics open a new world of possibilities.

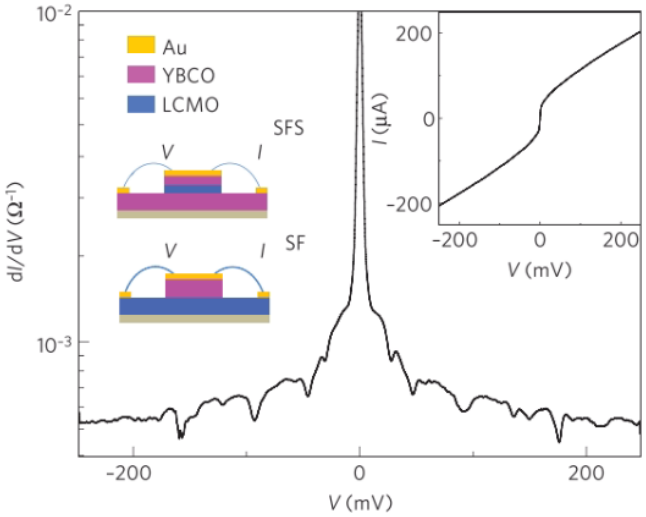

Figure 1.27.: Differential conductance vs Voltage for a vertical junction of YBCO and LCMO. There can be seen resonances at different voltages which correspond to both McMillan-Rowel and Tomasch resonances.

Spintronics adds a new degree of freedom to the traditional electronics, allowing not only to control the electron charge, but its spin. Spintronics have been a high step forward in data storage and transfer, as can be seen in the new solid state discs and magnetic RAMs. Also its future applications in quantum and neuromorphic computing [21,111–115] makes the field one of the most important and useful in condensed matter physics.

Superconductivity, on the other hand, adds very important properties to traditional electronics: zero resistivity and macroscopic quantum effects. The overheating of electrical components is a growing problem in the increasingly tendency of minimizing component size, in which the Joule heating limits the minimum size of, for example, transistors in a chip, which would be solved using superconductors, with the downside of having to work at liquid N2. Also, the macroscopic quantum effects of superconductivity can be exploited to quantum computing, specifically the possibility of continuously change the phase in Josephson junctions.

Superconducting spintronics joins the best of each worlds, the high data storage and transfer, and the zero resistance and quantum effects of superconductivity, making it the perfect field for the realization of quantum computing, and a field that has not stopped growing in the last decade.

1.4 FERROMAGNETIC MATERIALS: FROM PERMALLOY TO HALF-METALS

In this thesis the ferromagnetic materials used have been Permalloy ($Ni_{0.8}Fe_{0.2}$) and $La_{0.7}Sr_{0.3}MnO_3$ (LSMO). Permalloy [116] is a ferromagnetic alloy with a very high magnetic permeability, small coercivity, and significant anisotropic magnetoresistance. Also it has easy axis all along the plane, there is no preferred direction of magnetization [117]. LSMO [118] is a half-metal that presents colossal magnetoresistance (CMR) and its easy axis can be tuned depending on the strain induced by the substrate [119]. In our case LSMO was growth on top of STO, presenting easy axis of magnetization along the (110) and (1-10) directions, and the Py was grown on top of Au and with a capping layer of Al to prevent oxidation.

To understand better the experiments and how the ferromagnetism interacts with the superconductivity, an introduction on the underlying mechanisms producing magnetism will be explained [120].

1.4.1 ORIGIN OF FERROMAGNETISM

Depending on how a material behaves with an applied magnetic field, they can be classified as diamagnetic, paramagnetic or ferromagnetic. A diamagnet opposes its magnetic moment to the applied field; as we showed above, the superconductors behave as ideal diamagnets. Paramagnets align its magnetic moment along the applied field, but it does not have remanence, i.e. when the magnetic field is removed the paramagnet comes back to a non-magnetized state. For ferromagnets, the effect is as in paramagnets, when the field is applied the magnetic moments align, producing magnetizations much larger than in paramagnets. Also, there is a

remanence magnetic state even in the absence of applied field, one of the reasons why ferromagnetic materials are so important.

The origin of these states that interact with the magnetic field has to be found at the atomic level. The wave function of two electrons must be antisymmetric, which means that either the spin part is symmetric and spatial antisymmetric (triplet with both spins parallel) or the spin part is antisymmetric and spatial symmetric (singlet with antiparallel spins). Which state is more favorable for the system is given by the exchange integral J, defined by:

$$J = \frac{E_S - E_T}{2} = \int \psi_a^*(\boldsymbol{r_1})\psi_b^*(\boldsymbol{r_2})H\psi_a\ (\boldsymbol{r_2})\psi_b\ (\boldsymbol{r_1})d\boldsymbol{r_1}d\boldsymbol{r_2}$$

Where E_S is the energy of the singlet and E_T is the energy of the triplet. The spin-dependent term in the Hamiltonian can be written then as:

$$H^{spin} = -2J\boldsymbol{S_1}\cdot\boldsymbol{S_2}$$

If J<0 the singlet state with zero spin is favoured, and if J>0 the triplet state with S=1 is favoured. To generalize to a many-body system as a real material, interactions between all neighboring atoms must be considered, as can be seen in the Hamiltonian of the Heisenberg model:

$$H = -\sum_{ij} J_{ij}\boldsymbol{S_i}\cdot\boldsymbol{S_j}$$

Now, depending how these electrons interact there will be different types of exchange: direct, superexchange, RKKY and double exchange.

If the electrons interact directly with the electrons on neighboring magnetic atoms without the need for an intermediary it is known as direct exchange. But because usually there is insufficient overlap between neighboring magnetic orbital, exchange cannot be an important mechanism in magnetism.

If the electrons do not interact directly, we have different types of Indirect exchange: superexchange, RKKY and double change.

Superexchange is an indirect exchange interaction between non-neighboring magnetic ions mediated by a neighboring non-magnetic ion located between both magnetic ions. It arises because there is a kinetic energy advantage for antiferromagnetism. An example is two transition metals separated by an oxygen atom. If the system were perfectly ionic each metal ion would have an unpaired electron in a d orbital and the oxygen two p electrons in its outer occupied state. If both electrons in the metal are antiparallel, they can become delocalized over the whole structure, lowering the energy, but if they are parallel, they cannot, as can be seen in Figure 1.28 with Mn-O-Mn.

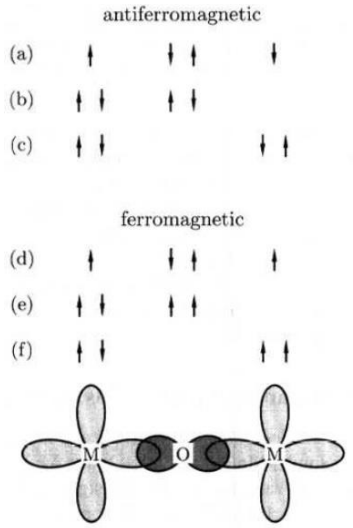

Figure 1.28: The arrows show the spins of the four electrons and how they are distributed over the transition metal. If the moments on the transition metal atoms are coupled antiferromagnetically (a. b, c), the ground state is (a) and this can mix with excited configurations like (b) and (c). The magnetic electrons can thus be delocalized over the M-O-M unit, thus lowering the kinetic energy. If the moments on the metal (M) atoms are coupled ferromagnetically (d,e,f) the ground state (d) cannot mix with excited configurations like (c) and (f) because these configurations are prevented by the exclusion principle. The ferromagnetic configuration therefore costs more energy.

In metals the exchange interaction between magnetic ions can be mediated by the conduction electrons. A localized magnetic moment spin-polarizes the conduction electrons and this polarization in turn couples to a neighboring localized magnetic moment a distance **r** away. The exchange interaction is thus indirect because it does not involve direct coupling between magnetic moments. It is known as the RKKY interaction (or also as itinerant exchange). The coupling takes the form of an r-dependent exchange interaction $J_{RKKY}(r)$ given by:

$$J_{RKKY} \propto \frac{\cos(2k_F r)}{r^3}$$

The interaction is long range and has an oscillatory dependence on the distance between the magnetic moments. Hence depending on the separation, it may be either ferromagnetic or antiferromagnetic. This is one of the explanations of why iron (and permalloy) are ferromagnetic.

In some oxides is possible to have a different form of ferromagnetic exchange interaction called double exchange. It occurs because the magnetic ion can show mixed valency, for example the same case as before Mn-O-Mn, but with one Mn having valence 3+ and the other 4+, as in $La_{0.7}Sr_{0.3}MnO_3$. Double exchange results from the coupling of hopping to magnetism to maximize kinetic energy. The parent compounds, $LaMnO_3$ and $SrMnO_3$ are antiferromagnetic insulators, mediated by superexchange through the oxygen. In $La_{0.7}Sr_{0.3}MnO_3$ the ferromagnetic alignment is due to the double exchange mechanism, in which an electron can hop to a neighboring site

only if there is a vacancy there with the same spin, not allowing an opposite spin due to the first Hund's rule. Because the ability to hop reduces the energy, the system aligns ferromagnetically to save energy. This also causes the material to become metallic. This can be better understood looking at Figure 1.29. One of the most important features of these double exchange ferromagnetic materials is the giant and colossal magnetoresistance, property that have made these materials of great interest for the electronics industry.

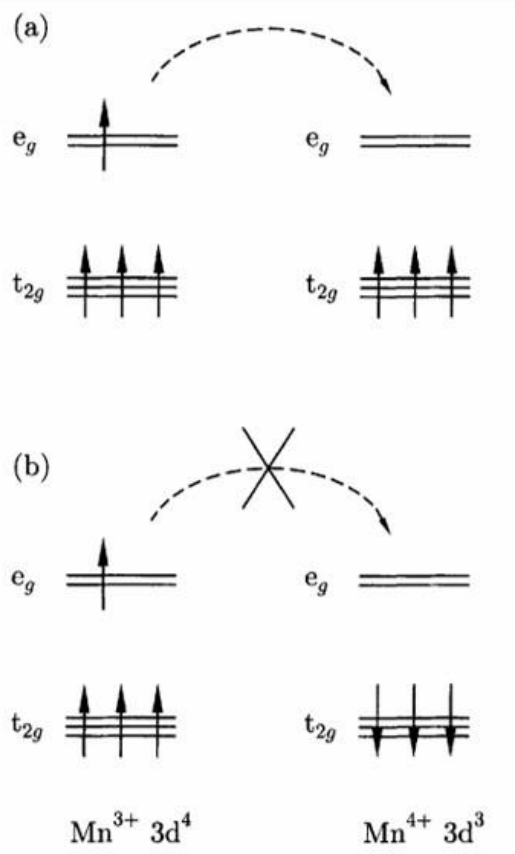

Figure 1.29: Double exchange mechanism gives ferromagnetic coupling between Mn3+ and Mn4+ ions participating in electron transfer. The single-centre exchange interaction favours hopping if (a) neighbouring ions are ferromagnetically aligned and not if (b) neighbouring ions are antiferromagnetically aligned.

1.4.2 PROPERTIES OF FERROMAGNETS: COLOSSAL MAGNETORESISTANCE

Magnetoresistance is the change in resistance of a material under an applied magnetic field. It is a technologically useful quantity because magnetoresistive sensors are extensively used in applications.

There are numerous types of magnetoresistance depending on its origin, as anisotropic, giant and colossal magnetoresistance.

Anisotropic magnetoresistance appears when there are differences in the resistance depending on the orientation of the magnetization with respect to the direction of the current. The physical origin of AMR is the reduction of the symmetry of a magnetized material compared to its non-magnetic state caused by the simultaneous presence of the magnetization and spin–orbit coupling [121].

The giant magnetoresistance is an effect due to the misalignment of magnetizations in multilayers containing ferromagnets. The first evidence of giant magnetoresistance was in Fe/Cr/Fe multilayers (Grünberg and Fert et al 1986, they won the 2007 Nobel prize for this discovery). It was found that the coupling between magnetic layers through a spacer layer oscillates in sign as the spacer thickness increases (which can be explained using the RRKY model, as explained before). For certain thicknesses it is ferromagnetic, and then is antiferromagnetic at larger thicknesses, and then returns to ferromagnetic. Also, the period of the oscillation depends on the non-ferromagnetic material and how good is the matching with the ferromagnet. But most important, the alignment between ferromagnetic layers can be changed from parallel to antiparallel in function of the applied magnetic field. When the layers are aligned ferromagnetically, the resistance is low, and when they are antiferromagnetic, the resistance increases. This phenomenon is what made this effect interesting for the implementation in classical computing, as hard drives and sensors.

Colossal magnetoresistance on the other hand, does not need multiple layers, but a single material. It is an effect that appears in materials with magnetism mediated by double exchange, because its magnetic state and conductivity are strongly related. Above Curie temperature the material is insulating and non-magnetic, but below Curie temperature it is metallic and ferromagnetic. Particularly near Tc the material shows an extremely large magnetoresistive effect, with a large difference between the state with and without applied magnetic field. One example (Figure 1.30) is the $La_{0.7}Ca_{0.3}MnO_3$, or $La_{0.7}Sr_{0.3}MnO_3$. [122]

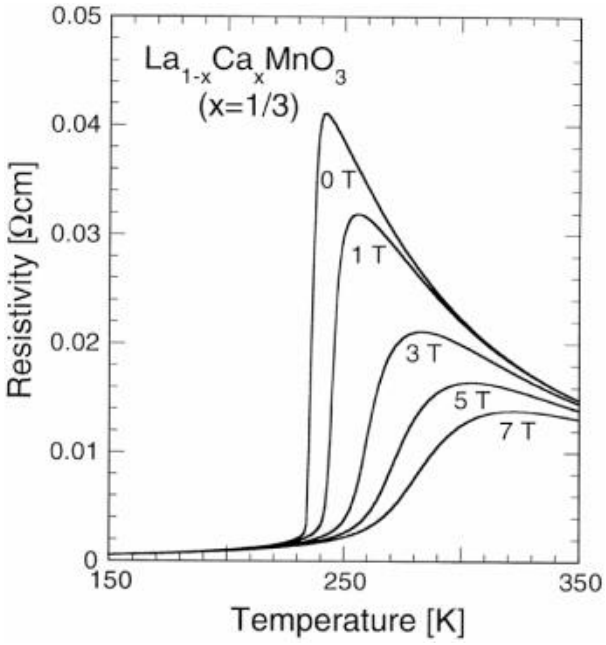

Figure 1.30: Colossal magnetorresistance in LCMO, showing the colossal change in resistance around the Curie temperature depending on the applied field.

1.4.3 PERMALLOY ($Ni_{0.8}Fe_{0.2}$)

Permalloy $Ni_{0.8}Fe_{0.2}$, or Py, is a ferromagnetic nickel–iron alloy that features high permeability, small coercivity, near zero magnetostriction, and weak magnetic anisotropy, which means that there is no preferential direction of magnetization, being possible to change it with a small

applied field yielding large anisotropic magnetoresistance. Its applications are of great interest in the field of electronics and computing, such as anisotropic magnetoresistance (AMR) and planar Hall effect (PHE) field sensors, magnetic recording heads and magnetoresistive random access memory (MRAM).

Py has a resistivity at room temperature around $\rho = 10^{-5}\ \Omega$ cm, a spin polarization close to 40%, a saturation magnetization of 1 Tesla and a damping parameter of α=0.006, and its properties does not change much with temperature, which shows how advantageous these properties are for spintronic experiments [117].

1.4.4 LANTANUM STRONTIUM MANGANITE ($La_{0.7}Sr_{0.3}MnO_3$)

LSMO is a complex oxide, as the YBCO and also a strongly correlated system, if the doping level or its composition is slightly changed, its properties change largely. Its Curie temperature is above room temperature at determined dopings, increasing its chances for practical applications. The phase diagram and resistivity vs. temperature for this compound at several dopings are shown in Figure 1.31 [123]. In this thesis we have used $La_{0.7}Sr_{0.3}MnO_3$. With this doping level the bulk Curie temperature is T_C = 369K, the saturation magnetization is M_S = 3.7μB/at Mn and the low temperature resistivity is $\rho = 8 \times 10^{-5}\ \Omega$ cm. Another important property of LSMO is that it is a half-metallic ferromagnet as demonstrated by spin resolved photoemission experiments [124]. The half metallic character of LSMO means that the minority spin conduction band is empty, so the material has 100% spin polarization at low temperature. This property is also related to the saturation magnetization of LSMO at low temperatures as it matches well the spin only value expected form all 3d electrons present in manganese ions: MS = 0.7 x Mn3+ (S=4/2) + 0.3 x Mn4+ (S=3/2) = 0.7 x 4μB + 0.3 x 3μB = 3.7 μB [125]. As previously explained, magnetism and conductivity are strongly related in this material due to the double exchange mechanism.

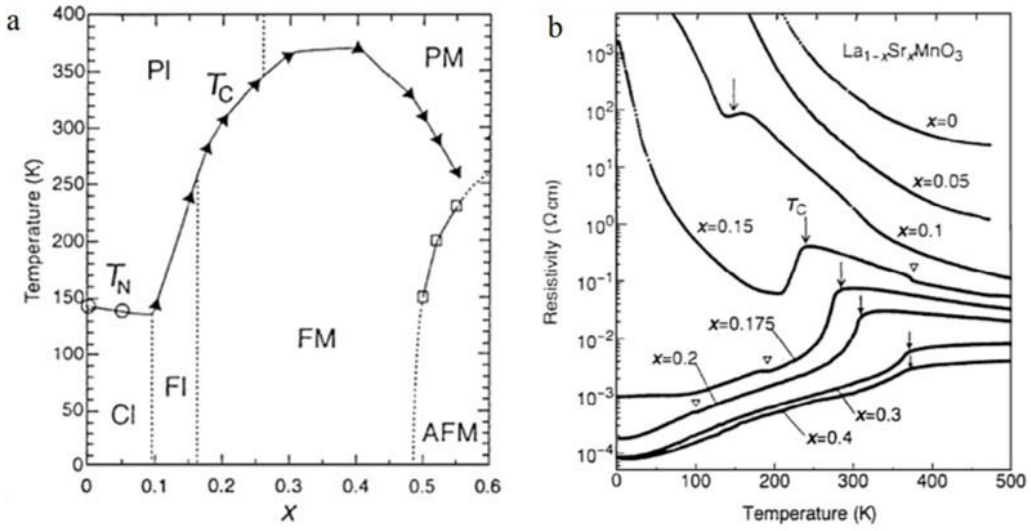

Figure 1.31: (a) Phase diagram of La1-xSrxMnO3 in function of Sr content. It can vary from antiferromagnetic, to ferromagnetic and from metal to insulator. (b) Resistance vs Temperature in function of the Sr content.

LSMO presents a rombohedral perovskite structure with a=3.876 A and α = 90.46º at room temperature. A scheme of its structure can be seen in Figure 1.32 [118]

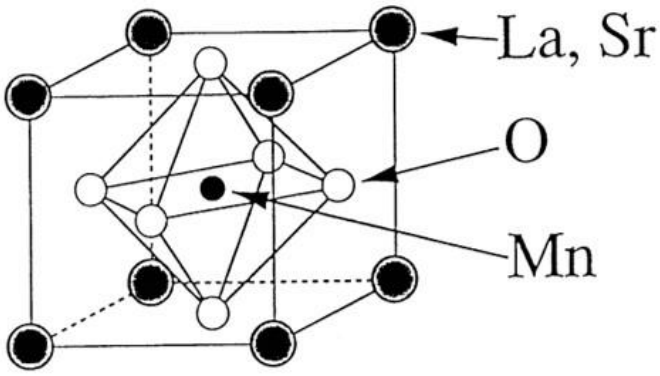

Figure 1.32: Arrangement of ions in the perovskite structure of manganites

A relevant issue related to LSMO thin film growth is the existence of so-called "dead layer" or critical thickness that can be defined as the thinnest layer for which metallic as well as ferromagnetic behaviors are observed. In different studies this dead-layer thickness for thin films was estimated to be 3-4 nm depending on the substrate chosen. For thin films grown on STO the LSMO dead layer thickness is estimated to be 8 u.c. [126]. The mechanism behind the dead layer problem is still controversial. The phase-separation phenomenon at the LSMO/STO interface where ferromagnetic insulating and metallic phases separate at a scale of a few nanometers is one of the possible explanations [118].

All these ferromagnetic materials have been used to study the superconducting proximity effect, by using magnetoelectrical measurements and ferromagnetic resonance measurements, which will be explained in next section.

1.5 FERROMAGNETIC RESONANCE (FMR)

Magnetization dynamics have relevant applications on a fundamental as well as on technological or industrial levels, what has boosted research in this field for the past decades. Knowing as much information as possible of the dynamics of a magnetic system is critical to understand the underlying physical mechanisms present in the system and to optimize device's performance based on the magnetic system. Magnetization dynamics are of interest in the magnetic recording and memory industry. In a hard drive, for example, when the information needs to be changed, the magnetic polarization needs to be reversed. How the magnetization behaves when this change is applied is of critical importance for device characteristics such as writing speed or power consumption. One of the most used techniques to measure magnetization dynamics is ferromagnetic resonance (FMR) [127–129]. This non-invasive method gives insight into both dynamic properties of samples, such as damping and loss mechanisms, and the static magnetic properties, such as magnetic saturation and anisotropy fields. FMR is one of the most used techniques for spintronics, as it is relatively easy to have information about spin-pumping process with it. FMR has been used for the last chapter of this thesis.

Ferromagnetic resonance measurement is a spectroscopic technique to probe the dynamic and static magnetic properties of a material, particularly the magnetization resulting from the magnetic moments of dipolar-coupled but unpaired electrons. FMR can be measured using two approaches: a cavity-based system where the sample is placed in a resonant cavity and

microwaves are applied at a fixed frequency whilst an applied magnetic field is scanned through the resonant condition, and measurements based on striplines and co-planar waveguides with the same procedure. Also, it is possible to use a fixed magnetic field and to vary the frequency, but it is much more time consuming and noisier.

In this thesis the method used has been a coplanar waveguide with a sweep in field at fixed frequencies, measuring the derivative of the absorbed power by using a lock-in.

1.5.1 MAGNETIZATION DYNAMICS

The origin of magnetism in transition metals appears due to the magnetic dipole moment of orbital electrons. The spin angular momentum is what generates a magnetic moment ***μ:***

$$\boldsymbol{\mu} = -g\frac{e}{2m_e}\boldsymbol{S} = \boldsymbol{\gamma S}$$

being g the Landé factor, e the electron charge, m_e the electron mass and γ the gyromagnetic ratio, which for a single electron has an approximate value of 28 GHz/T. Notice that the magnetic moment and the spin angular momentum have the same direction but different sign.

Now, when there is an applied magnetic field **H**, the **S** will be affected as follows:

$$\frac{d\boldsymbol{S}}{dt} = \boldsymbol{\mu} \times \boldsymbol{H}$$

But because S is proportional to μ, we can rewrite the equation as:

$$\frac{d\boldsymbol{\mu}}{dt} = \boldsymbol{\gamma}\,\boldsymbol{\mu} \times \boldsymbol{H}$$

Then the frequency of precession of the magnetic moments is proportional to the rotational of that magnetic moment and the applied field, and this equation describes the precession of an electron spin when a magnetic field is applied. When more than one spin is involved, we have to change the magnetic moment for the magnetization of the material **M**.

$$\boldsymbol{M} = \sum \frac{\boldsymbol{\mu}}{V}$$

$$\frac{d\boldsymbol{M}}{dt} = \boldsymbol{\gamma}\,\boldsymbol{M} \times \boldsymbol{H}$$

Of course, this is the ideal system, to make it closer to the real phenomenon we have to add several terms to address effects as demagnetization, anisotropy and possible losses.

Because our sample is a thin film, and we apply the field in plane, we will have only one component of the demagnetization field:

$$\boldsymbol{H_{demag}} = -4\pi\boldsymbol{M}$$

The anisotropy in the system, due to the orientation of the crystal lattice, also affects this phenomenon, causing an easy axis of magnetization in the material, so for example, a material with anisotropy along the (100) direction will experience an effective anisotropy field forcing the magnetization to point towards its easy axis:

$$H_{\boldsymbol{any}}\,\boldsymbol{x} = \frac{2K}{M_S}cos\varphi\,\boldsymbol{x}$$

with K the anisotropy constant and φ the angle from the x-axis. Of course, this is useful for calculating the easy axis of magnetization of a material.

Finally, we have losses in our system, and to take this into account, the Gilbert damping model is used, which adds a phenomenological damping term to the torque:

$$\frac{d\boldsymbol{M}}{dt} = \boldsymbol{\gamma}\, \boldsymbol{M} \times \boldsymbol{H} + \frac{\alpha}{\boldsymbol{M_s}} \boldsymbol{M} \times \frac{d\boldsymbol{M}}{dt}$$

with α being the Gilbert damping constant. This value gives us information of the rate at which the system losses energy in its precession. This is one of the most important parameters that can be measured using FMR, as it is closely related to the characteristic time scales for magnetization dynamics. This equation can be visualized in Figure 1.33.

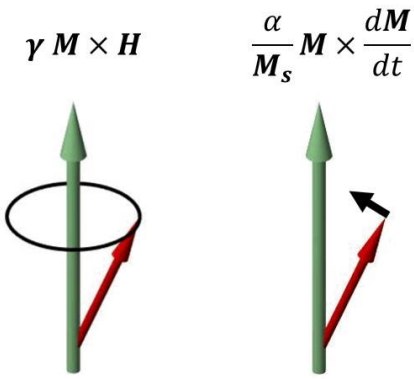

Figure 1.33: Visualization of the Gilbert daming model. The first term in the equation accounts for the precession of the magnetization around the applied field, and the second term accounts for the relaxation of the magnetization to its lowest energy state, in the same direction as the applied field.

In a simple case, with only the demagnetizing field and without energy losses, we can use an effective magnetic field to write:

$$\boldsymbol{H_{eff}} = \boldsymbol{H_{ext}} + \boldsymbol{H_{demag}}$$

$$\frac{d\boldsymbol{M}}{dt} = \boldsymbol{\gamma}\, \boldsymbol{M} \times \boldsymbol{H_{eff}}$$

By solving the differential equation, we can obtain the solution for the precession frequency, known as the Kittel equation [127] for in plane applied field:

$$\omega = |\boldsymbol{\gamma}| \sqrt{H_{ext}(H_{ext} + 4\pi M_s)}$$

Knowing then the magnetic saturation and the external magnetic field we can solve for the precession frequency, and vice versa, to obtain the magnetic saturation knowing the frequency.

Now, if we apply microwaves in our system, when the microwave frequency is the same as the magnetization precession frequency, the system will be at resonance, and a maximum power will be absorbed by the sample, ferromagnetic resonance or FMR. But first, to compensate the losses of the system, we have to apply an AC magnetic field perpendicular to the applied field. If not, the precession would disappear and the system would find the lowest energy state, without precession.

There are two ways to generate an FMR, by sweeping in field or in frequency. This can be understood looking at the Gilbert equation, which correlates the external field and the frequency. We can either fix a magnetic field and change the frequency or fix the frequency and

change the field, being this option the easiest way to measure FMR without a vector network analyzer, and the method that has been used in this thesis.

Something important to take into account, is that this precession is a classical macroscopic method to understand the system, but microscopically what happens is that the applied field creates a Zeeman splitting of the energy levels. The microwaves then can excite magnetic dipole transitions between these split levels (Figure 1.34) [130].

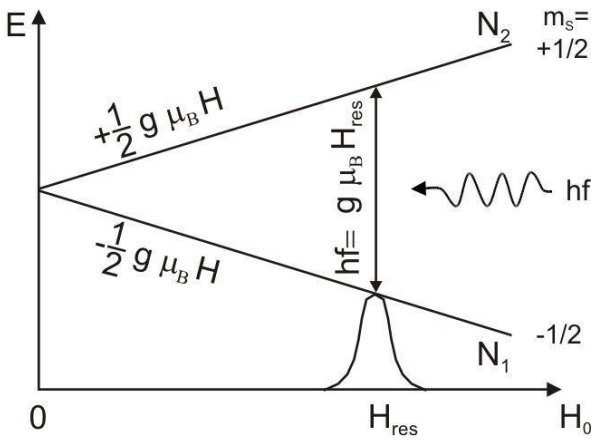

Figure 1.34: Microscopically, the magnetic field split the energy levels, and the resonance happens when the energy of the microwaves is the same as the hopping energy between the two states. Figure adapted from [39]

1.5.2 DAMPING AND SPIN PUMPING

One of the more important parameters that is measured by FMR is the damping (α). The damping gives us information about the magnitude of energy losses of the system. This can be better understood in Figure 1.35.

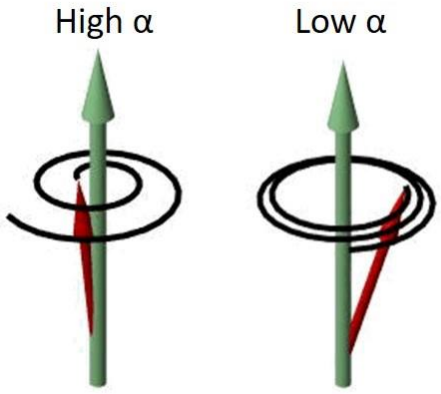

Figure 1.35: A material with high damping (α) will have a damped precession, but it will relax much faster than a material with low damping, in which the precession of the magnetization will have a larger lifetime.

This is of particular importance in the field of spintronics and magnonics, in which the lifetime of spin excitations is of extreme importance, needing then materials with low damping.

With FMR the damping is extracted by analyzing how the material behaves (its resonances) at different frequencies. A typical FMR signal is a Lorentzian absorption curve (or its derivative in the case of using a lock-in system). This signal gives two parameters of the system at that conditions: the resonance field H_{res} and the FMR linewidth ΔH (Figure 1.36).

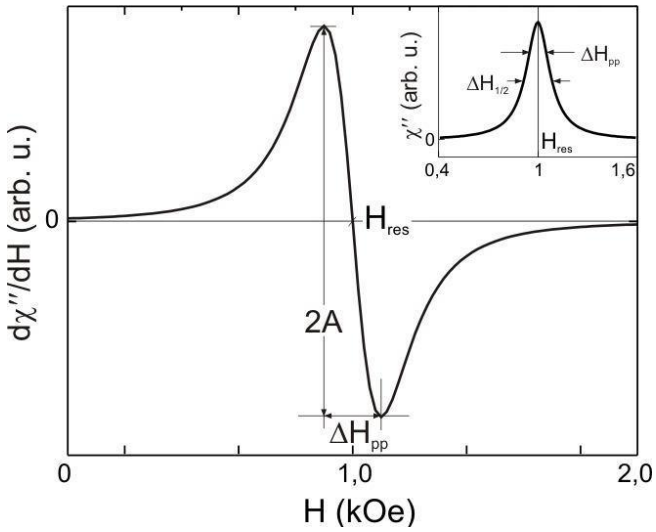

Figure 1.36: Usually it is easier to measure the derivative of the resonance, and not the pure signal (top right of the figure). The resonant field is the middle point of the resonance and ΔH is the linewidth, with $\Delta H_{pp} = \Delta H/\sqrt{3}$. Figure adapted from [39]

With the resonance field we can solve the Kittel equation to obtain the magnetic saturation M_s and with the ΔH_{pp} (or ΔH), we can calculate the damping:

$$\Delta H_{pp} = \frac{4\pi F}{\sqrt{3}\gamma}\alpha + \Delta H_0$$

Just measuring the signal at different frequencies and adjusting to the formula we obtain α. Now, we have an equation from which we can extract the damping, i.e., the losses of our system, but where does this energy go? There are numerous ways to relax the system, but the most important are three: magnons, heat and spin pumping.

The precession of the magnetization creates a spin imbalance in the direction perpendicular to the precession axis, generating a spin current. This spin current will eventually relax, depending on the spin diffusion length of the material, but if we have our ferromagnet in contact with another material, the spin current can be injected into it. In this case the spin current will also relax in the other material. Depending on the properties of the material different cases can occur. If the spin current relaxes quickly due to a small diffusion length, the system will appear as if it had a much bigger damping, but if there is no mechanism in the material to relax the spin current, then there should not be any change in the damping (Figure1.37).

An example of this is the case of a ferromagnet in contact with a superconductor. Because of the superconducting gap, there is no free states in the superconductor that can take the spin current, then it cannot relax in the superconductor, but when the temperature is above the critical temperature of the superconductor, there is no blockage of the spin current, which could relax in it, and the material behaves as a spin sink. This can be seen as a reduction of the damping as the temperature is lowered below Tc.

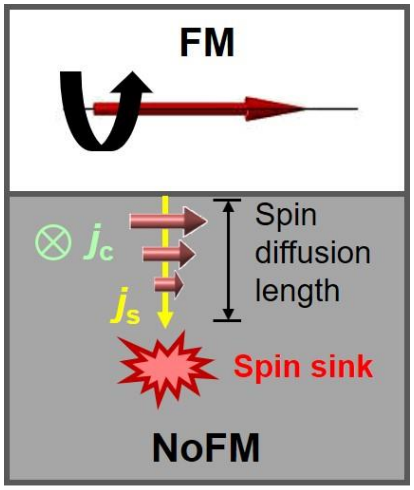

Figure 1.37: Spin pumping into a non ferromagnetic material. The spin current enters the NoFM and relax in it depending on its properties. It behaves as a spin sink, because it is an additional mechanism to relax the system

In this thesis the dissipation by spin-pumping into a superconductor has been studied, and how the proximity effect between a ferromagnet and a superconductor affects it.

1.5.3 PROXIMITY EFFECT IN FMR: STATE OF THE ART

Usually, when there is spin pumping from a ferromagnet into a normal metal, there is a relaxation all along the penetration depth of the spin current (Figure 1.38). The increase in damping caused by this relaxation will depend on the characteristics of the material, as a strong spin-orbit coupling or the presence of magnetic scattering centers.

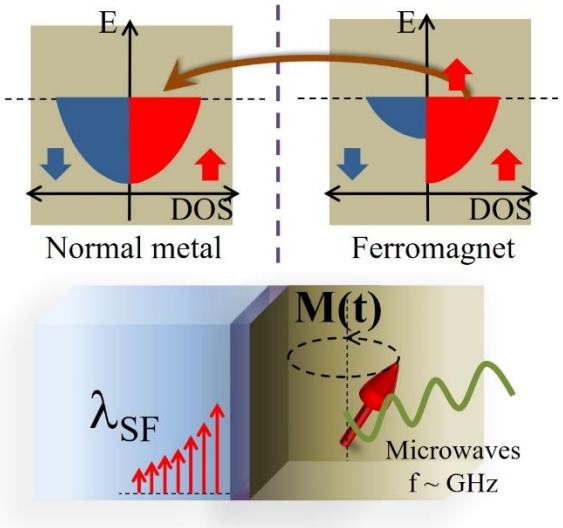

Figure 1.38: Spin pumping into a normal metal. The spin current can enter the metal because there is enough state to accommodate it. Then the spin current relaxes over a distance of λ_{SF}.

Now, if we have a superconducting material, the process changes completely. We have a spin current entering a material with its electrons aligned antiparallel, and also there is a gap in energies at the Fermi level (Figure 1.39). Above the critical temperature, the system behaves as a normal metal, but below T_c there is a blockage of the spin-current into the superconductor, lowering then the damping. Something important to notice is that the damping of the ferromagnet cannot be lowered when it is put in contact with another material, but the damping of the SC/FM system is lowered below T_c, compared with the damping above it.

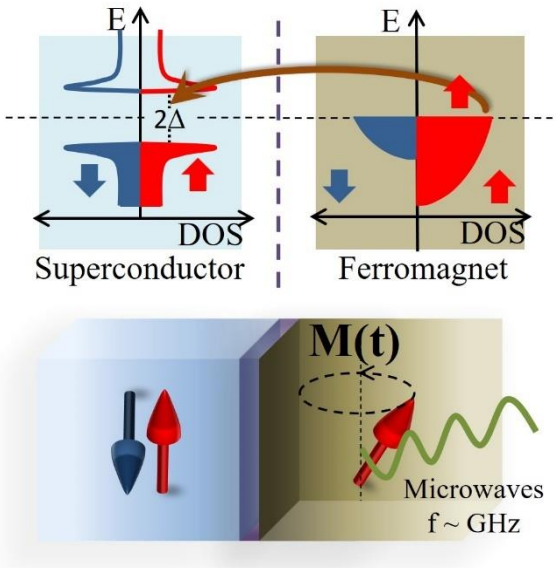

Figure 1.39: Spin pumping into a superconductor. The spin current cannot enter the superconductor because there is a gap in energies around the Fermi energy, avoiding then the relaxation of the spin current.

Of course, if there is a proximity effect due to triplet pairing in both the superconductor and in the ferromagnet, things should be different. If there are superconducting triplet pairs in the ferromagnet, there is a possibility of leakage into the superconductor, where the triplet is not stable and decays to a singlet (Figure 1.40). This process would increase the damping, contrary to the case with no triplet Cooper pairs, in which the damping diminishes due to the lack of penetration into the SC. Therefore, FMR can be a method to study the existence of a triplet superconducting state in ferromagnets.

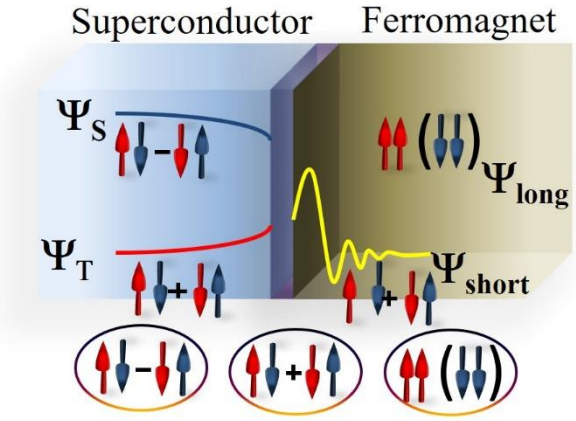

Figure 1.40: In a case of a superconducting proximity effect there is a mechanism by which the spin current, in the form of triplet Cooper pairs, can penetrate the superconductor and relax in it.

Another interesting case is the induction of a triplet pairing proximity effect due to a ferromagnetic resonance [131–136]. As explained in previous sections, to achieve triplet pairing a magnetic inhomogeneity is needed to allow the rotation between the S=0 and S=1 components of the triplet. But this rotation can also be produced by a temporal magnetic inhomogeneity, as present in a ferromagnetic resonance, instead of the usual spatial magnetic inhomogeneity (different magnetic domains).

In the last years FMR has been used to study the proximity effect, as the pioneering work of the group of J. Aarts [137] in which they measured superconductor/ferromagnet (Nb/Py) bilayers. They found that below the Tc of the SC, the linewidth of the resonance changed, diminishing its value compared with that of the normal state (Figure 1.41). It is important to take into account

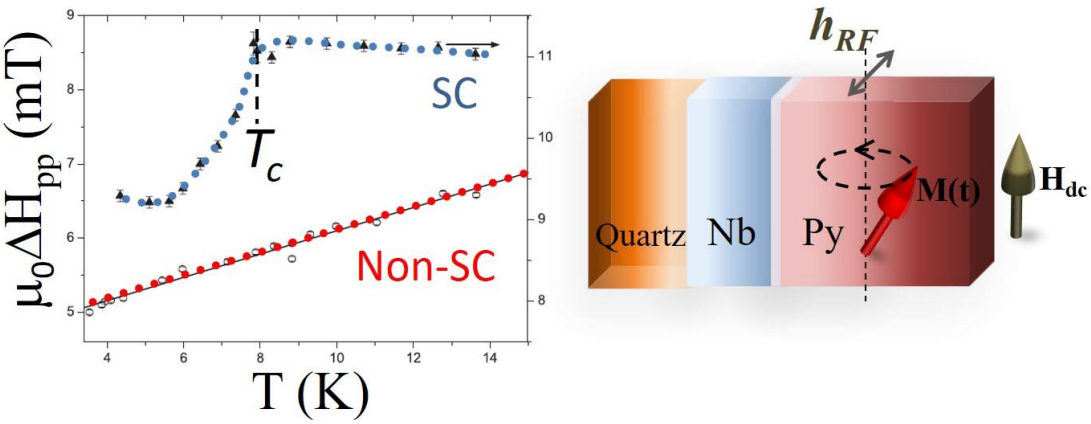

Figure 1.41: Comparison between the linewidth peak to peak of a samble of Nb/Py and a sample of Py. It is clear the decrease in the linewidth below the critical temperature of the ferromagnet. Adapted from [40]

that the linewidth at only one frequency is not enough to extract information about the damping of the system but can give hints about the underlying process. They conclude that there is a decrease in the Gilbert damping due to a decrease of the spin sink efficiency of the material when it becomes superconducting, which has been explained previously as an effect of the superconducting gap.

Another important experiment was carried out by the group of M.G. Blamire [110]. They used a similar system to the one used by Aarts' group, but included materials with strong spin-orbit coupling, such as platinum. They observed that in the case of trilayers Nb/Py/Nb, the damping of the sample decreased below Tc. Then, putting Pt contacts at both sides (Pt/ Nb/Py/Nb/Pt) the damping increased below Tc (Figure 1.42), for small thickness of Nb, but recover the previous behavior for thickness above 40nm. In this case they explain these results as the existence of a spin triplet supercurrent that can traverse the Nb (when it is thin enough) to reach the Pt, where due to the high spin orbit coupling it can relax.

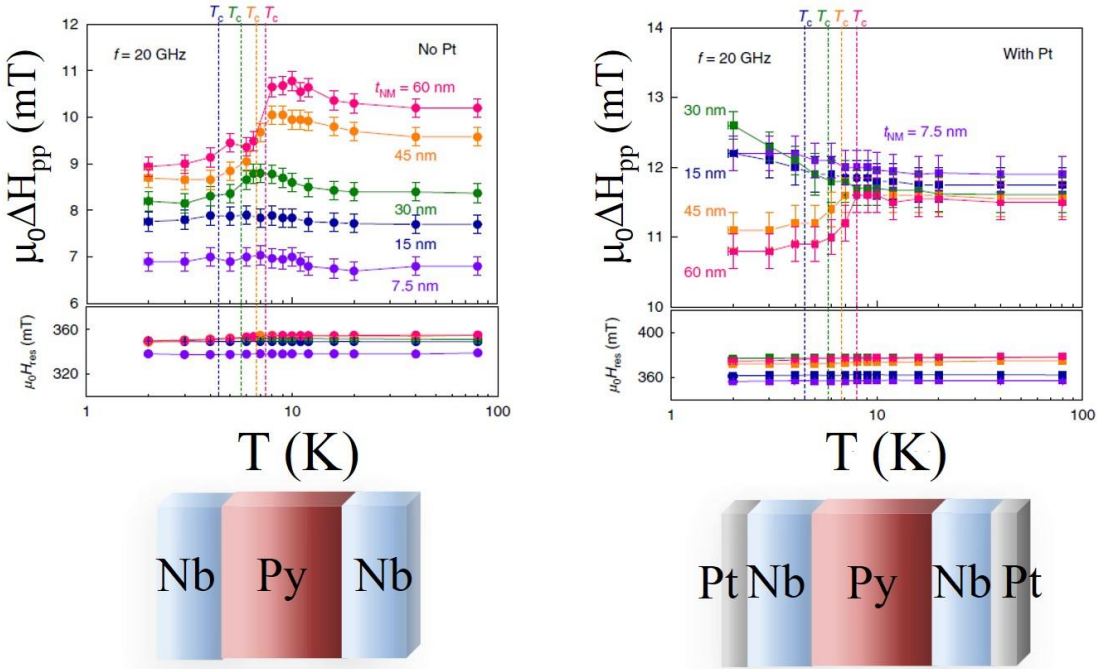

Figure 1.42: Comparison between the system with and without Pt, which acts as a spin sink, but only when the Nb layer is thin enough to allow the pass of the spin current.

As can be seen FMR is a powerful method to explore the superconducting ferromagnet proximity effect in new systems, and is widely used in the present days [110,138–143]. In this thesis we will study this effect with d-wave superconductors as the YBCO and ferromagnetic materials as Py and the half-metallic LSMO.

1.6 REFERENCES

[1] A. I. Buzdin, Rev. Mod. Phys. **77**, 935 (2005).

[2] V. S. Stolyarov, I. S. Veshchunov, S. Y. Grebenchuk, D. S. Baranov, I. A. Golovchanskiy, A. G. Shishkin, N. Zhou, Z. Shi, X. Xu, S. Pyon, Y. Sun, W. Jiao, G.-H. Cao, L. Y. Vinnikov, A. A. Golubov, T. Tamegai, A. I. Buzdin, and D. Roditchev, Sci. Adv. **4**, eaat1061 (2018).

[3] D. Aoki and Jaques Flouquet, J. Appl. Phys. **81**, 1 (2012).

[4] Y. Maeno, H. Hashimoto, K. Yoshida, S. Nishizaki, T. Fujita, J. G. Bednorz, and F. Lichtenberg, Nature **372**, 532 (1994).

[5] F. S. Bergeret, A. F. Volkov, and K. B. Efetov, Rev. Mod. Phys. **77**, 1321 (2005).

[6] M. Eschrig, J. Kopu, J. C. Cuevas, and G. Schön, Phys. Rev. Lett. **90**, 4 (2003).

[7] Y. V. Fominov, A. F. Volkov, and K. B. Efetov, Phys. Rev. B - Condens. Matter Mater. Phys. **75**, 104509 (2007).

[8] B. Crouzy, S. Tollis, and D. A. Ivanov, Phys. Rev. B - Condens. Matter Mater. Phys. **76**, 134502 (2007).

[9] M. Houzet and A. I. Buzdin, Phys. Rev. B - Condens. Matter Mater. Phys. **76**, 1 (2007).

[10] I. B. Sperstad, J. Linder, and A. Sudbø, Phys. Rev. B - Condens. Matter Mater. Phys. **78**, 104509 (2008).

[11] A. F. Volkov and K. B. Efetov, Phys. Rev. B - Condens. Matter Mater. Phys. **78**, 024519 (2008).

[12] K. Halterman, O. T. Valls, and P. H. Barsic, Phys. Rev. B - Condens. Matter Mater. Phys. **77**, 174511 (2008).

[13] A. I. Buzdin, A. S. Mel'Nikov, and N. G. Pugach, Phys. Rev. B - Condens. Matter Mater. Phys. **83**, 144515 (2011).

[14] J. N. Kupferschmidt and P. W. Brouwer, Phys. Rev. B - Condens. Matter Mater. Phys. **80**, 214537 (2009).

[15] F. S. Bergeret and I. V. Tokatly, Phys. Rev. Lett. **110**, 1 (2013).

[16] A. S. Mel'Nikov, A. V. Samokhvalov, S. M. Kuznetsova, and A. I. Buzdin, Phys. Rev. Lett. **109**, 237006 (2012).

[17] T. S. Khaire, M. A. Khasawneh, W. P. Pratt, and N. O. Birge, Phys. Rev. Lett. **104**, (2010).

[18] E. C. Gingrich, B. M. Niedzielski, J. A. Glick, Y. Wang, D. L. Miller, R. Loloee, W. P. Pratt, and N. O. Birge, Nat. Phys. **12**, 564 (2016).

[19] J. A. Glick, V. Aguilar, A. B. Gougam, B. M. Niedzielski, E. C. Gingrich, R. Loloee, W. P. Pratt, and N. O. Birge, Sci. Adv. **4**, eaat9457 (2018).

[20] J. W. A Robinson, J. D. S Witt, and M. G. Blamire, Science (80-.). **329**, 59 (2010).

[21] I. V. Vernik, V. V. Bol'Ginov, S. V. Bakurskiy, A. A. Golubov, M. Y. Kupriyanov, V. V. Ryazanov, and O. A. Mukhanov, IEEE Trans. Appl. Supercond. **23**, 1701208 (2013).

[22] R. S. Keizer, S. T. B. Goennenwein, T. M. Klapwijk, G. Miao, G. Xiao, and A. Gupta, Nature **439**, 825 (2006).

[23] M. S. Anwar, F. Czeschka, M. Hesselberth, M. Porcu, and J. Aarts, Phys. Rev. B - Condens. Matter Mater. Phys. **82**, 2 (2010).

[24] M. Eschrig and T. Löfwander, Nat. Phys. **4**, 138 (2008).

[25] S. Voltan, A. Singh, and J. Aarts, Phys. Rev. B **94**, 054503 (2016).

[26] Z. Sefrioui, D. Arias, V. Peña, J. E. Villegas, M. Varela, P. Prieto, C. León, J. L. Martinez, and J. Santamaria, Phys. Rev. B - Condens. Matter Mater. Phys. **67**, 214511 (2003).

[27] Y. Kalcheim, O. Millo, M. Egilmez, J. W. A. Robinson, and M. G. Blamire, **104504**, 1 (2012).

[28] K. Dybko, K. Werner-Malento, P. Aleshkevych, M. Wojcik, M. Sawicki, and P. Przyslupski, Phys. Rev. B - Condens. Matter Mater. Phys. **80**, 0 (2009).

[29] Y. Kalcheim, T. Kirzhner, G. Koren, and O. Millo, Phys. Rev. B - Condens. Matter Mater. Phys. **83**, 2 (2011).

[30] C. Visani, Z. Sefrioui, J. Tornos, C. Leon, J. Briatico, M. Bibes, a. Barthélémy, J. Santamaría, and J. E. Villegas, Nat. Phys. **8**, 539 (2012).

[31] C. Visani, F. Cuellar, A. P??rez-Mu??oz, Z. Sefrioui, C. Le??n, J. Santamar??a, and J. E. Villegas, Phys. Rev. B - Condens. Matter Mater. Phys. **92**, 1 (2015).

[32] M. Egilmez, J. W. A. Robinson, J. L. MacManus-Driscoll, L. Chen, H. Wang, and M. G. Blamire, EPL (Europhysics Lett. **106**, 37003 (2014).

[33] J. M. Rowell, Phys. Rev. Lett. **11**, 200 (1963).

[34] W. L. Rowell, J. M. & McMillan, Phys. Rev. Lett. **16**, 453 (1966).

[35] K. Lahabi, M. Amundsen, J. A. Ouassou, E. Beukers, M. Pleijster, J. Linder, P. Alkemade, and J. Aarts, Nat. Commun. **8**, 1 (2017).

[36] S. Shapiro, Phys. Rev. Lett. **11**, 80 (1963).

[37] H. K. Onnes., Phys. Lab. Comm. **12**, (1911).

[38] M. Tinkham, Phys. Rev. Lett. **61**, 1658 (1988).

[39] J. Bardeen, L. N. Cooper, and J. R. Schrieffer, Phys. Rev. **108**, 1175 (1957).

[40] C. C. Tsuei, J. R. Kirtley, C. C. Chi, L. S. Yu-Jahnes, A. Gupta, T. Shaw, J. Z. Sun, and M. B. Ketchen, Phys. Rev. Lett. **73**, 593 (1994).

[41] B. D. Josephson, Phys. Lett. **1**, 251 (1962).

[42] V. L. Ginzburg and L. D. Landau, in *Supercond. Superfluidity* (Springer Berlin Heidelberg, 2008), pp. 113–137.

[43] A. A. Abrikosov, JETP **5**, 1174 (1957).

[44] G. Blatter, M. V. Feigel'Man, V. B. Geshkenbein, A. I. Larkin, and V. M. Vinokur, Rev. Mod. Phys. **66**, 1125 (1994).

[45] L. Shubnikov and I. Nakhutin, Nature **139**, 589 (1937).

[46] J. G. B. and K. A. Müller., Zeitschrift Für Phys. B Condens. Matter **64.2**, 189 (1986).

[47] C. W. C. M. K. Wu, J. R. Ashburn, C. J. Torng, P. H. Hor, R. L. Meng, L. Gao, Z. J. Huang, Y. Q. Wang, Phys. Rev. Lett. **58**, 908 (1987).

[48] B. Keimer, S. A. Kivelson, M. R. Norman, S. Uchida, and J. Zaanen, Nature **518**, 179 (2015).

[49] T. Haugan, P. N. Barnes, R. Wheeler, F. Melsenkothen, and M. Sumption, Nature **430**, 867 (2004).

[50] C. C. Tsuei and J. R. Kirtley, Rev. Mod. Phys. **72**, 969 (2000).

[51] N. D.-L. & L. T. G. Grissonnanche, O. Cyr-Choinière, F. Laliberté, S. René de Cotret, A. Juneau-Fecteau, S. Dufour-Beauséjour, M. -È. Delage, D. LeBoeuf, J. Chang, B. J. Ramshaw, D. A. Bonn, W. N. Hardy, R. Liang, S. Adachi, N. E. Hussey, B. Vignolle, C. Proust, M. Suther, Nat. Commun. **5**, (2014).

[52] J. J. & C. Y. Yuanqing Chen, Weibai Bian, Wenhuan Huang, Xinni Tang, Gaoyang Zhao, Lingwei Li, Na Li, Wen Huo, Sci. Rep. **6**, (2016).

[53] H. Maeda, Y. Tanaka, M. Fukutomi, and T. Asano, Jpn. J. Appl. Phys. **27**, L209 (1988).

[54] Https://www.nobelprize.org/prizes/physics/1973/josephson/facts/, (n.d.).

[55] L. Esaki and R. Tsu, IBM J. Res. Dev. **14**, 61 (1970).

[56] S. S. P. Parkin, C. Kaiser, A. Panchula, P. M. Rice, B. Hughes, M. Samant, and S. H. Yang, Nat. Mater. **3**, 862 (2004).

[57] I. Giaever, Rev. Mod. Phys. **46**, 245 (1974).

[58] I. Giaever, Phys. Rev. Lett. **5**, 464 (1960).

[59] I. Giaever, Phys. Rev. Lett. **5**, 147 (1960).

[60] B. D. Josephson, Rev. Mod. Phys. **46**, 251 (1974).

[61] S. Shapiro, Phys. Rev. Lett. **11**, 80 (1963).

[62] M. Malnou, A. Luo, T. Wolf, Y. Wang, C. Feuillet-Palma, C. Ulysse, G. Faini, P. Febvre, M. Sirena, J. Lesueur, and N. Bergeal, Appl. Phys. Lett. **101**, (2012).

[63] C. Richard, M. Houzet, and J. S. Meyer, Phys. Rev. Lett. **110**, 1 (2013).

[64] M. Houzet, V. Vinokur, and F. Pistolesi, Phys. Rev. B - Condens. Matter Mater. Phys. **72**, 1 (2005).

[65] A. Buzdin, Phys. Rev. B - Condens. Matter Mater. Phys. **72**, 1 (2005).

[66] H. Sellier, C. Baraduc, F. Lefloch, and R. Calemczuk, Phys. Rev. Lett. **92**, 1 (2004).

[67] V. V. Ryazanov, V. A. Oboznov, A. Y. Rusanov, A. V. Veretennikov, A. A. Golubov, and J. Aarts, Phys. Rev. Lett. **86**, 2427 (2001).

[68] Y. Ota, M. Machida, T. Koyama, and H. Matsumoto, Phys. Rev. Lett. **102**, 237003 (2009).

[69] J. J. A. B. A. F. M. B. J. V. W. T. M. Klapwijk, Nature **397**, 43 (1999).

[70] J. Rokhinson, L., Liu, X. & Furdyna, Nat. Phys. **8**, 795 (2012).

[71] T. S. Khaire, M. A. Khasawneh, W. P. Pratt, and N. O. Birge, Phys. Rev. Lett. **104**, 2 (2010).

[72] M. Eschrig, Phys. Today **64**, 43 (2011).

[73] H. Pannetier, B. & Courtois, J. Low Temp. Phys. **118**, 559 (2000).

[74] A. F. Andreev, *THERMAL CONDUCTIVITY OF THE INTERMEDIATE STATE OF SUPERCONDUCTORS. II* (1965).

[75] M. J. M. De Jong and C. W. J. Beenakker, Phys. Rev. Lett. **74**, 1657 (1995).

[76] W. J. Tomasch, Phys. Rev. Lett. **16**, 16 (1966).

[77] P. W. McMillan, W. L. & Anderson, Phys. Rev. Lett. **16**, 85 (1966).

[78] M. M. B. and M. B. T. Fertig W A, Johnston D C, DeLong L E, McCallum R W, Phys. Rev. Lett. **38**, 987 (1977).

[79] M. Ishiwaka and O. Fischer, Solid State Commun. **24**, 747 (1977).

[80] V. S. Stolyarov, I. S. Veshchunov, S. Y. Grebenchuk, D. S. Baranov, I. A. Golovchanskiy, A. G. Shishkin, N. Zhou, Z. Shi, X. Xu, S. Pyon, Y. Sun, W. Jiao, G. H. Cao, L. Y. Vinnikov, A. A. Golubov, T. Tamegai, A. I. Buzdin, and D. Roditchev, Sci. Adv. **4**, 1 (2018).

[81] S. Ran, C. Eckberg, Q. P. Ding, Y. Furukawa, T. Metz, S. R. Saha, I. L. Liu, M. Zic, H. Kim, J. Paglione, and N. P. Butch, Science (80-.). **365**, 684 (2019).

[82] M. Eschrig, T. Löfwander, T. Champel, J. C. Cuevas, J. Kopu, and G. Schön, J. Low Temp. Phys. **147**, 457 (2007).

[83] M. Eschrig and T. Löfwander, Nat. Phys. **4**, 138 (2008).

[84] F. Hardy and A. D. Huxley, Phys. Rev. Lett. **94**, 247006 (2005).

[85] R. Matzdorf, Z. Fang, Ismail, J. Zhang, T. Kimura, Y. Tokura, K. Terakura, and E. W. Plummer, Science (80-.). **289**, 746 (2000).

[86] D. Fay and J. Appel, Phys. Rev. B **22**, 3173 (1980).

[87] R. G. Cai and R. Q. Yang, Phys. Rev. D - Part. Fields, Gravit. Cosmol. **91**, 026001 (2015).

[88] S. Mironov and A. Buzdin, Phys. Rev. B - Condens. Matter Mater. Phys. **92**, 184506 (2015).

[89] L. R. Tagirov, Phys. Rev. Lett. **83**, 2058 (1999).

[90] J. Linder and J. W. A. Robinson, Nat. Phys. **11**, 307 (2015).

[91] P. Fulde and R. A. Ferrell, Phys. Rev. **135**, A550 (1964).

[92] A. I. Larkin and Y. N. Ovchinnikov, Sov. Phys. JETP **20**, 762 (1965).

[93] D. R. T. Tokuyasu, J. A. Sauls, Phys. Rev. B - Condens. Matter Mater. Phys. **21**, 8823 (1988).

[94] M. Houzet, Phys. Rev. Lett. **101**, 1 (2008).

[95] V. V. Ryazanov, Phys. Rev. Lett. **86**, 2427 (2001).

[96] V. A. Oboznov, Phys. Rev. Lett. **96**, 2006 (2006).

[97] F. S. Bergeret, A. F. Volkov, and K. B. Efetov, Phys. Rev. Lett. **86**, 4096 (2001).

[98] J. Wang, M. Singh, M. Tian, N. Kumar, B. Liu, C. Shi, J. K. Jain, N. Samarth, T. E. Mallouk, and M. H. W. Chan, Nat. Phys. **6**, 389 (2010).

[99] A. Hoffmann, S. G. E. Te Velthuis, Z. Sefrioui, J. Santamaría, M. R. Fitzsimmons, S. Park, and M. Varela, Phys. Rev. B - Condens. Matter Mater. Phys. **72**, 140407 (2005).

[100] Z. Sefrioui, D. Arias, V. Peña, J. E. Villegas, M. Varela, P. Prieto, C. León, J. L. Martinez, and J. Santamaria, Phys. Rev. B - Condens. Matter Mater. Phys. **67**, 4 (2003).

[101] V. Peña, Z. Sefrioui, D. Arias, C. Leon, J. Santamaria, M. Varela, S. J. Pennycook, and J. L. Martinez, Phys. Rev. B - Condens. Matter Mater. Phys. **69**, 224502 (2004).

[102] V. Peña, Z. Sefrioui, D. Arias, C. Leon, J. Santamaria, J. L. Martinez, S. G. E. Te Velthuis, and A. Hoffmann, Phys. Rev. Lett. **94**, 057002 (2005).

[103] M. Varela, A. R. Lupini, S. J. Pennycook, Z. Sefrioui, and J. Santamaria, Solid. State. Electron. **47**, 2245 (2003).

[104] V. Peña, C. Visani, J. Garcia-Barriocanal, D. Arias, Z. Sefrioui, C. Leon, J. Santamaria, and C. A. Almasan, Phys. Rev. B - Condens. Matter Mater. Phys. **73**, 104513 (2006).

[105] Z. Sefrioui, M. Varela, V. Peña, D. Arias, C. León, J. Santamaría, J. E. Villegas, J. L. Martínez, W. Saldarriaga, and P. Prieto, Appl. Phys. Lett. **81**, 4568 (2002).

[106] C. Visani, Z. Sefrioui, J. Tornos, C. Leon, J. Briatico, M. Bibes, A. Barthélémy, J. Santamaría, and J. E. Villegas, Nat. Phys. **8**, 539 (2012).

[107] S. Mironov, H. Meng, and A. Buzdin, Appl. Phys. Lett. **116**, 162601 (2020).

[108] M. Eschrig, A. Cottet, W. Belzig, and J. Linder, New J. Phys **17**, 83037 (2015).

[109] A. V. Samokhvalov, J. W. A. Robinson, and A. I. Buzdin, Phys. Rev. B **100**, 014509 (2019).

[110] K. R. Jeon, C. Ciccarelli, A. J. Ferguson, H. Kurebayashi, L. F. Cohen, X. Montiel, M. Eschrig, J. W. A. Robinson, and M. G. Blamire, Nat. Mater. **17**, 499 (2018).

[111] A. K. Feofanov, V. A. Oboznov, V. V Bol'ginov, J. Lisenfeld, S. Poletto, V. V Ryazanov, A. N. Rossolenko, M. Khabipov, D. Balashov, A. B. Zorin, P. N. Dmitriev, V. P. Koshelets, and A. V Ustinov, Nat. Phys. **6**, 593 (2010).

[112] T. Yamashita, K. Tanikawa, S. Takahashi, and S. Maekawa, Phys. Rev. Lett. **95**, 1 (2005).

[113] L. B. Ioffe, V. B. Geshkenbein, M. V Feigel'man, A. L. Fauchère, and G. Blatter, Nature **398**, 679 (1999).

[114] G. Tatara and N. Garcia, Phys. Rev. Lett. **91**, 1 (2003).

[115] V. V. Ryazanov, V. V. Bol'ginov, D. S. Sobanin, I. V. Vernik, S. K. Tolpygo, A. M. Kadin, and O. A. Mukhanov, Phys. Procedia **36**, 35 (2012).

[116] H. D. Arnold and G. W. Elmen, Bell Syst. Tech. J. **2**, 101 (1923).

[117] G. Nahrwold, J. M. Scholtyssek, S. Motl-Ziegler, O. Albrecht, U. Merkt, and G. Meier, J. Appl. Phys. **108**, 013907 (2010).

[118] E. Dagotto, T. Hotta, and A. Moreo, Phys. Rep. **344**, 153 (2001).

[119] J. E. Ordóñez, L. Marín, L. A. Rodríguez, P. A. Algarabel, J. A. Pardo, R. Guzmán, L. Morellón, C. Magén, E. Snoeck, M. E. Gómez, and M. R. Ibarra, Beilstein J. Nanotechnol. **11**, 651 (2020).

[120] S. Blundell, *Magnetism in Condensed Matter* (2001).

[121] P. Perna, D. Maccariello, F. Ajejas, R. Guerrero, L. Méchin, S. Flament, J. Santamaria, R. Miranda, and J. Camarero, Adv. Funct. Mater. **27**, 1700664 (2017).

[122] Y. Tokura, Reports Prog. Phys. **69**, (2006).

[123] A. Urushibara, Y. Moritomo, T. Arima, A. Asamitsu, G. Kido, and Y. Tokura, Phys. Rev. B - Condens. Matter Mater. Phys. **51**, (1995).

[124] J. Park, E. Vescovo, H. Kim, C. Kwon, R. Ramesh, and T. Venkatesan, Nat. **392**, 794 (1998).

[125] M. B. Salamon and M. Jaime, Rev. Mod. Phys. **73**, 583 (2001).

[126] M. Huijben, L. W. Martin, Y.-H. Chu, M. B. Holcomb, P. Yu, G. Rijnders, D. H. A. Blank, and R. Ramesh, Phys. Rev. B - Condens. Matter Mater. Phys. **78**, 094413 (2008).

[127] C. Kittel, J. Phys. Radium **12(3)**, 291 (1951).

[128] C. Kittel, Phys. Rev. **73**, 155 (1948).

[129] T. L. Gilbert, IEEE Trans. Magn. **40**, 3443 (2004).

[130] Https://www.physik.fu-berlin.de/einrichtungen/ag/ag-kuch/research/techniques/fmr/index.html, (n.d.).

[131] S. I. Hikino, M. Mori, S. Takahashi, and S. Maekawa, J. Phys. Soc. Japan **77**, 53707 (2008).

[132] C. Richard, M. Houzet, and J. S. Meyer, Phys. Rev. Lett. **109**, 057002 (2012).

[133] A. Brataas and Y. Tserkovnyak, Phys. Rev. Lett. **93**, 087201 (2004).

[134] J. X. Zhu and A. V. Balatsky, Phys. Rev. B - Condens. Matter Mater. Phys. **67**, 174505 (2003).

[135] S. Takahashi, S. Hikino, M. Mori, J. Martinek, and S. Maekawa, Phys. Rev. Lett. **99**, 057003 (2007).

[136] M. Houzet, Phys. Rev. Lett. **101**, 057009 (2008).

[137] C. Bell, S. Milikisyants, M. Huber, and J. Aarts, Phys. Rev. Lett. **100**, 1 (2008).

[138] I. A. Golovchanskiy, N. N. Abramov, V. S. Stolyarov, P. S. Dzhumaev, O. V. Emelyanova, A. A. Golubov, V. V. Ryazanov, and A. V. Ustinov, Adv. Sci. **6**, 1900435 (2019).

[139] K. Rogdakis, A. Sud, M. Amado, C. M. Lee, L. McKenzie-Sell, K. R. Jeon, M. Cubukcu, M. G. Blamire, J. W. A. Robinson, L. F. Cohen, and H. Kurebayashi, Phys. Rev. Mater. **3**, 014406 (2019).

[140] K. R. Jeon, C. Ciccarelli, H. Kurebayashi, L. F. Cohen, X. Montiel, M. Eschrig, S. Komori, J. W. A. Robinson, and M. G. Blamire, Phys. Rev. B **99**, 024507 (2019).

[141] G. A. Ovsyannikov, A. E. Sheyerman, A. V. Shadrin, Y. V. Kislinskii, K. Y. Constantinian, and A. Kalabukhov, JETP Lett. **97**, 145 (2013).

[142] G. A. Ovsyannikov, K. Y. Constantinian, V. V. Demidov, and Y. N. Khaydukov, Low Temp. Phys. **42**, 873 (2016).

[143] S. E. Barnes, M. Aprili, I. Petkovic, and S. Maekawa, Supercond. Sci. Technol. **24**, (2011).

Chapter 2: Experimental Techniques

This chapter summarizes all the experimental techniques used during the thesis work to grow, characterize and measure all samples.

2.1. SAMPLE GROWTH

Planar superconductor-ferromagnet samples measured in this thesis have been grown using a high oxygen pressure sputtering system placed in a ISO7 clean room at CAI de Técnicas Físicas. FMR samples have been grown using Pulsed Laser Deposition (PLD) at CNRS-Thales.

2.1.1. HIGH OXYGEN PRESSURE SPUTTERING

This technique is based on the deposition of material from a target into a substrate heated at high temperatures, and at relatively high oxygen pressure. This technique is perfectly appropriate for the growth of high-quality epitaxial complex oxides thin films, as it allows to control with high precision the growth rate and the oxygen proportion in the samples. [1]

High oxygen pressure sputtering consists on the deposition of atoms on a substrate after being sputtered from a target of the stoichiometric compound that is wanted to grow. To allow this we need to apply a high voltage (in the case of DC-sputtering, used for conducting materials) or a high-power RF signal (RF-sputtering, for high resistance materials) to create a plasma in the surface of the target. The ions in this plasma will collide with the target, ejecting particles from it, and these particles will travel ballistically impacting into the substrate. Oxygen is used as sputtering element since all samples grown are oxides. All samples in this thesis have been grown on $SrTiO_3$ substrate (100)-oriented, purchased from CrysTec. [2]

In our set-up the substrate is placed on a heater plate furnace which can be up to 1000 ºC, and it can work on an interval between 10^{-6} and 10^{3} mbar. The process starts putting a substrate on the furnace inside the sputtering chamber (Figure 2.1.) and making vacuum through a membrane pump first (up to 10^{-1} mbar) and turbo molecular pump (up to 10^{-6}mbar). Then the temperature is increased to 900 °C while a constant oxygen flow is injected into the chamber until the pressure reaches the desired value. The DC-voltage and the RF power are applied to the targets, forming a plasma, and after 30 minutes of pre-sputtering time the target is put on top of the furnace with the substrate, then the growing starts. The growing rate and the crystalline quality will depend on parameters such as substrate temperature, oxygen pressure and applied power. After the growth, an in-situ annealing at 1000 mbar of oxygen pressure is needed to fully oxygenate the samples.

The materials grown in this system have been $YBa_2Cu_3O_7$(YBCO), $La_{0.7}Ca_{0.3}MnO_3$ (LCMO) and $La_{0.7}Sr_{0.3}MnO_3$(LSMO). Each material has different growth conditions, as it can be seen in Table 2.1.

A low growth rate is achieved, allowing a growth control down to one-unit cell of each material. This low rate also favors a good crystalline quality and the epitaxial growth of the sample.

Figure 2.1. View of the sputtering chamber of YBCO and LSMO.

Material	YBCO	LCMO	LSMO
Substrate	5x5x1 mm^3 STO (100)		
Sputtering type	DC	RF	
Growth temperature	900 ºC		
Growth pressure	3,4 mbar		3,2 mbar
Oxigenation temperature	620ºC	800ºC	
Annealing temperature	550ºC		750ºC
Annealing pressure	1000 mbar		
Annealing time	5 min	30 min	1 h
Growth rate	0,6 nm/min	0,23 nm/min	0,28 nm/min

Table 2.1.: Growth conditions and rates for high pressure sputtering materials

2.1.2. PULSED LASER DEPOSITION

Pulsed Laser Deposition (PLD) is a technique which uses a high-power laser beam focused into a target of the material that is wanted to grow, in a high-vacuum chamber. Similar to the sputtering technique, the ejection of material from the target goes to a substrate heated to high temperatures. After the growth, samples also need an annealing at 1000 mbar oxygen pressure [3]. This technique allows a large pressure range to deposit materials, from ultrahigh vacuum to 1 mbar, which is perfect for both the growth of oxides and metals. Also, the use of a pulsed laser enables a precise control over the growth rate of the sample, reaching sub-monolayers per pulse.

PLD has been used for the growth of the oxides in FMR samples, growth performed at CNRS-Thales.

2.2. STRUCTURAL CHARACTERIZATION

The soft X-Ray characterization have been carried out at CAI de Difracción de Rayos X, with a Philips X'pert MRD diffractometer, using a Cu tube as X-ray source (λx=0.15418 nm) operating at 45kV and 40mA. The data has been analyzed using GenX [4] to extract thickness and crystalline quality.

2.2.1. X-RAY REFLECTIVITY (XRR)

When coherent and collimated x-rays are applied on a sample, it reflects on the interface between layers with different electron densities, specifically on the interface between the layer and air, and between the layer and the substrate. This way, also a layered structure produces an interference pattern, which we can obtain by measuring the reflectivity as a function of the angle 2θ (Figure 2.2.). We can then extract information about the thickness of the layer and the roughness of both interfaces.

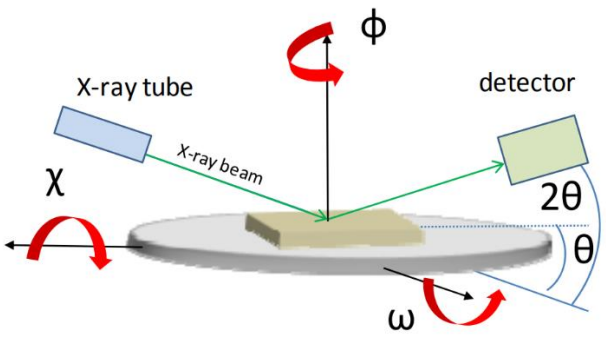

Figure 2.2.: Bragg (2θ) geometry to measure XRR (for low angles) and XRD (for high angles).

The period of the oscillations caused by this interference is related with the thickness ***d*** of the samples in function of the incident angle following the next equation:

$$\sin^2\theta = \left[\frac{(m-k)\lambda_x}{2d}\right] + 2\delta$$

Where m is the position of the maxima (minima), k=1/2 (k=0) and δ is the real part of the refraction index, which is 2.5 x 10^{-5} in our system.

In (Figure 2.3.) we can see a representative XRR measurement of a thin film used in this thesis.

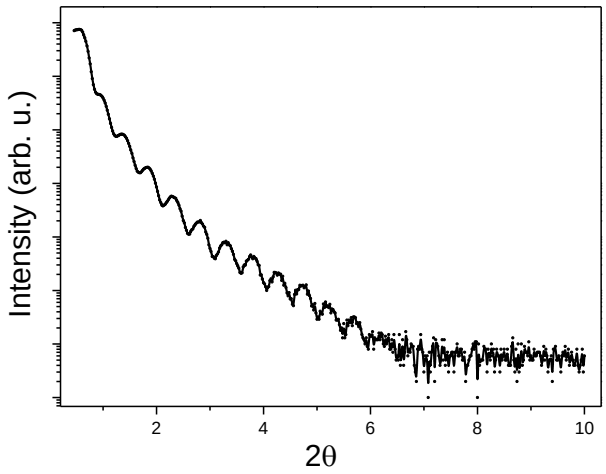

Figure 2.3.: XRR scan from an 18 nm thick LCMO thin film

2.2.2. X-RAY DIFFRACTION (XRD)

Similar to the XRR measurements, in XRD an interference pattern is measured, but this time the atomic planes are the ones that cause the interference. The atomic layers are separated, then the x-rays will have different paths depending on which layer they reflect, and thus, will have a constructive interference if the difference in the path is a multiple of the x-ray wavelength. For an epitaxial structure a diffraction scan carried out in θ-2θ geometry, after optimizing around one of the (00*l)* diffraction peak of the substrate will show only the Bragg peaks of the same family [5]. The diffraction condition described by the Bragg law is:

$$2d_{hkl}\sin\theta = n\lambda_x$$

For epitaxial monocrystalline films, the only planes that fulfill Bragg conditions will be the ones parallel to the surface of the substrate. Then, the peaks we obtain correspond to the (001) direction, allowing us to measure the c parameter of the crystalline lattice.

Also, when we look at the infinite thickness maxima of the XRD measurement, we can use the following equation to calculate the thickness (t) of the thin film [6]:

$$4t\sin(\theta) = (2n+1)\lambda_x$$

In (Figure 2.3.) we can observe a typical XRD measurement.

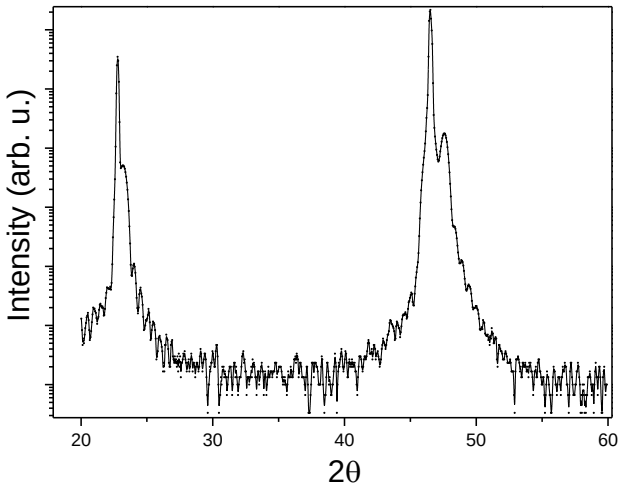

Figure 2.3.: XRD scan from an 18 nm thick LCMO thin film

2.3. MORPHOLOGICAL CHARACTERIZATION

We have performed three principal methods to study the morphological characterization of the samples in this thesis:

- AFM (Atomic Force Microscopy), carried out at *Centro Nacional de Microscopia Electronica* in Madrid using a Veeco MultiMode Scanning Probe Microscopy with a TESP tip.
- SEM (Scanning Electron Microscopy), carried out in an ISO7 clean room at *CAI Tecnicas Fisicas UCM* using a SEM Zeiss EVO50 with thermionic emission using a LaB_6 filament.
- Optical Microscopy, carried out at GFMC UCM using a *400X Zoom Coaxial Light Monocular C-mount Microscope Lens USB VGA AV Camera PCB.*

2.3.1. ATOMIC FORCE MICROSCOPY

AFM is a non-destructive technique based on the interaction between a tip and the surface of a material. It has 3 usual modes: contact mode, non-contact mode and tapping mode. All images acquired by AFM were taken using tapping mode.

This mode maps topography by lightly tapping the surface with an AFM probe that is oscillating at its resonant frequency. A piezo excites the cantilever substrate vertically, causing the cantilever to oscillate vertically. As the cantilever oscillates vertically, the reflected laser beam deflects in a regular pattern over a photodiode array, generating a sinusoidal, electronic signal or “detector signal”.

Before the AFM probe is engaged on the sample, the cantilever oscillates in free air close to its resonant frequency. As the probe approaches and encounters the sample surface, the amplitude of this oscillation decreases. By monitoring changes in amplitude and continuously feeding back on a user-specified amplitude setpoint, the tip moves up and down to maintain constant

oscillation amplitude (Figure 2.4.). By this means, a high-resolution three-dimensional image of the sample surface topography is produced.

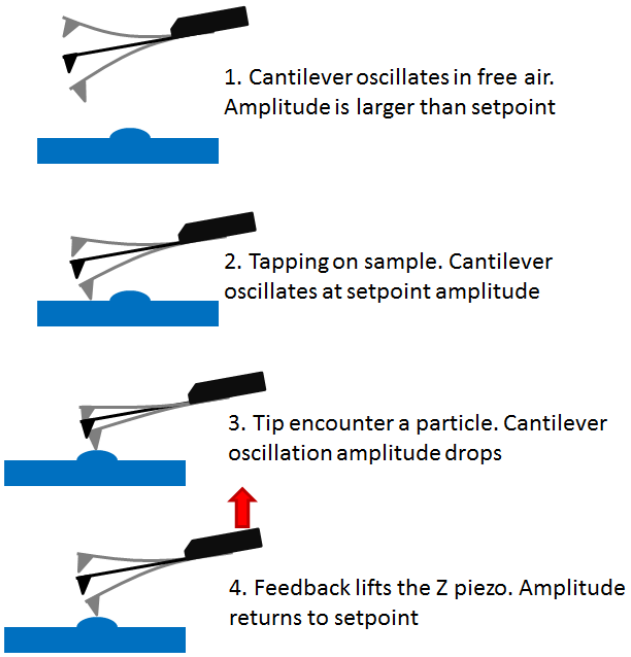

Figure 2.4.: Tapping mode operation.

Here, we can see two typical images acquired using AFM in tapping mode (Figure 2.5.)

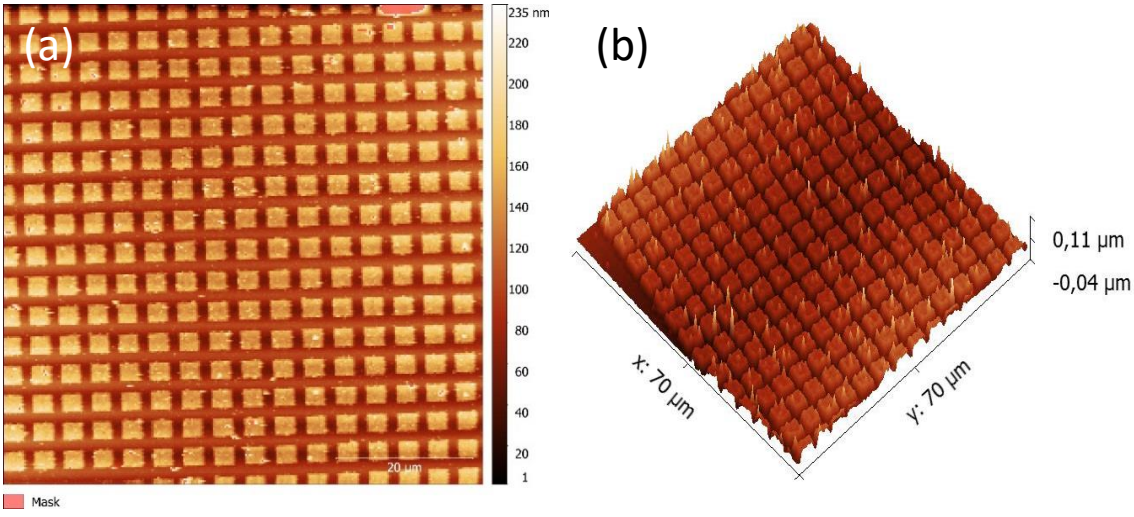

Figure 2.5.: (a) 2D Image of an YBCO squares array. (b) 3D image of a different YBCO squares array.

2.3.2. SCANNING ELECTRON MICROSCOPY

SEM is a technique that allows us to measure a topographic image of the surface of a material using a focused beam of electrons. These electrons will interact with the atoms in the sample generating, among others, the emission of secondary electrons (SE), which can be collected to obtain information about the surface and the first atomic layers of the sample. Depending on

which detector we use we can collect different electrons or electromagnetic radiation (Figure 2.6.)

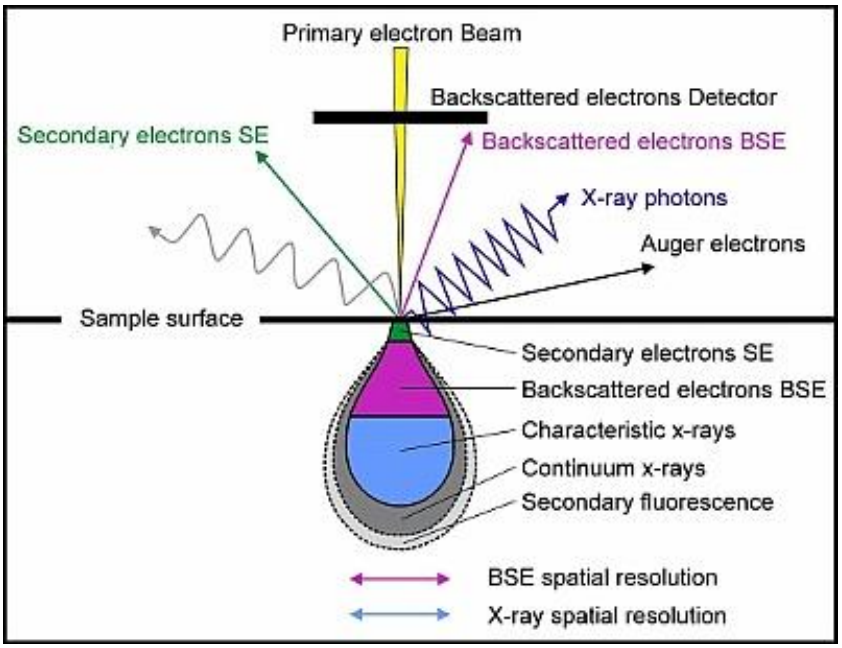

Figure 2.6.: When an electron beam is applied a wide variety of particles are emitted from the samples, from electrons to electromagnetic radiation. Secondary electrons, Backscattered electrons and Auger electrons are the ones that give us more information about the surface [7]

The two types of electrons detected in our system are SE and BSE and are used for the analysis of the surface of the sample.

- Secondary electrons come from the surface or near surface regions of the sample. They are originated due to inelastic interactions between the primary electron beam and the first tens of nanometer of the sample, with energies lower than 50 eV. These electrons are the most useful for the inspection of the topography of surfaces.
- Backscattered electrons come from a wide region within the interaction volume. They are originated due to elastic collisions of electrons with atoms. This causes a change in electrons direction. Atoms with bigger atomic number Z will cause more collisions than the lighter ones, this gives the BSE contrast depending on the sample compositions. Also, it provides information on topography, crystallography and magnetic field of the sample.

There are two types of SEM: Field effect (FE-SEM) and Thermionic (SEM). The main difference between them is the emitter type, where the electron beam comes from. In this thesis we have used a Thermionic SEM.

Thermionic SEM uses filaments of CeB_6, LaB_6 or W to obtain the electron beam. The emission starts when the electrons on the filament are provided with enough energy to cross the potential barrier, proportional to the work function of the material. This energy comes from the heating produced by a current flowing through the filament. A Wehnelt electrode that is negatively charged with respect to the cathode pushes the unwanted electrons back into the filament, effectively determining the size of the emitting area. Below the cathode and the Wehnelt electrode, an anode provides a strong electric field, or a strong lens that makes the electron beam converge into a crossover between the Wehnelt and the anode.

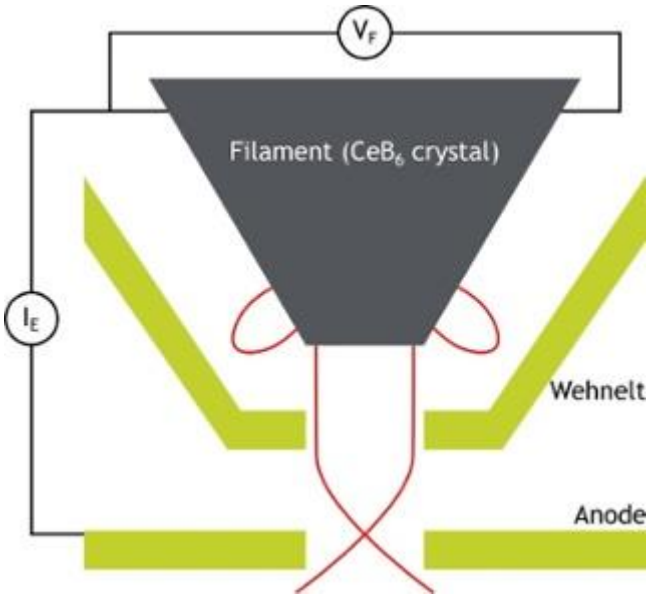

Figure 2.7.: Schematic representation of a thermionic source

The current density needed for the emission of electrons is given by the Richardson law:

$$J_c = AT^2 e^{-\frac{\phi}{kT}}$$

Where ϕ is the work function of the material, k is the Boltzmann constant, A is the Richardson constant and T is the temperature in Kelvin. In Table 2.2. we compare the 3 thermionic sources.

	CeB_6	LaB_6	Tungsten
Work function (eV)	2,6	2,7	4,5
Temperature (K)	1800	1800	2800
Pressure (Pa)	10^{-4}	10^{-4}	10^{-3}
Current density (A/cm²)	20-50	20-50	3
Lifetime (hours)	1500+	1000+	100

Table 2.2. Thermionic sources and its physical properties

In our system, a LaB_6 filament has been used.

Once the electrons have been generated, they go through the SEM column (Figure 2.8.), where the magnetic lenses and apertures adjust the geometrical and electronic parameters of the beam. Also an astigmatism corrector is used to reduce the astigmatism due to several defects that can be present in the column. Then the beam enters the sample chamber, where the detectors and the sample are located. After the interaction with the sample, the signal goes to the detectors and is processed allowing the reconstruction of the surface image.

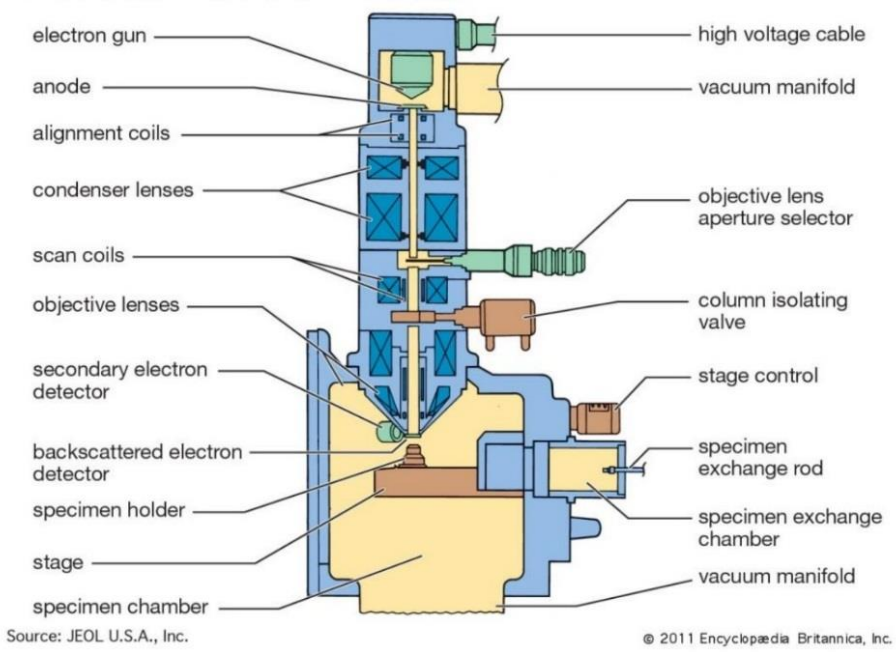

Figure 2.8. Typical scanning electron microscope architecture.

In (Figure 2.9.) we can observe a typical image taken using SEM of a 600nm diameter Au dots.

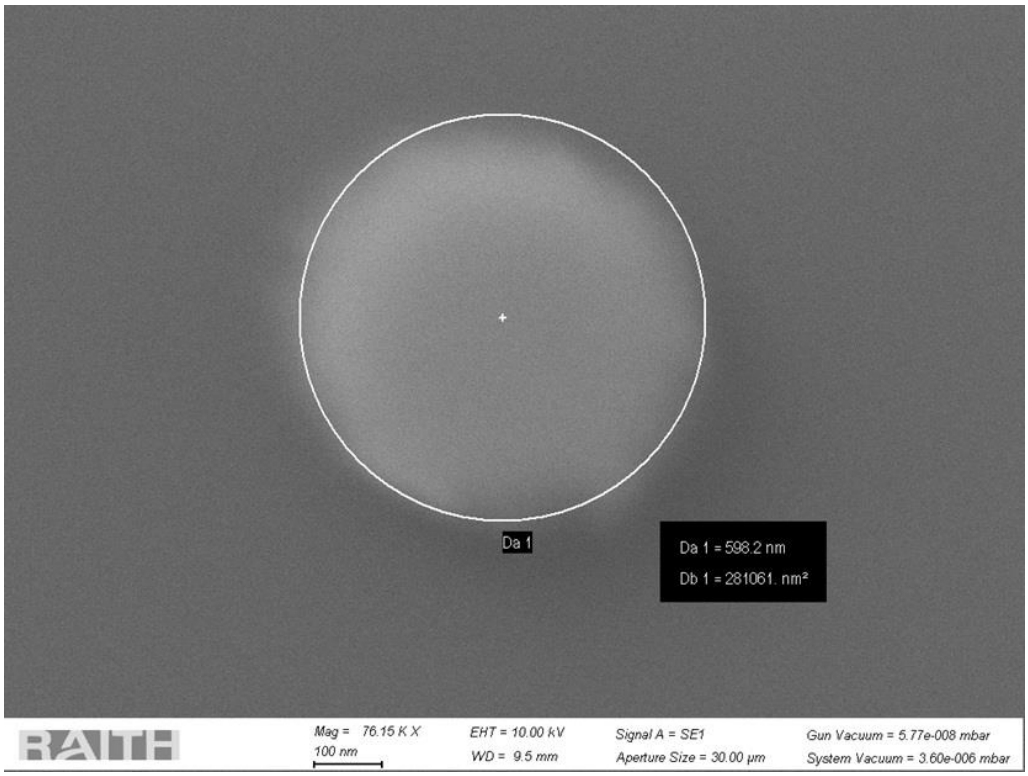

Figure 2.9: Au nanodot on NbSTO after lithography process.

2.3.3. OPTICAL MICROSCOPY

Optical microscopy is the most useful and faster technique to measure and observe the surface of a sample when the dimension of the designs to check is bigger than the wavelength of visible light. It has been used mainly for checking the continuity of microwires, as can be seen in (Figure 2.10.)

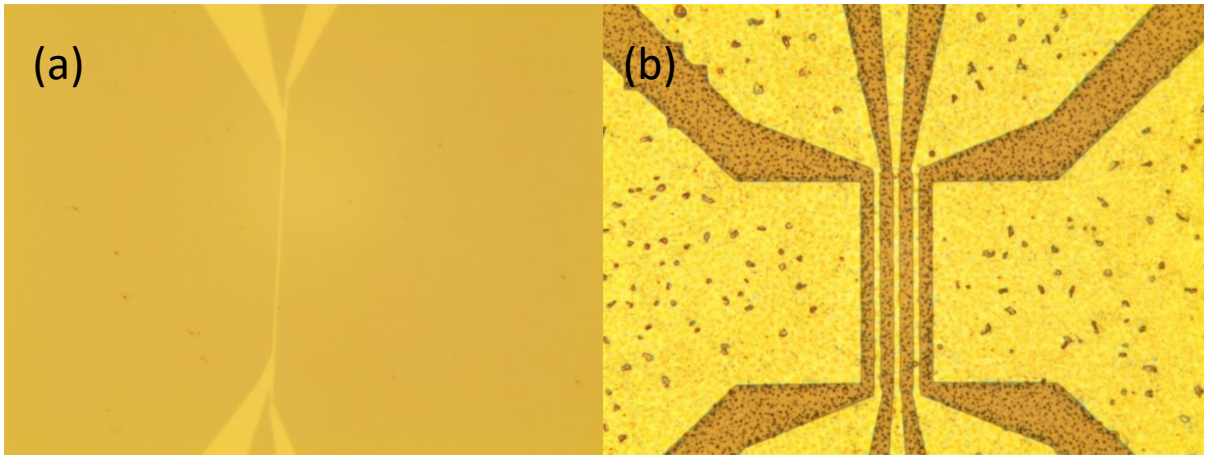

Figure 2.10. Optical images of: (a) LSMO nanowire (800nm). (b) ALO pattern (yellow) with YBCO on top of it (brown).

2.4. MICRO- AND NANOFABRICATION PROCESS

The micro- and nanofabrication processes have been carried out at Universidad Complutense de Madrid, and wedge bonding has been carried out at Insituto de Ciencia de Materiales de Madrid (ICMM-CSIC).

The process to fabricate micro- or nanostructured samples is as follows:

a) Sample thin film growth and electron beam lithography to obtain micro- or nanopatterns.
b) Wet etching of the sample to define the micro- or nanostructures.
c) (Optional) Growing of a second material and second lithography with wet etching or growing of second material to be used as mask.
d) Design of contacts using photolithography.
e) Contact deposition via sputtering or evaporation.
f) Wire bonding of the finished device.

These steps will be explained in detail.

2.4.1. ELECTRON BEAM LITHOGRAPHY

The electron beam lithography has been done using a Raith50 system adapted for the SEM Zeiss Evo50 at Universidad Complutense de Madrid (Figure 2.11.).

On top of the SEM it consists on an external module to control the deflection of the electron beam to be able to expose patterns, a beam blanker and a laser interferometer-controlled stage. This system allows the design of lithographic patterns via software. Then, the pattern generator deflects the electron beam forming the shape designed on the sample with a maximum resolution of 50nm.

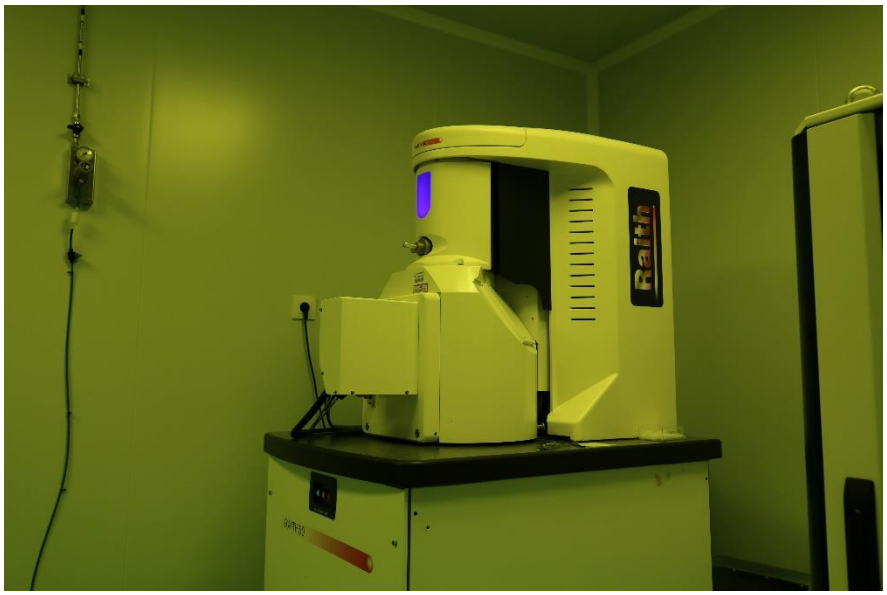

Figure 2.11: RAITH 50 system, located at CAI de Ciencias Físicas, used for all the electronic lithography process in this thesis.

This process is based on the transference of a pattern to a layer of resist that can interact with the radiation applied (in this case, electrons) [8]. We can use two types of resist, negative or positive, depending on if the irradiated zones are going to remain on the sample or the irradiated zones are going to be removed using the developer (Figure 2.12.)

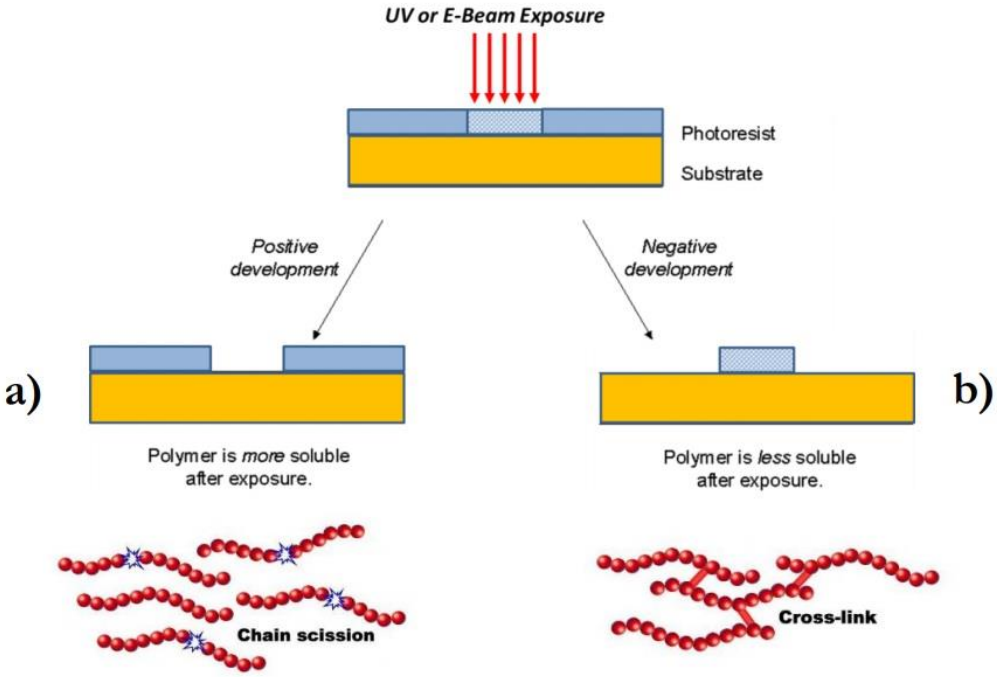

Figure 2.12. Depending on which resist we use the irradiated zone can remain or be removed. Radiation breaks the polymeric chains and causes that the exposed resist can be removed using positive resist (a). When we use negative resist (b) the process is the opposite, the irradiated zones remain on the substrate after the developing process.

Negative resist is commonly used to define patterns on top of layers that are going to be etched, and positive resist to grow materials on top and use it as sacrificial layer.

The steps to perform an electron beam lithography and photolithography are as follow:

a) Substrate cleaning and preparation

We start with a substrate or a sample that we clean applying acetone and isopropanol, to remove all dust particles that can be in the surface. Also, we heat the sample to 100 ºC degrees to desorb possible remains of water.

b) Resist spinning and bake

After cleaning the sample, we put it in the resist spinner (Figure 2.13), where the resist will be deposited by spin-coating. The sample is attached to a base with an orifice which is connected to a pump system. Then the sample rotates at 6000 or 7000 r.p.m., depending on the resist used (Table 2.3.). The rotation time depends on the thickness of resist desired. To assure the correct deposition and homogeneity of the resist the time is usually set to 30 seconds.

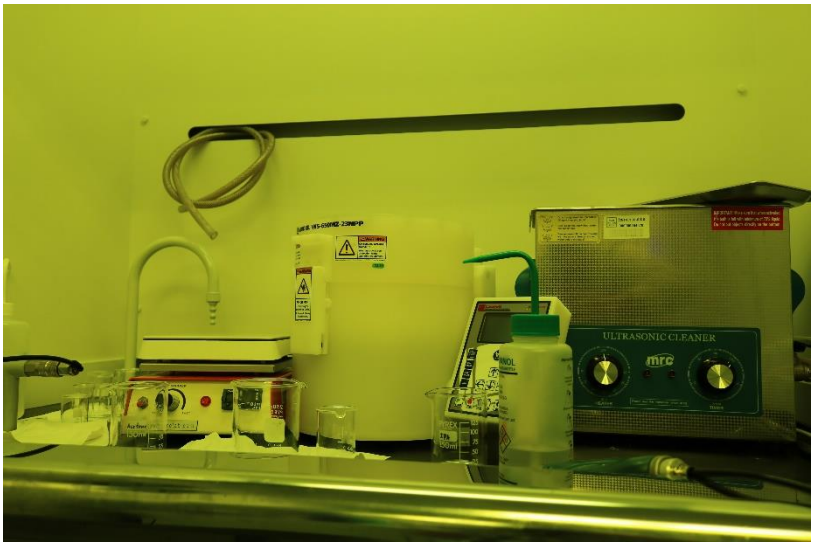

Figure 2.13: From left to right: hot plate to bake the samples with resist, resist spinner and ultrasound cleaner.

When the resist is correctly deposited a soft bake is done. The sample with the resist on top of it is placed in a heating plate at a temperature that depends on the resist we are using (Table 2.3.). If the substrate or material we are using is insulator, a deposition of a conductive polymer will be necessary to assure there is no charging problems when the sample receives the electron beam. We scratch the upper right corner to make easier to define a coordinate system in the EBL. Then, the sample is cooled to room temperature and ready for the next step.

Resist	nLof-2070	ma-N2403	PMMA 950K A4
Tone	Negative	Negative	Positive
Type	Photo	EBL/Photo	EBL
Rotation speed	6000 rpm	7000 rpm	6000 rpm
Thickness	1 um	300 nm	300nm
Bake Temperature	115ºC	90ºC	180ºC
Bake time	70'/120'	90'	90'

Table 2.3. Resists and its conditions. For nLoF-2070 two bakes are needed, one before exposure and one before development.

c) Pattern exposure

Once the sample has the resist on it, the next step is to introduce it in the Raith50 electron beam lithography. In its stage, it has three positions with metallic clamps (to assure the sample does not charge) and the chamber can achieve a pressure of 10^{-8} mbar. When we turn on the beam, we have to set all the parameters for the corresponding resist. These parameters can be seen in table 2.4.

Resist	ma-N2403	PMMA 950K A4
Tone	Negative	Positive
EHT	10 KV	
Working distance	10 mm	
Write-field	100 x 100 um	200 x 200 um
Beam Current	90-150 pA	
Step size	6-20 nm	50-100 nm
Area dose	35uC/cm^2	100 uC/cm^2

Table 2.4. EBL parameters for the two ebl-resists. Usually ma-N2403 is used for small designs and PMMA is used for contacts or big designs.

First step is to define a coordinate system, in which the lower left corner is our origin. Then we take the lower left corner to be (x,0), being x the lateral size of our sample. This way we can correct a possible tilt angle in the sides of the sample. To focus the beam, we go to the upper right corner, where small pieces around the scratch are used. At this point we have two possibilities, depending on the sample.

If it's an overlay (the sample already has a design on it) we have to adjust the coordinates again using a 3 points method. This way our second lithography will be in a place relative to the previous design. For example, if we have a microwire and we want to put contacts on top of it, we will need to perform a three points adjustment.

If we have a sample without previous designs or we already have performed the three points adjustment, we have to correct the write-field alignment, to prevent overlaps or separations between different write-fields (A write-field is the area the beam can expose by deflecting the beam, without any spatial movement). After the correction is done it

only remains to load the design we want to use, and to check the beam current to correct the doses.

An example of EBL design, the used for one of the experiments of this thesis is in Figure 2.15. It is an example of a two-layer lithography in which the purple design is the first step and then on top of it the blue design is the second lithography layer, with squares as marks to ease the alignment for the second lithography.

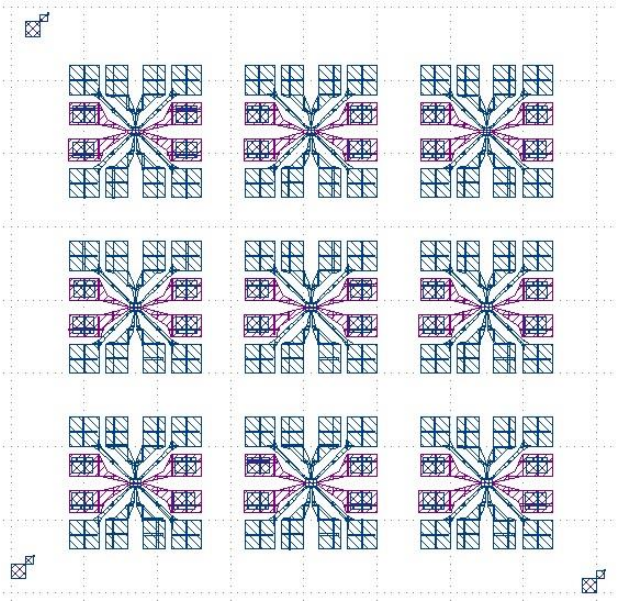

Figure 2.15: Josephson microwires design. It has been design using KLayout and then loaded into the EBL computer.

d) Resist development

After we have exposed the resist to the electron beam, it has changed its properties (depending on the tone, negative resist exposed has hardened and positive resist has softened). For the development we use different chemicals in function of the resist used, and the conditions and times can be seen in table 2.5.

Resist	ma-N2403	PMMA 950K A4
Tone	Negative	Positive
Developer	MF-319	MIBK:IPA (3:1)
Development time	20'	30'
Stopper	Deionized water	Isopropanol (IPA)
Stopper time	15'	

Table 2.5. Development characteristics for each EBL resist

The idea is to introduce the samples in the developer and move them by circling. The resist that is not hardened will fall and we will obtain our pattern. Then we introduce the sample in the stopper and afterwards we put it in the hot plate to remove all remaining liquids, as water or IPA, and to harden the resist that remains in the sample. Now we are ready to the wet etching process.

2.4.2. WET ETCHING

With our sample with resist on it we perform the wet etching. This mechanism consists on using an acid to etch the material that it's not protected by the resist. For example, if we have a single layer with a microwire of resist on it, after we introduce it in the acid for a certain amount of time, the only part of the layer that will not be etched will be the one under the resist. This acid depends on the material we want to etch, but in our case the base is HCl for all materials (YBCO, LCMO and LSMO). The recipe for each one is as follows:

For YBCO: HCl 0.0037%.

For LSMO: 4 ml of HCl 37% + 4 ml of KI + 70 ml of H2O deionized.

For LCMO: 6 ml of HCl 37% + 6 ml of KI + 70 ml of H2O deionized.

The process is the same for all of them. We have 3 recipients: one with our recipe and two with deionized water. The etching takes between 1 and 5 seconds depending on the thickness of the sample when introduced into the acid, then it is introduced 1 second into the first recipient with water during 1 second, and immediately into the second recipient with water for at least 10 seconds. This removes any remaining acid from the sample. After this step we measure the conductance of the sample at the borders, to assure that all the material has been etched in the case of insulating substrates, and check with an optical microscope to see if it has been correctly etched. If it is not, the process is done again.

When the etching has finished, the sample is cleaned with acetone and isopropanol, to remove the resist and any residual present in the sample.

This method has a limit when etching YBCO, because of the deoxygenation of this material. Small devices of YBCO show lower critical temperatures when wet etched than the ones patterned with alumina template, as will be seen in next sections.

2.4.3. PHOTOLITHOGRAPHY

The photolithography (PL)has been done using Karl Suss Mask Aligner MBJ3 located at CAI de Ciencias Fisicas at Universidad Complutense de Madrid (Figure 2.16). In this thesis, photolithography has been used as a complementary method to EBL, for example to put large contacts on top of micron-size devices. One important thing to take into account is the size limit of the PL, the minimum resolution of this technique is limited by the diffraction of the incident radiation, being 1 micron in our system.

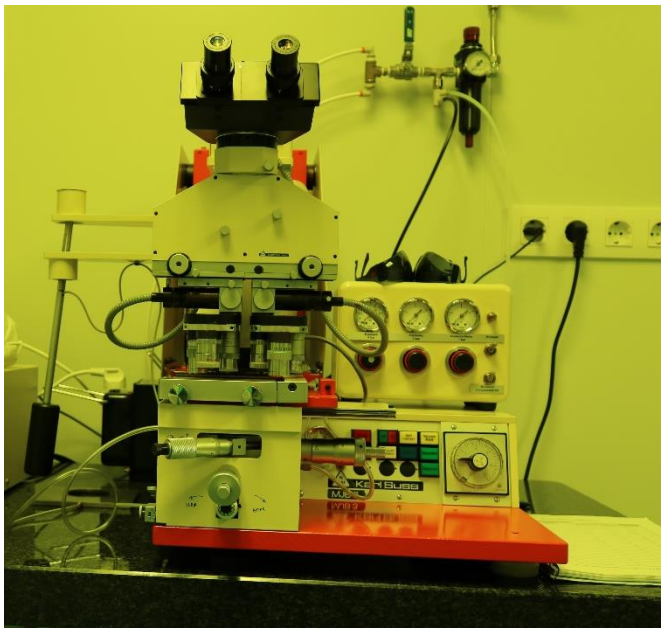

Figure 2.16: Karl Suss Mask Aligner MBJ3 located at CAI de Ciencias Fisicas at Universidad Complutense de Madrid where the photolithography process has been carried out.

Photolithography is a very similar process to EBL, but in this case the particles that change the properties of the resist are photons. For all samples, nLof-2070 (Table 2.3) has been used. The exposure time is 6.3 second, and the developer is MF-319 during 1 minute with deionized water as stopper. To expose the resist (the only different step from the EBL process), a mechanical mask is put between the sample and the radiation source, a mercury lamp that emits ultraviolet radiation with a wavelength close to 400nm. The mechanical masks can be designed using software like Klayout. The designs have to be centered and be larger than 1 micron or separated

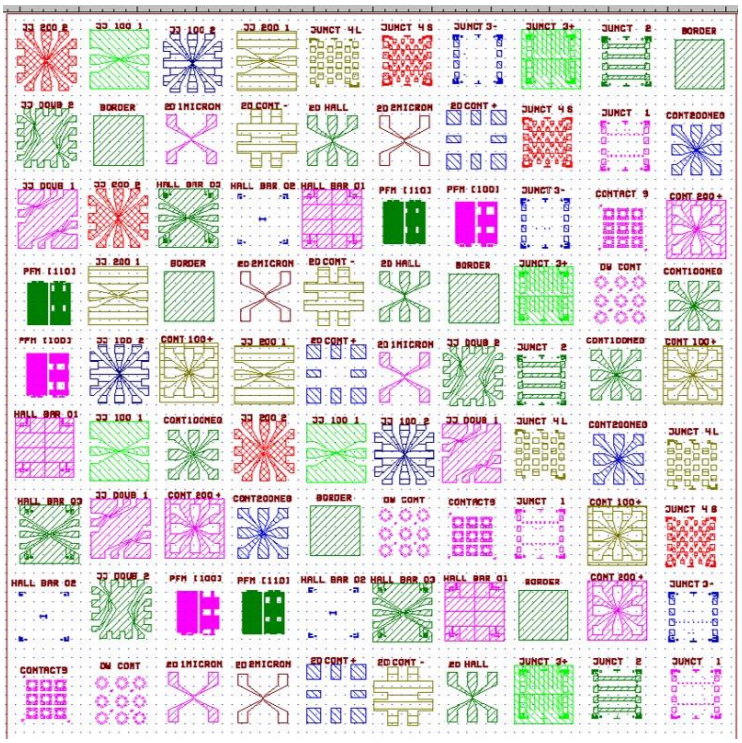

Figure 2.17: Mechanical mask used to perform photolithograpy. It fits 100 designs used for different experiments.

more than 1 micron, but the masks can fit as much as 100 designs (Figure 2.17). This pattern is

then imprinted using chromium into a glass, allowing the UV radiation to go through the glass. Consequently, everything will be illuminated except the designs. That is why some of them are negatives of other, to allow the use of negative and positive resist. Finally, the steps to perform a photolithography are as follow:

1. Turn on the UV lamp and wait until its emission in stable.
2. Put the resist on the sample with the spinner at 6000 rpm and 30''. Bake 1'30'' the resist at 110 degrees.
3. Align the mechanical mask and the device in the sample in which we want to put the metallic contacts.
4. Exposure of the sample: 6.3 seconds. Second bake at 110 degrees 1'30''.
5. Development of the resist using MF-319 1' and 30'' in deionized water as stopper.

Now we have holes opened where the metal will be deposited. For the complete removal of the resist and the metal on top of it, MR-Remover can be used, but acetone functions perfectly well.

2.4.4. METAL AND INSULATOR DEPOSITION

For the deposition of metals and insulator, a magneton sputtering (Figure 2.18) at room temperature has been used, located at Laboratorio de Materiales Complejos at Universidad Complutense de Madrid. It has two places to attach targets of different materials and an oxygen and argon pressurized line. Some of the materials that can be grown on it are: Au, Ag, Pt, Fe, Al, Py ITO, ALO, etc. The most used materials in this thesis have been Au for electrical contacts and ALO for YBCO templates.

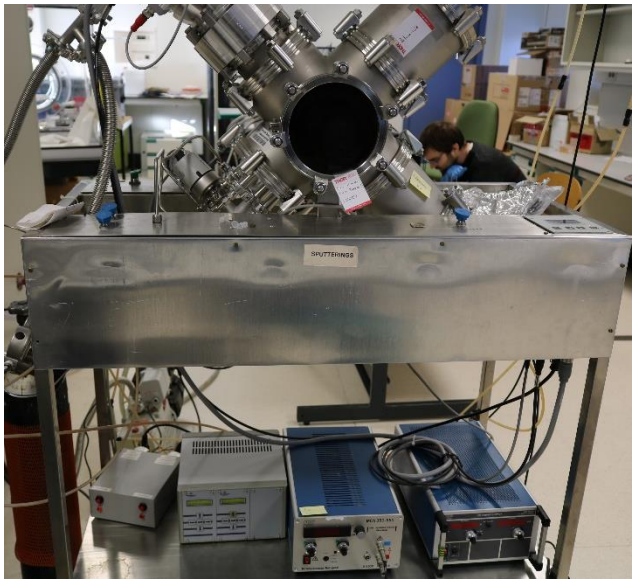

Figure 2.18: Magneton sputtering for metal and insulator deposition. It has both oxygen and argon accessible. Each of the two targets has a DC source, but it can also work with RF sources.

To metalize contacts the procedure is as follows:

1. Introduce the sample with the pattern from photolithography into the chamber and wait until it reaches 10^{-7} mbar.
2. Turn on the target desired, usually Au, at a pressure of Ar of $7.4 \cdot 10^{-3}$ mbar and with a current applied of 100mA. After 5 minutes of presputtering to clean the surface of the target, the growth starts.

3. With 10 minutes of sputtering enough Au (~200nm) is deposited. Chamber is open and the sample removed to do the lift off.
4. The lift-off is done in MR-Remover, for 5 minutes with the sample upside down, so the metallic layer on top of the resist can fall without problems.

After this procedure our sample is ready to be bonded and measured.

To deposit AlO_x as template for the YBCO the procedure is similar:

1. Turn on the Al target at a pressure of $Ar:O_2(2:1)$ of $7.4 \cdot 10^{-3}$ mbar and with a current applied of 300mA. After 30 minutes of presputtering to clean the surface of the target, the growth starts.
2. With 3h 30' of sputtering 50nm of ALO is deposited. Chamber is open and sample removed.
3. The lift off of ALO is much more difficult than a simple metal. It requires MR-Remover for 10 minutes and ultrasounds to soften the resist that has been under a plasma for more than 3 hours. Then a cotton swab is used to assure the resist has been completely removed, but even then, sometimes it remains with ALO on top of it in some devices.

After the ALO deposition, the sample is ready to grow on top of it the YBCO. YBCO will grow insulating in top of ALO, but epitaxial and superconducting in the zones that were covered by resist. Even though, this method is extremely sensible. Too much ALO and the resist will harden so the lift-off won't be successful and the YBCO will be completely insulating in top of it.

2.4.5. WEDGE BONDING

Wedge bonding has been carried out at Instituto de Ciencia de Materiales de Madrid (ICMM-CSIC) and at CNRS-Thales (Palaiseau) using a K&S 4526 auto-stepback wedge bonder with aluminum microwires (Figure 2.19).

Wedge bonding is needed when the devices are too small to contact them with usual copper wires. For example, if the contact areas are smaller than 0.5x0.5 mm^2, the process has to be done with wedge bonding, which works perfectly with contact areas of 100x100 um^2.

To perform it, the sample is glued to our chip. We will contact the device to the metallic pad in the chip and from there we can work with copper wires. The first contact is done in the device with these parameters, but they can vary depending on the materials used:

Force: 7/10 Time: 5.5/10 Power: 1.5/10

The second step is done in the chip with these parameters:

Force: 9/10 Time: 5.5/10 Power 4/10

This procedure also has its problems. When the Al wire is bonded directly to the YBCO it starts to oxidize, and creates a bad electrical contact after some weeks, also causing the YBCO to deoxygenate. Usually a gold contact is put on top of the YBCO to prevent this effect. When the

YBCO is nanostructured is more efficient to put the Al wire directly on it, because the lithography process to metalize the contacts usually reduces its critical temperature from 90K to 40K.

Figure 2.19: K&S 4526 auto-stepback wedge bonder used for the bonding of samples.

After this process, the sample is ready to be measured.

2.5. LOW TEMPERATURE MEASUREMENTS

Low temperature magnetotransport measurements have been performed at Universidad Complutense de Madrid and at CNRS-Thales (Palaiseau). Additional measurements have been carried out at ESPCI Paris.

2.5.1. CLOSED CYCLE CRYOSTAT

Most of the magnetotransport measurements have been done in a closed-cycle APD Cryogenics helium cryostat (Figure 2.20) which works with the expansion of highly-pure He-gas compressed in a Gifford McMahon cycle. The expansion through the capillaries undergoes two steps at 50K and at 8.5K. The sample is mounted onto a cooled copper piece in contact with the second cooling step. The system is evacuated by a rotary pump capable of a pressure down to 10mTorr,

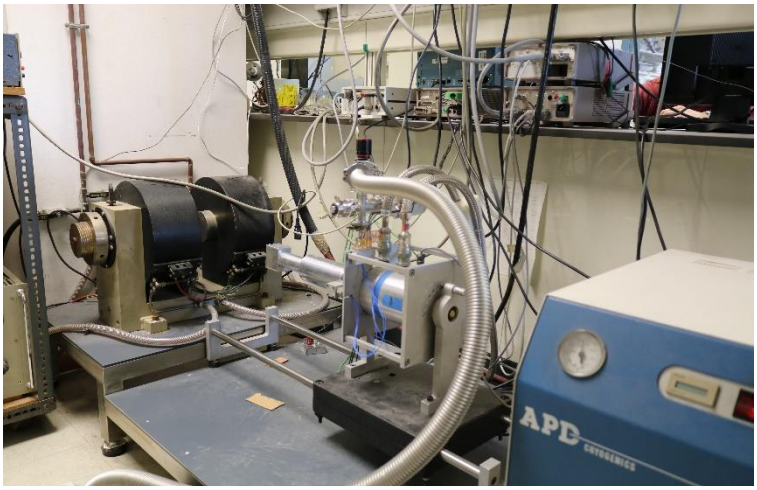

Figure 2.20: APD cryogenics cryostat located at laboratory 123 at UCM. It can reach 12K and rotated 90 degrees to perform out of plane magnetic measurements with the electromagnet.

measured with a Pirani vacuum sensor. A silicon diode thermometer is in contact with the sample holder calibrated for measuring between 15K and 325K. Another cryostat used has been the Cryostation Montana (Figure 2.21), sold by Montana Instruments, which works with the

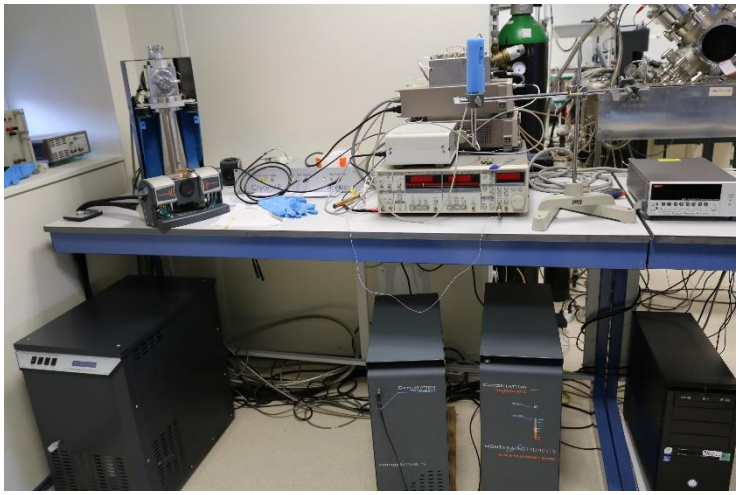

Figure 2.21: Montana Cryostation located at laboratory 10 at UCM. It has been used both in magnetotransport measurements as in FMR measurements.

same principle but can reach temperatures as low as 3.2K. Also, all cryostats count with an electromagnet which can apply up to 5000 Oe. These systems have been used for the magnetoelectrical characterization of the samples.

2.5.2. HELIUM FLOW CRYOSTAT

Another type of cryostat used in this thesis has been a helium flow cryostat (Figure 2.22). It consists on a closed space thermally isolated by vacuum chambers in which a continuum flow of liquid helium is introduced. It cools the sample faster and can reach 1.8K, but it needs large amounts of liquid He, which is expensive. It needs then a method to recover the used helium, in gas form to reutilize it.

Figure 2.22: Helium flow cryostate located at CNRS-Thales were FMR measurements were performed. The helium is stored in a dewar and is introduced into the cryostat using a canne connected to a pump.

2.5.3. PHYSICAL PROPERTIES MEASUREMENT SYSTEM (PPMS)

The PPMS (Figure 2.23) is an automated low-temperature and magnet system for the measurement of material properties like specific heat, magnetic AC and DC susceptibility and both electrical and thermal transport properties (like Hall Effect, thermoelectric figure of merit and Seebeck Effect). PPMS was used both for magnetotransport measurements and for FMR measurements.

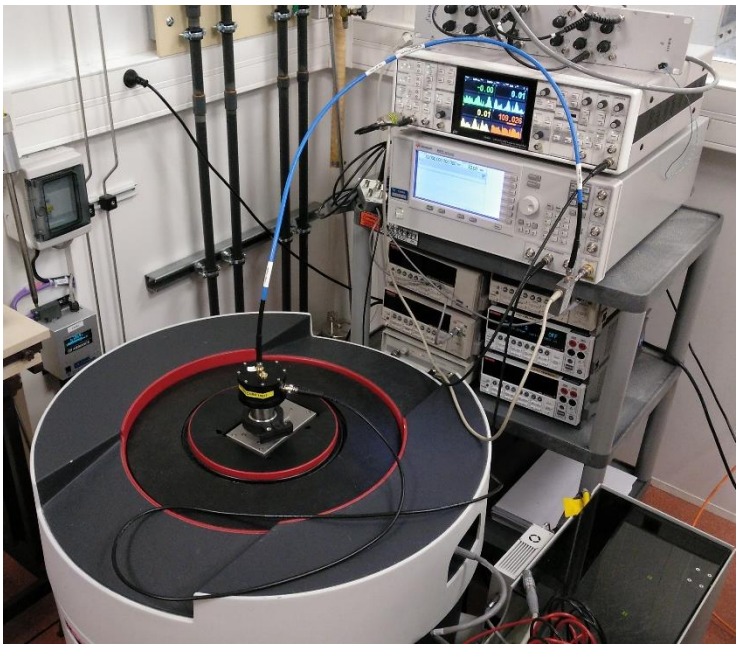

Figure 2.23: PPMS located at CNRS-Thales used for magnetoelectrical and FMR measurements. It is a new model that works with a compressor and not charging it with helium.

2.6. MAGNETOTRANSPORT MEASUREMENTS

For all these measurements we have used the above cited cryostats and the currents sources Keithley 6221 and 6220, and the nanovoltmeter Keithley 2182A.

2.6.1. ELECTRICAL MEASUREMENTS

One big problem with electrical measurements of superconductors is the contact resistance. Even with YBCO at lower temperature, if we put two wires and measure its resistance, it is not zero, because we are measuring in series the resistance of the two wires and the two contacts. Then, all measurements have to be done using a 4-points (or 4 wires) measurement.

4-point measurements consist on separating the current and voltage electrodes to eliminate the wire and contact resistance from the measurement. For example, if we have a superconducting wire and we want a 4-point measurement, the current is injected through the extremes of the wire, and the voltage is measured in the wire (Figure 2.24). This way, the voltage is measured exclusively in the superconducting wire, not including the contacts.

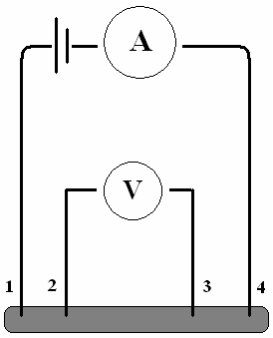

Figure 2.24: Four points measurement. Current is applied through 1 and 4, but voltage is measured between 2 and 3. The voltage measured is due only to the current flowing between 2 and 3, avoiding the contact resistance.

Using this method, we can measure how the resistance behaves with temperature (RvsT), the current-voltage characteristics of the system (IV) and the differential conductance to search for superconducting (or tunnel) signatures.

2.6.2. MAGNETIC MEASUREMENTS

The magnetic measurements have been carried out at the cryostats mentioned before, using an electromagnet to apply the field. To assure a good measurement of the field, a Hall sensor have been used, located close to the sample. It is important to place it correctly so positive field (positive voltage applied to the electromagnet) is measured correctly and without any change of sign.

The typical magnetic measurements are the Resistance vs applied field (RH), IV in function of the applied field (IVH) and these measurements in zero field cooled (ZFC) or field cooled (FC)

Additionally, hysteresis loop measurements have been performed in a SQUID, which is mounted in a similar set-up as the PPMS. It is a very sensitive magnetometer to measure small magnetic fields, as the one generated by the small 5x5 mm^2 samples we use.

Another method used to measure magnetic properties has been Scanning PhotoEmission Electron Microscopy (SPEEM).

2.7. SCANNING PHOTOEMISSION ELECTRON MICROSCOPY (SPEEM)

The SPEEM measurements have been carried out at the synchrotron BESSY II at the Helmholtz Zentrum Berlin. In SPEEM we apply on our sample a photon beam with energies between 100 and 1000 eV, enough to excite the electrons of the outer shells of the atoms we want to image. These method collects the secondary electrons generated in the electron cascade that follows the creation of the primary core hole in the absorption process. This implies that it is a selective technique, if you measure a certain energy, there is only one atomic species that is going to interact with the applied beam. Something important to consider is that SPEEM is a surface sensitive technique, because the emitted electrons originate close to the surface of the sample.

The “scanning” part of the technique means that there is spatial resolution in the information that acquires. This is very useful for seeing phase separation in alloys, for example, to observe magnetic domains and to observe different magnetic textures, as skyrmions, magnetic vortex or domain walls.

2.7.1. X-RAY ABSORPTION SPECTRA (XAS)

With SPEEM we can measure how much electrons are emitted in function of the incident photon energy, which is proportional to how much photons the materials absorb. This is known as X-ray absorption spectra. With this method we can detect for example different oxidation states in a material, ions with different valence states, or more generally which atomic species we are probing. An example of a XAS is in Figure 2.25.

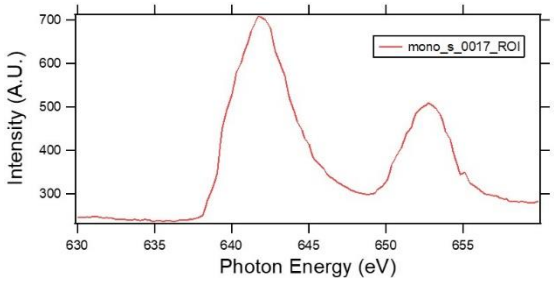

Figure 2.25: XAS of a LSMO layer. It can be seen both peaks of energy, one due to Mn3+ and the other one for Mn4+

XAS is also useful for choosing the good energy (the one with bigger intensity) for conducting X-ray Magnetic Circular Dichroism, XMCD, experiments.

2.7.2. X-RAY MAGNETIC CIRCULAR DICHROISM (XMCD)

XAS is measured with linearly polarized light. But what does happen when light is circular polarized? Absorption spectra behaves differently to left circularly polarized light and right circularly polarized light, but only when the material is magnetic. The difference between both signals is proportional to the magnetization of the sample, hence providing a powerful element resolved spectroscopic method to measure magnetism. If we put this together with the spatial resolution of SPEEM, we can have images of the magnetization behavior of the surface of our sample. An example of an XMCD image spatially resolved is Figure 2.26.

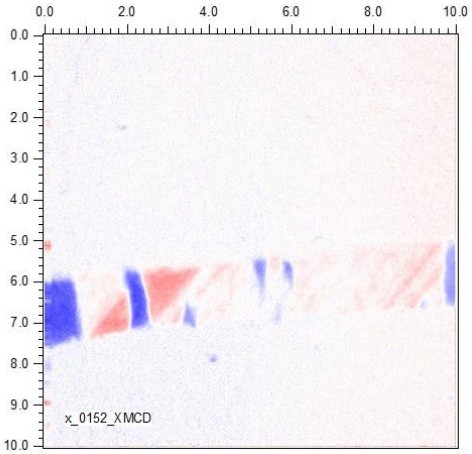

Figure 2.26: Image of the separation of two YBCO bridges (white) on top of a 25um LSMO microwire, in which can be seen different domains (different shades of blue and red)

In this figure, we can observe domains in different colors. The magnitude of the XMCD signal depends on the projection of the magnetization with respect to the beam. Blue color means negative signal, magnetization antiparallel to the photon beam, red color means parallel to the beam, and the white means no magnetization or magnetization perpendicular to the beam. If we rotate the sample to change the projection of the magnetization on the beam, we can obtain a 2D map with the direction of the magnetization pixel to pixel (Figure 2.27).

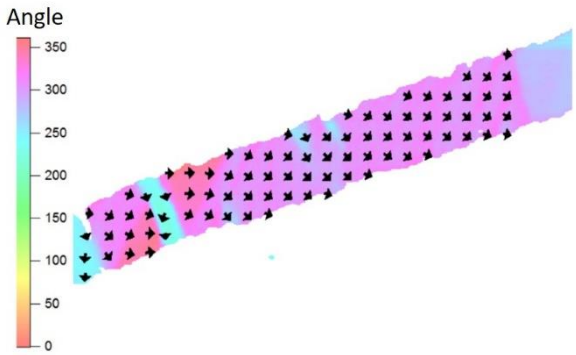

Figure 2.27: 2D map of the magnetization of a LSMO wire. The color scale is the angle between the magnetization and the photon beam direction.

Thanks to XMCD it has been possible to study the formation of domain and domain walls when a ferromagnet as LSMO is in proximity with superconducting YBCO.

2.8. FERROMAGNETIC RESONANCE SPECTROSCOPY

FMR (FerroMagnetic Resonance) is a measurement technique that allows to study the magnetism and spin dynamics of a sample using the precession of its magnetization.

The theory of FMR has been explained in the introduction, now we need to make it real. Part of this thesis work has been installing two new FMR set-ups, one DIY at CNRS-Thales, and one provided by Montana Instruments and NanoOsc at Universidad Complutense de Madrid. In this technique, we use an RF-signal and magnetic fields to make the magnetization precess. When the frequency of precession is equal to the frequency of the RF-signal, we have a resonance of the alternating magnetic field of the microwaves and the one of the sample. It will give rise to a maximum at the absorbed power. This gives us information about the magnetic properties. We can reach the resonance condition by changing the field (ergo, the frequency of precession) or changing the frequency of the RF signal. Experimentally it is much easier to change the magnetic field because the equipment needs more time to stabilize a frequency than a field.

In the next sections, it will be explained how to build an FMR set-up and how to measure and analyze the data that we can extract.

2.8.1. FMR SET-UP

First, Figure 2.28 shows a scheme of the experimental set-up with all the equipment for the DIY set-up installed at CNRS-Thales in a liquid He flow cryostat. In the next list, all the equipment of the scheme is explained:

- RF-source: A Keysight E8257D Analog signal generator, with capacity to generate frequencies between 250 KHz and 20 GHz with powers between -20 and 20 dBm. It is used to apply the microwaves at frequency and power desired. It is convenient to turn it on 10 minutes before starting measurements (Figure 2.29 (b)).
- Circulator: It is a device in which a microwave signal entering any port is transmitted to the next port in rotation. Our circulator has 3 ports. The first one is connected to the RF-source, the second one to the sample and the third one to the lock-in. The RF-signal goes to the sample, where it is absorbed, or not. Then it reflects at the end of the coplanar wave guide, returns and goes to the lock-in.

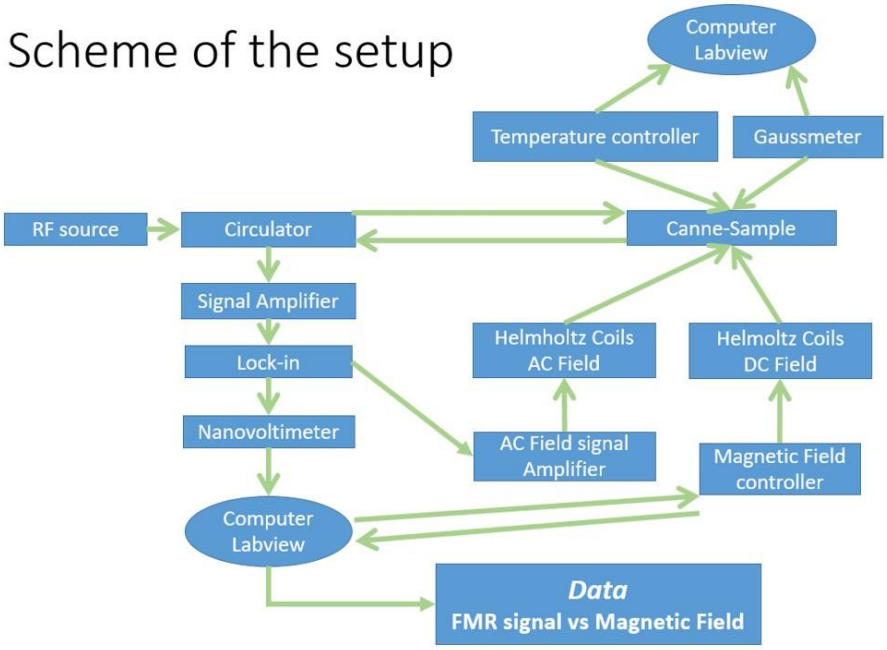

Figure 2.28: Scheme of the FMR set-up with all the equipment necessary to perform the measurements. At the Canne-Sample is located a coplanar waveguide.

Figure 2.29: (a) Magnetic field controller. (b) RF-signal generator. (c) Electromagnet coils and Helmoholtz coils.

- Coplanar waveguide (CPW): It is the sample holder where the sample receives the microwaves. A schematic image can be seen in Figure 2.30. In order to have the largest effect into the sample, this should be placed up-side-down. The microwaves generate a magnetic field perpendicular to its direction. Thus, to achieve a resonant condition, a magnetic DC field has to be applied to the sample, perpendicular to the field created by the MW. After the signal has passed through the sample, it is measured at the lock-in.
- Lock-in: It is used to reduce the noise in the measurement. To do so, an AC magnetic field of low amplitude is applied to the sample, so the signal is modulated by this AC component. The lock-in measures at that same frequency, reducing largely the noise at other frequencies. Also, due to the wiring, the signal that the lock-in extracts is the derivative of the original signal (original signal is a Lorentzian curve), which simplifies the analysis, as will be seen in next sections.

- Nanovoltimeter: This part is not necessary usually; it simply was put as a simpler way to communicate the used lock-in with the computer via Labview. The connection can be done directly from the lock-in to the computer. It provides the FMR signal.

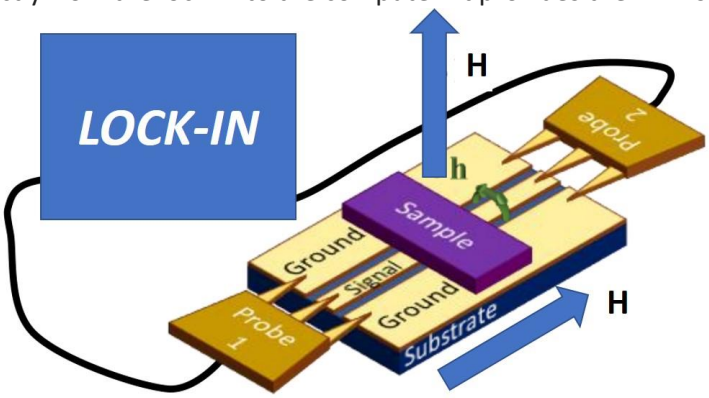

Figure 2.30: Scheme of a CPW for the transmission case. When it is in reflection, the second probe is removed, and a circulator is needed.

- AC signal amplifier: It receives an AC signal from the output of the lock in and amplify it so its magnitude is enough to create magnetic fields of the order of 2-5 Oe.
- Magnetic Field controller: It applies a voltage or current to the coils to have a DC magnetic field with values up to 0.5T (Figure 2.29 (a)).
- Electromagnet and Helmholtz coils: The electromagnet supplies the DC field and is connected to the controller. The Helmholtz coils applies the AC field and is connected to the lock-in via amplifier (Figure 2.29 (c)).
- Temperature controller: It measures and controls the temperature using a resist to warm the sample. It communicates with the Lavbiew program to provide a value of temperature.
- Gaussimeter: Measures both the DC and AC magnetic field. It is important that the AC magnetic field is not higher than the size of the linewidth of the resonance, to not distort the FMR signal by putting an AC field too big. It communicates with the Labview program to provide a value of the magnetic field.
- Computer and LabVIEW: The Labview program is used to change the measurement parameters and to record the measured data. It plots and save the FMR signal, magnetic field, temperature and frequency for each.

On the other hand, a commercial FMR set-up has been installed at Universidad Complutense de Madrid. It is a module that can work together with a Montana Cryostation, a closed cycle cryostat which can reach T=3K and H=0.5T. Something important to note is that this set-up works in transmission. The RF goes to the sample, it is absorbed and we measure the RF that has not been absorbed. All the electronics are mounted in a module called CryoFMR, which acts as RF-source, lock-in, gaussmeter and field controller (Figure 2.31). It is provided with two small Helmholtz coils to attach to the Cryostation magnet, a Hall sensor to measure the magnetic field, and a CPW to place the sample and measure.

It is provided also a Labview program that controls frequency, magnetic field and different parameters to optimize the FMR signal. It also can analyze the signal and extract the damping, but it is not so reliable when the signal is noisy or if there is more than one FMR peak.

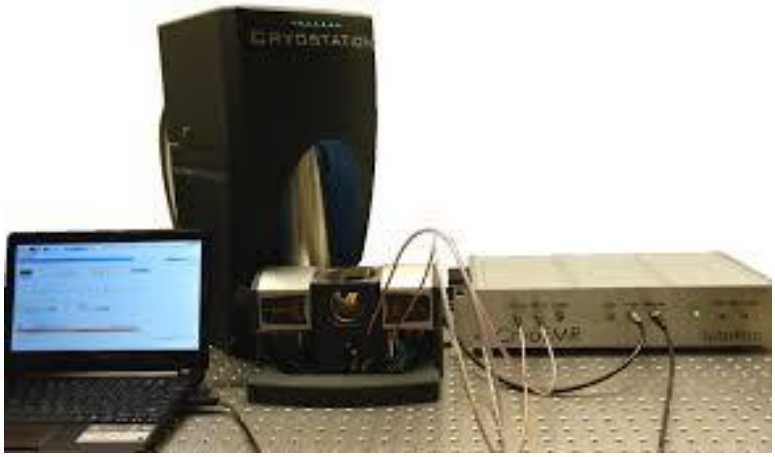

Figure 2.31: CryoFMR connected to the Cryostation. This device applies the RF, DC and AC magnetic field and measures the field and the RF signal.

2.8.2. HOW TO MEASURE

To start measuring is important first to calibrate all the parameters so we can have a maximum FMR signal. But first we have to find the resonance field at some frequency. One good start is to measure at 6 GHz and 20 dBm, with an AC field amplitude of 2 Oe. With these parameters, we can sweep in field from 5000 Oe to 0 Oe with a step big enough so the measurement takes less than 2 minutes. We will not have enough accuracy in this measurement but is an easy way to find the first resonance field. Once we have localized a resonance, we can optimize the signal. Some of the parameters that can be optimized are:

- AC field: Its amplitude and frequency can be changed until we reach the largest signal to noise ratio. It is important to have an amplitude smaller than the linewidth of the resonance we are measuring (for all frequencies). One good start is 2 Oe of amplitude and 490Hz of frequency.
- Power: The higher the power, the higher the signal, but if it is too high it can heat the sample, at least at low temperatures.
- Amplifiers: Both the input and the output of the signal can be amplified. Amplifying the input is almost the same as increasing the power but amplifying the output can be useful.
- Rate and number of samples: If we change the number and sample rate of readout values from the lock-in (which are averaged to obtain the signal), we can obtain better signal to noise ratios.
- Wiring: Special cables are needed due to the RF-signal. To have a good signal, the wires must be able to carry RF up to 40 GHz with minimum loses. The better wiring, the better signal.

Once the signal has been optimized it is time to start measuring. It is always a good idea to make a measurement at room temperature before cooling down. To perform a measurement to obtain the damping of a sample it is needed to measure at several frequencies. Again, if the M_S of the sample is not known to calculate the resonant frequency

using the Kittel formula, a good method is to measure with a high step field to localize the resonance at all frequencies. When we know (approximately) at which field are the resonances we start measuring.

A good interval to measure is between 6 and 20GHz, with steps of 1GHz or 0.5GHz (depending on the available time). With the resonance at these frequencies damping and M_S can be extracted. Next step is to cooldown and start measuring at low temperatures to have information on both damping and M_S in function of temperature. Also it is good to start saturating the sample with the highest field before measuring and starting by the highest frequencies, so the magnetic state is the most homogeneous possible.

After this step we will have measurements of the FMR signal in function of signal and temperature, which will be analyzed to extract the desired parameters.

2.8.3. HOW TO ANALYZE DATA

Once we have everything measured, it is time to analyze the data. A typical FMR signal at a certain temperature and frequency can be seen in Figure 2.32.

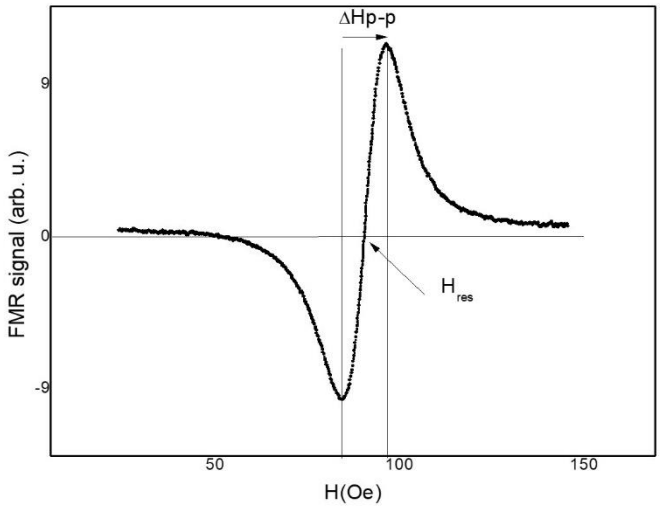

Figure 2.32: FMR signal of Py at room temperature. Two parameters can be easily extracted, the linewidth peak to peak and the resonant field.

There is two ways of analyzing this signal. To obtain the peak to peak linewidth just subtract the field for maximum and minimum FMR signal, and for the resonance field add them and divide by 2. This is an easy way to obtain these parameters, but only when the signal is homogeneous and there is only one peak. For all the other cases, a fitting must be done.

For the fitting, we use the derivative of a typical Lorentzian curve where ΔH is the full width at half maximum and H_{res} is where it is centered:

$$\mathrm{FMRsignal} = K_1 \cdot \frac{\frac{\Delta H}{2}(H - H_{res})}{\left((H - H_{res})^2 + \left(\frac{\Delta H}{2}\right)^2\right)^2} + K_2 \cdot \frac{\left(\frac{\Delta H}{2}\right)^2 - (H - H_{res})^2}{\left((H - H_{res})^2 + \left(\frac{\Delta H}{2}\right)^2\right)^2} + \mathrm{Offset} + H \cdot \mathrm{Slope}$$

This $\Delta H = \sqrt{3}\Delta H_{pp}$ so either of these values can be used without problem to calculate the damping.

To calculate the damping, the ΔH for different frequencies is needed, as it follows the next relation:

$$\Delta H = \frac{4\pi\alpha F}{\gamma} + \Delta H_0$$

where α is the damping constant (or Gilbert damping), F is the frequency, γ is the gyromagnetic ratio and ΔH_0 is the inhomogeneous broadening. This value gives information about magnetic inhomogeneities on the sample. Doing a linear fit of the data with this equation we can extract both damping and ΔH_0 as can be seen in Figure 2.33.

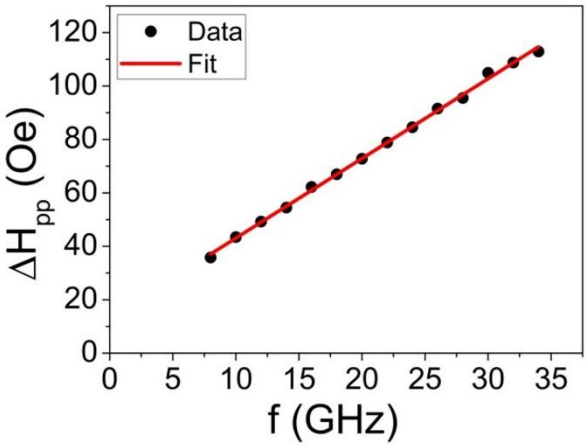

Figure 2.33: Plot of the ΔH_{pp} vs frequency. The slope of the curve is the damping and the intercept is the ΔH_0.

With the frequency as a function of the resonance field we can extract the gyromagnetic ratio, the M_S and the anisotropy field, H_k, by fitting to the Kittel equation:

$$F = \frac{\gamma\mu_0}{2\pi}\sqrt{(M_S + H_k + |H_{res}|)(H_k + |H_{res}|)}$$

A typical fit with this equation is portrayed in Figure 2.34:

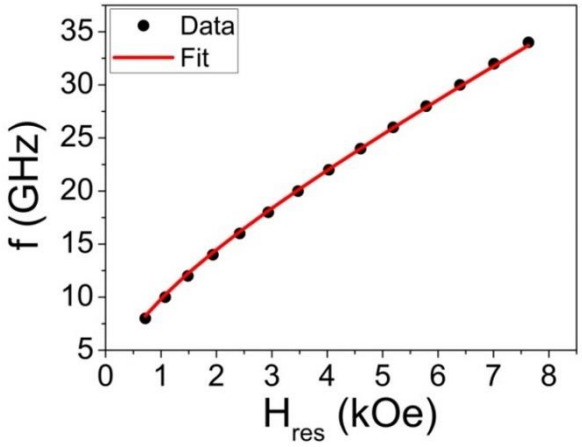

Figure 2.34: Fitting of experimental FMR data to the Kittel formula. To make it easier is better to put the frequency in the y-axis, contrary to the damping case.

With these parameters we can extract the magnetic behavior of a material in function of temperature. Damping will tell us about its dynamic properties, and M_S tell us about static properties. In this thesis, this study in function of temperature has been used to observe a proximity effect when the ferromagnet measured is put in contact with a superconductor. Hence, all parameters can be studied above and below the critical temperature of the superconductor to observe any possible change.

2.9. REFERENCES

[1] M. Varela, Z. Sefrioui, D. Arias, M. Navacerrada, M. Lucía, M. López de la Torre, C. León, G. Loos, F. Sánchez-Quesada, and J. Santamaría, "Intracell Changes in Epitaxially Strained YBa2Cu3O7-x Ultrathin Layers in YBa2Cu3O7-x/PrBa2Cu3O7 Superlattices," Phys. Rev. Lett. 83, 3936–3939 (1999).

[2] http://www.crystec.de/daten/srtio3.pdf

[3] Pulsed Laser Deposition of Thin Films, by Douglas B. Chrisey (Editor), Graham K. Hubler (Editor), pp. 648. ISBN 0-471-59218-8. Wiley-VCH, May 2003.

[4] Björck, M. and Andersson, G. GenX: an extensible X-ray reflectivity refinement program utilizing differential evolution. *Journal of Applied Crystallography*, 40(6), pp.1174-1178 (2007).

[5] A. Guinier, X-ray diffraction in crystals, imperfect crystals, and amorphous bodies (Dover Publications, 1994).

[6] J.G. Barriocanal, PhD Thesis "*Efectos de Interfaces en Superrredes de Oxidos Complejos" (2007)*

[7] https://www.gla.ac.uk/schools/ges/researchandimpact/researchfacilities/isaac/services/scanningelectronmicroscopy/

[8] I. Brodie and J. J. Murray, The Physics of Micro/Nano-Fabrication (1992).

Chapter 3: Proximity effect in Half-metal/Superconductor Josephson junctions

3.1 MOTIVATION AND OBJECTIVES

Ferromagnetism and conventional superconductivity are antagonistic phenomena. This is due to the pair breaking effect of the exchange field of the ferromagnet on opposite-spin singlet Cooper pairs. Pioneering theoretical works have raised the possibility of a long-range proximity effect in ferromagnet/superconductor (F/S) structures driven by triplet correlations, either for weak ferromagnets [1] or half-metals [2]. Recent experiments in multilayers composed of low temperature superconducting electrodes and transition metal ferromagnetic spacers have shown indications of Josephson coupling [3–5]. These experiments show the emergence of triplet Cooper pairing proximity effect. However, a clear signature of a Josephson effect has not been found yet.

The reason why conventional superconductivity and ferromagnetism are antagonistic phenomena relies ultimately in the spin sector. Superconductivity is mediated by Cooper pairs, and in singlets the spins of the electrons are antiparallel. On the contrary, in ferromagnetic materials the exchange interaction favors the parallel alignment of spins. Despite this, coexistence of superconductivity and ferromagnetism has been found, in materials like UGe_2, URhGe, UCoGe and $EuFe_2(As_{0.79}P_{0.21})_2$ [6,7] . The only way to explain this coexistence is via triplet pairing of Cooper pairs, in which the superconducting correlations are mediated by electrons with parallel spins. These triplet Cooper pairs and their creation have been widely studied, both theoretically [2,8–10], and experimentally [3–5,11–13]. The process of generating these triplet pairs needs for certain ingredients, as magnetic inhomogeneities [2] or spin orbit coupling [10]. For a spin-singlet pair to become a spin triplet pair it must pass through two different processes: spin mixing and spin rotation. Due to the spin mixing we can obtain both singlet (S=0) and triplet (S_z=0), and by spin rotation the spin triplet (S_z=0) can becomes S_z=1, allowing the survival of Cooper pairs in a ferromagnet. Note that such a mechanism involves the magnetic inhomogeneity directly in an interface barrier, rather than in a metallic region. Once in the ferromagnet, triplet Cooper pairs can survive long distances (of the order of 1 micron) much longer than the few nanometers that a singlet Cooper pair can penetrate in ferromagnets.

The main objective of this thesis has been to examine proximity effect between a ferromagnet and a superconductor in a planar configuration, by using high-Tc superconductors (YBCO) and half-metals (LCMO and LSMO). To this end, we have used two strategies to design the devices:

- To use microwires of half-metal with larger superconductor bridges on top of them.
- To use superconductor arrays of pillars with a single layer of half-metal covering it.

The most fascinating results have been found using microwires of YBCO and LSMO. However, signs of proximity effect have also been observed on samples with arrays of superconducting pillars connected by LCMO layers, as will be seen in next sections.

Inspiring theoretical studies [14] exposed that triplet Cooper pairs can be generated at the interface between a ferromagnet (F) and a superconductor (S). Much work has followed to identify various mechanisms that can lead to the opposite-spin singlet to equal-spin triplet conversion. Generally, these include spin-mixing, which leads to generation of opposite-spin (S_z=0) triplet component out of the singlet one, and spin-flip, which produces the equal-spin (S_z=± 1) triplet component. At the microscopic level, those processes result from spin dependent scattering at interfaces with strong ferromagnets [2], and from the presence of an inhomogeneous magnetization [15–22] or a momentum dependent exchange field due to the spin-orbit interaction [10,23]. A number of experiments based on conventional (s-wave) low-temperature superconductors have found critical currents across S/F/S junctions for F thickness in the tens of nanometers range [5,24–27], which is much larger than expected for the singlet superconductor/ ferromagnet proximity effect, and therefore supports the triplet scenario. In these vertical junctions, the triplet generation was engineered through the artificial design of a magnetic inhomogeneity at the interface with the superconductor, e.g. by intercalating various ferromagnetic layers with different magnetic anisotropy or spin texture. Experiments on lateral (planar) devices, particularly based on the half-metallic ferromagnet CrO_2, found critical currents that decay over even longer distances −up to a few hundred of nm [3,4]. Because in half-metals the conduction electrons are fully spin-polarized, and consequently the penetration of opposite-spin singlet correlations is forbidden, that experimental observation was considered evidence for the generation of triplet superconductivity, which was explained [28] by the presence of strong spin dependent scattering at S/F interface combined with intrinsic magnetic inhomogeneities [29].

Because of their fundamental and technological interest, heterostructures of unconventional (d-wave) high-temperature cuprate superconductors combined with half-metallic manganites have attracted much attention, and hints for triplet proximity effect have accumulated along the years: unexpected superconducting proximity effect [30], an induced superconducting gap [11,13,31], Andreev reflection and coherent transport [32,33], as well as supercurrents [34] over length scales of the order few tens-of-nm have been experimentally observed in vertical junctions (although at relatively low temperatures ~10 K). Notwithstanding, the demonstration of long-range Josephson effects has remained elusive. Proving Josephson coupling requires evidencing the macroscopic phase coherent state. A first signature is the observation of flux quantization effects in the critical current: in principle, the Josephson current must vanish for integer number of flux quanta, giving rise to the well-known Fraunhofer diffraction pattern [35,36] . While realized in triplet Josephson junctions based on low-temperature superconductors [25,26,37], flux quantization effects have been never observed in cuprate/manganite junctions. They are clearly demonstrated in the present experiments. The second signature are the so called Shapiro steps in the I(V) characteristics measured under microwave radiation [38]. These originate from the current phase relation $I = I_0 \sin\varphi$, where the phase φ difference between the electrode evolves in time under application dc voltage bias V according to $\frac{\partial\varphi}{\partial t} = \frac{2\pi}{\Phi_0}V$, with $\Phi_0 = \frac{h}{2e}$ is the flux quantum, yielding an ac current with the Josephson frequency $\nu_J = \frac{V}{\Phi_0}$. Resonant absorption of microwave radiation occurs when the Josephson frequency is a multiple of the microwave's frequency, yielding steps in the I(V) curve

measured under microwave illumination at voltages given in the conventional case by $V = n\Phi_0\nu$, with $n = 0, 1, 2, \ldots$ To the best of our knowledge, these phase locking effects have never been reported for triplet Josephson junctions. They are very clear in the present experiments, and they present the anomalous periodicity expected in the context of triplet Josephson effects.

3.2 ARRAYS OF LCMO/YBCO PILLARS

We first describe the results obtained in superconductor arrays of pillars with a single layer of half-metal connecting them. Usually Josephson junctions are just two superconductors with a barrier between them. The process to make planar configurations of this type of device with oxides has a lot of technical problems and either embodies many lithography steps or ex-situ strategies which may give rise to degradation of sample properties (particularly superconducting) mostly due to deoxygenation of the samples. Due to this difficulty we decided to take a different approach: putting more than only one junction. This can be done by making arrays of Josephson junctions interconnected. The idea of using arrays of micropillars of superconductors with ferromagnet between them is the same: two superconductors (adjacent micropillars) connected with a barrier between them (ferromagnet). But this way allows for a very efficient interconnection of many superconducting pillars. If two SC micropillars are not perfectly Josephson coupled, it is possible that other two in a different path are coupled and gives us a superconducting correlation. Of course, there can be drawbacks and even when there is a proximity effect, we may not be able to measure it because of the higher resistance of other paths in the micropillars array. In this section we will see how these arrays of micropillars are fabricated, measured and which results and conclusions we extract from them.

The fabrication of the samples is quite simple, the steps are as follows:

- Growth of 25nm of YBCO on top of STO (100).
- EB lithography of arrays of micropillars, with different sizes and separations.
- Wet etching of the YBCO to obtain the array of pillars.
- Growth of 30nm of LCMO (or LSMO) on top of the micropillars and STO. In this way the whole sample is covered and the separations between micropillars is through a ferromagnetic over layer. Our individual Josephson junctions are composed by two superconducting micropillars connected by a half-metal.
- Photolithography of contacts.
- Au deposition of contacts.

To ensure the correct separation between micropillars and the good quality of the lithography, AFM and optical microscopy has been performed (Figure 3.1).

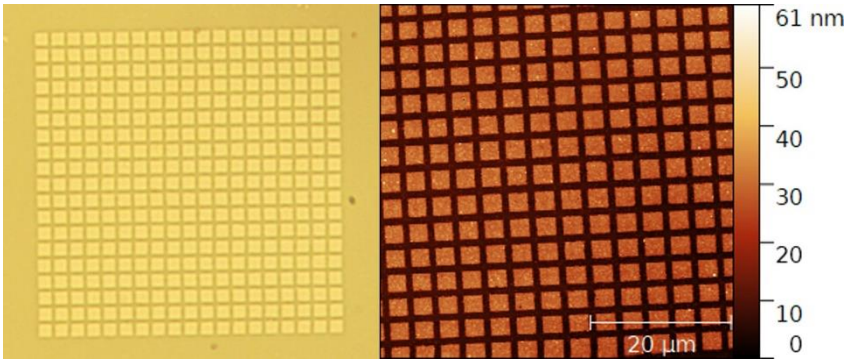

Figure 3.1: Devices of LCMO and YBCO micropillars under an optical microscope and AFM scanning. Micropillars are perfectly separated and there is no YBCO between them.

A sketch of the contacts geometry for magnetoelectrical measurements for the samples are displayed in Figure 3.2.

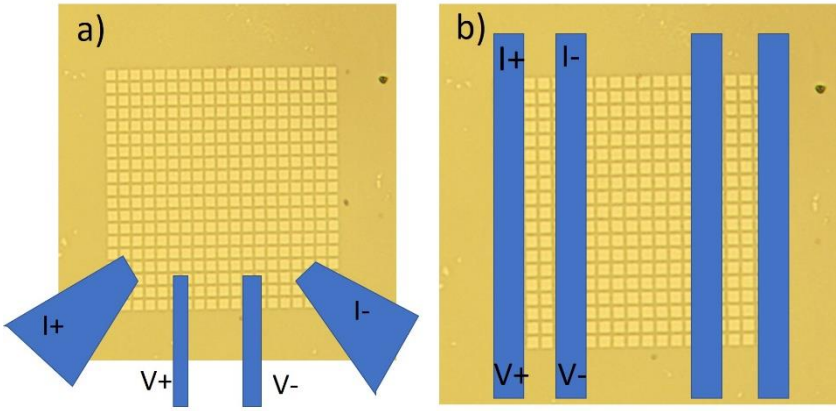

Figure 3.2: Scheme of the electrical contact for micropillar samples. Contacts in figure (a) were used on samples YBC60A4+LCMO and YBC13A1+LCMO, and contacts in figure (b) were used for sample YBC34A2+LCMO. Due to problems with this last sample provoked that only two contacts were used to measure.

To measure the samples, we used a 4-wire configuration to remove the contact resistance. Samples were mounted on a cryostat with electromagnet. The first measurement is always a resistance curve (RvsT) in zero magnetic field to check the resistance while going to low temperature. This is followed by IV curves, measured to localize any non-linear behavior due to the superconducting proximity effect. Once the virgin state is fully characterized, resistance vs magnetic field measurements were performed at different temperatures. Magnetoelectric measurements have been performed in three samples: YBC34A2+LCMO, YBC60A4+LCMO and YBC13A1+LCMO. The magnetic field is applied parallel to the current, which is applied parallel to the sides of the micropillar, in the (100) direction.

3.2.1 PILLARS ARRAY SAMPLE YBC34A2+LCMO

The sample YBC34A2+LCMO measured had a micropillar area of 2,75x2,75 μm^2 and a thickness of 22 nm (only the YBCO). The separation between micropillars was 986nm. It is important to notice that for sample YBC34A2+LCMO due to problems with the contacts the measurements

are not 4 wires, as can be seen in Figure 3.2. Therefore, contact resistance between the gold and the sample cannot be extracted, but we can remove the contact resistance of the wiring of the sample. In this sample observed a RvsT curve with a shallow peak probably related to the metal-insulator transition of the LCMO follow by a decrease of resistance. This decrease becomes more prominent at the Tc of YBCO at T=88K and lasts until 75K. After that the resistance keeps descending until 3,2K, but with a much smaller ratio (Figure 3.3).

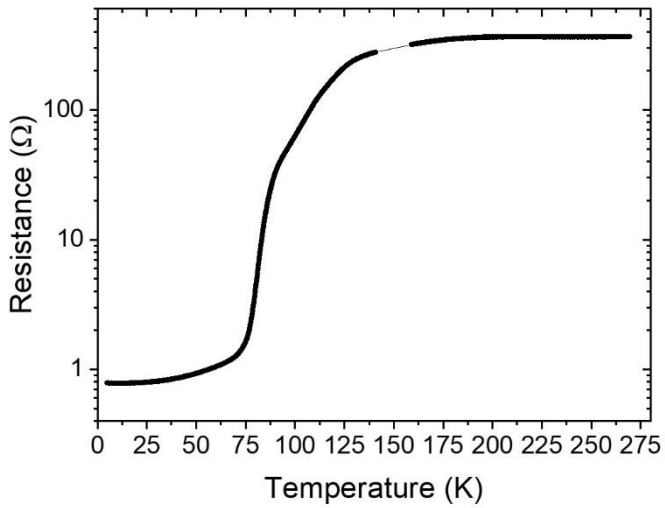

Figure 3.3: Resistance as a function of temperature for sample YBC34A2+LCMO. A clear superconducting transition can be observed, but the maximum of resistance due to the metal insulator transition of the LCMO is very weak although it can be identified at 190K.

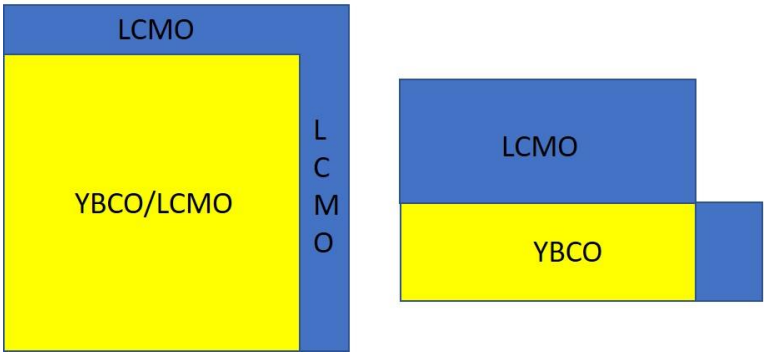

Figure 3.4: Upper and lateral sketch of the unit cell used to calculate the resistance of the device. We have two parts: the LCMO/YBCO micropillar, in which the current can flow in parallel across both layers (so we calculate the resistance as a parallel contribution of each one) and the LCMO between micropillars, which is connected in series with them.

If we calculate the resistance taking into account the resistivity of LCMO and YBCO depending on temperature, using a "single cell" as the one in Figure 3.4, we can compare the expected change in resistance and the real change in resistance to test if there is proximity effect in the ferromagnet, in which case the resistance should be lower than the estimated value. To do this we have to consider the YBCO/LCMO bilayer (in parallel) and the LCMO separation between micropillars (in series). Also is important how many micropillars are between the voltage contacts to calculate the resistance. We have estimated the resistance at 100 K to be 54,5 Ohms. Taking into account that between voltage contacts there are two non-complete micropillars we have found a good agreement with the measured resistance R_m(T=100K) = 63 Ohms. When we look at the estimated resistance value below the critical temperature of the superconductor, we observe a larger difference with an expected value of R(T=65K) = 8,8 Ohms and a measured value

of R_m(T=65K) = 1,62 Ohms. This gives us a decrease in resistance 5 times bigger for the measured case. This is a simplified case, in which we have not included interface resistance and we have assumed materials free of defects, but even so, the measured drop is large enough to think that there is a proximity effect in this system.

We have measured the differential conductivity as a function of temperature. Below the critical temperature, we observe a zero-bias peak between 81K and 35K (Figure 3.5). At temperatures

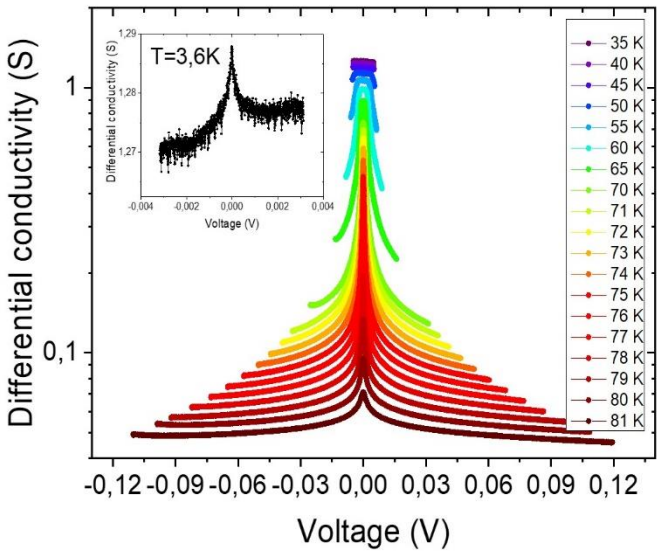

Figure 3.5: Differential conductivity of the sample. Inset: differential conductivity at lowest temperature possible. At T=3.6K there is a peak of conductance at zero bias showing an indication of superconductivity.

close to the critical temperature of the YBCO it could be explained simply as a superconducting effect, but at lower temperatures it could indicate that the LCMO is displaying superconducting correlations. Nevertheless, due to the measurement conditions (not 4 points resistance measurement), the small low temperature peak at zero-bias can be interpreted as a residual resistance (with a value of less than 1 ohm). This small resistance corresponds to LCMO as identified by measuring at currents above 100uA in the magnetoresistance curves. This is an indication that the proximity effect is not complete or at least we do not have the voltage sensitivity to measure it. The resistance vs magnetic field curves for this sample are typical of LCMO for currents above 100uA (Figure 3.6), but below that value the voltage measured is not large enough to be above the noise level. Because of the signal to noise ratio at low currents, this measurement cannot be used to conclude or discard a proximity effect as the expected Fraunhofer-like pattern in the superconducting state could not be measured.

To sum up, for this sample we have found indications of a superconducting proximity effect both in the RvsT and in the differential conductance, but the (uncorrected) contact resistance does not allow us to reach a zero-resistance state. Also, the magnetoresistance at low currents cannot be measured, which prevents the measurement of a possible Fraunhofer pattern.

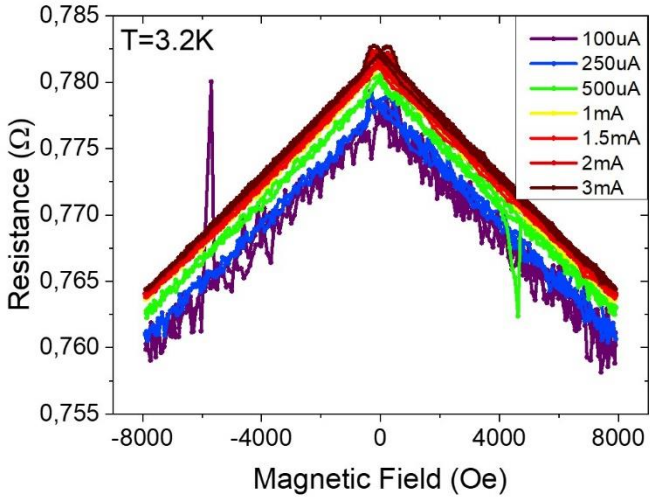

Figure 3.6: Resistance vs magnetic field for currents above 100uA. At lower currents the slope of the linear part of the signal is reduced, compared with the ones at higher currents. This could be a hint of a critical temperature.

3.2.2 PILLARS ARRAY SAMPLE YBC60A4+LCMO

The sample YBC60A4+LCMO had a micropillar area of 3x3 μm^2 of area and a thickness of the YBCO layer of 25 nm. The separation between micropillars was 1µm. The measurement configuration shown in Figure 3.2(a) was used. This allowed us to perform 4-points measurements. Looking at the resistance vs temperature R(T) curve, the metal-insulator transition of the LCMO at T=200K can be clearly recognized. In the two wires measurement the critical temperature of the YBCO can be identified, but not as clearly in the 4 wires configuration. The resistance of the system experiences a drop at Tc of the YBCO and keeps descending towards lower temperatures (Figure 3.7). One possible explanation of the rather small drop at the superconducting critical temperature compared with the previous sample, could be a degraded interface contact between both materials. In this direction, the second bump in the resistance around 125K, could correspond to a different phase of LCMO transitioning to the ferromagnetic

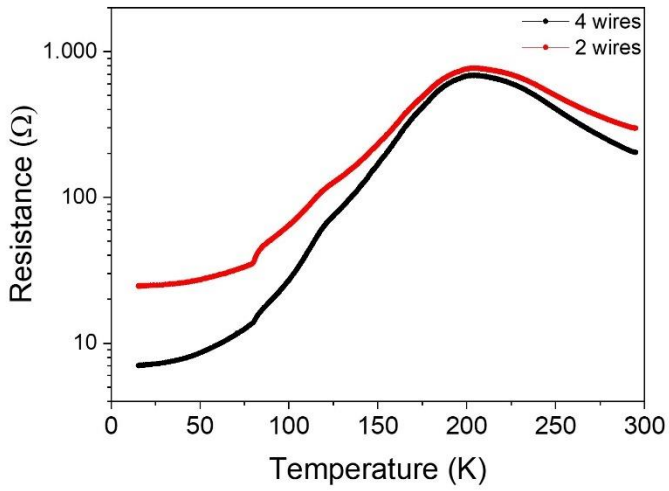

Figure 3.7: Resistance as a function of temperature for sample YBC60A4+LCMO. The 2 wires configuration helps to identify the critical temperature of YBCO. The 4 wires configuration shows both the Curie temperature of LCMO and the critical temperature of YBCO.

state. In the differential conductance no superconducting behavior is observed, but surprisingly oscillations appear at the RvsH curves at low currents. These oscillations resemble a Fraunhofer pattern and can be suppressed by increasing the current which points towards a superconducting effect (Figure 3.8). It can be clearly seen that the oscillations decrease in amplitude and period with increasing current. Although there was no constant period of the oscillations, making it impossible to assure these oscillations are due to a Fraunhofer pattern. It is worth noting that under in plane magnetic field this sample shows a negative anisotropic

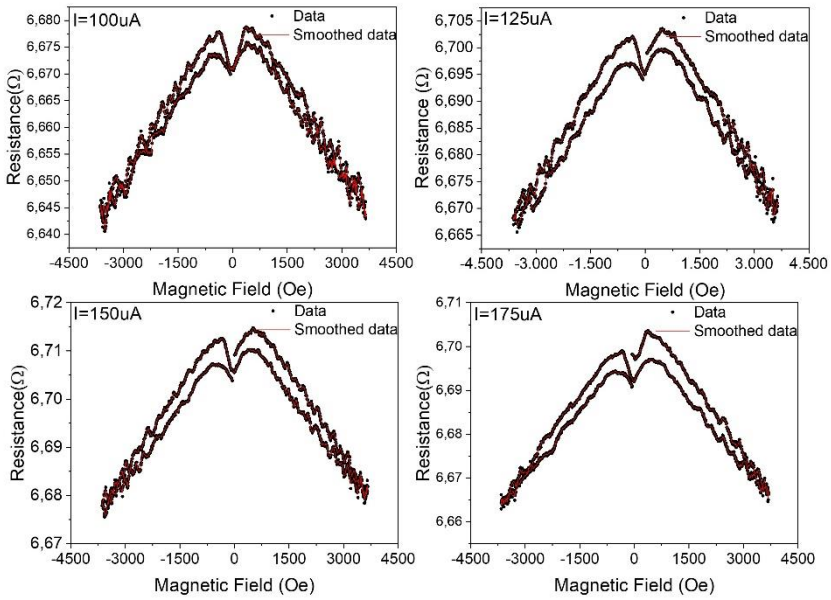

Figure 3.8: Oscillations on magnetoresistance at different currents. When increasing the current the oscillations disappear at 200uA.

magnetoresistance, AMR, effect which in the LCMO system indicates that the current is perpendicular to the applied field.

To examine these oscillations more closely, the sample was rotated 45 degrees, as if the oscillations are related to a Fraunhofer pattern in a Josephson junction the period of them should change. We, in fact, observed that the oscillations either disappeared or their period become much smaller. Figure 3.9 displays curves at different angles between current and magnetic field for different current levels. When going back to zero degrees the oscillations were not recovered. This could indicate that the oscillations are related to the domain structure of the ferromagnet, and changing the direction of the applied field, the domain structure was irreversibly changed. This may be understood if one keeps in mind that the easy magnetization axis of the LCMO is the (110) direction, hence applying the field in that direction could saturate the magnetization of the sample.

To sum up, in sample YBC60A4+LCMO we observed oscillatory behavior of the magnetoresistance that depends on the applied current, which points towards (Josephson) proximity coupling between the superconducting pillars. The fact that it could not be observed a clear superconducting transition could indicate a degraded interface. The effect observed should be then ascribed to pillars with the best contact properties, which produce the oscillations in the magnetoresistance.

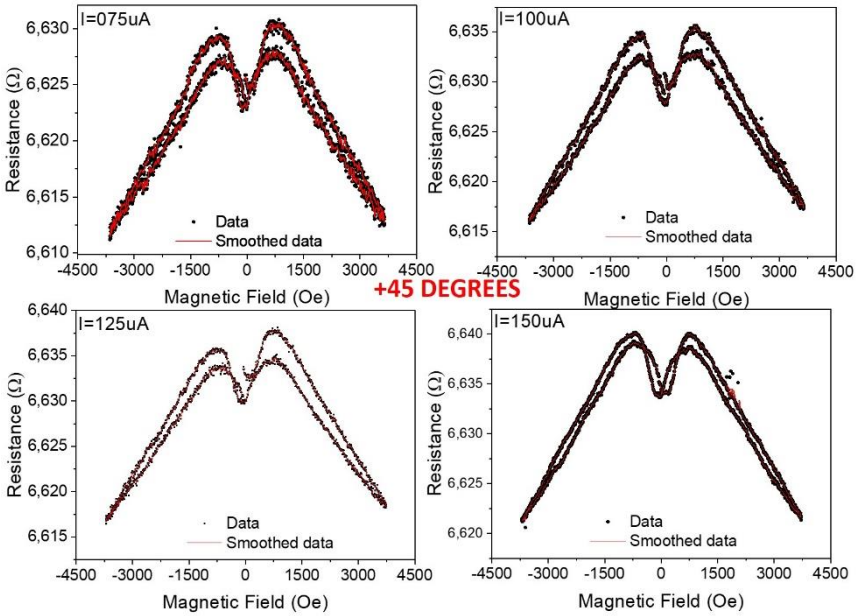

Figure 3.9: Resistance vs Magnetic field after rotating the sample 45 degrees. Now the field is applied along the diagonal of the sample and oscillations disappear. The previous state could not be recovered when initial conditions are restored.

3.2.3 PILLARS ARRAY SAMPLE YBC13A1+LCMO

Sample YBC13A1+LCMO was measured using the same contact pattern as YBC60A4. Sample YBC13A1+LCMO had a micropillar area of 3,5x3,5 μm^2 and a YBCO thickness of 24 nm. The separation between micropillars was 1,33µm. For this sample we have found both signatures present in previous samples, but at the same time, a clear superconducting transition was measured, with a clear superconducting differential conductance. It also showed oscillations in the magnetoresistance, which could be a signature of a Fraunhofer pattern.

For sample YBC13A1+LCMO we observed similar anomalies in the resistance curve as in the previous samples. We see two peaks in the normal state resistance, one at 225K and another one at 125K (the typical Curie temperature of LCMO on STO). This means that there are two different LCMO regions in the device, with different temperatures of the metal to insulator transitions. This could be due to the different properties of the LCMO when it grows on top of the YBCO as compared to its growth on STO. As it will be discussed from photoemission electron microscopy (PEEM) measurements, the LCMO with depressed Curie temperature is the one between the micropillars. This was already observed in sample YBC60A4+LCMO, but it is now much clearer.

At T=87K we observe a drop in resistance corresponding to the critical temperature of the YBCO as expected and a further gradual decrease below 75K. This decrease continues down to 4,6K without reaching the zero resistance level (Figure 3.10).

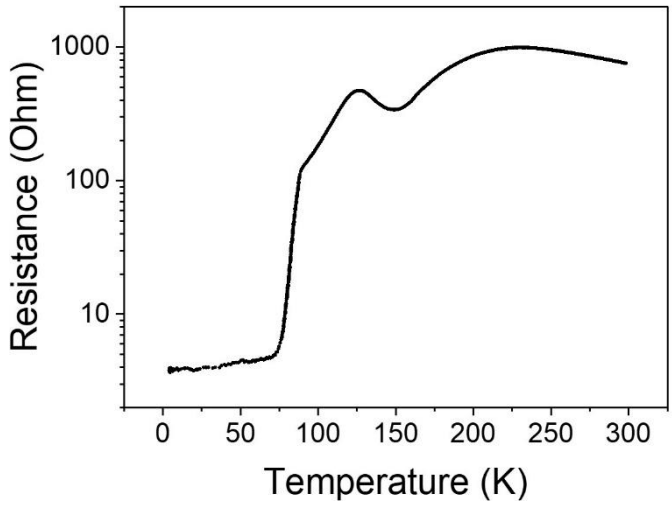

Figure 3.10: Resistance vs Temperature for sample YBC13A1+LCMO. It clearly shows two metal insulator transitions for the LCMO and the superconducting transition of the YBCO. After that, resistance keeps descending continuously until temperature reaches the lowest limit of the cryostat.

If, as before (for sample YBC34A2+LCMO), we estimate resistance of the device using a "unit cell" formed by the YBCO/LCMO micropillar and the LCMO between micropillars (Figure 3.4), we can compare its value to the measured one. We obtain a resistance of 63,5 Ohms for the unit cell at 100K, but there are 3 micropillars so the total resistance would be R(T=100K) =190,5 Ohms, a value close to the measured resistance R_m(T=100K) =182,64 Ohms. If we make the same calculation below the critical temperature of YBCO we obtain a R(T=65K) =27,5 Ohms, which is almost 8 times larger than the measured resistance R_m(T=65K) =4,6 Ohms. This, again, constitutes a good preliminary indication of proximity effect between YBCO and LCMO.

The differential conductance shows a zero-bias increase, which could be an indication of a superconducting critical current. This increase growths in intensity as the temperature is lowered until the differential conductance reaches a plateau in the lower temperature levels. In the plateau state, we observe the appearance of a sharp zero-bias peak at temperatures below 15K, which is characteristic of tunneling into d-wave superconductors and could be the signature of the proximity effect in the LCMO (Figure 3.11).

The magnetoresistance of the sample, again, displays periodic oscillations similar to the ones of a Fraunhofer pattern. Once again, if the sample is rotated in plane to change the angle between current and magnetic field, the period of the oscillations changes drastically (Figure 3.12).

One more feature found on the resistance oscillations is their reduction in intensity and eventual disappearance upon increasing the current, which points to the existence of a critical current Figure 3.13. This is confirmed further when we look at the increasing of temperature Figure 3.14 which makes the amplitude of the oscillations become smaller until they disappear. Unfortunately, due to the degradation of the sample after measuring at synchrotron we could not measure with out of plane magnetic field to observe if these oscillations were also affected by it.

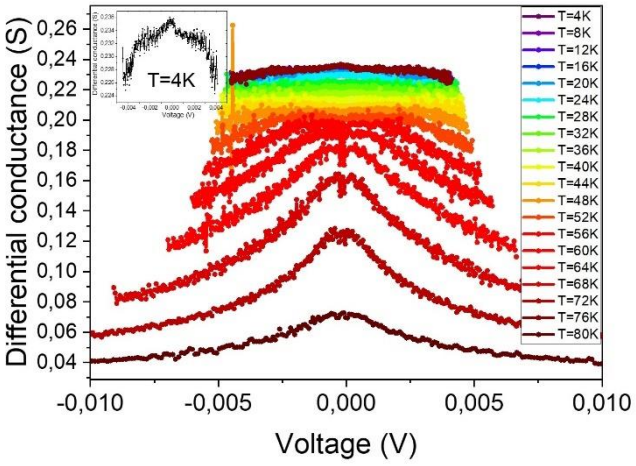

Figure 3.11: Differential conductance showing the zero-bias peak which turns into a plateau at low temperatures. The inset shows the differential conductance at T=4K. Notice the small zero bias conductance peak characteristic of tunneling into d-wave superconductors.

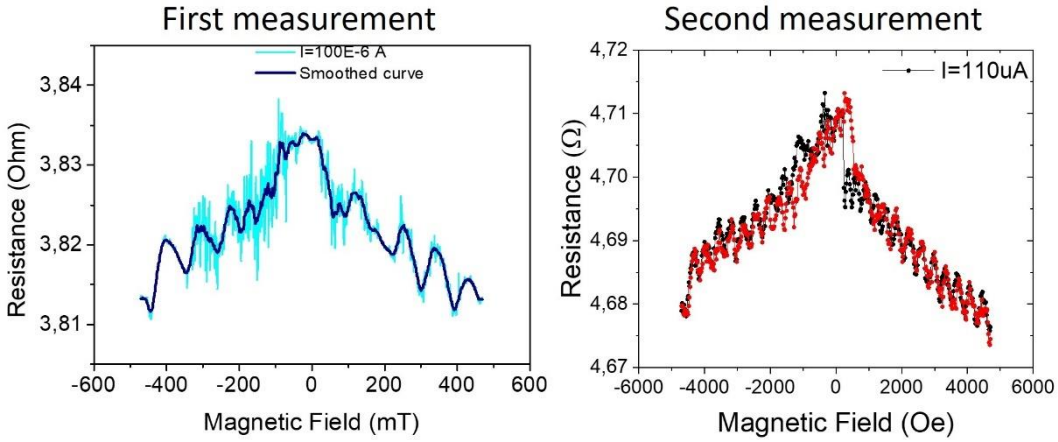

Figure 3.12: First measurement of the magnetoresistance. The sample was removed and wired again to try to remove the noise. The sample was mounted nominally in the same position, but there could be a slight misalignment. This caused a change in the frequency of the oscillations and a reduction of the noise.

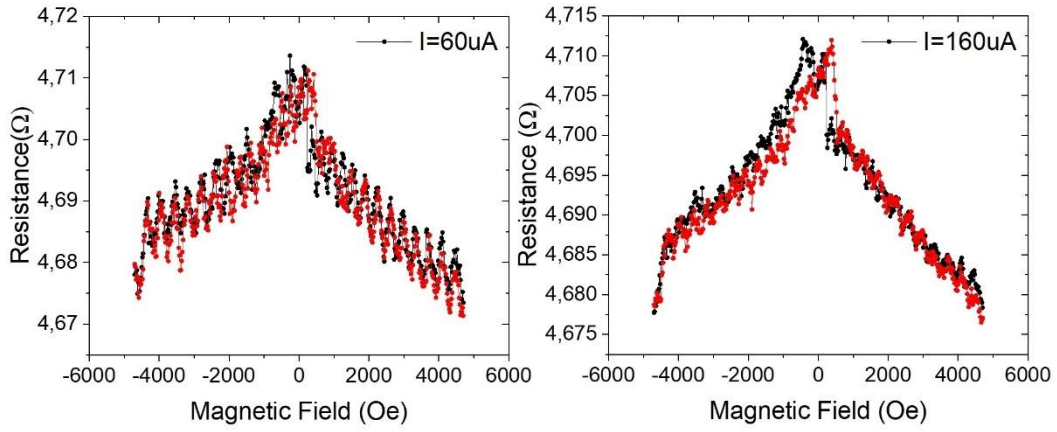

Figure 3.13: Magnetoresistance oscillations for 60 and 160 uA. At currents above 200uA no oscillations can be observed.

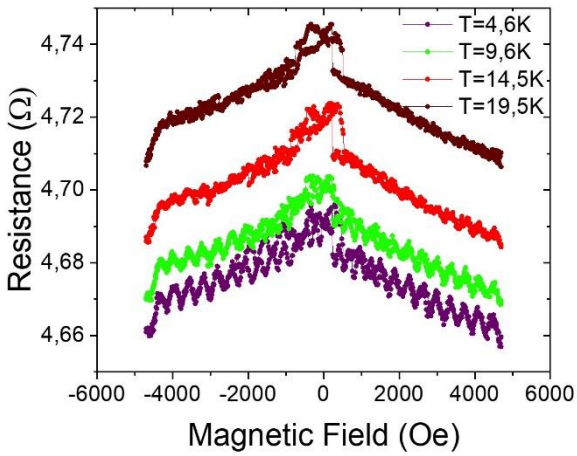

Figure 3.14: Magnetoresistance oscillations for different temperatures. Increasing temperature or current level produces a decrease in the amplitude of the oscillations.

Further insight into the origin of magnetoresistance oscillation and their possible connection to proximity interaction can be obtained from the geometrical analysis in terms of flux quantization. This is not straightforward because of the large connectivity in our device geometry. There are multiple possible couplings in this type of device, and we can identify the one fitting that fits better with the observed oscillation pattern. Keeping in mind that the oscillation period corresponds to a flux quantum threading the Josephson junction area, looking at it we can estimate the dimensions of this junction. Since we have a period of 372Oe, our junction should have an area of 0,055 μm^2:

- For a possible Josephson coupling between the LCMO and YBCO in the micropillar we would have a junction of 0,189 μm^2 if we consider both materials, or 0,105 μm^2 if we only consider the LCMO.
- For a possible effect due only to the superconductor (proximity effect between the center of the superconductor and its edges, which have a lower critical temperature), we obtain an area of 0,084 μm^2
- For the usual Josephson junction, the LCMO between two consecutive YBCO micropillars, we obtain an area of 0,04 μm^2

The closest value to the expected is the one of the LCMO between YBCO micropillars (Figure 3.15). The difference can be due to errors in the size measurement.

With all these features in mind, we can conclude that the observed signatures of Josephson coupling correspond to the LCMO in between YBCO micropillars which (Josephson) couples them. We cannot see a zero-resistance state because of the configuration of the sample involving the series connection of three micropillars between voltage contacts. The effect could be masked if one or more of the junctions is not superconducting, but others are not. This could explain the superposition of a Fraunhofer oscillation and a typical magnetoresistance of the LCMO seen in RvsH measurements. A final question is whether or not this is a triplet proximity effect. The LCMO between the superconducting micropillars could be just metallic and then the proximity effect could be due to singlets travelling through a normal metal.

To assess the magnetic state of the LCMO, both on top of the YBCO and between micropillars, photoemission electron microscopy (PEEM) measurements were performed in this same

sample. With these measurements we can demonstrate that the LCMO is ferromagnetic, both on top of YBCO and in between the micropillars.

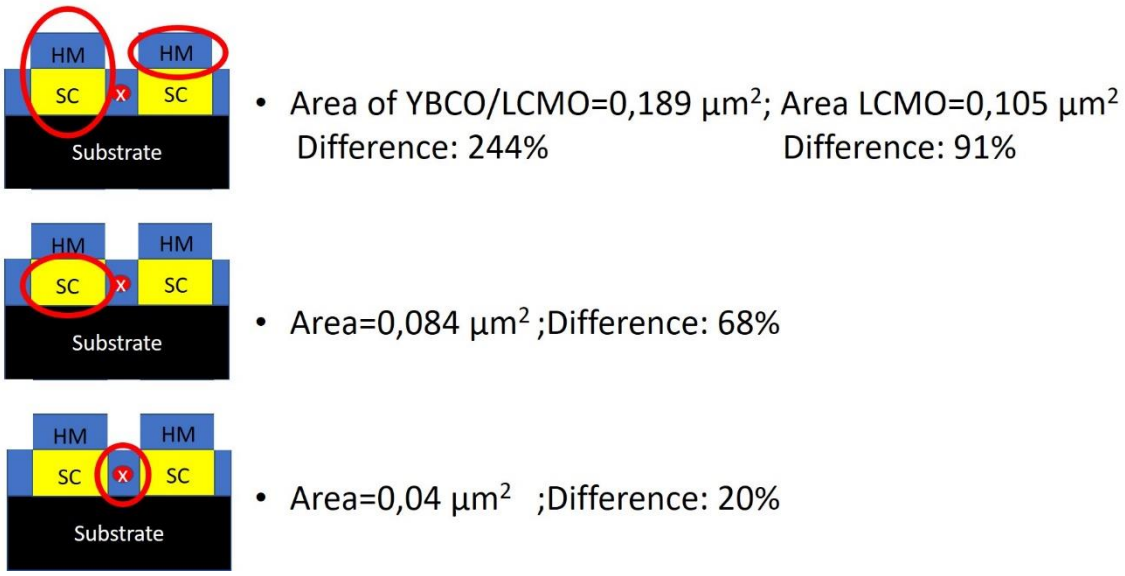

Figure 3.15: Schematics of the possible Josephson junctions' geometries giving rise to the oscillations of the magnetoresistance.HM is the half-metal LCMO and SC the superconducting YBCO. The junction with more possibilities to be the one we are measuring is the YBCO/LCMO/YBCO junction between two consecutive micropillars.

PEEM measurements were performed at synchrotron BESSY II Helmholtz Zentrum Berlin using circular polarized light of energy 641.7 eV to look at the magnetic state of the Mn ions. The photon beam and the magnetic field where applied parallel to the (100) direction, as in the magnetoresistance measurements. It is important to recall that the easy axis of magnetization of the LCMO is in the (110) direction, so that measuring in the (100) direction may require higher magnetic fields to saturate the sample and obtain the highest dichroic XMCD signal possible. In Figure 3.16 we show an AFM image, x ray absorption XAS image and a XMCD image of the same zone of the device.

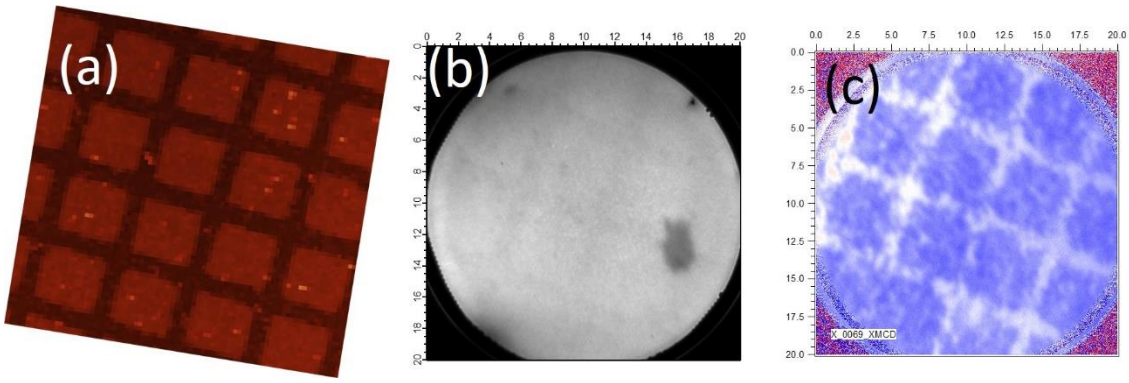

Figure 3.16: (a) AFM image of sample YBC13A1+LCMO. (b) X ray absorption XAS image of the same sample. (c) XMCD image of the same sample after applying a field of 750 Oe at T=175K.

We identify two different LCMO zones, the one on top of YBCO with stronger intensity (higher magnetic moment) and the one in between the YBCO pillars with reduced intensity (smaller magnetic moment). This indicates higher values of the Curie Temperature of the LCMO on top of the YBCO than for the LCMO in between pillars. Although as displayed in Figure 3.17 there is also magnetism irregularly distributed in the zone between YBCO, most of the magnetic signal corresponds to the top of the YBCO. This coexistence of two different LCMO phases explains the

observation of two metal insulator transitions (corresponding to two Curie temperatures) in the resistance curve.

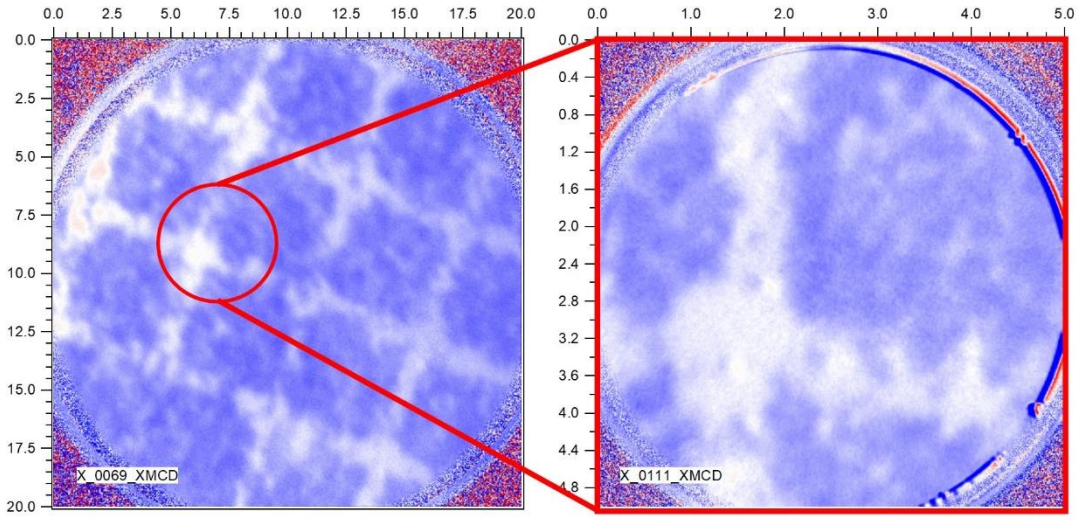

Figure 3.17: Close up of the device, showing that the different LCMO phases are not perfectly separated between the LCMO on top of the micropillars and the LCMO outside the micropillars.

Examining the evolution of the system with the temperature (Figure 3.18), we can clearly observe the two LCMO phases, with Curies temperatures of 210K and 145K, with the LCMO on top of the YBCO with larger Curie temperature. At low temperatures, especially below YBCO Tc, it can be seen that the LCMO between micropillars (and outside the device) has a more homogeneous magnetization. Meanwhile, the LCMO on top of YBCO shows a large quantity of magnetic inhomogeneities with magnetization pointing perpendicular to the applied field and

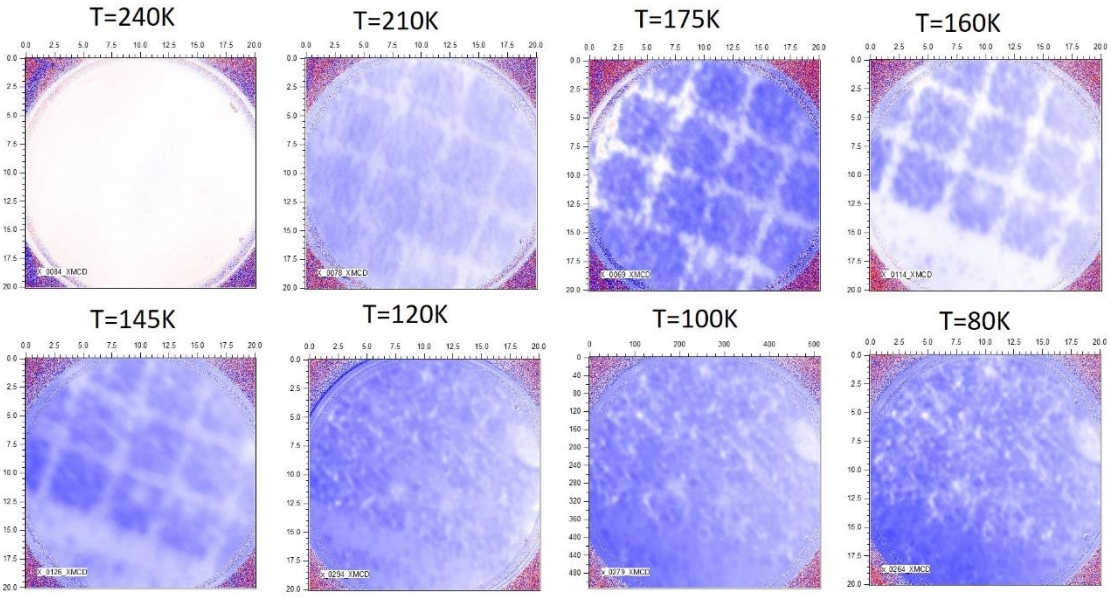

Figure 3.18: Evolution of YBC13A1+LCMO sample with temperature. After each measurement a magnetic field of 750Oe was applied. Between T=175K and T=160K a different zone of the device was selected to better observe the transition of the LCMO in between of the YBCO micropillars.

the photon beam. This effect becomes even clearer if we compare measurements at T=120K and T=55K (Figure 3.19). We could not measure below 50K because of limitations of the experimental set-up, but it would be interesting to observe how the magnetization behaves at

the temperature we observe the oscillations in the magnetoresistance. In the image at 55K we can see the structure of squares, the LCMO on YBCO has more magnetic domains perpendicular to the beam that the "bulk" and in between LCMO. Above Tc, at 120K, we can still see the difference between the LCMO in the device and out of the device, but no between the LCMO on top and between the YBCO.

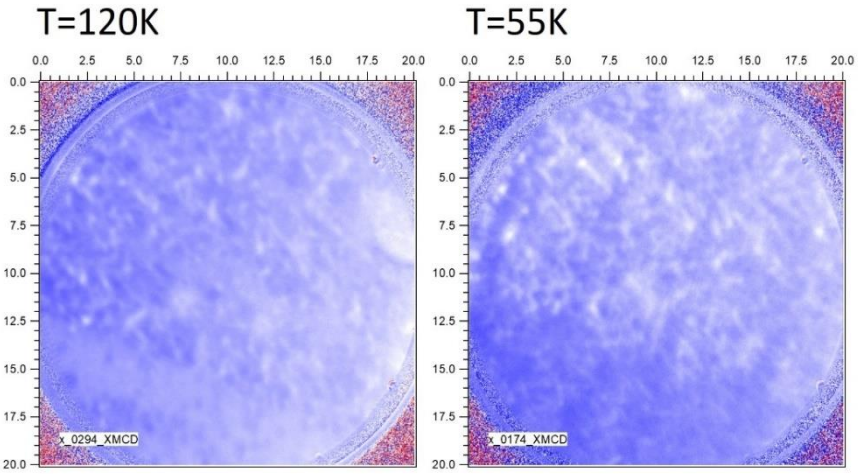

Figure 3.19: XMCD signal above and below the critical temperature of the YBCO. The LCMO on top of YBCO seems magnetized in a direction perpendicular to the beam and with much more domain formation below Tc. The LCMO outside the micropillar appears more homogeneous.

With these measurements we have demonstrated that the LCMO in between the YBCO micropillars is in fact magnetic, hence proving that the proximity effect in this case could only be driven by the formation of triplet pairs.

3.2.4 PRELIMINARY CONCLUSIONS

We have found indications of Josephson coupling in the LCMO/YBCO system from oscillatory behavior of the magnetoresistance curves in samples consisting of arrays of YBCO pillars separated by micron distances, connected by a LCMO overlayer. Since we have demonstrated that resistance oscillations occur in a temperature range where the LCMO in between the YBCO pillars is magnetic, this coupling can only be due to a proximity effect involving spin-triplet formation at the interface between LCMO and YBCO. All samples have shown indications of proximity effect, but with sample YBC13A1+LCMO evidence is stronger, as we observe typical superconducting behavior of the LCMO with both current and temperature changes. This indicates that interface quality is of extreme importance for the observation of these effects.

Although device architecture is very efficient to pinpoint the proximity effect, having many pillars interconnected also makes samples more susceptible to artefacts related to damaged individual pillars or locally degraded interface quality. Having obtained clear hints of proximity effects in our samples with arrays of pillars, we decided to take a more ambitious route to explore the proximity effect, using isolated single junctions instead of arrays of junctions.

3.3 LCMO/YBCO PLANAR JOSEPHSON JUNCTIONS

The approach relies in the fabrication of planar Josephson junctions based on microwires of YBCO and LCMO. Basically, the junction is constructed by engineering two YBCO microwires separated micron size distances on top and perpendicular to a LCMO wire. The LCMO portion in between the two YBCO wires defines the "barrier" of the junction. To measure it, current will be injected through the YBCO wires and voltage detected in the extremes of the LCMO wires. In this device geometry, current will enter through one YBCO wire, then cross the interface with the LCMO, flow through the LCMO wire and then cross the second interface with the YBCO. If there is a proximity effect in the LCMO due to the presence of triplets, we should observe a Josephson coupling between the two YBCO contacts, and indications of a critical temperature and critical current should appear. In this section we will see how these microwires are fabricated, measured and which results and conclusions we can extract from them. We found evidence of a proximity effect in the LCMO, but not as clear as in the micropillar samples. Unfortunately, not all samples measured presented this effect, probably due to defects in the fabrication of the samples, deoxygenation of the YBCO and resistive interfaces between the materials.

3.3.1 *SAMPLE FABRICATION*

The fabrication of these samples involves more steps and is technologically more difficult than the fabrication of YBCO/LCMO micropillars. This is due to the use of an amorphous alumina templates to define the YBCO microwires. We use this method to avoid the degradation of the superconducting properties of the YBCO (particularly at edges and surfaces) in processes involving wet etching or ion beam etching the YBCO, arising mainly due to deoxygenation of the YBCO. Typically wires of less than 1 micron etched these ways are no longer superconducting (at least with the thickness we use ~50nm). For this reason and due to the importance of optimized superconductivity to address the proximity effect, we decided to use an alumina template. In this way, the YBCO wire is defined by growing it onto a trench previously etched in an amorphous alumina layer. The YBCO grown on top of the alumina is a poorly crystalline insulator with a high resistance (>MΩ) meanwhile the YBCO grown on the trench on top of the substrate (without alumina) is fully crystalline and superconducting. This process does not require from etching of the YBCO and fully preserves its superconducting properties. On the other hand, this process is amenable to define very sharp YBCO micro- or nano structures. As we will see, in some samples the critical temperature of the YBCO is lower than the nominal one or they may become even insulating due a defective lift off of the ALO or to deoxygenation of the sample. Another problem is that when the samples of YBCO with ALO undergo another lithography process (to put metallic contacts for example), the properties of the YBCO can be seriously affected. Even then, ALO template has been the method that produced the best results. Luckily, LCMO layers are robust enough and do not present any degradation after the nano- and microfabrication process, preserving their properties even at nanometric scale (65nm).

To fabricate a microwire LCMO/YBCO sample (sketch in Figure 3.20) to measure proximity effect, the steps are as follows:

- Growth of 30nm of LCMO on top of STO (100).
- Electron beam (EB) lithography of 9 microwires of different sizes.
- Wet etching of the LCMO to obtain microwires Figure 3.21 (a).

- EB lithography of one of the two possible ALO templates. Figure 3.21 (b).
- Growth of 30-50nm of ALO on top of the sample and resist. The lift off is the most difficult part of this process, as the resist is usually overexposed and hardened after the 3 to 4 hours that takes the deposition of ALO.
- Growth of 40-50nm of YBCO on top of the template and LCMO microwires.
- Photolithography of contacts. After some test, it was discovered that this process reduces heavily the critical temperature of YBCO (from 87K to 50K). This step was only performed for sample LCM51A2+ALO+YBCO.
- Au deposition for contacts. As the previous step, this was only performed for sample LCM51A2+ALO+YBCO.

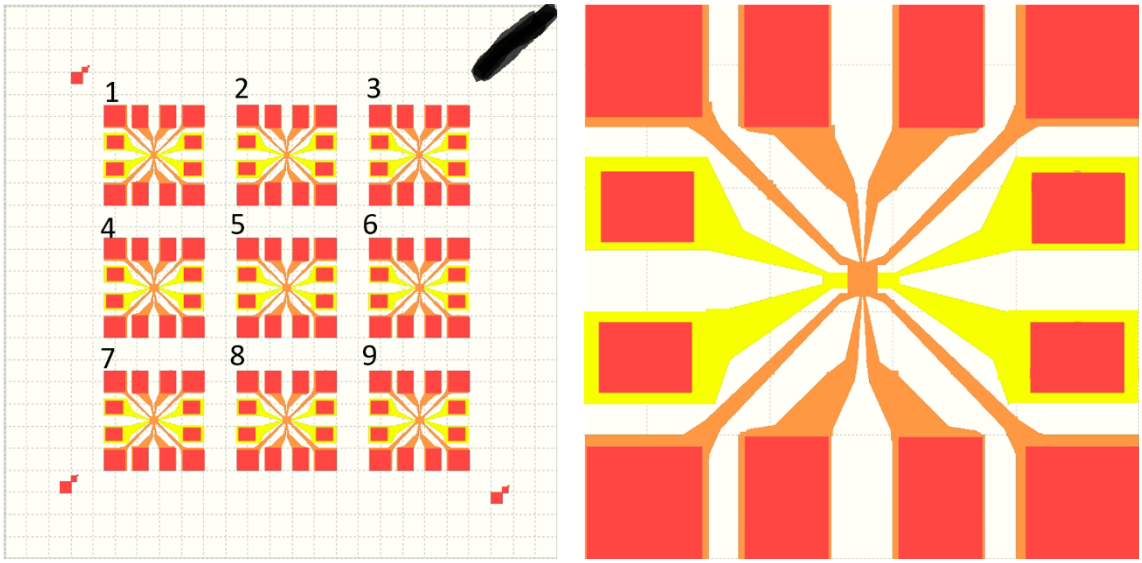

Figure 3.20: YBCO/LCMO microwires. The yellow wires are the LCMO, orange wires are superconducting YBCO and red rectangles are gold contacts. Everything but the red and Orange zones are covered by insulating YBCO on top of ALO. The number of LCMO microwires vary from 1 to 2 for each device and the number of YBCO microwires from 2 to 4.

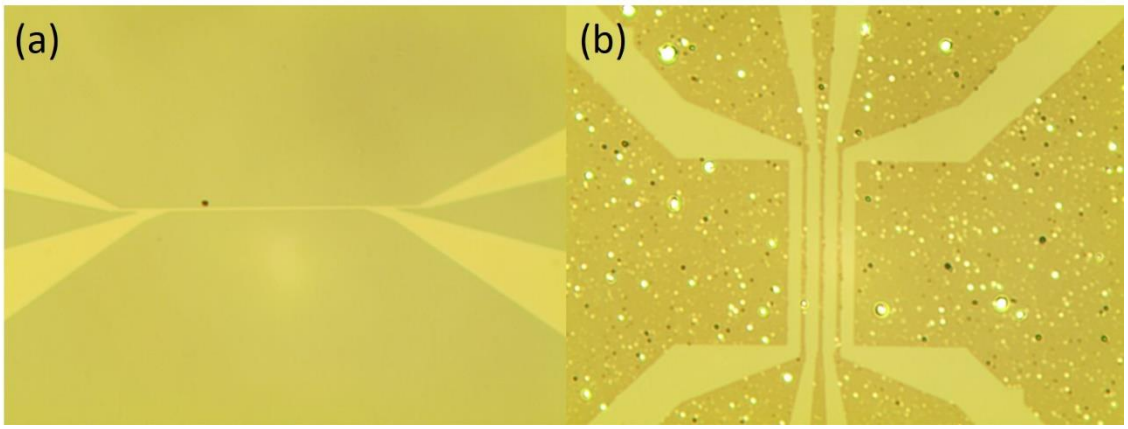

Figure 3.21: (a) LCMO microwire fabricated using wet etching. (b) Alumina template for the deposition of YBCO (the more uniform zones (the ones exposed) are parts of the STO substrate after removing the ALO)

To assess and the good quality of the ALO lithographies, and that the trenches for YBCO deposition are well separated, AFM and optical microscopy was performed. A sketch of the contacts for magnetoelectrical measurements for both samples can be seen in Figure 3.20.

To ensure that the YBCO microwires are perfectly separated and that there was no conducting path between them, we performed resistance measurements as a function of temperature (Figure 3.22). While each microwave was superconducting, attempts to measure between different microwires produced resistances above MΩ in the 100 K range and unmeasurably high resistances at low temperature.

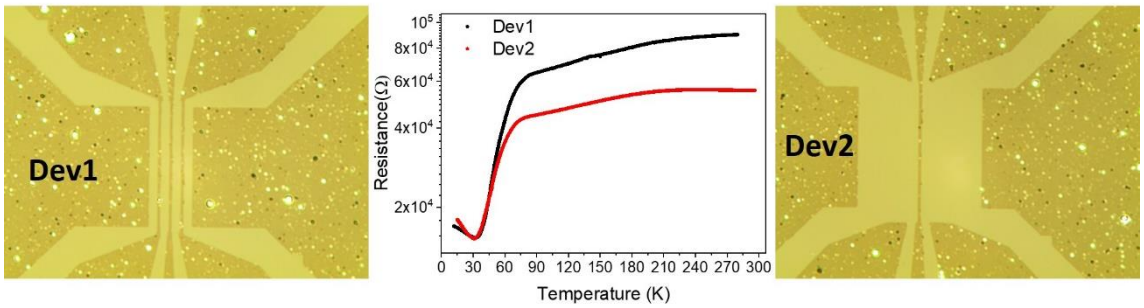

Figure 3.22: Optical image and resistance vs temperature curve of two different YBCO devices fabricated using the ALO template technique. Microwires measured were the ones at the left of each device. Measurements were performed after Au deposition for the contacts. Both devices have a critical temperature close to 60K and a high contact resistance. It was impossible to measure the resistance between two different microwires, due to the (open circuit) high resistance.

To measure the samples, we used a 4-wire configuration to correct for the contact resistance. Samples were mounted on a closed cycle cryostat equipped with an electromagnet. The first measurement is always a resistance curve without applied magnetic field to look for a low temperature superconducting state. Afterwards, IV curves were measured to identify non-linear behaviors which could be hints of a critical current due to the superconducting proximity effect. Finally, resistance vs field, RvsH measurements were performed at different temperatures. Magneto-transport measurements have been performed in two samples: LCMO365D+ALO+YBCO and LCM51A2+ALO+YBCO.

3.3.2 *SAMPLE WITH MULTIPLE PLANAR JUNCTIONS LCMO365D+ALO+YBCO*

The first sample that was measured was LCMO365D+ALO+YBCO. In this case we engineered 4 YBCO microwires on top and perpendicular to 2 LCMO microwires. This sample is somewhere in between of the array micropillar samples with multiple junctions and the single junction which will be analyzed in the sext section.

Notice there is 3 possible S/HM/S junctions in each LCMO wire. In Figure 3.23, an optical image of the device and an AFM profile of the two LCMO microwires can be seen. Separations between YBCO microwires (i.e. the junctions) are 1,2µm. We will call the junctions 1, 2 and 3 attending to their position between YBCO microwires, and (a) or (b) for the thinner (950nm) and thicker (1,8um) LCMO wires respectively. Also, interfaces between YBCO and LCMO have been measured.

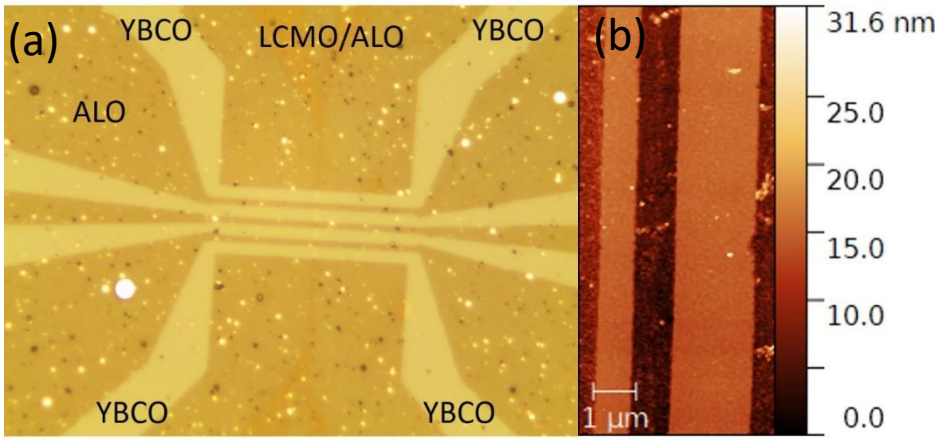

Figure 3.23: (a) Optical image of the device. LCMO can be seen below the ALO as a darker yellow line in the middle of the image. (b) AFM image of the 2 LCMO microwires.

First measurement is a Resistance vs Temperature R (T) curve to observe any change in resistance below the critical temperature of YBCO. In Figure 3.24 (a) (b) the R (T) of junctions

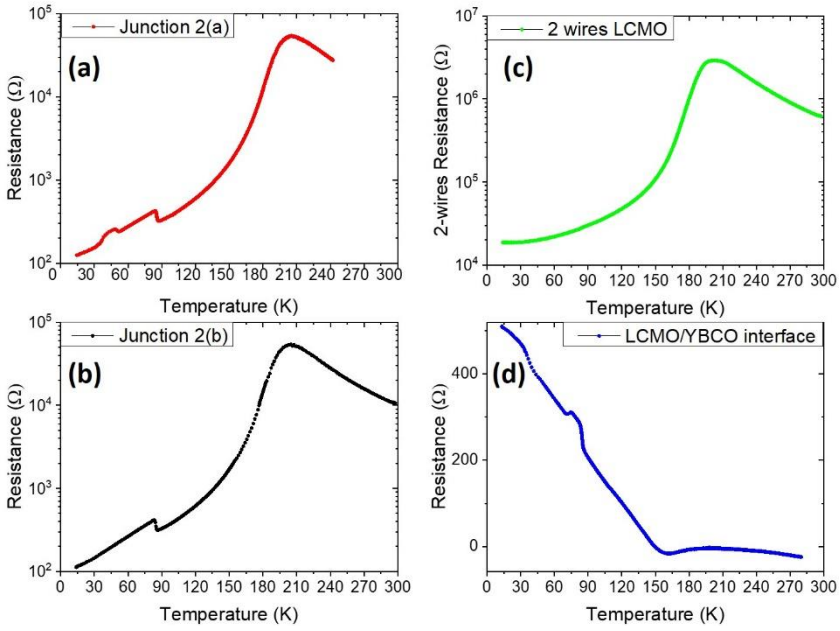

Figure 3.24: Junction 2(a), 2(b), LCMO microwire and interface RvsT. (a) and (b) are the junctions between the two central YBCO microwires, on both LCMO microwires. Their resistance is almost the same even when they have different sizes. As with the micropillars, we cannot be sure of the current trajectory, as the two LCMO junctions are connected in parallel. LCMO microwire (c) behaves similar as the junctions, but without the increase in resistance at critical temperature. Also, the behavior below Tc is different, as in the bare LCMO the resistance reaches a minimum value at 20K, but in the junction it seems to keep decreasing. For the interface in junction 2(b) we observe an increase in resistance at critical temperature (d), but the curve comes back to its previous behavior at 70K.

2(a) and 2(b) are displayed. In both of them we observe a typical LCMO curve with its Curie temperature at 215K. At the critical temperature of YBCO (87K), we observe an increase in resistance, contrary to the case of the micropillars. Also, for junction 2(a) we observe another

small increase of resistance at 45K, that is not related to the single LCMO or single YBCO. A bare LCMO microwire (Figure 3.24(c)) shows a Curie temperature of 215K. To examine the cause of the sharp resistance increase we have measured an interface between the YBCO and LCMO microwire (Figure 3.24(d)). This is done by injecting current across the interface and measuring voltage between two contacts at both sides of that interface. We observe that interface resistance increases linearly below 160K. Notice that while in the case of the two wires measurement of the LSMO or the measurement of the interface the resistance either saturates or increases at low temperatures, in the case of the junctions resistance continues decreasing when temperature is reduced. This is a preliminary indication of a proximity effect, which deserves further study.

The differential conductance of the LCMO-YBCO interface (see Figure 3.25) was measured by applying current between the YBCO and LCMO and measuring voltage between the other sides of the same YBCO and LCMO microwires. Below the superconducting critical temperature, the interface becomes more resistive at lower currents, similar to what is found in a tunnel junction, and this non-linearity slightly increases upon lowering the temperature. However, the non-linearity appears also above Tc, and thus it is not related to the opening of a superconducting gap. But interestingly, the more pronounced increase appears at the critical temperature of YBCO, what suggest a possible connection between interface resistance and superconductivity.

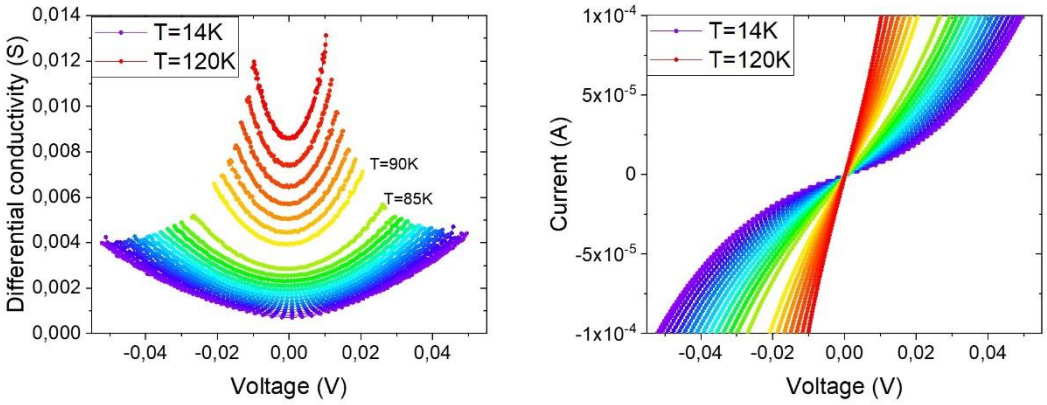

Figure 3.25: Measurement of the interface in junction 2(b) in function of temperature. A clear non-linear effect is observed, similar to the one found in a tunnel junction with higher differential resistance at lower currents.

On the other hand, the behavior of the differential conductance of the junction (injecting current through the YBCO and measuring voltage across the LCMO wire), see Figure 3.26, is markedly different. Notice that we observe a different non-linearity with the junction becoming less resistive at lower currents suggesting the presence of a superconducting critical current. Interestingly, the zero-bias increase of the differential conductance appears below the critical temperature of the YBCO, at 70K, the temperature at which we conjecture the proximity effect may be kicking in. The nonlinear feature becomes more pronounced when temperature is decreased. This is a typical behavior expected in a Josephson junction, but in this case, we could not reach a zero-resistance state or observe a Fraunhofer pattern. Even without having a critical current, a superconducting-like behavior can be observed at low temperatures, where the LCMO magnetoresistance is also present. In Figure 3.27 a R(H) curve at T=20K shows that the AMR peaks of the LCMO at low fields persist at this temperature, but the rest of the curve show a clear superconducting behavior in which the resistance increases with magnetic field.

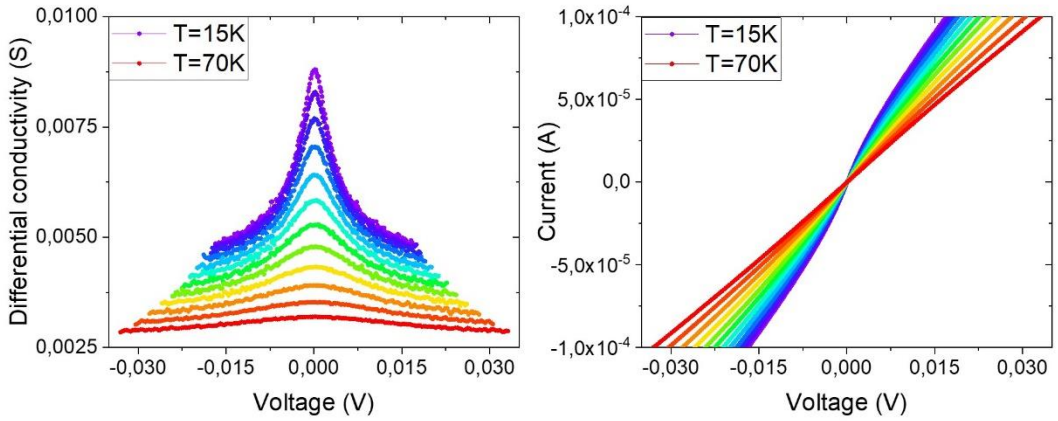

Figure 3.26: Measurement of the junction 2(b) in function of temperature. A zero-bias increase of the differential conductance can be observed which becomes more pronounced upon lowering temperature. No zero-resistance state was found down to the lowest temperature T=15K.

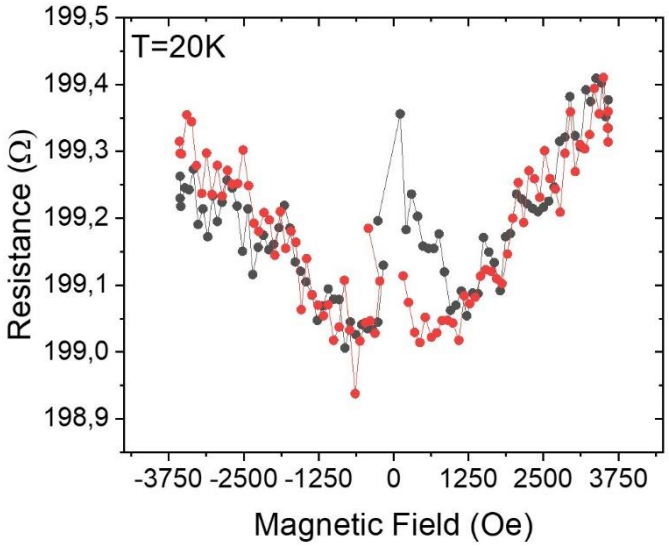

Figure 3.27: Resistance vs applied magnetic field at T=20K on junction 2(b). Contrary to a bare LCMO wire with a typical CMR behavior, in this measurement an increase in resistance is observed at higher fields. This superconducting behavior plus the AMR signature at close to zero fields is a hint of the transition of the LCMO into a superconducting state.

Nevertheless, strong evidence of the creation of triplet Cooper pairs is supported by the interface and junction electrical measurements. This makes the seek for a complete proximity effect in these materials of large interest, due to its relatively high functioning temperatures.

3.3.3 *SAMPLE WITH MULTIPLE PLANAR JUNCTIONS*
LCM51A2+ALO+YBCO

The presence of two LCMO microwires in the previous sample LCMO365D+ALO+YBCO makes the interpretation of the data difficult, as it is difficult to ascribe the observed behavior to a particular junction. Hence, we decided to switch to samples with a single LCMO wire. We are now discussing sample LCM51A2+ALO+YBCO with just have one LCMO microwire. Also, we reduced the number of YBCO microwires to 3, making them larger so they are more robust against degradation. An AFM image of the device is presented in Figure 3.28.

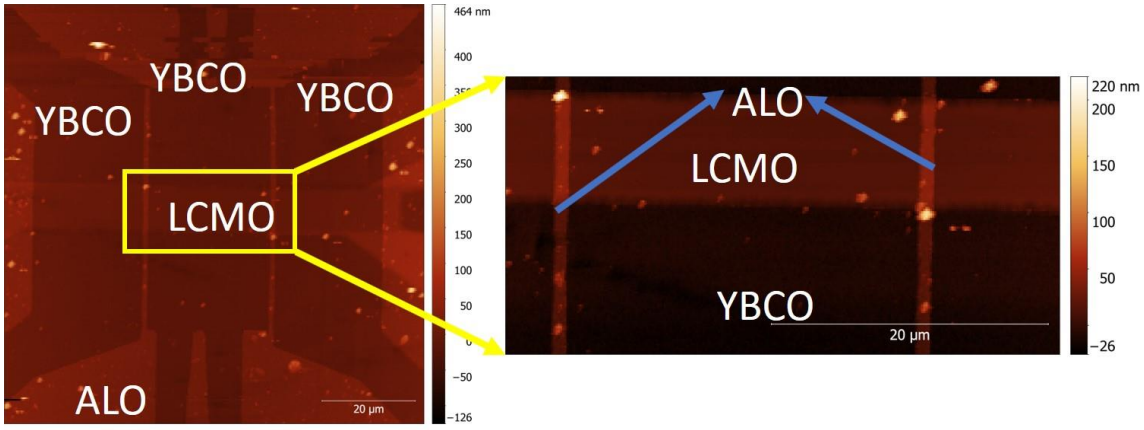

Figure 3.28: AFM images of LCM51A2+ALO+YBCO device 5. It consists on a 5um LCMO microwire crossed by three 30um YBCO microwires. Separation between YBCO microwires is 1,1um.

Separation between YBCO microwires is 1,1µm and LCMO microwire is 5µm wide, providing 2 junctions of 1,1 x 5 μm^2. Only one of the junctions was measured due to technical problems with the gold contacts. Some noise was observed in resistance curves which disappeared when temperature was reduced. In Figure 3.29 the R(T) is shown. It has a usual LCMO behavior with a resistance peak at the Curie temperature and a metallic behavior below. At 81K a transition of

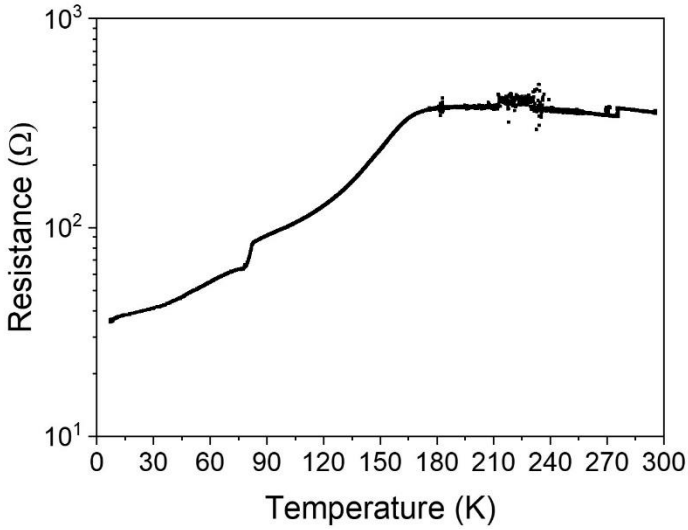

Figure 3.29: Resistance vs Temperature for sample LCM51A2+ALO+YBCO with an injected current of 1uA. Above the Curie temperature (T=178K) there is some noise in the measurement which disappears when decreasing temperature. At T=81K the superconducting transition of YBCO in the electrodes is observed. Below, a continuous decrease in resistance follows instead of the saturation or resistance increase typically observed in bare LCMO.

the YBCO can be identified. At lower temperatures, there is a step-like in the shape of the curve, and the resistance decrease becomes more pronounced which is not typically observed in LCMO RvsT curves. This result is a first indication of a superconducting proximity effect induced in the LCMO.

The differential conductance shows an increase at low voltages, as in previous samples, but not as pronounced (Figure 3.30(a)). Surprisingly, for this sample after a magnetic field was applied to measure a RvsH (Figure 3.30(b)), the shape of the differential conductance changed completely. Before applying field, it behaved as expected for a superconducting critical current with a higher conductivity at lower voltages, but after applying magnetic field, the behavior changed to one similar of a tunnel junction (Figure 3.30(c)) with lower conductivity at lower voltages. The measurement is noisy at low temperatures, but if we increase the temperature up to 14K we can observe highly anomalous oscillations in the differential conductance (Figure 3.31). These oscillations persisted upon consecutive measurements and we carefully excluded that they were due to noise or experimental artefacts. Attempts to fit these oscillations to the McMillan-Rowell [36] or Tomasch [39] resonances, did not produce confident results.

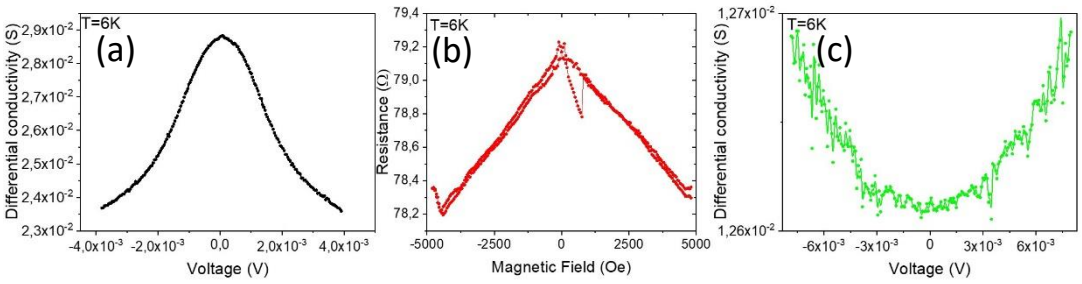

Figure 3.30: (a) Differential conductivity of the junction before applying field. (b) RvsH curve for a current of 100uA. (c) Differential conductivity after applying field.

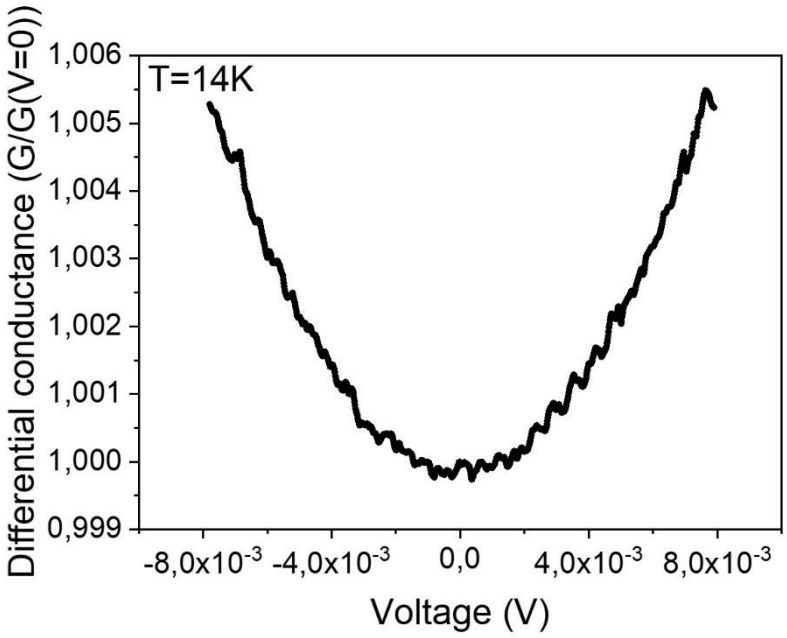

Figure 3.31: Oscillations in the differential conductance at T=14K averaged for different applied magnetic fields.

Finally, after the measurements with applied field, a resistance curve was measured going up in temperature (Figure 3.32). It showed a markedly different behavior than the resistance curve

measured when cooling down. The resistance below the critical temperature of YBCO decreases for a small range of temperature, but it starts increasing when temperature is further reduced. Also, a clearer metal insulator transition of the LCMO can be observed, probably due to an improved interface contact or to the ordering of its magnetic state after applying the field.

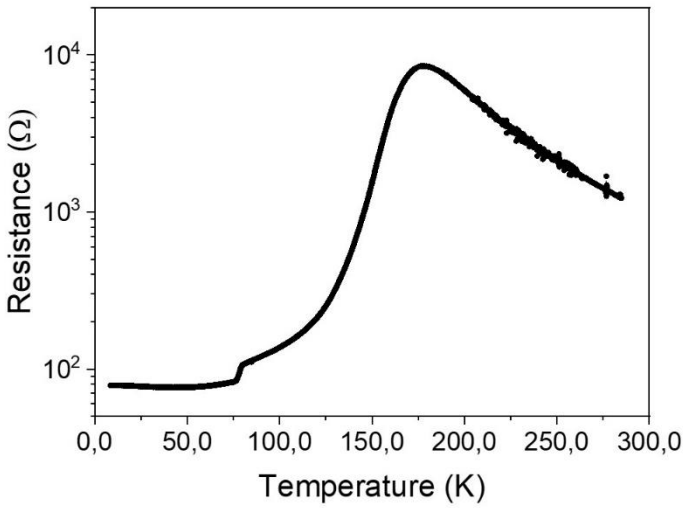

Figure 3.32: Resistance vs Temperature after measuring the differential conductance and RvsH. It presents a more pronounced metal insulator transition of the LCMO and an insulating behavior of the resistance at low temperatures.

3.3.4 *PRELIMINARY CONCLUSIONS*

We have confirmed the indications of proximity effect in this system, although not a fully superconducting state was found which is the goal of this thesis. By changing the device geometry to a planar geometry with a reduced number of junctions we can analyze better where and how is the origin of a proximity effect in an LCMO/YBCO system. Considering the resistance measurements one possible problem in this system is the large resistance of the LCMO. One possible approach is to use another half-metal with a lower resistance, making the material more amenable for the superconducting proximity effect. Another problem can be the high resistance of the YBCO/LCMO interface due to the ex-situ character of the fabrication, which could affect heavily the generation of triplet Cooper pairs. These conclusions lead us to the use of LSMO, a half-metallic material similar to the LCMO but with lower resistance (due to its larger bandwidth) and higher Curie temperature. The fabrication process will also be optimized with special attention to the interface structure to enable the generation of triplets. In the next section we describe these LSMO/YBCO devices.

3.4 LSMO/YBCO PLANAR JOSEPHSON JUNCTIONS

After all the experiments performed using LCMO, the use of LSMO seems the natural next step towards finding a proximity effect. The idea behind this selection is keeping the half metallic state with a larger bandwidth, what is expected to result in lower values of the interface resistance. What else do we need to have a superconducting proximity effect in a half-metal? The answer is simple, triplet Cooper pairs will be transported long distances into the ferromagnet, but the path to generate them may not be so simple. To generate triplet pairing, spin mixing and spin rotation are needed, and for these processes to occur, an inhomogeneous magnetic structure is needed [2,28]. LSMO is the perfect candidate for this. The Cu-O-Mn superexchange path at the interface between YBCO and LSMO provides a mechanism for the singlet Cooper pairs on the YBCO to feel the exchange field of the ferromagnet and suffer the spin mixing process of the singlet and the zero Sz triplet component. Once in the LSMO, the fact that it has biaxial magnetic anisotropy, i.e., two easy magnetization axis in the (110) and (1-10) directions yields the inhomogeneous magnetic (domain) structure allowing for a spin rotation process. Since the previously described samples convinced us about the existence of the proximity effect in our samples, to facilitate the analysis of the data we engineered the new samples with a single junction, between two YBCO microwires and just one LSMO microwire.

3.4.1 SAMPLE FABRICATION AND CHARACTERIZATION

The ferromagnetic-superconducting proximity effect in this system was studied by using planar structures where current is injected in a single LSMO microwire through two YBCO microwires. As in the previous planar samples, we have defined the YBCO bridges on previously fabricated LSMO wires using rf sputtered amorphous alumina (a- Al_2O_3) templates. The YBCO grew on trenches previously etched in the a- Al_2O_3 pattern using electron beam lithography. Figure 3.33(a) shows an optical microscopy image of one of the final devices fabricated according to the sketch depicted in Figure 3.33(b). The spacing between YBCO bridges was ~1um (see Figure 3.33(c) and an enlarged view in Figure 3.33(d)).

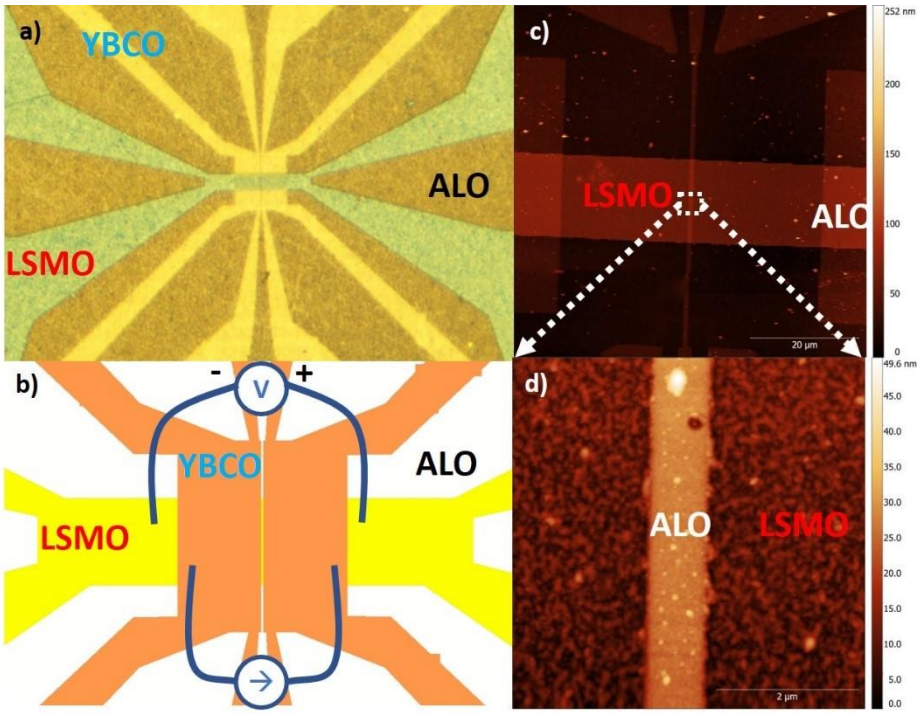

Figure 3.33: (a) Optical image of the device. ALO and YBCO are on top of the LSMO microwire. (b) Sketch of the device and measurement configuration. The nominal separation between YBCO bridges is 1um. (c) AFM image of the device before YBCO deposition. The ALO between YBCO bridges is continuous all along the LSMO. (d) AFM image of the ALO separator on top of the LSMO.

A reasonable caveat about this fabrication process is the degree that the interface can be affected by the ex-situ growth of the YBCO. A demonstración of the high quality of the YBCO/LSMO interface grown ex-situ is shown in the scanning transmission electron microscopy (STEM) images displayed in Figure 3.34. A low magnification high angle annular dark field (HAADF) image in Figure 3.34 (a) shows that the sample grows flat and continuous over long lateral distances. In Figure 3.34 (b and c) the high-resolution image displays the YBCO/LSMO interface, which appears epitaxial, atomically smooth and free of disorder with the same crystalline quality as the interfaces grown in situ. As it turns out, the growth at 900 ºC in a pure oxygen plasma has the effect of (re)conditioning the surface after exposure to atmosphere or processing. Figure 3.34 (d) displays an atomic resolution EELS chemical map of the interface alongside a high resolution HAADF image. While the HAADF image indicates which atom corresponds to each atomic column, the colored map presents a color mixing of Ba M4,5 (red), La M4,5 (yellow) and Mn L2,3 (blue) elemental EELS maps, where the interface is observed to be chemically sharp with no intermixing detected. The interfacial termination planes between YBCO and LSMO are also evidenced and, as in the in-situ samples, correspond to BaO facing MnO2 planes with missing CuO chains at the interface [40,41]. The Cu-O-Mn superexchange path across the interface induces a magnetic state in the Cu which may play a central role in the triplet generation [32,33].

To check the magnetic state of the LSMO in contact with the YBCO, photoemission electron microscopy SPEEM measurements were performed. The magnetic domain structure of the ferromagnet superconducting hybrids was examined by means of photoemission electron microscopy (PEEM) using X-ray magnetic circular dichroism (XMCD) as magnetic contrast mechanism. Experiments have been done at the SPEEM station at the UE49/PGMa beam line of the synchrotron radiation source BESSY II at Helmholtz-Zentrum Berlin [42]. The angle of incidence of the incoming radiation with respect to the sample surface is 16°. The sample was mounted on a sample holder which allows application of in plane magnetic field pulses up to ±1000 Oe. Magnetic imaging was done in remanence after applying the desired magnetic field

value. Images with a 10 µm field of view were collected at the Mn L3-edge (640.3 eV) for circularly polarized radiation with clockwise (σ+) and counterclockwise (σ-) helicities. The data has been normalized to a background image and drift corrected before their averaging. The XMCD images were calculated as (σ--σ+)/(σ-+σ+). Measurements were conducted at 50 K.

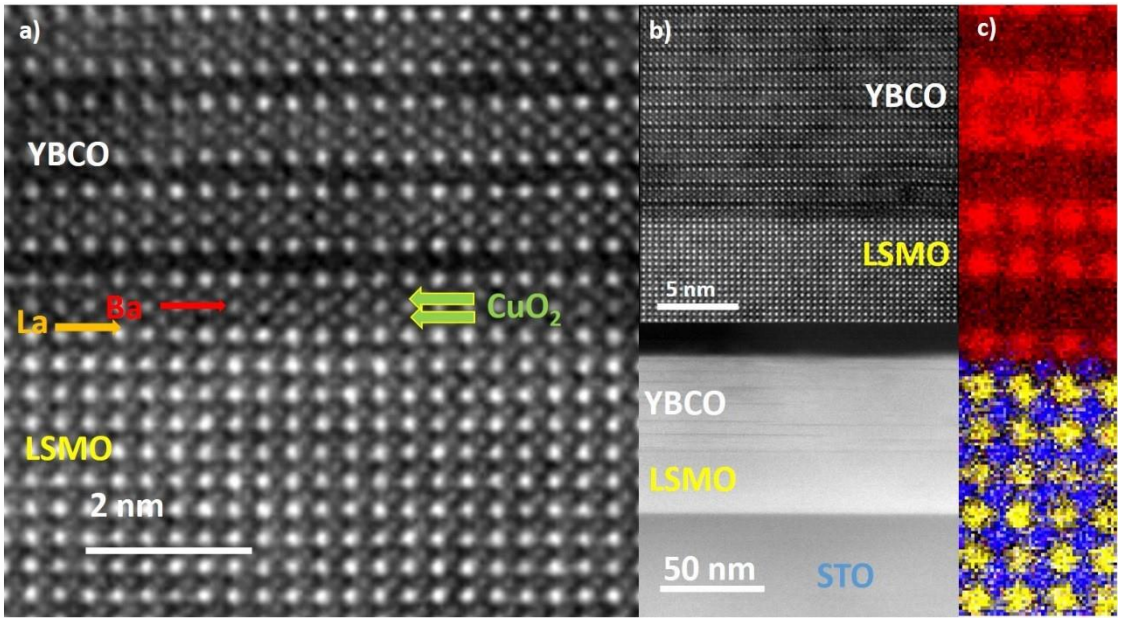

Figure3.34: (a) Structure of the YBCO/LSMO Interface grown ex-situ. The interface terminations are Ba-Mn. (b) Low magnification images of the interface showing the long-range high quality of the interface. (c) Ba-Mn-La EELS map, Ba in red, Mn in blue and La in yellow.

Images of magnetic domains were acquired in LSMO/ YBCO hybrids with a continuous LSMO layer is grown on top of 25-micron side YBCO squares grown on STO (Figure 3.35). YBCO squares with sides along [100] directions, were separated by 1-micron wide LSMO long rectangles. XMCD was measured at the Mn L_3-edge (640.3 eV) as the normalized difference in absorption of circular polarized radiation with left and right helicity. Color contrast in the image of Figure 3.35 is set by the projection of the sample magnetization along the direction of propagation of the beam. Images are taken at remanence after applying in plane magnetic field directed along [100]. Notice that domains are along [110], which is known to be the one of the easy axis of thin film manganite. Also, the density of domains increases below the superconducting transition temperature. These domains nucleate above the superconductor and cross the LSMO rectangle. Typical domain width is 1-2 microns and typical domain wall size is in the tens of nm range. The magnetization in these domains points in the direction of the (biaxial) easy axes, blue domains have magnetization in the (110) direction and red domains in the (1-10) direction. Within domain walls spin rotates continuously. Even though this is the structure of the LSMO on top of YBCO it provides a good indication of the effect of the superconductor on the domain structure of LSMO. We conjecture that the 90 degrees rotation of the magnetization between domains provides a natural scenario for the generation of finite Sz triplet Cooper pairs.

Finally, magnetoelectric measurements were performed in two samples: LSM139A1+ALO+YBCO and LSM139A2+ALO+YBCO.

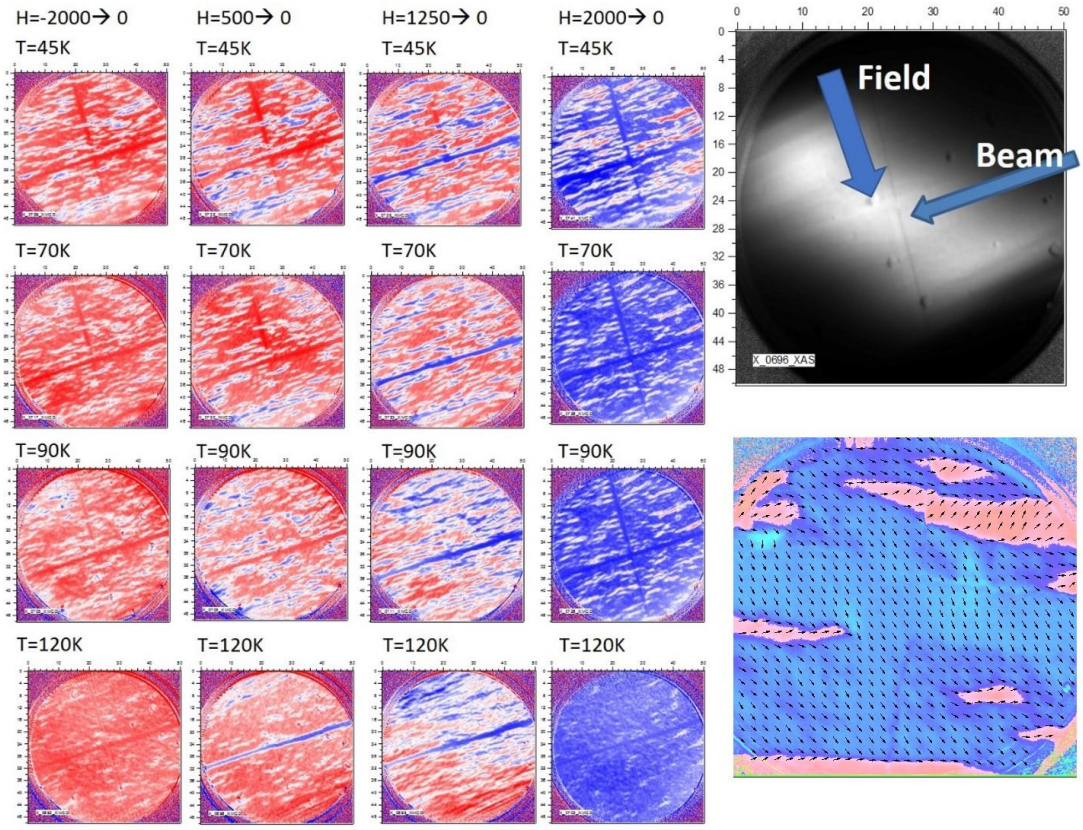

Figure 3.35: The domain structure of LSMO radically changes when the YBCO becomes superconductor, below 90K. Filament like domains appears perpendicular to the applied field with magnetic moments directed along the biaxial 110 easy axes, i.e. at 45 degrees to the applied field. The direction of the magnetization in different domains is orthogonal and pointing along the two easy magnetization axes of the LSMO.

3.4.2 SINGLE JUNCTION SAMPLE LSM139A2+ALO+YBCO

For sample LSM139A2+ALO+YBCO two different devices were measured: device 1 and device 2 (Figure 3.20). As usual, resistance curves R (T) as a function of temperature were first measured to seek for the indications of proximity effect before applying magnetic field.

Figure 3.36 (a) shows 4-points resistance curves of three different samples with the same YBCO bridge width and 25 and 20 micron wide LSMO wires (green curve is from device 1 of sample LSM139A1+ALO+YBCO). Current is injected across the neighboring YBCO wires while voltage is measured in the LSMO ends. I.e., the resistance corresponds basically to the LSMO segment in between the YBCO bridges. Notice that below room temperature and down to the transition temperature of the YBCO contacts (90 K) the resistance follows the characteristic dependence of LSMO. Figure 3.36 (b) shows a comparison between the resistance of an LSMO film and the LSMO microwire in between the two YBCO contacts. At 90 K there is a small resistance drop in all samples corresponding to the superconducting transition of the YBCO contacts. Below 90 K there is a gradual resistance decrease down to a temperature of (roughly) 60 K where a second superconducting transition is observed down to zero resistance level (see inset in Figure 3.36 (a)). This is a superconducting transition of the LSMO proximized to the YBCO.

Figure 3.37(a) shows a 2 points measurement of the superconducting transition of the YBCO bridges which identifies the first transition found in the 4 points measurement slightly below 90 K. Below this temperature the YBCO is fully superconducting and the zero-resistance state is due

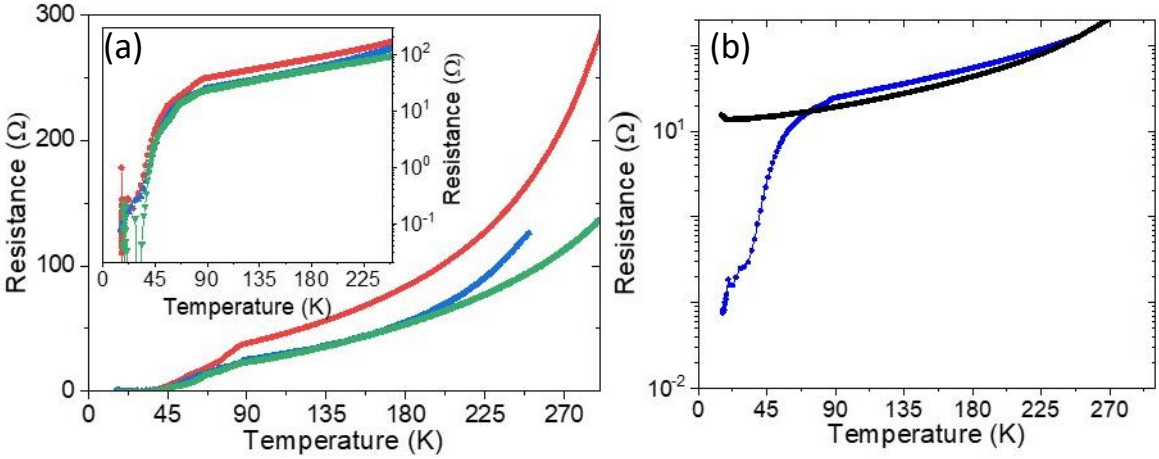

Figure 3.36: (a) RT of different devices on samples LSM139A2+ALO+YBCO devices 1 and 2; and LSM139A1+ALO+YBCO device 1. We observe a first superconducting transition corresponding to the YBCO electrodes followed by a gradual decrease at lower temperatures. (b)Comparison of the resistance of a LSMO thin film, and the wire in the junction device.

to the proximity effect in the LSMO wire connecting the two YBCO bridges, as can be seen in the 4 points measurement. The control experiment displayed in Figure 3.37 (b) shows that this low temperature transition is not observed in devices fabricated with no LSMO wire, being this measurement without LSMO wire the only one with resistance small enough to be measured by our set-up. It is worth pointing that this was one of the few cases that this resistance could be measured, and that it became unmeasurably high when temperature was reduced. I.e., as noted before, the YBCO growing on top of the amorphous ALO is highly insulating.

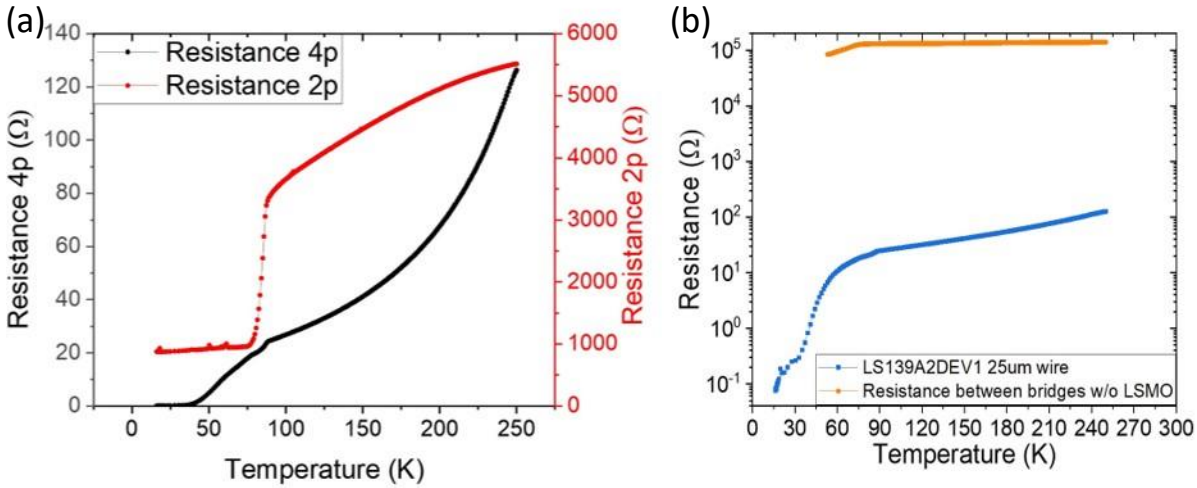

Figure 3.37: (a) 2-points and 4-points resistance of the device. For 2-`points, the contribution of LSMO is much smaller than the one of YBCO, and for 4-points only the LSMO is being measured. (b) Resistance of LSMO device compared to a device without LSMO wire.

The zero-resistance state in the half-metallic LSMO was analyzed for non-linear transport denouncing the presence of a critical current. In Figure 3.38 (a) we show an IV curve clearly showing a critical current below a certain temperature T=50K and non-linearity below T=60K. Also, to clarify the existence of a critical current, a plot of the differential resistivity as a function of current is displayed in Figure 3.38 (b). The evolution of this critical current seems quadratic with the temperature down to 20K, the lowest temperature we could stabilize in the cryostat used (Figure 3.38 (c)).

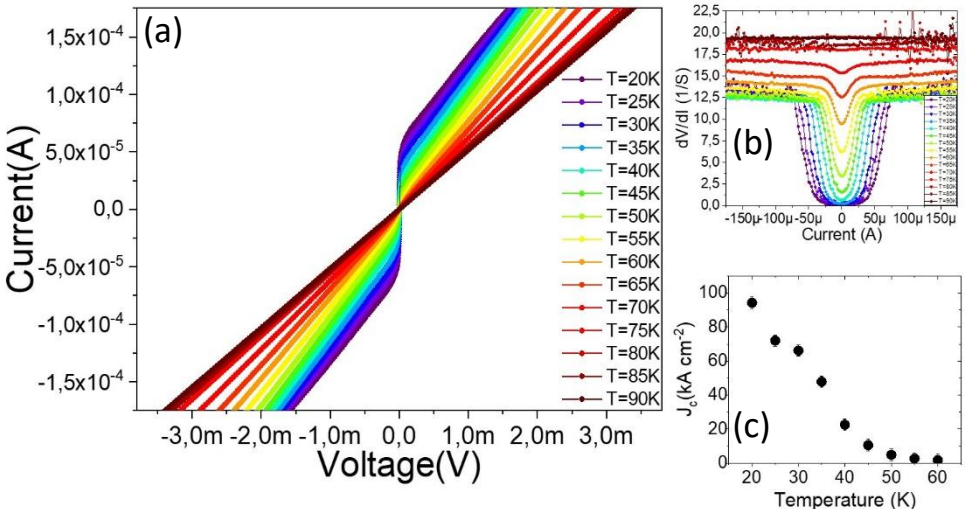

Figure 3.38: (a) IV curves of the device LS139A2DEV1 as a function of temperature. We can observe a non-linearity appearing around 60K which becomes a critical current at lower temperatures. (b) dV/dI vs I for different temperatures. We observe the non-dissipative state at low temperatures. (c) Critical current density in function of Temperature. The voltage criterion a for Jc measurement is 1,5uV

IV curves as a function of temperature become nonlinear below 60K evidencing that the LSMO wire becomes non dissipative at low temperatures. This demonstrates that the proximized LSMO has in fact a critical current which takes values between 1 and 4 10^4 A/cm^2, much lower than the values (10^7 A/cm^2) typically found in YBCO wires at the same temperatures. This is the first time a critical current has been found in half-metals in contact with d-wave superconductors at such high temperatures. Of course, to establish that there is in fact a Josephson junction with a LSMO weak link more measurements are needed to demonstrate that there is a macroscopic quantum state. In particular, it is necessary to show current interference effects as a function of magnetic field periodic in the magnetic flux quantum (Fraunhofer pattern) and phase locking under microwave illumination (Shapiro steps).

This last case was confirmed by applying a microwave of frequency F=9.997GHz at different powers close to the superconducting transition of the LSMO (T=37K). For the measurement of the Shapiro steps the microwave signal was delivered through a semi-rigid coaxial cable terminated by a wide band spiral antenna placed in front of the sample (~1 cm above it) and connected to a generator in a continuous wave mode at frequency f and power P. Differential resistance curves were obtained by numerically differentiating the I(V) characteristic after applying a moving average window to smooth the data. The presence of Shapiro steps confirms that our devices exhibit Josephson physics (Figure 3.39). This resonant response constitutes direct evidence of the sinusoidal current phase relationship of the Josephson junction. Strikingly, though, steps appear at half-integer factors of the Josephson voltage $V_{Josephson} = \Phi_0 f$ evidencing a doubling of the Josephson frequency and thus the preponderance of the second harmonic term in the current phase relation. Half-integer Shapiro steps have been experimentally observed in S/F/S vertical (tunnel) junctions with weak ferromagnets at the verge of the 0-π transition [43,44]. Theoretically, it has been argued that Josephson junctions with ferromagnetic barriers can be markedly non-linear, and that precisely, the strong suppression of the critical current at the 0-π transition explains the predominance of the second harmonic term in the current phase relation [23,45–47] . It is clear, then, that the non-integer Shapiro steps observed in our junctions are an additional fingerprint of the ferromagnetic

proximity effect governing the Josephson coupling, although our system with unconventional superconductor and half metallic electrodes in a planar geometry calls for further theoretical studies to achieve a complete understanding of the phenomenon.

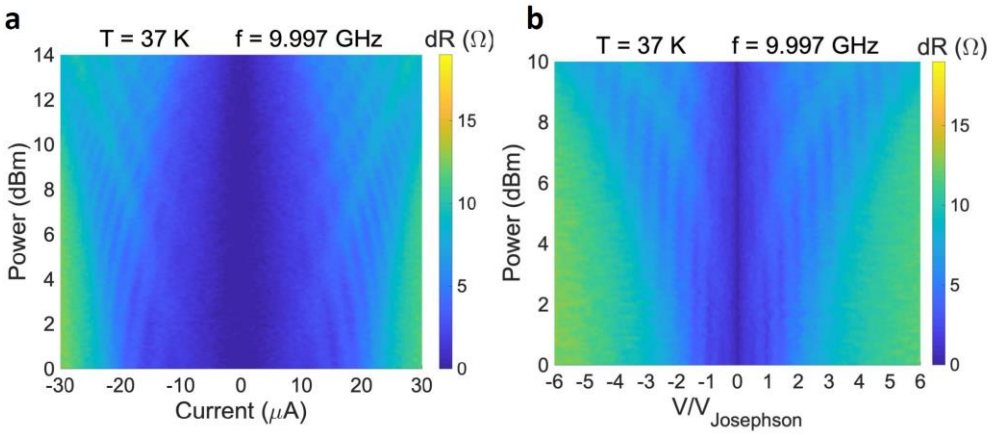

Figure 3.39: (a) Shapiro interference pattern of the differential resistance as a function of current for different microwave power levels for a frequency of 9.997GHz. (b) Shapiro steps as a function of voltage normalized to the Josephson voltage ($V_{Josephson}$=hf/2e) for microwave radiation of 9.997 GHz.

Another important point to address is the magnetic state of the LSMO. Above the Tc of YBCO magnetoresistance with the magnetic field applied in plane in the direction of the microwire shows a behavior typical of LSMO. The shape of the curve changes when lowering the temperature to end up with the aspect of a typical superconductive RvsH at low temperatures with resistance increasing with field. Figure 3.40 shows magnetoresistance R (H) curves at

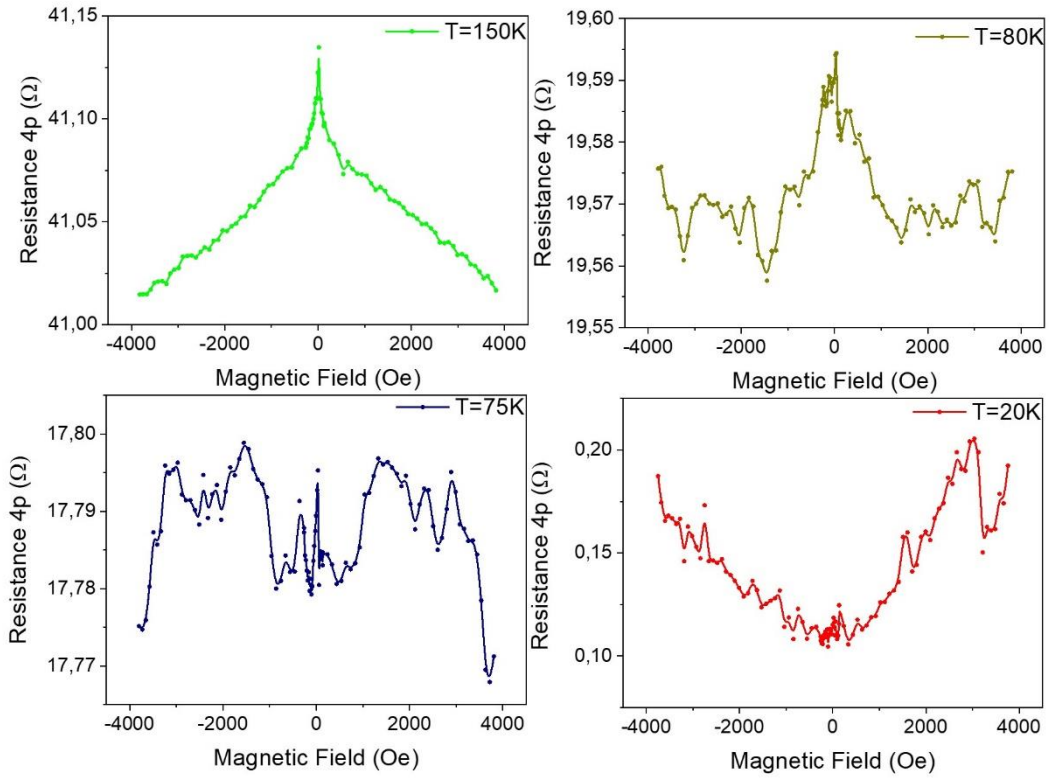

Figure 3.40: RvsH of the junction at different temperatures and same current (25uA). Above the critical temperature of YBCO the junction has a typical LSMO magnetoresistance, that starts to change below Tc. Finally, when the LSMO is fully superconducting we can observe a magnetoresistance more similar to the one of a superconductor. Of course, to measure this RvsH a current higher than the critical current had to be applied.

different temperatures measured with the same current level of 25 μA. The inversion of the sign of the magnetoresistance below the superconducting transition temperature can be readily seen. A direct proof that this sign inversion results from the transition into a superconducting proximity state is obtained from its dependence on the current level. Notice that when the current is well above the critical current (what destroys proximity effect) the sign inversion of the magnetoresistance is not observed, as illustrated in Figure 3.41 in which a RvsH is measured with different currents. Notice that at 800uA, well above the critical current, a typical LSMO behavior is recovered, with higher resistance at lower fields and at 20uA close to the critical current, the junction exhibits a superconducting behavior. This is the behavior that we would expect of a proximized LSMO, but to confirm it is a Josephson junction we must measure with an applied magnetic field perpendicular to the junction to observe a Fraunhofer pattern. In this case, as we will see, the role of the magnetic domains of LSMO is of great importance.

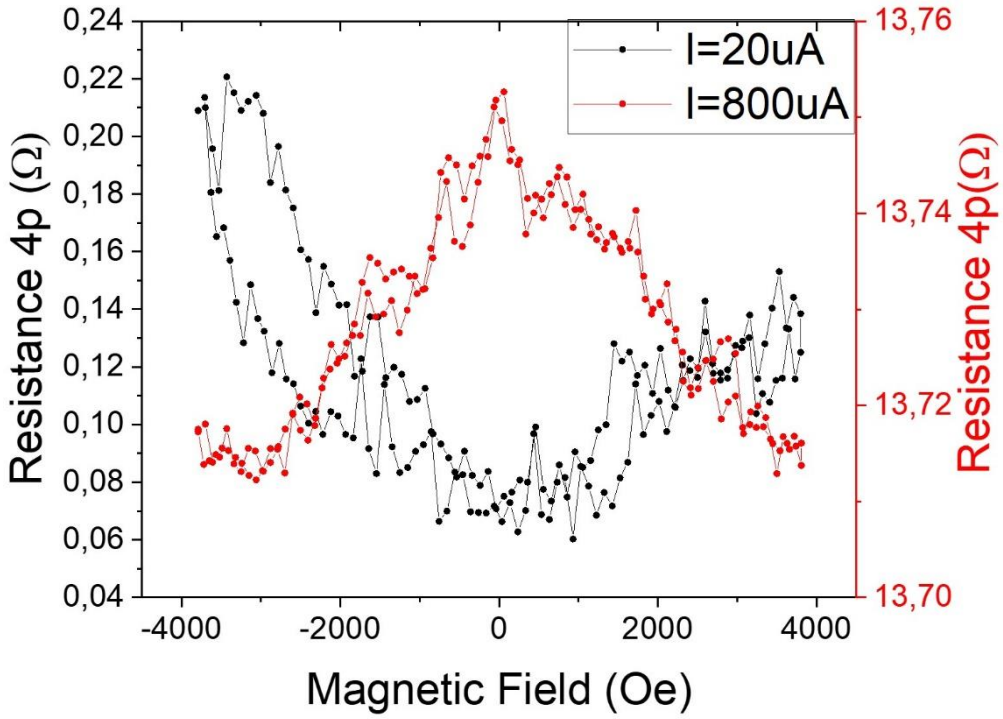

Figure 3.41: RvsH of the junction at different currents but the same Temperature T=15K. A superconducting behavior is found at low current, but at larger currents, well above the critical current of LSMO, the comportment changes to a CMR manganite magnetoresistance.

In device 1, two YBCO microwires are separated by a LSMO wire. The LSMO wire is 30 nm thick and its width is 25 microns. The separation between YBCO microwires is 1 micron. We have examined the Fraunhofer pattern with magnetic fields directed out of plane and in plane. These two magnetic fields geometries will probe very different junction areas (Figure 3.42).

To better understand the results, it is important to look at the structure of magnetic domains in the junction. The magnetic domain structure of the LSMO microwire has been investigated using x-ray photo electron microscopy, PEEM, at the synchrotron BESSY II (Figure 3.43). The x-ray beam is directed along the wire. Blue regions correspond to magnetization with a component antiparallel to the beam and red regions to magnetization with a component parallel to the beam. The LSMO microwire (Figure 3.43(a)) has biaxial magnetic anisotropy with easy axes

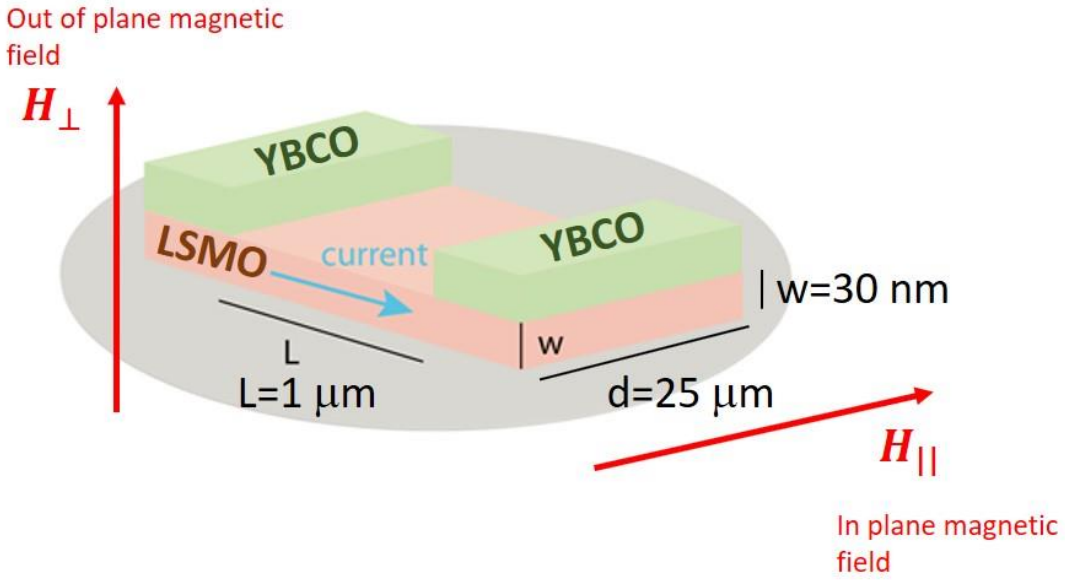

Figure 3.42: Sketch of the device for the Fraunhofer pattern measurements.

directed 45º away from the wire axis. Domain walls are also (approximately) 45º away from the wire axis. The magnetization within neighboring domains points 90º apart (the colored arrows show the directions of magnetization within each domain). PEEM images of Figure 3.43(b) show that the LSMO bridge can be homogenously magnetized along [110] directions corresponding to the biaxial easy axes of the manganite, although in some situations remanence states with coexisting micron size domains were observed. This domain geometry ensures that there are wide regions with homogeneous magnetization connecting the YBCO contacts where the triplet

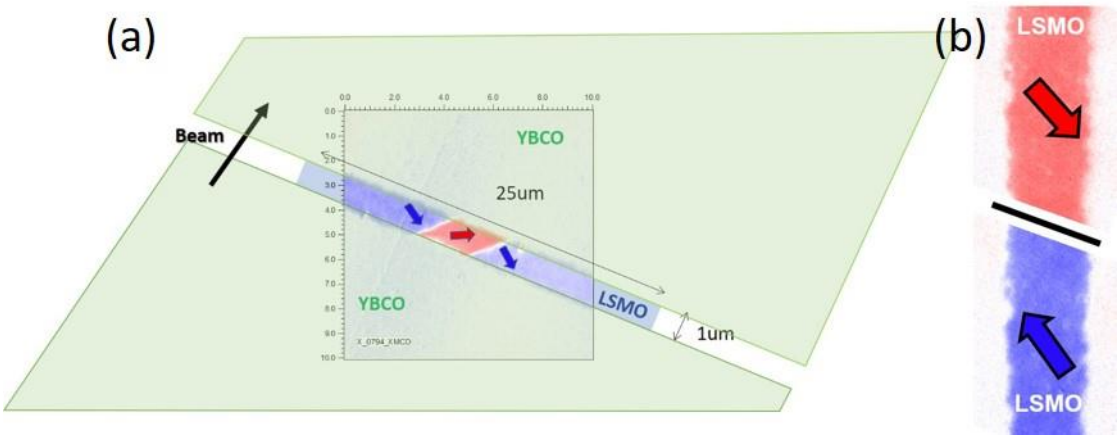

Figure 3.43: Magnetic domain structure of the LSMO junction measured using PEEM. Clear domains at 45 degrees with the wire appear with its magnetization perpendicular to the contiguous domain.

pairs can propagate freely.

Now, there is two ways of Josephson coupling possible in this structure due to the presence of triplet Cooper pairing (Figure 3.44):

(1) **Coupling between YBCO microwires across a magnetic domain (blue and red solid arrows).** Triplets generated at the (spin active) LSMO/YBCO interface where magnetization is known to be depressed and eventually also rotated, are long range

transported between the YBCO electrodes within the magnetic domain. This is the usual behavior of a Josephson junction.

(2) **Coupling between proximitized domains across the domain wall (White arrow).** Triplets crossing the domain wall experience a phase difference due to the different orientation of the magnetization at both sides of the domain wall. I.e., the domain wall acts as a barrier between the neighboring proximized domains. In this case, the Josephson junction is the domain wall between two superconducting LSMO magnetic domains. This is a completely new form of triplet proximity effect which has never been found experimentally

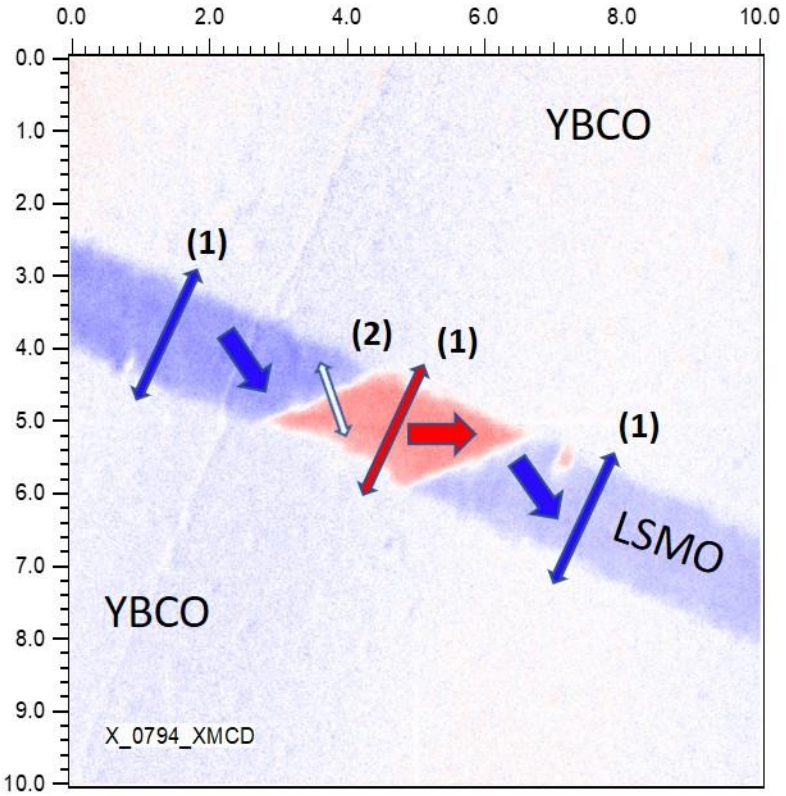

Figure 3.44: Magnetic domain structure as measured by PEEM. Thick arrows indicate the directions of the magnetization. Possible paths of Josephson coupling are marked with thin arrows.

It is important to notice that these two mechanisms of Josephson coupling are in parallel, so the less resistive will contribute more to the macroscopic behavior.

Once we have defined our two possible Josephson junctions, we have to measure them to observe is this hypothesis is valid. First, we carry out measurements with the magnetic field in plane. If we measure the magnetoresistance of the device while changing the angle in which the field is applied, we should observe a Fraunhofer pattern following the next equation:

$$I_c = I_0 \left| \frac{\sin\left(\frac{\pi\phi}{\phi_0}\right)}{\left(\frac{\pi\phi}{\phi_0}\right)} \right| = I_0 \left| \frac{\sin\left(\frac{\pi H_\perp w(L+2\lambda_{eff})}{\phi_0}\right)}{\left(\frac{\pi H_\perp w(L+2\lambda_{eff})}{\phi_0}\right)} \right| = I_0 \left| \frac{\sin\left(\frac{\pi H \sin\theta\, w(L+2\lambda_{eff})}{\phi_0}\right)}{\left(\frac{\pi H \sin\theta\, w(L+2\lambda_{eff})}{\phi_0}\right)} \right|$$

With $H_\perp$ the magnetic field perpendicular to the junction and λ_{eff} the effective junction length below YBCO contacts. Notice that we haven't used the London penetration depth since for magnetic field in plane it fully penetrates the thin superconductor (much thinner than the London penetration depth). But we have two junctions (Figure 3.45), so they will behave differently with the direction of the in-plane field:

- **In plane magnetic** field directed perpendicular to the LSMO wire (90º) will probe the main junction coupling the YBCO banks. Its cross section is marked in magenta (1).
- **In plane magnetic** field directed perpendicular to the domain wall (45º) will probe the junction between LSMO domains (2 in the sketch) defined by a magnetic domain wall separating two LSMO domains. Its cross section (2) is marked in green.

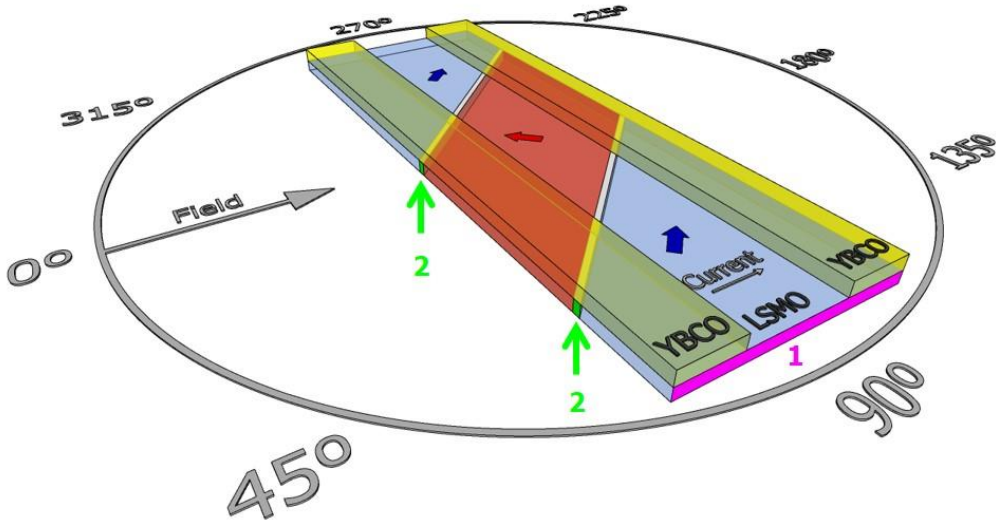

Figure 3.45: Sketch of the different junctions probed with the magnetic field applied in plane.

As these two junctions are in parallel, the total critical current of the system will be:

$$I_c = I_0\left|\frac{\sin\left(\frac{\pi\phi}{\phi_0}\right)}{\left(\frac{\pi\phi}{\phi_0}\right)}\right| = I_0\left|\frac{\sin\left(\frac{\pi H_\perp wL}{\phi_0}\right)}{\left(\frac{\pi H_\perp wL}{\phi_0}\right)}\right| = I_0\left|\frac{\sin\left(\frac{\pi H \sin\theta\, wL}{\phi_0}\right)}{\left(\frac{\pi H \sin\theta\, wL}{\phi_0}\right)}\right| \quad \text{(JJ coupling across magnetic domains)}$$

$$+\; I_c = I_0\left|\frac{\sin\left(\frac{\pi\phi}{\phi_0}\right)}{\left(\frac{\pi\phi}{\phi_0}\right)}\right| = I_0\left|\frac{\sin\left(\frac{\pi H_\perp wL}{\phi_0}\right)}{\left(\frac{\pi H_\perp wL}{\phi_0}\right)}\right| = I_0\left|\frac{\sin\left(\frac{\pi H \sin(\theta+\frac{\pi}{4})\, dL}{\phi_0}\right)}{\left(\frac{\pi H \sin(\theta+\frac{\pi}{4})\, dL}{\phi_0}\right)}\right| \quad \text{(JJ coupling across magnetic domain walls)}$$

Now, we can study both the Fraunhofer pattern due to the coupling across magnetic domains, if we measure with applied magnetic fields below 0.4T, and the Fraunhofer pattern due to both the domain wall and magnetic domains, by measuring up to 0.6T.

Measurements of the junction resistance *R* as a function of the magnetic field *H* applied in the plane of the LSMO microwire allowed for the observation of quantum interference effects demonstrative of Josephson coupling. At low temperatures (below the critical temperature of the proximitized LSMO) and sufficiently high injected current *I*, the junction's resistance periodically oscillates as a function of the applied field. This is shown in the example displayed in Figure 46 (a), which corresponds to a *R(H)* measured at T=30 K with I=25 μA.

The oscillations' period depends on the angle between the in-plane magnetic field and the LSMO wire. This is evidenced in Figure 46 (c), which displays a contour plot of the resistance (color

scale) as a function of the magnetic field magnitude and angle θ with respect to the LCMO wire [geometry shown in Figure 46 (b)]. The contour plot is obtained from a large set of R(H), measured for varying θ (every 0.2° for $0° \leq \theta \leq 360°$) at constant T=30K and I=25 μA. In this plot, the magnetoresistance oscillations show as a "wavy pattern" with mirror symmetry around θ=0°, 90°, 180° and θ=270°. The pattern results from the oscillations' period being the shortest when magnetic field is perpendicular to the LSMO wire (θ=90° and θ=270°) and gradually increasing as the magnetic field is rotated towards the direction of the LSMO wire (θ=0° and θ=180°). The periodic magnetoresistance oscillations [Figure 46 (a)] result from the Fraunhofer oscillation of the critical current as a function of the magnetic flux threading the junction Φ. The angular (θ) dependence of the oscillations [Figure 46 (c)] results from the junction's geometry, in particular from the angular dependence of the magnetic flux across the junction, $\Phi(H,\theta) = \mu_0 H A_{eff} |\sin(\theta)|$, with A_{eff} an effective junction area as shown in Figure 46 (b). Thus the experimental behavior [Figure 46 (c)] is qualitatively reproduced [see Figure 46 (a)] by $I_c(H,\theta) = I_{c0}\left|\frac{sin\pi\frac{\Phi}{\Phi_0}}{\pi\frac{\Phi}{\Phi_0}}\right|$, with I_{c0} being the maximum critical current, Φ_0 the flux quantum (2.07 10^{-15} Wb), and $\Phi(H,\theta)$ as described above. Assuming that the magnetic flux is an integer number of flux quanta, the experimental oscillations' period [~0.03T for θ=55°] implies A_{eff} ~ 0.087 μm^2. Considering the vertical dimension of the wire is limited by the LSMO thickness ($w =$ 30 nm) and that the effective junction area is given by $A_{eff} = L_{eff} \times w$, we extract an effective junction width L_{eff} ~ 3 μm, 2μm in excess of the distance between the YBCO electrodes (1 μm). That is reasonable since YBCO covers LSMO over a large area and therefore

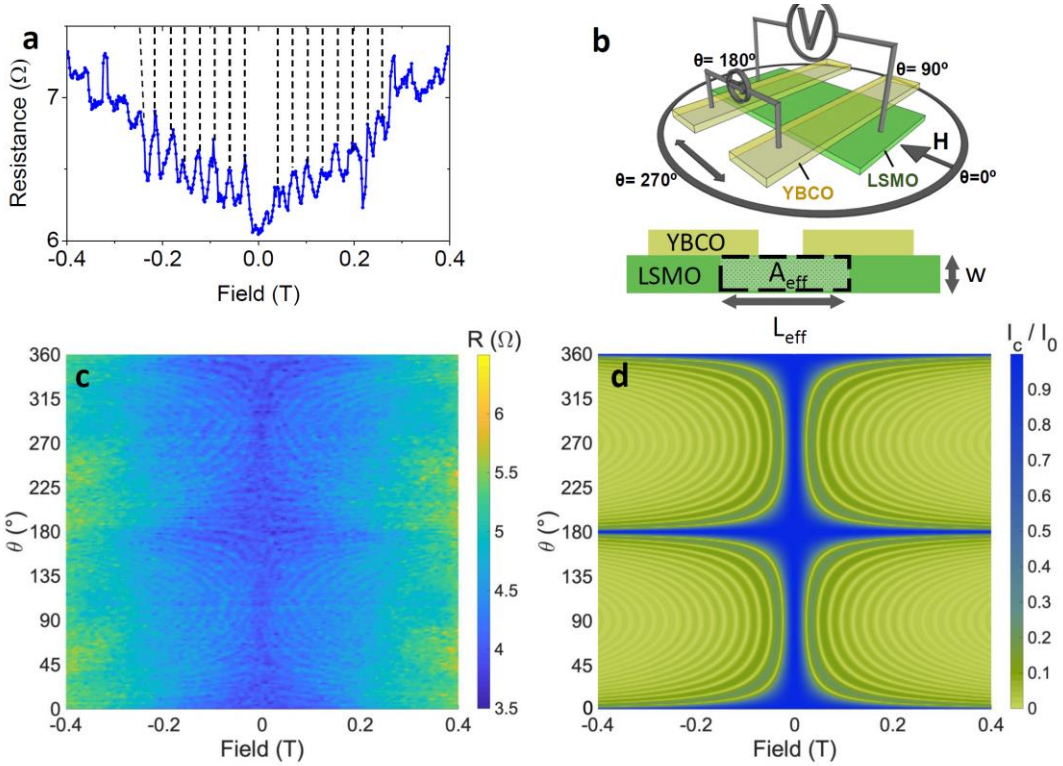

Figure 3.46 (a) Resistance oscillations as a function of magnetic field (-0.4T<H<0.4T) oriented at 45 º with LSMO wire. (b) Schematic illustrating the orientation of magnetic field. (c) Contour plot of the resistance as a function of magnetic field (-0.4T<H<0.4T) with different orientations relative to the LSMO wire. Angle is varied in steps of 0.2 º (d) Simulation of the oscillation pattern of the I_c/I_0 assuming a Fraunhofer dependence of the critical current of the magnetic flux.

one does not expect the effective width of the Josephson junction L_{eff} to be defined by the distance between the edges of the YBCO electrodes.

When we measure up to higher (in plane) fields (Figure 3.47), apart from the rapid Josephson oscillations corresponding to Josephson coupling across the domains, an additional much longer period oscillation appears at 45º and 225 º (marked with white dotted line domes) which corresponds to the Josephson coupling across the domain wall (which as shown in Figure 3.44 it is at 45º with the wire). Making use of the junction area defined by **w=30nm x h=30nm** (with **h** the typical size of the domain wall in LSMO) and considering that the Josephson junction between SC bridges and between LSMO domains are in parallel, the Fraunhofer pattern results from the sum of two parallel contributions as noted in the previous equation.

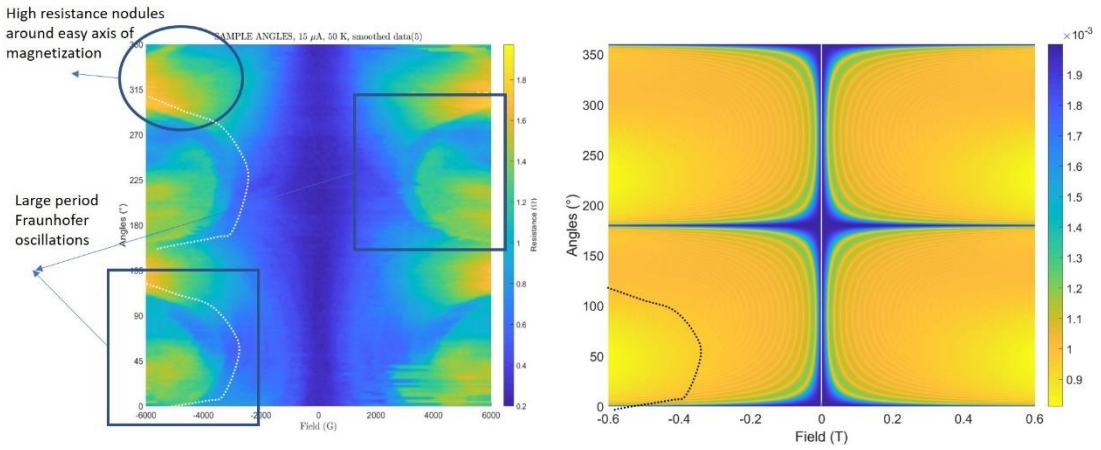

Figure 3.47: Fraunhofer pattern for higher fields. A clear oscillation can be seen at 45 and 225 degrees, corresponding to the domain wall Josephson junction. A simulation of the system agrees with the measurement almost perfectly.

We also observe high resistance states around the easy magnetization axes at 135º and 315 º. This can be due to the saturated magnetization on both bulk and interface of the LSMO, which prevents the formation of spin-triplets. Alternatively, it can be due to a modified domain pattern in the wire, triggered by magnetic field rotation, due to its biaxial magnetic anisotropy.

In this way with the magnetic field applied in plane, both Fraunhofer resistance oscillations are measured, and compatible with both Josephson junctions, one between YBCO microwires and the other one between LSMO superconducting domains. But this must be confirmed also by the measurements with the out of plane magnetic field.

For the out of plane magnetic field measurement, we have again two Josephson junctions, but with different dimensions than before (Figure 3.48):

- The junction (1) (between YBCO banks) will show minima of the Fraunhofer patterns separated by a very small (4 Oe) period due to the large section.
- Junction (2) (between domain walls) will display minima separated 600 Oe. I.e., the critical current of junction (1) will be strongly suppressed as compared to junction (2), which is being observed experimentally (both junctions are in parallel).

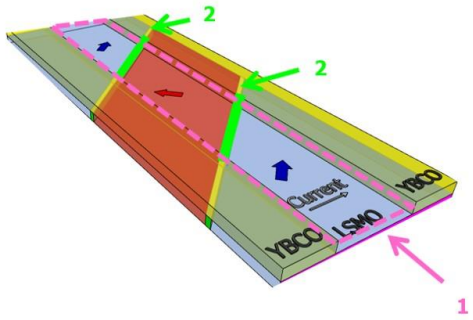

Figure 3.48: Sketch of the two Josephson junctions in the device when the magnetic field is applied out of plane.

In Figure 3.49 (a) we show the resistance vs. applied out of plane magnetic field swept between -3800 Oe and 3800 Oe in an hysteresis loop sequence. Above 70 K magnetoresistance (MR) is featureless in this scale, but below this temperature an oscillating behavior emerges reminiscent of an hysteretic Fraunhofer pattern. Below 50 K zero resistance is reached at low fields and shorter period oscillations show up. We have a MR minimum at positive magnetic field when

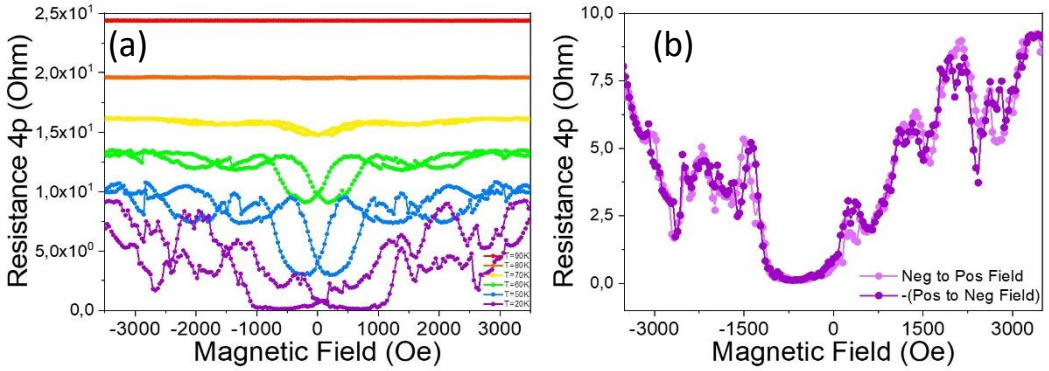

Figure 3.49: (a) Resistance vs Applied Field for different temperatures. We observe oscillations similar to a Fraunhofer pattern below Tc, and an additional shorter period oscillation at lower temperatures. (b) RH at 20K where a perfect hysteretic behavior is observed (the positive-to-negative field sweep has been mirrored to assess hysteresis).

approaching from positive fields and another minimum MR at negative fields when approaching from negative fields, possibly due to Meissner currents. It is important to notice that mirrored magnetoresistance curves (for example corresponding to up to down magnetic field sweeps) almost perfectly match the corresponding down to up sweeps. This demonstrates that the short period oscillations do not result from noise Figure 3.49 (b). The simultaneous hysteresis and Fraunhofer-like features reinforce the scenario of a ferromagnetic superconductor weakly coupling the two superconducting bridges.

Looking at these oscillations the next step is to measure the critical current as a function of the magnetic field to confirm there is a Fraunhofer pattern. To do so we have measured IV curves as a function of out of plane magnetic field (swept in an hysteresis loop sequence) at fixed temperatures. Figure 3.50 (a) (b) display contour plots with full IV curves measured at each 25 Oe step when magnetic field is ramped from negative to positive (Figure 3.50 (a)) and from positive to negative (Figure 3.50 (b)). Temperature of the experiment was 20 K. Voltages range between $+10^{-6}$ and $+3{\cdot}10^{-4}$ V from bottom to top. The white curve in both plots correspond to a voltage of 10^{-5} V and can be taken as a good estimate of the critical current. Notice that both sets of curves display the characteristic features of a Fraunhofer pattern with a somewhat

irregular oscillation pattern probably resulting from the superposition of long and short period oscillations (see magnetoresistance curves at low temperatures). An estimate of the oscillation period of the Fraunhofer pattern of 600 Oe yields a length scale of 30 nm assuming that the other dimension of the junction is 1.2 micron. The 30 nm corresponds to the width of the domain wall between different magnetic domains in LSMO, the junction (2) in Figure 3.48. Triplets crossing the domain wall have to change phase, thus giving a phase difference (weak link) between magnetic domains**.** The fact that we cannot see the oscillation due to the junction (1) in Figure 3.48 is due to the small period of those oscillations. Also, because the junctions are in parallel, the coupling between domains in LSMO dominates due to its higher critical current. These estimates agree well with the junction dimensions estimated previously with the magnetic field in plane, confirming that both Fraunhofer patterns, in plane and out of plane, originate at the same junctions.

Hence, we have found and probed correct a proximity effect generated by triplet correlations in a half-metal as LSMO.

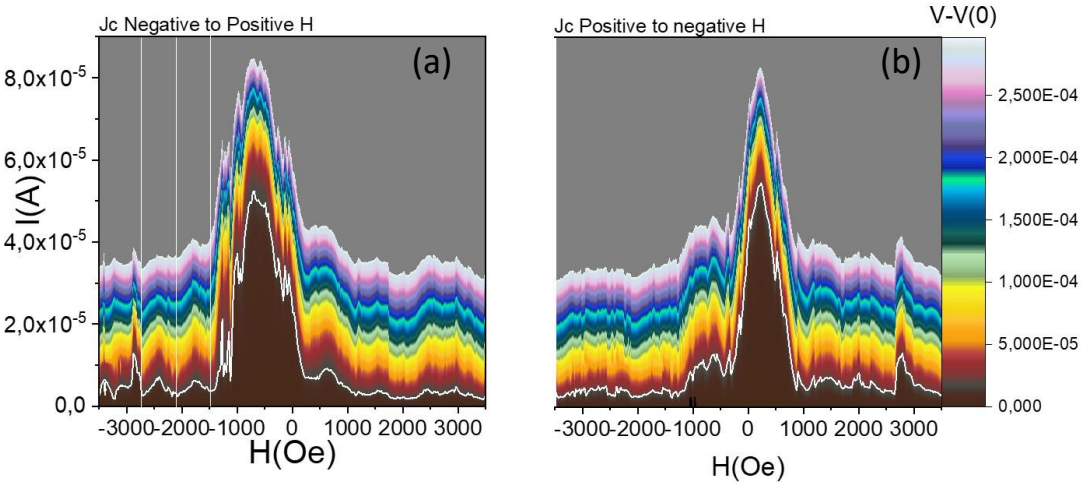

Figure 3.50: Contour plot of the IVH curve. The white line represents Voltage=10^{-5} V. White vertical lines are located at the minima of the Fraunhofer pattern, giving a period of 600 Oe. In (a) the field is swept from negative to positive and in (b) from positive to negative values of magnetic field.

3.4.3 SINGLE JUNCTION SAMPLE LSM139A1+ALO+YBCO

The finding of a superconducting proximity effect in half-metallic weak link is an extraordinary new result which unearths a lot of unexplored scenarios. Some of them are illustrated in the case of sample LSM139A1+ALO+YBCO.

The resistance curve in zero magnetic field is displayed in Figure 3.36 (green curve), but for clarity it is displayed separately in Figure 3.51 (a). The IV (Figure 3.51 (b)) curves show again the emergence of a critical current growing when temperature is reduced. In this sample the contact resistance was too high, and hence the range in current we could apply without producing sample heating extended only till only 50 uA, a smaller range than in previous samples.

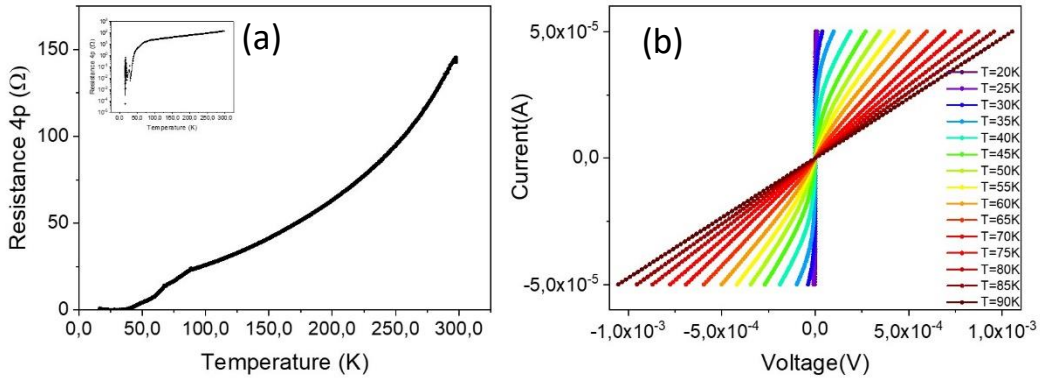

Figure 3.51: Resistance curves and current – voltage IV curves at different temperatures. Both measurements illustrate that the LSMO weak link becomes superconductive.

In this sample, differently to the previous ones, the shape of magnetoresistance curves with field applied out of plane changed substantially when the direction of the current was reversed. In Figure 3.52 we compare magnetoresistance measurements in this sample and in the previous one. In the first sample, the RH curve is hysteretic with the applied magnetic field, i.e., it is not the same to start at positive field than at negative fields (pos to neg meaning starting at positive field and ending at negative field and vice versa). Also, in this sample there is almost no difference between measuring with positive current (R+ meaning resistance for positive current) or negative current (R- meaning resistance for negative current). On the contrary, for sample LS139A2+ALO+YBCO there is almost no change when the direction of magnetic sweeps is reversed (from positive to negative or from negative to positive fields). But, surprisingly, a large difference is observed when we reverse current direction. A very important observation is that if we had measured the magnetoresistance in the usual way (averaging measurements with positive and negative currents to correct for thermoelectric voltages) we would have erroneously ascribed the effect to magnetic hysteresis. This is interesting form of ratchet effect

in this sample, could result from asymmetric pinning of superconducting vortices on the LSMO, or to more exotic scenarios such as topological superconductivity [48–50].

Magnetoresistance measurements at different temperatures showed that this effect occurs at all temperatures below the critical temperature of LSMO in this sample (T=45K). Most importantly, we discover that this effect results from concurrent current hysteresis and magnetic field hysteresis. This means that the shape of the magnetoresistance curve is invariant in sweeps with positive current (R+) where magnetic field goes from positive fields to negative fields (pos to neg) and in sweeps with negative current (R-) where magnetic field goes from negative fields to positive fields (neg to pos). This is illustrated in Figure 3.53. The fact that there is both magnetic and current hysteresis supports both the possibilities of a topological effect and an effect due to the domain structure.

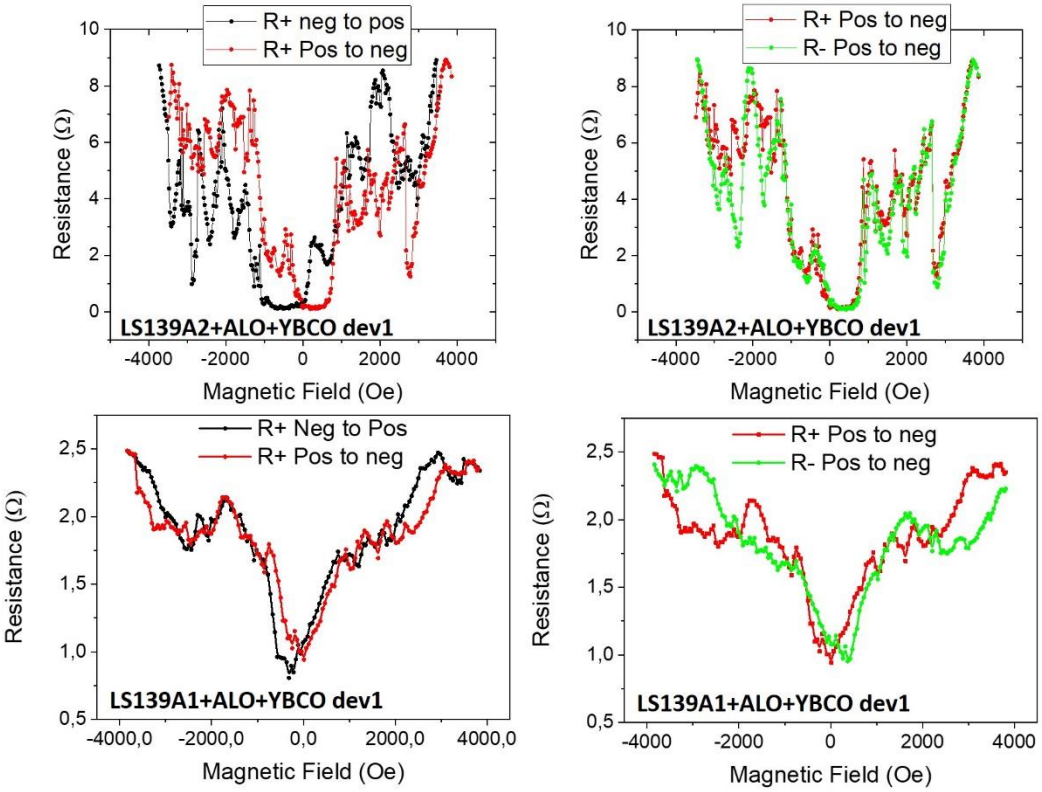

Figure 3.52: Magnetoresistance out of plane curves for different samples with superconductor/half-metal proximity effect. For device 1 in sample LS139A2 there is magnetic hysteresis, but for device 1 in sample LS139A1 the hysteresis results when current direction is reversed.

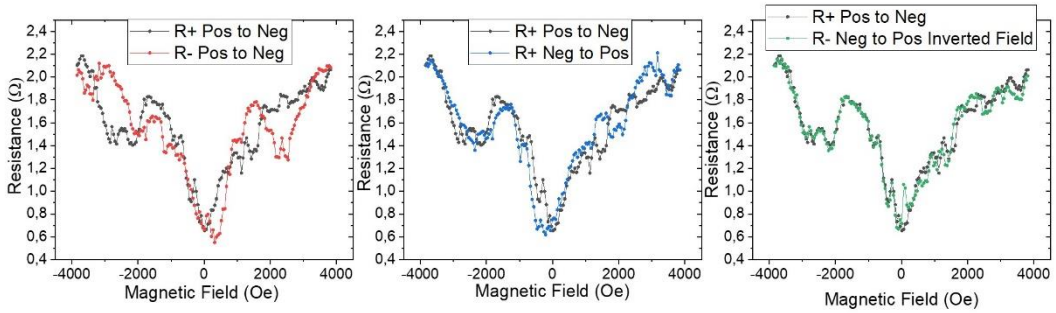

Figure 3.53: Magnetoresistance out of plane at T=35K. It can be clearly seen that the hysteresis is both due to the current and the magnetic field, as to recover the same curve R+ Pos to Neg, we have to invert both the direction of the current and the field.

We examined the occurrence of the effect with in plane magnetic fields, and as in the previous measurements, we also observed both current and magnetic hysteresis. But in this case, current hysteresis was more pronounced than in the out of plane measurement (Figure 3.54). This may indicate an effect of the interaction between vortex and antivortex present in the magnetic domain walls in LSMO. The direction of motion of vortex and antivortex is opposite for a given current direction. One interesting possibility is that the ratio vortex/antivortex at domain walls depends on the magnetic history of the material. In Bloch-type domain walls the magnetization at domain walls is out of plane and could, in principle, equally point up (vortex) or down (antivortex). Magnetic history may cause an imbalance in the vortex/antivortex ratio, which manifests in changes in dissipation when current direction is reversed. This effect could cause the current hysteresis which summed to the magnetic hysteresis due to the magnetism of LSMO would explain the observed behavior. One possible way to examine this possibility this is to cooldown the sample with an applied out of plane magnetic field, not large enough to release magnetization from the plane of the layer but possibly large enough to favor one magnetic field orientation at the domain wall. This may favour vortex over antivortex (or the opposite) at the domain wall. This is the observed behavior with out of plane field, as illustrated in Figure 3.55.

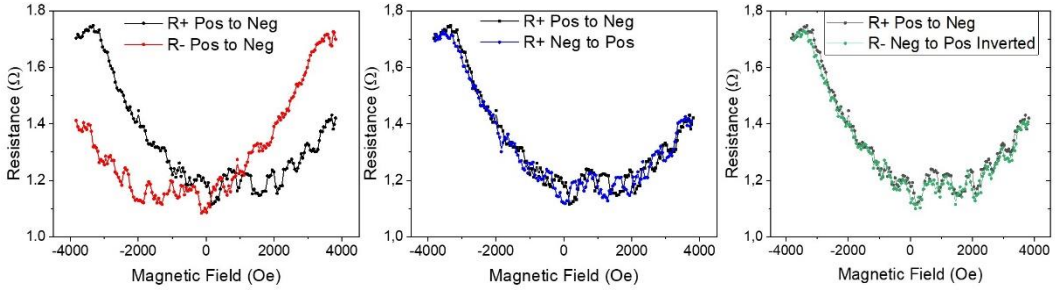

Figure 3.54: Magnetoresistance with the field applied in plane at T=25K. It can be clearly seen that the hysteresis is both due to the current and the magnetic field, as to recover the same curve R+ Pos to Neg, we have to invert both the direction of the current and the field. In this case the current hysteresis is much larger than with the field out of plane.

In the case of zero field cooling magnetoresistance curves are symmetrical for positive and negative current (left panel in Figure 3.55). In this case there is the same number of vortex and antivortex. Now, if we cooldown under a positive field an asymmetry appears (central panel in Figure 3.55) which reverses when the direction of the cooling field is reversed (right panel in Figure 3.55). The (imprint) effect of the cooling field demonstrates that magnetic history is crucial for the observation of the anomalous current hysteresis. This may be, as discussed, due to an imbalance between vortices and antivortices at the domain wall or to chiral magnetic field

structure of the domain wall which may result from the topological nature of the induced superconductivity in the LSMO. This surprising new effect calls for further theoretical investigation in the next future. But, for time constraints it is beyond the scope of the present dissertation.

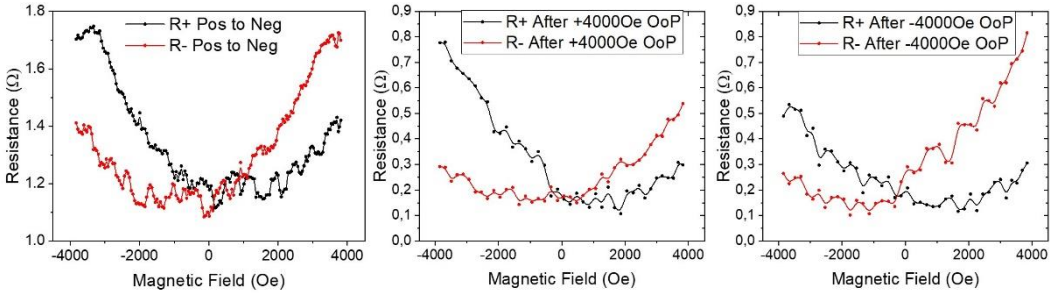

Figure 3.55: Difference in hysteresis upon: zero field cooling (right panel), +4000Oe applied out of plane (central panel) and -4000Oe applied out of plane (right panel).

3.4.4 PLANAR JUNCTIONS CONCLUSIONS

We have found compelling evidence for an extremely long range proximity effect in a half-metal LSMO weak links between unconventional superconducting YBCO banks. Josephson coupling has been unambiguously demonstrated in planar junctions which, in addition to large critical currents and, quite remarkably, display the hallmarks of Josephson physics: i) critical current oscillations driven by magnetic flux quantization; and ii) quantum phase locking effects under microwave excitation (Shapiro steps). The latter, unreported in the context of induced triplet superconductivity, display here an anomalous doubling of the Josephson frequency predicted by several theories. In addition to its fundamental interest, the marriage between high temperature, dissipation-less, quantum coherent transport and full spin polarization brings unique opportunities for the practical realization of novel superconducting spintronics concepts, and signals a path for novel strategies in quantum computing.

3.5 CONCLUSIONS

The demonstration of extremely long-range (micrometric) triplet Josephson coupling between high-temperature d-wave superconducting electrodes across a half-metallic ferromagnets is important at various levels. Fundamentally, it brings up various questions, for instance which is the mechanism governing the singlet to triplet conversion (especially considering the planar geometry), or what the induced pairing symmetry in the LSMO is, i.e. whether nodal pairing is preserved or more likely a conversion into s-wave occurs [51]. Also, the present findings have much relevance in the field of superconducting spintronics. This is because the gathering of i) the very high temperature (tens of K) for which triplet Josephson current is observed ii) the very, long micrometric distance over which phase coherence is preserved in the half-metal in a planar device. Moreover, the fact that triplet supercurrents are necessarily fully spin polarized in a half metal, and that both ac and dc Josephson effects are demonstrated for the first time opens

unprecedented opportunities as they pave the way to novel logic gates, full superconducting switches, nonvolatile random access memories [27] and quantum computing. Furthermore, the half-metallic Josephson junctions should reveal an anomalous Josephson effect with a non-zero phase difference φ_0 at the ground state, which is determined by the mutual orientation of the magnetization in the half-metal and interface magnetizations [28,52–54]. Such unusual φ_0 junction could serve as an important building block of "quiet qubit" [55] and may provide a unique mechanism of direct coupling between magnetism and phase dynamics in Josephson junctions [56].

3.6 REFERENCES

[1] F. S. Bergeret, A. F. Volkov, and K. B. Efetov, Phys. Rev. Lett. **86**, 4096 (2001).

[2] M. Eschrig, J. Kopu, J. C. Cuevas, and G. Schön, Phys. Rev. Lett. **90**, 4 (2003).

[3] R. S. Keizer, S. T. B. Goennenwein, T. M. Klapwijk, G. Miao, G. Xiao, and A. Gupta, Nature **439**, 825 (2006).

[4] M. S. Anwar, F. Czeschka, M. Hesselberth, M. Porcu, and J. Aarts, Phys. Rev. B - Condens. Matter Mater. Phys. **82**, 2 (2010).

[5] J. W. A Robinson, J. D. S Witt, and M. G. Blamire, Science (80-.). **329**, 59 (2010).

[6] D. Aoki and Jaques Flouquet, J. Appl. Phys. **81**, 1 (2012).

[7] V. S. Stolyarov, I. S. Veshchunov, S. Y. Grebenchuk, D. S. Baranov, I. A. Golovchanskiy, A. G. Shishkin, N. Zhou, Z. Shi, X. Xu, S. Pyon, Y. Sun, W. Jiao, G.-H. Cao, L. Y. Vinnikov, A. A. Golubov, T. Tamegai, A. I. Buzdin, and D. Roditchev, Sci. Adv. **4**, eaat1061 (2018).

[8] M. Eschrig and T. Löfwander, Nat. Phys. **4**, 138 (2008).

[9] F. S. Bergeret, A. F. Volkov, and K. B. Efetov, Rev. Mod. Phys. **77**, 1321 (2005).

[10] F. S. Bergeret and I. V. Tokatly, Phys. Rev. Lett. **110**, 1 (2013).

[11] K. Dybko, K. Werner-Malento, P. Aleshkevych, M. Wojcik, M. Sawicki, and P. Przyslupski, Phys. Rev. B - Condens. Matter Mater. Phys. **80**, 0 (2009).

[12] Z. Sefrioui, D. Arias, V. Peña, J. E. Villegas, M. Varela, P. Prieto, C. León, J. L. Martinez, and J. Santamaria, Phys. Rev. B - Condens. Matter Mater. Phys. **67**, 4 (2003).

[13] Y. Kalcheim, T. Kirzhner, G. Koren, and O. Millo, Phys. Rev. B - Condens. Matter Mater. Phys. **83**, 2 (2011).

[14] F. S. Bergeret, A. F. Volkov, and K. B. Efetov, Rev. Mod. Phys. **77**, 1321 (2005).

[15] Y. V. Fominov, A. F. Volkov, and K. B. Efetov, Phys. Rev. B - Condens. Matter Mater. Phys. **75**, 104509 (2007).

[16] B. Crouzy, S. Tollis, and D. A. Ivanov, Phys. Rev. B - Condens. Matter Mater. Phys. **76**, 134502 (2007).

[17] M. Houzet and A. I. Buzdin, Phys. Rev. B - Condens. Matter Mater. Phys. **76**, 1 (2007).

[18] I. B. Sperstad, J. Linder, and A. Sudbø, Phys. Rev. B - Condens. Matter Mater. Phys. **78**,

104509 (2008).

[19] A. F. Volkov and K. B. Efetov, Phys. Rev. B - Condens. Matter Mater. Phys. **78**, 024519 (2008).

[20] K. Halterman, O. T. Valls, and P. H. Barsic, Phys. Rev. B - Condens. Matter Mater. Phys. **77**, 174511 (2008).

[21] A. I. Buzdin, A. S. Mel'Nikov, and N. G. Pugach, Phys. Rev. B - Condens. Matter Mater. Phys. **83**, 144515 (2011).

[22] J. N. Kupferschmidt and P. W. Brouwer, Phys. Rev. B - Condens. Matter Mater. Phys. **80**, 214537 (2009).

[23] A. S. Mel'Nikov, A. V. Samokhvalov, S. M. Kuznetsova, and A. I. Buzdin, Phys. Rev. Lett. **109**, 237006 (2012).

[24] T. S. Khaire, M. A. Khasawneh, W. P. Pratt, and N. O. Birge, Phys. Rev. Lett. **104**, (2010).

[25] E. C. Gingrich, B. M. Niedzielski, J. A. Glick, Y. Wang, D. L. Miller, R. Loloee, W. P. Pratt, and N. O. Birge, Nat. Phys. **12**, 564 (2016).

[26] J. A. Glick, V. Aguilar, A. B. Gougam, B. M. Niedzielski, E. C. Gingrich, R. Loloee, W. P. Pratt, and N. O. Birge, Sci. Adv. **4**, eaat9457 (2018).

[27] I. V. Vernik, V. V. Bol'Ginov, S. V. Bakurskiy, A. A. Golubov, M. Y. Kupriyanov, V. V. Ryazanov, and O. A. Mukhanov, IEEE Trans. Appl. Supercond. **23**, 1701208 (2013).

[28] M. Eschrig and T. Löfwander, Nat. Phys. **4**, 138 (2008).

[29] S. Voltan, A. Singh, and J. Aarts, Phys. Rev. B **94**, 054503 (2016).

[30] Z. Sefrioui, D. Arias, V. Peña, J. E. Villegas, M. Varela, P. Prieto, C. León, J. L. Martinez, and J. Santamaria, Phys. Rev. B - Condens. Matter Mater. Phys. **67**, 214511 (2003).

[31] Y. Kalcheim, O. Millo, M. Egilmez, J. W. A. Robinson, and M. G. Blamire, **104504**, 1 (2012).

[32] C. Visani, Z. Sefrioui, J. Tornos, C. Leon, J. Briatico, M. Bibes, a. Barthélémy, J. Santamaría, and J. E. Villegas, Nat. Phys. **8**, 539 (2012).

[33] C. Visani, F. Cuellar, A. P??rez-Mu??oz, Z. Sefrioui, C. Le??n, J. Santamar??a, and J. E. Villegas, Phys. Rev. B - Condens. Matter Mater. Phys. **92**, 1 (2015).

[34] M. Egilmez, J. W. A. Robinson, J. L. MacManus-Driscoll, L. Chen, H. Wang, and M. G. Blamire, EPL (Europhysics Lett. **106**, 37003 (2014).

[35] J. M. Rowell, Phys. Rev. Lett. **11**, 200 (1963).

[36] W. L. Rowell, J. M. & McMillan, Phys. Rev. Lett. **16**, 453 (1966).

[37] K. Lahabi, M. Amundsen, J. A. Ouassou, E. Beukers, M. Pleijster, J. Linder, P. Alkemade, and J. Aarts, Nat. Commun. **8**, 1 (2017).

[38] S. Shapiro, Phys. Rev. Lett. **11**, 80 (1963).

[39] W. J. Tomasch, Phys. Rev. Lett. **16**, 16 (1966).

[40] A. Hoffmann, S. G. E. Te Velthuis, Z. Sefrioui, J. Santamaría, M. R. Fitzsimmons, S. Park, and M. Varela, Phys. Rev. B - Condens. Matter Mater. Phys. **72**, 140407 (2005).

[41] J. Salafranca and S. Okamoto, Phys. Rev. Lett. **105**, 256804 (2010).

[42] F. Kronast and S. Valencia Molina, J. Large-Scale Res. Facil. JLSRF **2**, 1 (2016).

[43] H. Sellier, C. Baraduc, F. Lefloch, and R. Calemczuk, Phys. Rev. Lett. **92**, 1 (2004).

[44] V. V. Ryazanov, V. A. Oboznov, A. Y. Rusanov, A. V. Veretennikov, A. A. Golubov, and J. Aarts, Phys. Rev. Lett. **86**, 2427 (2001).

[45] A. Buzdin, Phys. Rev. B - Condens. Matter Mater. Phys. **72**, 1 (2005).

[46] C. Richard, M. Houzet, and J. S. Meyer, Phys. Rev. Lett. **110**, 1 (2013).

[47] M. Houzet, V. Vinokur, and F. Pistolesi, Phys. Rev. B - Condens. Matter Mater. Phys. **72**, 1 (2005).

[48] R. Wakatsuki, Y. Saito, S. Hoshino, Y. M. Itahashi, T. Ideue, M. Ezawa, Y. Iwasa, and N. Nagaosa, Sci. Adv. **3**, e1602390 (2017).

[49] J. E. Villegas, S. Savel'ev, F. Nori, E. M. Gonzalez, J. V. Anguita, R. García, and J. L. Vicent, Science (80-.). **302**, 1188 (2003).

[50] F. Ando, Y. Miyasaka, T. Li, J. Ishizuka, T. Arakawa, Y. Shiota, T. Moriyama, Y. Yanase, and T. Ono, Nature **584**, 373 (2020).

[51] A. F. Volkov and K. Efetov, Phys. Rev. Lett. **102**, 077002 (2009).

[52] V. Braude and Y. V. Nazarov, Phys. Rev. Lett. **98**, 077003 (2007).

[53] M. Eschrig, A. Cottet, W. Belzig, and J. Linder, New J. Phys **17**, 83037 (2015).

[54] S. Mironov and A. Buzdin, Phys. Rev. B - Condens. Matter Mater. Phys. **92**, 184506 (2015).

[55] L. B. Ioffe, V. B. Geshkenbein, M. V Feigel'man, A. L. Fauchère, and G. Blatter, Nature **398**, 679 (1999).

[56] S. Mironov, H. Meng, and A. Buzdin, Appl. Phys. Lett. **116**, 162601 (2020).

Chapter 4: Proximity effect in Superconductor/Ferromagnet structures studied by Ferromagnetic Resonance

4.1. MOTIVATION AND OBJECTIVES

The main objective of this thesis is to study the proximity effect between superconductors and ferromagnets, and to explore new avenues towards future superconducting spintronics using oxides materials such as high Tc superconductors and half-metallic ferromagnets. The possibility to inject a spin angular momentum into superconductors is under an intense research activity in the field of superconducting spintronics, as it may open the possibility to eliminate heating effects limiting the feasibility of many spintronic devices

Spin injection into superconductors constitutes a very active research topic within the field of superconducting spintronics. This aims at addressing some of the limitations of classical spintronics (e.g those associated to Joule heating and usually short spin lifetimes in normal metals) as well as at expanding its functionalities, by exploiting the dissipationless electron transport and quantum coherence characteristic of superconductivity [1–5].

Theory and experiments have shown that spin currents can flow into s-wave superconductors carried by equal-spin triplet Cooper pairs [1,2,6–9] or by superconducting quasiparticles [10,11], whose lifetime can exceed those of spin-polarized electrons in the normal state [12–16]. Spin-polarized quasiparticles can be efficiently injected into the superconductor (S) using an adjacent ferromagnet (F) by applying across the S/F interface a bias voltage that exceeds the superconducting gap [10,17]. This mechanism has been extensively explored in transport experiments with spin valves [13,18–21]. Another mechanism for inducing spin accumulation in superconductors is spin-pumping [22] by the resonant precession of the ferromagnet's magnetization [23,24], induced for example by microwave excitation. In these ferromagnetic resonance (FMR) experiments, the superconductor's efficiency as a spin-sink is evaluated via spin hall effect [25] or microwave absorption measurements [8,25–28], by monitoring the evolution of the resonant peak linewidth across the superconducting transition. The assumption is that the changes in the magnetic damping (which lead to a narrowing/broadening of the linewidth [23,24]) reflect variations in the spin absorption when the superconducting gap opens, because this alters both the spin transmittivity across the superconductor/ferromagnet interface and the relaxation mechanisms. Pioneering experiments performed on $Ni_{80}Fe_{20}$/Nb (Py/Nb) bilayers found that the opening of the superconducting gap induces a sharp FMR linewidth narrowing below the critical temperature T_C [26]. This was explained by considering that the opening of the superconducting gap leads to a vanishing electronic density of states at the Fermi level, thereby hindering the absorption of spin polarized electrons. More recent work

on GdN (F) / NbN (S) multilayers has found a different behavior, in which the Gilbert damping initially peaks across the superconducting transition, and diminishes below the normal-state value upon further temperature decrease [29]. That behavior was associated to the presence of impurity spin-orbit scattering at the interface [30]. In contrast to the two examples above, studies carried out on Py/Nb multilayers with an adjacent strong spin-orbit coupling metal (Pt) found a steady broadening of the linewidth below T_C, which was interpreted in terms of enhanced spin transport across the superconductor due to the generation of equal-spin triplet superconductivity [7,8]. The strikingly different behaviors observed in these experiments illustrate the complexity of the underlying physics, and the fact that the predominance of different microscopic mechanisms strongly depends on the interfacial properties. Interestingly, all those examples also evidence that superconductivity may be exploited for tuning magnetization dynamics.

The experiments discussed so far are based on conventional (low-T_C) s-wave superconductors, which present an isotropic superconducting gap. In contrast, in unconventional (high-T_C) d-wave ones the gap is suppressed along particular directions of the momentum space, and there exists a π superconducting-phase shift between d-wave lobes [31–33]. While spin diffusion effects in d-wave superconductors have been discussed in the context of electrical measurements [34–39], to our knowledge no spin-pumping experiments similar to those discussed above have been reported. In particular, whether the onset of superconducting pairing has any effect on the spin-sink behavior of cuprates such as YBCO remains unexplored. Notice that, at variance to s-wave superconductors, the presence of zero-gap nodes should provide channels for injection of spin-polarized electrons at the Femi level even in superconducting state. Consequently, the effects of superconductivity on spin-pumping and magnetization dynamics are expectedly weaker than in the case s-wave superconductors. Despite this, in our experiments with YBCO/Py bilayers we observe a significant linewidth narrowing across the superconducting transition, similar to that observed with Py/Nb s-wave superconductors [26], which suggests that the opening of the d-wave gap significantly suppress spin-pumping. In addition to that, some samples show a steady linewidth broadening upon further temperature decrease below T_C. This broadening is reminiscent of that observed in Py/Nb/Pt multilayers, which was attributed to the generation of equal-spin triplet pairs [7,8]. In all cases, the broadband measurements allow us to univocally ascribe the linewidth changes to variations of the Gilbert damping factor, to exclude any spurious effect related to frequency-independent inhomogeneous broadening, and to conclude that they reflect changes in the spin absorption by the superconductor. These results demonstrate the potential of high-temperature superconductors for manipulating the magnetization dynamics of metallic ferromagnets. On the other hand, they also underline the need for further developing theory that specifically addresses the role of the various mechanisms at play (reduction of the electronic density of states [40], changes in the nonequilibrium spin-imbalance relaxation [41] and dynamic generation of triplet pairs [42,43]) in the context of d-wave superconductivity.

Motivated by the discovery of a proximity effect mediated by triplet pairs in YBCO/LSMO structures, we have also explored ferromagnetic resonance in this system to examine possible changes in the ferromagnetic resonance of the LSMO when the YBCO becomes superconducting. On general grounds we expect a change in the FMR signal due to the spin transmittivity by the triple correlations driving the proximity effect, which should manifest as an increase of damping On the other hand, in absence of proximity effect the damping should decrease due to the blockage of spin transport by the superconducting gap. FMR is thus a simple non-invasive

measurement to get further insight into the generation of triplets in superconductor-ferromagnet systems.

A DC magnetic field H is applied parallel to the sample plane in order to saturate the magnetization of the ferromagnet and the excitation of the spin system is obtained with an RF magnetic field applied perpendicular to the DC field, using a coplanar waveguide. A DC field sweep is performed around the resonance field H_{res}, where the lorentzian dynamical susceptibility of the spin system has a peak. A magnetic field modulation at low frequency (2 kHz) is used to measure the derivative of the absorbed power dP/dH with respect to the DC component of the magnetic field to improve the signal to noise ratio. When the Kittel resonant condition is fulfilled the resonant microwave frequency f and field H_{res} are related according to the Kittel formula [44].

$$\boldsymbol{f = \gamma \mu_0 \sqrt{H_{res}(H_{res} + M_s)}}$$

where γ is the gyromagnetic factor and Ms is the saturation magnetization. For each microwave frequency and temperature, the peak-to-peak linewidth H_{pp} and the resonance field H_{res} were determined by fitting the FMR absorption spectrum to the derivative of a Lorentzian function, as is shown in Fig. (2)(a). For all samples studied the linewidth is well described by the usual linear expression [24],

$$\boldsymbol{\Delta H_{PP} = \frac{2\alpha f}{\sqrt{3}\mu_0 \gamma} + \Delta H_0}$$

where $\boldsymbol{\Delta H_0}$ is the frequency-independent contribution or inhomogeneous broadening and α is the Gilbert damping factor.

In Figure 4.1 a typical ferromagnetic resonance signal is displayed together with a fit to the line shape. Middle and right panels illustrate data analysis to extract damping parameters using Kittel formula and modifications of the line width due to magnetic inhomogeneities.

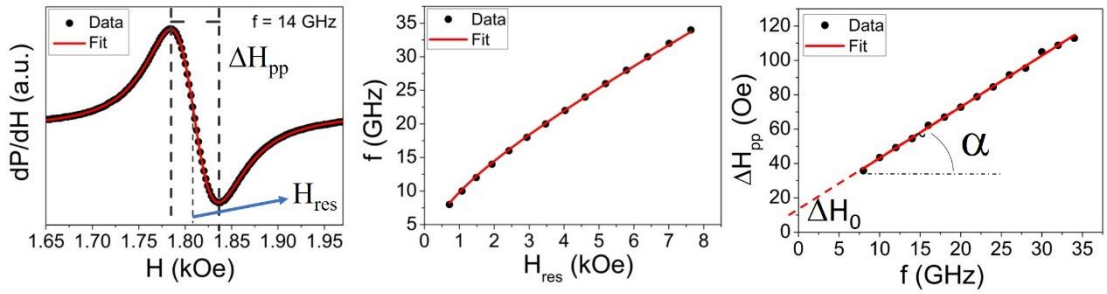

Figure 4.1: FMR data analysis. Measurement of the resonance yields resonant field and the linewidth, fit of the resonance frequency dependence on the resonant field using Kittel formula, and fitting of the damping with the linewidth and frequency.

4.2. PERMALLOY/YBCO STRUCTURES

The goal of this section of the thesis has been to study the change of the damping constant (α) in different Superconductor/Ferromagnet structures to observe the signatures of a superconducting proximity effect, mediated by triplet Cooper pairing. We have used permalloy as ferromagnetic layer, always covered by a thin (3 nm) layer of aluminum to prevent surface

oxidation. As superconductor, YBCO has been used, with a critical temperature of 87K. PBCO has been used to substitute the YBCO as non-superconducting material for control samples. In most samples an Au interlayer between the permalloy and the oxide (PBCO, YBCO or STO) has been added also, to prevent oxidation of the permalloy at the interface. This Au interlayer does not affect the measurements because the spin diffusion length of Au (50 nm at 10 K) is larger than the interlayer thickness and spin polarized electrons can flow through the conducting spacer with almost no interaction. This interlayer, on the other hand, could assist the generation of triplet Cooper pairing, due to its large spin-orbit coupling. Also, two different substrates have been used: STO and NGO, to assess possible effects of epitaxial strain in the measurements. Typical sample stacking was: Substrate//SC/Au/Py/Al. Control samples were prepared where the SC was eliminated or substituted by $PrBa_2Cu_3O_7$ (PBCO), a material with the same crystalline structure as the YBCO and similar lattice constant but with a semiconducting groundstate. In Figure 4.2 measurements of the damping of the different control samples are displayed. For both samples of Py on the bare substrate damping is temperature independent. In the case of

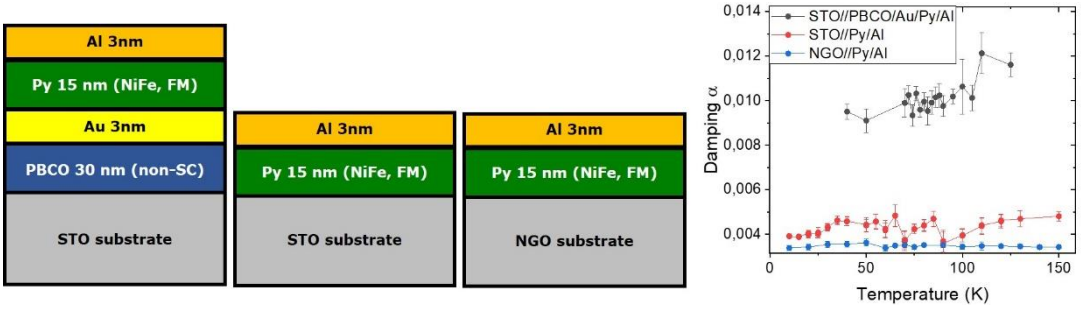

Figure 4.2: Control samples for the experiment with YBCO. In neither of the three samples a change is observed close to the critical temperature of the YBCO T=87K. This proves that any change observed when YBCO is incorporated has to be due to its superconducting state.

the PBCO sample a higher damping value are observed, though also rather temperature independent. Increased damping in this system may result from an additional spin relaxation mechanism, the spin-pumping into the PBCO.

4.2.1. STRAIN AND OXIDATION EFFECT

In this thesis we have focused on oxide materials due to their very different electronic groundstates (high Tc superconductivity, half metallic ferromagnetism, large spin-orbit coupling, etc.). There are however counterparts related to the interfacial interaction with non-oxide materials. When an oxide is put into contact with a non-oxide material, the latter frequently tends to oxidize. In this process, the loss oxygen changes carrier concentration, a parameter critically controlling the rich phase diagram of this materials and hence the properties, which are closely related to the oxygen content with multiple electronic responses.

All the selected oxides have a perovskite structure and were grown on STO or $NdGaO_3$ (NGO). Specifically, the YBCO has in plane lattice parameters of a: 3.807Å and b: 3,882Å, meanwhile STO has a parameter of 3,905Å and the NGO (in the (110) plane, the orientation used to grow the sample, a lattice parameter of 3,86Å). Notice then the lower epitaxial mismatch in the case of the NGO substrates.

In this section we have studied how strain and interface oxidation affect ferromagnetic resonance by looking at the inhomogeneous broadening (ΔH_0), which can be extracted from the damping equation as the intercept (linewidth of the resonance at zero frequency). This parameter supplies information about extrinsic contributions to the damping, as magnetic inhomogeneities or imperfections at the interfaces. One expects larger value of the inhomogeneous broadening for samples without gold, caused by an oxidation of the permalloy in direct contact with the YBCO (or in the case of the control samples, with the PBCO, STO or NGO). Also, we would expect changes between samples with different substrates, as the oxygen could migrate more easily in the STO samples due to higher strain. Strain could also influence the interfacial reconstruction between the YBCO (or PBCO) and gold.

It is important to take into account that changes in the inhomogeneous broadening do not imply changes in damping. In our system the more probable origin of inhomogeneities is the interface, with little effect on bulk properties which largely determine the behavior of damping. We have measured a set of samples including both control (the same ones as in Figure 4.2) and final samples (Figure 4.3).

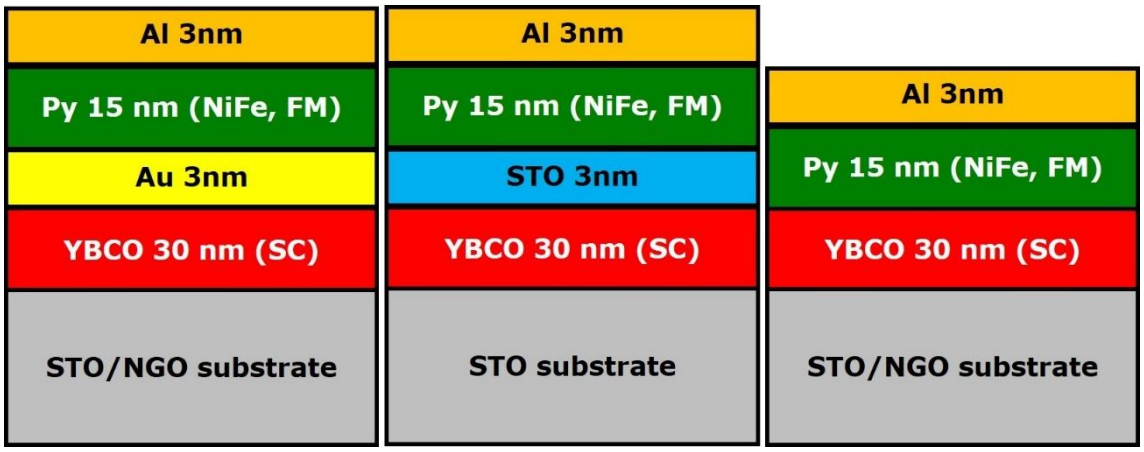

Figure 4.3: Layer sequence of samples with superconducting layer. The inhomogeneous broadening was measured for these samples, together with the ones without YBCO to investigate possible effects due to the oxidation of the permalloy or to strain effects induced by the substrate.

Figure 4.4 displays the data of inhomogeneous broadening for the different samples sketched in Figure 4.3. We can clearly observe large differences between samples with (Figure 4.4(a)) and without (Figure 4.4 (b)) gold. Samples with gold present a constant behavior over all the range of temperature, meanwhile the samples without gold experience an increase in ΔH_0 at low temperatures.

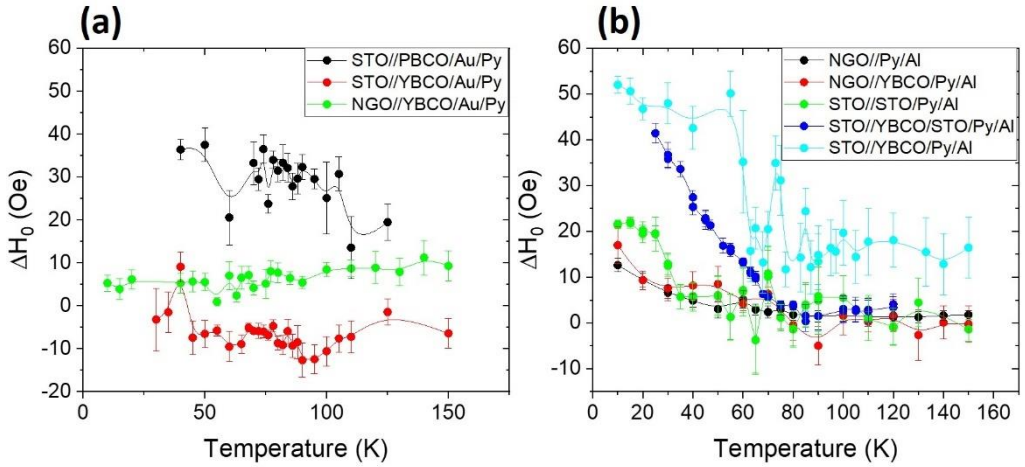

Figure 4.4: (a) Inhomogeneous broadening for samples with gold interlayer and (b) without gold interlayer. Samples were grown both on STO and NGO substrates.

If we look at the samples with gold, we can observe that the substrate has little influence on the ΔH_0. When the PBCO is placed instead of the YBCO we observe an increase of the value, but it still remains constant with temperature. However, there were no pronounced changes of ΔH_0 at the critical temperature of YBCO, meaning that ΔH_0 is not affected by the superconducting state, neither when the YBCO is on STO or on NGO. The gold then acts as a barrier that reduces the inhomogeneities that can be induced in the permalloy (mostly at the interface). Thus, the gold interlayer acts reducing the inhomogeneities probably resulting from the oxidation of the permalloy allowing for the generation and stabilization of triplet pairs [45] (see below).

The samples without gold experience an increase in the ΔH_0 close to YBCO Tc for samples on STO, and around 40K for samples grown on NGO. Comparing these data with the previous ones with gold interlayer we can link the increase of ΔH_0 with the oxidation of the permalloy. Another possibility is that the magnetic inhomogeneity was caused by vortex nucleation when YBCO enters the superconducting state (due to its type-II behavior), but this should affect also the samples with gold. We believe, then, that the most probable effect is the oxidation of the interface. Also, it is clear that the temperature at which the ΔH_0 increase depends on the substrate, so it must be linked to the strain effect of the oxidation of the interface probably due to differences in the oxygen diffusivity for the different strain states. For the samples on STO which has a structural transition close to 100K triggered by antiferrodistortive rotation of oxygen octahedra, the YBCO experiences a higher degree of strain, which probably provokes a higher oxygen diffusivity to the permalloy, even with an STO interlayer between them. Result with the STO interlayer rule out the interesting additional possibility that the magnetic inhomogeneity was (partly) originated by modifications in the domain structure of the ferromagnet driven by proximity to the superconductor (and determined by the tendency to minimize its exchange field at the interface).

On the other hand, the samples on NGO and the Py alone on STO, do not experience high strains nor any structural transition, what might explain that the increase in ΔH_0 is more gradual. The fact that the YBCO/Py on NGO behaves as the Py on STO supports the idea that the it is the strain on the STO//YBCO the main factor affecting ΔH_0. Even though, we observe an increase at low temperatures both in the bare Py on STO and NGO, and in the YBCO/Py on NGO. This increase appears to be intrinsic of the Py, but the fact that it did not appear with a gold interlayer points

towards interface oxidation being its ultimate cause. This phenomenon will be further examined in next sections.

4.2.2. PROXIMITY EFFECT

Having looked at the oxidation and strain effects that can affect our sample, we will examine their effect on the damping which is the parameter which expectedly will be stronger affected by changes in the proximity interaction at the interface. We observe the fingerprints of proximity effect behavior both in samples with Au interlayer and without it (Figure 4.5).

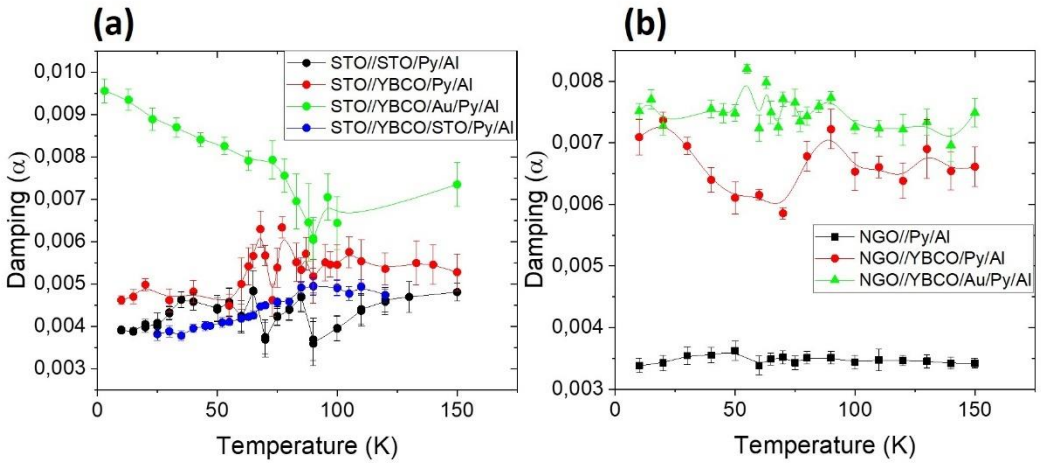

Figure 4.5: Damping for (a) YBCO samples on STO and (b) on NGO. In (a) two control samples are shown with an insulator between the Py and YBCO (blue symbols), and a bare Py layer on STO (black). In (b) both samples with and without gold are plotted in green and red symbols respectively. A control sample of Py on NGO is plotted in black.

For samples on STO (Figure 4.5 (a)) without gold interlayer we observe an almost constant behavior with a decrease in damping below the critical temperature of the superconductor. This could be explained in the case superconductivity is caused only by singlet Cooper pairs in terms of the superconducting gap blocking the spin current which cannot penetrate and relax. But when a gold interlayer is between the superconductor and the permalloy we observe a sharp increase of the damping. This may indicate the generation of triplets at the interface, which offer an additional route for penetration and relaxation of the spin current in the YBCO in the superconducting state producing the noticeable increase in the damping constant displayed in Figure 4.5 (a). When an STO layer is placed instead of the gold, a similar behavior to the one of bare permalloy is found. It turns out that by putting or removing a gold interlayer between the ferromagnet and the superconducting we can tune the effect from a case with singlet Cooper pairing to triplet Cooper pairing, changing drastically the properties of the system. The effect of the Au layer is two-fold in protecting the Py at the interface from oxidation (and the YBCO from degradation from oxygen loss) and promoting the formation of triplets via its strong spin orbit interaction. A simple scheme can be seen in Figure 4.6. It is important to notice that this increase in damping due to triplet formation is highly dependent on the quality of the interface. This is illustrated in Figure 4.7 showing the damping and ΔH_0 of two different YBCO/Py samples ((a, c) without gold and (b, d) with gold) show a decrease in damping. If we compare the sample with gold with

the one of Figure 4.5, we observe a different behavior both in damping and in ΔH_0. The increase in ΔH_0 below Tc could mean that there is more interfacial inhomogeneities which could possibly prevent the generation of spin-triplets.

In the samples on top of NGO (Figure 4.5 (b)) we observe a similar scenario, but not as clear. For both the sample with and without gold interlayer we observe a decrease in the damping close to the critical temperature of YBCO, followed by an increase in its value at lower temperatures. When a gold interlayer is placed between the YBCO and Py, there is no substantial change in the damping below critical temperature, even when the YBCO is superconducting. This could indicate a smaller degree of YBCO deoxygenation in the case of NGO and thus smaller degree of Py oxidation (hence the similar behavior with and without Au interlayer). The increase of damping could indicate to onset of triplet generation.

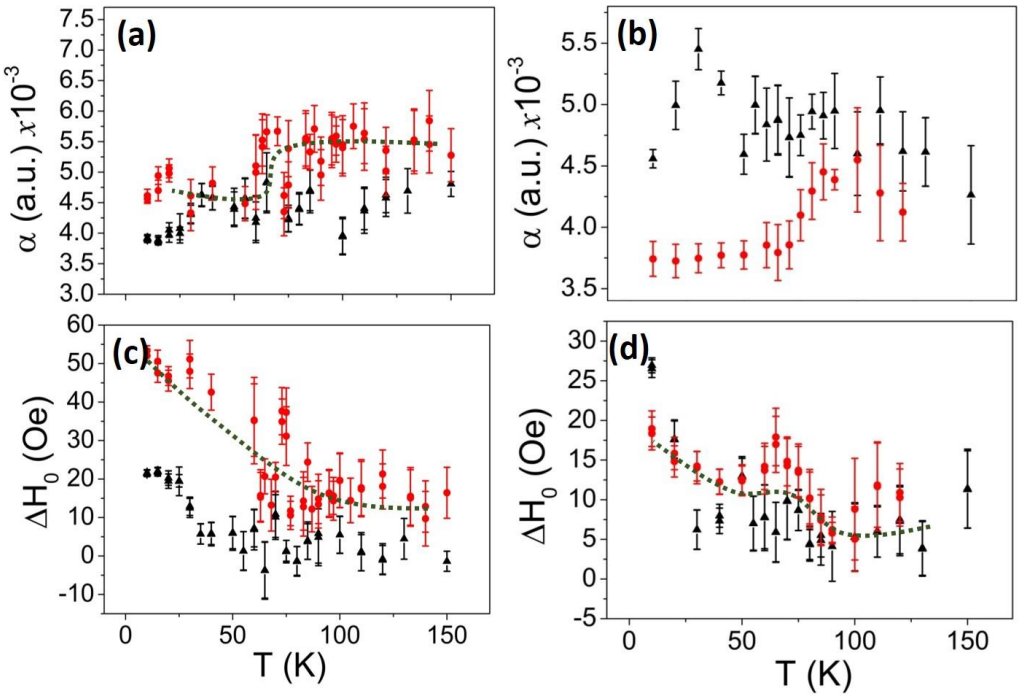

Figure 4.7: Damping and ΔH_0 (bare Py in black and Py/YBCO in red) for additional superconducting samples without (a,c) and with (b,d) gold interlayer, growth on STO. In both samples we observe a decrease in damping close to the critical temperature of YBCO (T=87K). Also, an increase in ΔH_0 is observed.

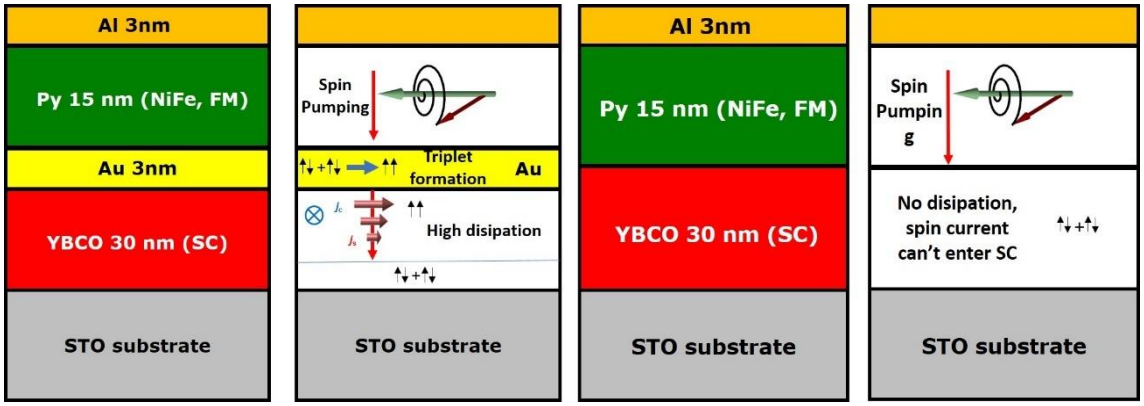

Figure 4.6: When a gold interlayer is placed between the Py and YBCO, not only prevents the oxidation of the Py, but enhances the generation of triplet Cooper pairs.

In the case of samples on NGO the increase in the damping ascribed to triplets is less pronounced indicating that there may other factors affecting proximity interaction. Further experiments will be directed in the future to a better understanding of this scenario.

4.3. PROXIMITY EFFECT IN LSMO/YBCO STRUCTURES

The results of the FMR experiments on Py/YBCO structures have demonstrated the possibility of detecting proximity interactions at the interface but only when there is an interlayer of a material (Au) that protects the ferromagnet from oxidation and which generates the triplet pairs through its strong spin orbit interaction. The next step is then to find a system that can generate and stabilize triplet Cooper pairs by itself. As we have shown in chapter 3 of this thesis, the LSMO/YBCO system meets these conditions. In this case, where we have already demonstrated that triplet Cooper pairing is possible, we would expect an increase in damping below the critical temperature due to the relaxation of the spin current in the superconductor.

In this section we describe two different types of samples in which both the superconductor and the ferromagnet are complex oxides together with their respective control samples (Figure 4.8). First, LSMO/YBCO samples were measured. In this samples the triplet Cooper pairs are generated at the LSMO/YBCO interface, as demonstrated in chapter 3. Different behaviors of the damping constant are expected when temperature is reduced below the superconducting transition. In the case of singlet superconductivity, a decrease in the damping is expected caused by the blocking of the spin current into the superconductor by its superconducting gap. On the other hand, if there is triplet superconductivity, we should observe an increase in damping due to the additional relaxation channel (a triplet spin-supercurrent relaxing to spin-singlets into the superconductor).

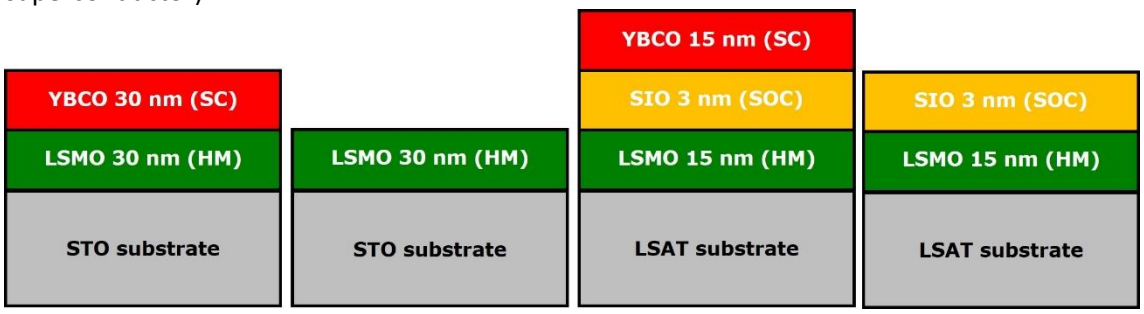

Figure 4.8: Sketches of all oxide samples to measure proximity effect by FMR measurements. LSMO and LSMO/SIO have been used as control samples.

Additionally, we have measured LSMO/SIO/YBCO samples (SIO being $SrIrO_3$, a semimetal oxide with high spin-orbit coupling), to see if the triplet state is enhanced as we saw in the permalloy samples. The SIO has a smaller spin diffusion length than the gold, only 3 nm, which puts it in the limit to affect spin injection due to spin relaxation. This could cause that the spin current could not reach the superconductor, but as we will see in next sections, it can indeed reach it. This case should be similar to the previous one, without SIO, but in this case there could be four scenarios:

- The SIO promotes the formation of triplet-pairs more than in the LSMO/YBCO interface, in which case we should observe a higher increase in damping.

- The SIO promotes the formation of triplet-pairs less than in the LSMO/YBCO interface, which could show as a constant behavior of damping in the superconducting state or a smaller increase in damping compared with previous cases.
- The SIO does not affect the triplets, but because there is no LSMO/YBCO interface, these pairs cannot be created. Then a decrease in the damping should be observed.
- The SIO relaxes all the spin current due to its small spin diffusion length, and there is no change in damping at the critical temperature.

These hypotheses could be easily checked by analyzing the measurements of the samples, but in the practice, several experimental problems occur which greatly difficult extracting clear-cut conclusions. For all samples with YBCO, below critical temperature the FMR signal became difficult to measure, due to the increase of the resonance linewidth. This increase in the linewidth means that the power absorbed (the integral over the absorption signal) is higher, and consequently that there is more relaxation. This effect is particularly important on the LSMO/YBCO samples, in which below 80K no signal could be measured. In the case of LSMO/SIO/YBCO the signal became so distorted that the calculation of damping was not possible. In this case, again, the linewidth was used to analyze the proximity effect.

4.3.1. LSMO/YBCO BILAYERS

For the LSMO/YBCO samples, an STO substrate was used, as in the case of the planar junctions of Chapter 3. Even though there are substrates which exert less strain on the LSMO (as LSAT), STO was used because it worked before in the Josephson junctions. Bare LSMO layers have been widely studied [46–48] and do not show any change in damping across the critical temperature of YBCO (T=87K).

In Figure 4.9 we can observe both the linewidth for 6GHz and the damping constant of LSMO/YBCO bilayers. Looking at the temperature dependence of the line width we observe a dramatic change at the superconducting T_c of the YBCO. A clear change of slope in the linewidth in function of temperature. When the sample is below critical temperature of YBCO, the linewidth starts to increase at a higher rate than before. At 80K we can no longer measure the resonance with accuracy, due to the large linewidth and small signal to noise ratio. The strong

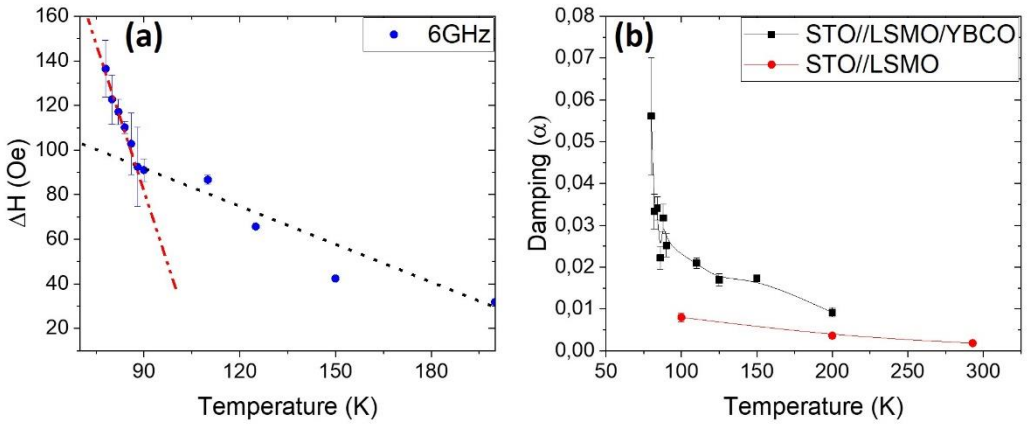

Figure 4.9: (a) Linewidth and (b) damping of LSMO/YBCO samples. In (a) a clear change in the slope of the linewidth is observed at the critical temperature of the YBCO. In (b) a bare LSMO damping is showed, with values of damping comparable to those found in literature.

increase in linewidth may indicate an increase of magnetic inhomogeneity due to changes in the domain structure or an increase of damping consistent with the penetration of the spin supercurrent in the superconductor in the form of triplets which relax into singlets. This would make the superconductor a perfect spin-sink, even more efficient than a normal metal and would be the demonstration of the presence of triplet Cooper pairing in the system.

Another way of looking at the superconducting effect using FMR is by measuring an "FMR hysteresis loop" (Figure 4.10). The superconductor should have magnetic hysteresis if there is a small out of plane field, due to the vortex lattice. This could affect the magnetic properties of the LSMO, or it could affect the formation of triplets and its dissipation. This effect is difficult to measure, as below the critical temperature of YBCO the FMR signal becomes highly inhomogeneous and the linewidth becomes larger. Even though, we could measure the FMR at 5GHz for temperature below Tc. The measurement sequence consists on going to the highest positive magnetic field (5000Oe), measure the resonance from positive to negative fields, going to the highest negative magnetic field (-5000Oe) and measure the resonance from negative to positive fields. Notice that in this way we can measure resonance in the same field range in ascending and descending branches, and if there is any hysteresis effect, we should be able of detecting it. We see that below 85K it begins to appear some differences in the shape of the curve depending on the initial field. This change is related to the superconducting transition, which could affect the magnetic properties of the interface due to the proximity effect. At 70K we start to observe a hysteretic behavior that we could not observe in any of the Py samples. Finally, at 60K we have almost undetectable signal but there is still a clearly observable hysteresis effect. This is a strange hysteresis, as the background signal is also being affected, not

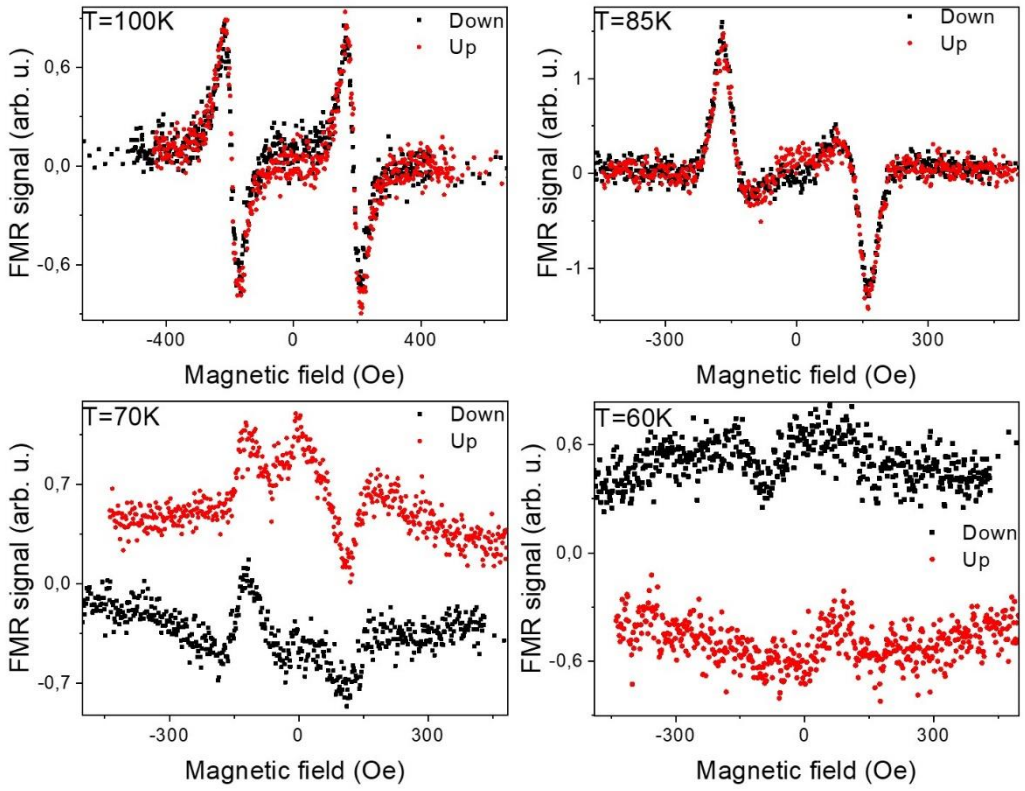

Figure 4.10: FMR hysteresis measurements of LSMO/YBCO bilayers when lowering temperature. Red curve corresponds to a magnetic field sweep from negative to positive values and black curve from positive to negative values. When the critical temperature is crossed, a clear change in the shape of the signal appears which depends hysteretically on the sense of the sweeps.

only the shape of the resonance. This effect could be caused by the absorption of microwaves by the YBCO in the vortex state. Alternatively, it could be related to modifications of the domain state of the ferromagnet due to proximity interactions which are affected by the magnetic history through the effect of magnetic field on the stray field of the domain walls, as discussed in Chapter 3. Further work will be necessary to clarify this point.

4.3.2. LSMO/SIO/YBCO TRILAYERS

The aim in thus section was to reproduce the experiment of YBCO/Au/Py with an all oxide structure, using the LSMO as ferromagnet and the SIO as a large spin-orbit coupling material. We observed in previous sections that when a large spin-orbit material is put between the ferromagnet and the superconductor, it promotes the generation of triplet correlations. It is important to take into account that the process of triplet generation is different in this sample than in the LSMO/YBCO bilayer. In the bilayer triplets are originated at interface. But in LSMO/SIO/YBCO trilayers there is no LSMO/YBCO interface, and the triplets are generated in the SIO due to the high spin-orbit coupling [49]. The main objective of this section is investigating if either process is more or less efficient than the other.

We used LSAT as substrate, to ensure a metallic state in the SIO sample resulting from compressive strain (3nm thick SIO on STO becomes insulating at low temperatures). Also, to assure that any possible change in the FMR signal of the samples is due to the YBCO superconducting state, the same sample has been used in all the process in an ex-situ sequential growth process (Figure 4.8). First, a LSAT//LSMO (15nm)/SIO (3nm) sample was grown and measured from T=151K to T=22K. After all the measurements it was cleaned and 15 nm of YBCO were deposited on top of the LSMO/SIO. As showed in chapter 3, there is no interface degradation in the ex-situ growth, where the high oxygen pressure sputtering at high temperatures (900^{o}C) conditions the surface of the sample, producing clean interfaces without any type of defects. After the growth, the same measurements were performed on the, now, trilayer. Due to the inhomogeneous behavior of the FMR signal for the trilayer, no damping constant could be calculated, hence using the linewidth and shape of the resonance to compare between samples.

The LSMO/SIO sample showed an inhomogeneous behavior while decreasing temperature. It presented two different FMR peaks, which means there is two different bulk components of the magnetization, probably due to the presence of two magnetic easy axis in the LSMO. It did not present any change close to 87K, the critical temperature of the YBCO. On the other hand, the LSMO/SIO/YBCO trilayer had only one FMR peak and showed interesting changes below Tc, as illustrated in Figure 4.11, which compares the LSMO/SIO and LSMO/SIO/YBCO samples.

A clear change in the shape of the curve below the critical temperature (between 82K and 77K) can be identified. This effect is delayed compared with the LSMO/YBCO sample in which the superconducting effect can be measured just below the critical temperature. This can be due in this to the proximity effect caused by the superconductor across the SIO layer. The change in the shape of the resonance becomes clearer when decreasing the temperature. This change, although clearly showing that there is a proximity effect caused by the superconductor, prevents the calculation of a precise resonance linewidth (specially at higher frequencies), and hence the damping. Nevertheless, the fact that the superconductor can produce the observed profound

changes in the absorption properties of the sample points toward the generation of triplet Cooper pairs.

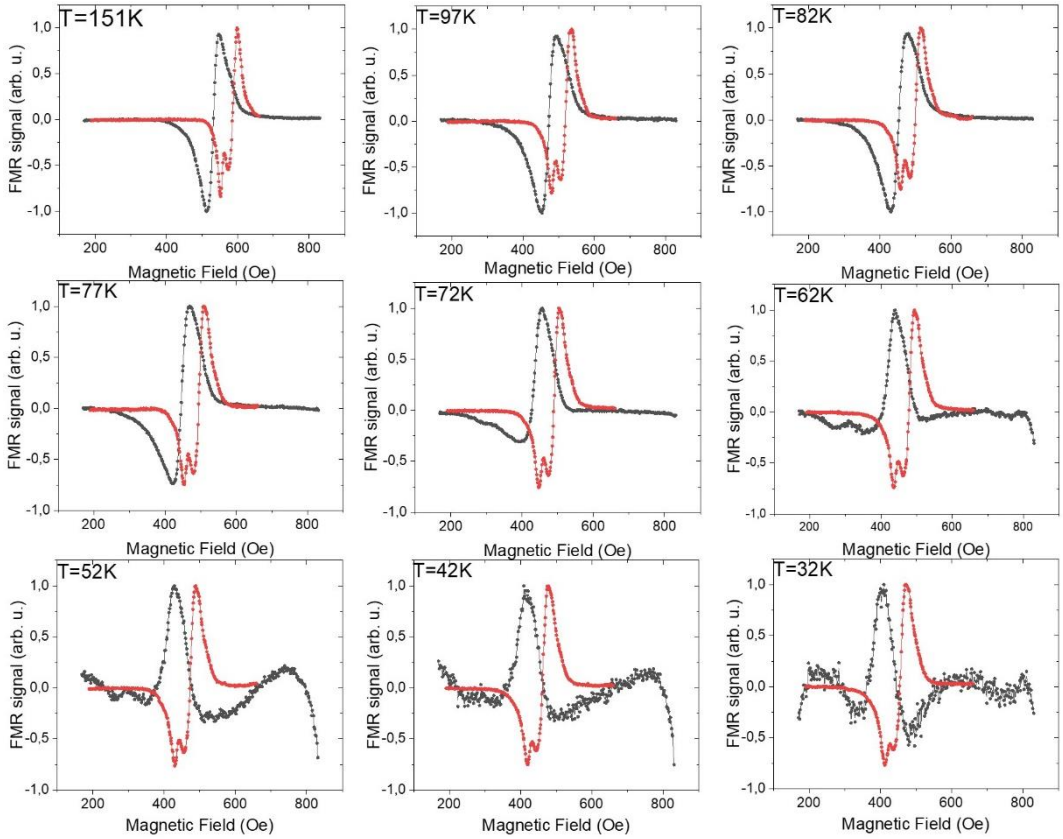

Figure 4.11: Temperature evolution of FMR curves for (black curves) LSMO/SIO/YBCO samples and (red curves) LSMO/SIO samples at 6GHz.

A study of the change in linewidth was also performed to quantitively observe the effect of the superconductor in the resonance. In Figure 4.12 the linewidth and resonant field of both LSMO/SIO and LSMO/SIO/YBCO samples are displayed. Above the superconducting state of the YBCO the behavior is similar for both samples, with both samples showing a steady increase of the linewidth and a decrease of the resonance field. The larger linewidth in samples with YBCO in the normal state can be explained in terms of an increase in the relaxation rate of the spin current when it enters the normal state YBCO. This proves that the spin current does not

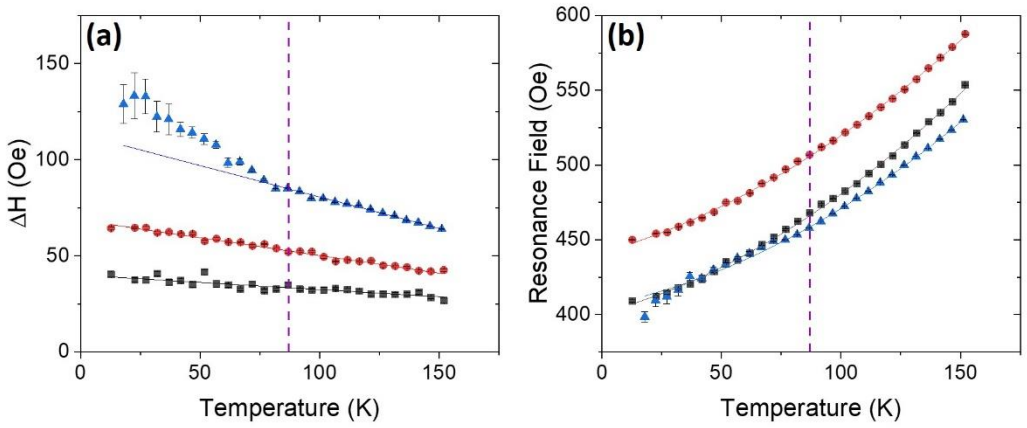

Figure 4.12: (a) Linewidth and (b) resonance field of the samples. In red and black are the first and second resonance of LSMO/SIO, and in blue the resonance of LSMO/SIO/YBCO.

completely relax in the SIO despite the small value of its spin diffusion length, it can pass to the YBCO. Instead, the resonance field of the LSMO/SIO/YBCO is practically the same as the one of the first resonance on LSMO/SIO, indicating that the growth process probably favored one magnetization direction on the sample.

When the critical temperature of the superconductor is reached there is no change in the values of linewidth or resonance field, as there were no changes in the shape of the FMR signal, and it is at 77K when a change in the behavior appears. A clear increase in the linewidth, compared with the sample without YBCO, appears. This increase could be due to the generation of triplet Cooper pairs mediated by the superconducting proximity effect in presence of the strong spin-orbit coupling present in the SIO. An increase in the linewidth is associated with an increase in the absorption of the microwaves, caused by a fast relaxation of the spin current induced by the FMR. In absence of triplet generation, the linewidth could have either decreased, due to the impossibility to inject a spin current into the superconductor; or maintained its as in the normal state. Although a more exhaustive study could be done by extracting the damping constant, the fact that there is a clear superconducting effect that enhance the absorption is a strong indication of the triplet generation. It is worth pointing out that the increase in linewidth below the superconducting Tc could have also resulted from a modification of the domain state in the superconducting state as observed in chapter 3, which in itself is also a strong hint of triplet proximity effect. In fact, the change observed in the resonance field shows that the magnetic structure of the LSMO could be changing due to the proximity effect. However, this change is small compared with the field values that we are measuring, and this slight change could be related to the presence of triplet Cooper pairs or also to the appearance of vortices in the YBCO caused by a small out of plane component of the field. Clarifying this point will require examining the temperature dependence of damping which will be accomplish in new samples in the future.

4.4. CONCLUSIONS

In this chapter we have proven that FMR is a powerful tool to measure proximity effect in superconductor/ferromagnet systems. The fact that there is no need of nano-structuring samples, neither complex processes apart from the sample growth, FMR is a relatively fast technique to study proximity interaction at interfaces.

We found that the opening gap in d-wave superconductor/ferromagnet YBCO/Py multilayers reduces the spin pumping effects and results in a significant damping reduction below the critical temperature. This demonstrates that high-temperature superconductors can be used to efficiently manipulate the magnetization dynamics in S/F hybrids. Incorporating a layer with strong spin orbit material (Au in our case) increases damping what is consistent with a new route of spin relaxation through the generation of triplets and their relaxation into singlets into the superconductor. Also, we have found strong indications of triplet pairs in all oxide structures, both with and without an interlayer of a strong spin-orbit material (SOM). This finding supports the existence of two alternative routes for triplet generation at ferromagnet (FM) /superconductor (SC) oxide interfaces, one driven by magnetization inhomogeneity at bare FM/SC interfaces and the other one mediated by Spin Orbit interaction at FM/SOM/SC interfaces. These results call for further experiments and theoretical studies as they could impact future superconducting spintronics making it more accessible at the high temperatures

of cuprate superconductors and externally manipulable by electric fields due to the tunability of the spin orbit interaction in ultrathin 5d oxides.

4.5. REFERENCES

[1] F. S. Bergeret, A. F. Volkov, and K. B. Efetov, Phys. Rev. Lett. **86**, 4096 (2001).

[2] M. Eschrig, Phys. Today **64**, 43 (2011).

[3] M. G. Blamire and J. W. A. Robinson, J. Phys. Condens. Matter **26**, 453201 (2014).

[4] J. Linder and J. W. A. Robinson, Nat. Phys. **11**, 307 (2015).

[5] M. Eschrig, Reports Prog. Phys. **78**, 104501 (2015).

[6] A. Kadigrobov, R. I. Shekhter, and M. Jonson, Eur. Lett. **54**, 394 (2001).

[7] K.-R. Jeon, C. Ciccarelli, A. J. Ferguson, H. Kurebayashi, L. F. Cohen, X. Montiel, M. Eschrig, J. W. A. Robinson, and M. G. Blamire, Nat. Mater. **17**, 499 (2018).

[8] K.-R. Jeon, C. Ciccarelli, H. Kurebayashi, L. F. Cohen, X. Montiel, M. Eschrig, S. Komori, J. W. A. Robinson, and M. G. Blamire, Phys. Rev. B **99**, 024507 (2019).

[9] F. S. Bergeret, A. F. Volkov, and K. B. Efetov, Rev. Mod. Phys. **77**, 1321 (2005).

[10] S. Takahashi, H. Imamura, and S. Maekawa, Phys. Rev. Lett. **82**, 3911 (1999).

[11] S. Takahashi and S. Maekawa, Phys. Rev. B **67**, 052409 (2003).

[12] N. Poli, J. P. Morten, M. Urech, A. Brataas, D. B. Haviland, and V. Korenivski, Phys. Rev. Lett. **100**, 136601 (2008).

[13] H. Yang, S. H. Yang, S. Takahashi, S. Maekawa, and S. S. P. Parkin, Nat. Mater. **9**, 586 (2010).

[14] H. L. Zhao and S. Hershfield, Phys. Rev. B **52**, 3632 (1995).

[15] S. A. Kivelson and D. S. Rokhsar, Phys. Rev. B **41**, 11693(R) (1990).

[16] C. H. L. Quay, D. Chevallier, C. Bena, and M. Aprili, Nat. Phys. **9**, 84 (2013).

[17] M. Johnson, Appl. Phys. Lett. **65**, 1460 (1994).

[18] A. K. Suszka, F. S. Bergeret, and A. Berger, Phys. Rev. B **85**, 24529 (2012).

[19] T. Wakamura, N. Hasegawa, K. Ohnishi, Y. Niimi, and Y. Otani, Phys. Rev. Lett. **112**, 36602 (2014).

[20] K. Ohnishi, Y. Ono, T. Nomura, and T. Kimura, Sci. Rep. **4**, 6260 (2014).

[21] J. Y. Gu, J. A. Caballero, R. D. Slater, R. Loloee, and W. P. Pratt, Phys. Rev. B **66**, 140507 (2002).

[22] S. Takahashi, in edited by Y. Xu, D. D. Awschalom, and J. Nitta (Springer Netherlands, Dordrecht, 2016), pp. 1445–1480.

[23] E. Landau, Lev Davidovich Lifshitz, Phys. Z. Sowjet. **8**, 153 (1935).

[24] T. L. Gilbert, IEEE Trans. Magn. **40**, 3443 (2004).

[25] K.-R. Jeon, C. Ciccarelli, H. Kurebayashi, J. Wunderlich, L. F. Cohen, S. Komori, J. W. A. Robinson, and M. G. Blamire, Phys. Rev. Appl. **10**, 014029 (2018).

[26] C. Bell, S. Milikisyants, M. Huber, and J. Aarts, Phys. Rev. Lett. **100**, 1 (2008).

[27] K.-R. Jeon, C. Ciccarelli, H. Kurebayashi, L. F. Cohen, S. Komori, J. W. A. Robinson, and M. G. Blamire, Phys. Rev. B **99**, 144503 (2019).

[28] K. R. Jeon, C. Ciccarelli, H. Kurebayashi, L. F. Cohen, X. Montiel, M. Eschrig, T. Wagner, S. Komori, A. Srivastava, J. W. A. Robinson, and M. G. Blamire, Phys. Rev. Appl. **11**, (2019).

[29] Y. Yao, Q. Song, Y. Takamura, J. P. Cascales, W. Yuan, Y. Ma, Y. Yun, X. C. Xie, J. S. Moodera, and W. Han, Phys. Rev. B **97**, 224414 (2018).

[30] M. Inoue, M. Ichioka, and H. Adachi, Phys. Rev. B **96**, 24414 (2017).

[31] Z.-X. Shen, D. S. Dessau, B. O. Wells, D. M. King, W. E. Spicer, A. J. Arko, D. Marshall, L. W. Lombardo, A. Kapitulnik, P. Dickinson, S. Doniach, J. DiCarlo, T. Loeser, and C. H. Park, Phys. Rev. Lett. **70**, 1553 (1993).

[32] H. Aubin, K. Behnia, M. Ribault, R. Gagnon, and L. Taillefer, Phys. Rev. Lett. **78**, 2624 (1997).

[33] J. R. Kirtley, C. C. Tsuei, Ariando, C. J. M. Verwijs, S. Harkema, and H. Hilgenkamp, Nat. Phys. **2**, 190 (2006).

[34] V. Peña, Z. Sefrioui, D. Arias, C. Leon, J. Santamaria, J. L. Martinez, S. G. E. Te Velthuis, and A. Hoffmann, Phys. Rev. Lett. **94**, 057002 (2005).

[35] C. Visani, Z. Sefrioui, J. Tornos, C. Leon, J. Briatico, M. Bibes, A. Barthélémy, J. Santamaría, and J. E. Villegas, Nat. Phys. **8**, 539 (2012).

[36] Z. Sefrioui, D. Arias, V. Peña, J. E. Villegas, M. Varela, P. Prieto, C. León, J. L. Martinez, and J. Santamaria, Phys. Rev. B - Condens. Matter Mater. Phys. **67**, 214511 (2003).

[37] Z. P. Niu and D. Y. Xing, Phys. Rev. Lett. **98**, 57005 (2007).

[38] S. Soltan, J. Albrecht, and H.-U. Habermeier, Phys. Rev. B **70**, 144517 (2004).

[39] N.-C. Yeh, R. P. Vasquez, C. C. Fu, A. V Samoilov, Y. Li, and K. Vakili, Phys. Rev. B **60**, 10522 (1999).

[40] T. T. Heikkilä, M. Silaev, P. Virtanen, and F. S. Bergeret, Prog. Surf. Sci. **94**, 100540 (2019).

[41] F. S. Bergeret, M. Silaev, P. Virtanen, and T. T. Heikkilä, Rev. Mod. Phys. **90**, 41001 (2018).

[42] M. Houzet, Phys. Rev. Lett. **101**, 057009 (2008).

[43] T. Yokoyama and Y. Tserkovnyak, Phys. Rev. B **80**, 104416 (2009).

[44] C. Kittel, Phys. Rev. **73**, 155 (1948).

[45] C. M. Puetter and H.-Y. Kee, EPL (Europhysics Lett. **98**, 27010 (2012).

[46] M. Belmeguenai, S. Mercone, C. Adamo, L. Méchin, M. Belmeguenai, S. Mercone, C. Adamo, L. Méchin, C. Fur, P. Monod, P. Moch, and D. G. Schlom, (2010).

[47] G. Y. Luo, M. Belmeguenai, Y. Roussigné, C. R. Chang, J. G. Lin, and S. M. Chérif, AIP Adv.

5, 097148 (2015).

[48] H. K. Lee, I. Barsukov, A. G. Swartz, B. Kim, L. Yang, H. Y. Hwang, and I. N. Krivorotov, AIP Adv. **6**, 55212 (2016).

[49] F. S. Bergeret and I. V. Tokatly, Phys. Rev. Lett. **110**, 1 (2013).

Chapter 5: Conclusions

In this thesis we have explored the superconducting proximity effect in ferromagnet/superconductor structures combining complex oxide cuprates (YBCO) and manganites (LSMO). We have succeeded in fabricating planar YBCO/LSMO/YBCO microstructures where the superconducting YBCO banks are separated micron distances by a half metallic ferromagnet LSMO using amorphous alumina templates defined by electron beam lithography.

We have found compelling evidence for an extremely long-range proximity effect in the half-metal LSMO weak links induced by the unconventional superconducting YBCO banks. Josephson coupling has been unambiguously demonstrated in planar junctions which, in addition to large critical currents and, quite remarkably, display the hallmarks of Josephson physics: i) critical current oscillations driven by magnetic flux quantization; and ii) quantum phase locking effects under microwave excitation (Shapiro steps). The latter, unreported in the context of induced triplet superconductivity, display here an anomalous doubling of the Josephson frequency predicted by several theories. Long period Fraunhofer oscillation patterns in resistance vs field sweeps have provided strong indications of a completely new triplet Josephson effect driven by the rotation of the magnetization in a Bloch type domain wall in the LSMO. Proposed theoretically[1–7], this is to our knowledge the first experimental evidence of such an effect.

We have proven that FMR is a powerful tool to measure proximity effect in superconductor/ferromagnet systems. The fact that there is no need of nano-structuring samples, neither complex processes apart from the sample growth, FMR is a relatively fast technique to study proximity interaction at interfaces.

We found that the opening gap in d-wave superconductor/ferromagnet YBCO/Py multilayers reduces the spin pumping effects and results in a significant damping reduction below the critical temperature. This demonstrates that high-temperature superconductors can be used to efficiently manipulate the magnetization dynamics in S/F hybrids.

An increase of damping below the superconducting Tc has been found in all oxide YBCO/LSMO structures (showing the long-range proximity effect). This finding constitutes a strong indication of the generation of triplet pairs these structures, providing additional support to the discovery of proximity effect. This enhancement of damping is also found in samples with an interlayer made of strong spin orbit 5d iridate oxide. This supports the existence of two alternative routes for triplet generation at ferromagnet (FM) /superconductor (SC) oxide interfaces, one driven by magnetization inhomogeneity at bare FM/SC interfaces and the other one mediated by Spin Orbit interaction at FM/SOM/SC interfaces. These results call for further experiments and theoretical studies as they could impact future superconducting spintronics making it more accessible at the high temperatures of cuprate superconductors and externally manipulable by electric fields due to the tunability of the spin orbit interaction in ultrathin 5d oxides.

The demonstration of extremely long-range (micrometric) triplet Josephson coupling between high-temperature d-wave superconducting electrodes across a half-metallic ferromagnets is important at various levels. Fundamentally, it brings up various questions, for instance which is

the mechanism governing the singlet to triplet conversion[8–10] (especially considering the planar geometry), or what the induced pairing symmetry in the LSMO is, i.e. whether nodal pairing is preserved or more likely a conversion into s-wave occurs[11]. Also, the present findings have much relevance in the field of superconducting spintronics. This is because the gathering of i) the very high temperature (tens of K) for which triplet Josephson current is observed ii) the very, long micrometric distance over which phase coherence is preserved in the half-metal in a planar device. Moreover, the fact that triplet supercurrents are necessarily fully spin polarized in a half metal, and that both ac and dc Josephson effects are demonstrated for the first time opens unprecedented opportunities as they pave the way to novel logic gates, full superconducting switches, nonvolatile random access memories[12] and quantum computing. Furthermore, the half-metallic Josephson junctions should reveal an anomalous Josephson effect with a non-zero phase difference φ_0 at the ground state, which is determined by the mutual orientation of the magnetization in the half-metal and interface magnetizations[13–16]. Such unusual φ_0 junction could serve as an important building block of "quiet qubit"[17] and may provide a unique mechanism of direct coupling between magnetism and phase dynamics in Josephson junctions[18].

This thesis is the crystallization of longstanding research effort, which started more than eight years ago with the thesis of Mirko Rocci. Apart from the work done at Universidad Complutense de Madrid and the Unidad Asociada ICMM-CSIC UCM, the important findings of this thesis have been possible thanks to the collaboration of Dr. Javier Villegas and Dr. Salvatore Mesoraca at CNRS-Thales, where numerous experiments were done including the set-up of an FMR experiment; Dr. Nicolas Bergeal and Prof. Jerome Lesueur at ESPCI Paris where we conducted the measurements of Shapiro steps; Dr Sergio Valencia at the Bessy synchrotron (Helmholtz Zentrum Berlin) where the PEEM characterization was done and Prof. Alexander Buzdin at the Université Bordeaux-CNRS which have helped us with the theoretical understanding of the phenomenon.

5.1. REFERENCES

1. Eschrig, M. Spin-polarized supercurrents for spintronics. *Phys. Today* **64**, 43–49 (2011).
2. Eschrig, M. & Löfwander, T. Triplet supercurrents in clean and disordered half-metallic ferromagnets. *Nat. Phys.* **4**, 138–143 (2008).
3. Eschrig, M. Spin-polarized supercurrents for spintronics: A review of current progress. *Reports Prog. Phys.* **78**, 104501 (2015).
4. Eschrig, M., Kopu, J., Cuevas, J. C. & Schön, G. Theory of Half-Metal/Superconductor Heterostructures. *Phys. Rev. Lett.* **90**, 4 (2003).
5. Bergeret, F. S. & Tokatly, I. V. Singlet-triplet conversion and the long-range proximity effect in superconductor-ferromagnet structures with generic spin dependent fields. *Phys. Rev. Lett.* **110**, 1–6 (2013).
6. Bergeret, F. S., Volkov, A. F. & Efetov, K. B. Odd triplet superconductivity and related phenomena in superconductor- ferromagnet structures. *Rev. Mod. Phys.* **77**, 1321–1373 (2005).
7. Bergeret, F. S., Volkov, A. F. & Efetov, K. B. Long-range proximity effects in superconductor-ferromagnet structures. *Phys. Rev. Lett.* **86**, 4096–4099 (2001).

8. Tanaka, Y. & Golubov, A. A. Theory of the proximity effect in junctions with unconventional superconductors. *Phys. Rev. Lett.* **98**, 037003 (2007).

9. Sperstad, I. B., Linder, J. & Sudbø, A. Josephson current in diffusive multilayer superconductor/ferromagnet/ superconductor junctions. *Phys. Rev. B - Condens. Matter Mater. Phys.* **78**, 104509 (2008).

10. Halterman, K., Valls, O. T. & Barsic, P. H. Induced triplet pairing in clean s -wave superconductor/ferromagnet layered structures. *Phys. Rev. B - Condens. Matter Mater. Phys.* **77**, 174511 (2008).

11. Volkov, A. F. & Efetov, K. Proximity Effect and Its Enhancement by Ferromagnetism in High-Temperature Superconductor-Ferromagnet Structures. *Phys. Rev. Lett.* **102**, 077002 (2009).

12. Vernik, I. V. *et al.* Magnetic josephson junctions with superconducting interlayer for cryogenic memory. *IEEE Trans. Appl. Supercond.* **23**, 1701208 (2013).

13. Braude, V. & Nazarov, Y. V. Fully developed triplet proximity effect. *Phys. Rev. Lett.* **98**, 077003 (2007).

14. Eschrig, M., Cottet, A., Belzig, W. & Linder, J. General boundary conditions for quasiclassical theory of superconductivity in the diffusive limit: application to strongly spin-polarized systems. *New J. Phys* **17**, 83037 (2015).

15. Mironov, S. & Buzdin, A. Triplet proximity effect in superconducting heterostructures with a half-metallic layer. *Phys. Rev. B - Condens. Matter Mater. Phys.* **92**, 184506 (2015).

16. Eschrig, M. & Löfwander, T. Triplet supercurrents in clean and disordered half-metallic ferromagnets. *Nat. Phys.* **4**, 138–143 (2008).

17. Ioffe, L. B., Geshkenbein, V. B., Feigel'man, M. V, Fauchère, A. L. & Blatter, G. Environmentally decoupled sds -wave Josephson junctions for quantum computing. *Nature* **398**, 679–681 (1999).

18. Mironov, S., Meng, H. & Buzdin, A. Magnetic flux pumping in superconducting loop containing a Josephson ψ junction. *Appl. Phys. Lett.* **116**, 162601 (2020).

Resumen en español

En esta tesis hemos explorado el efecto de proximidad superconductor en estructuras de ferromagnéticos/superconductores que combinan cupratos de óxido complejos (YBCO) y manganitas (LSMO). La tesis a su vez ha sido dividida en 5 capítulos:

- Capítulo 1: Introducción. En este capítulo se describen y analizan los fundamentos teóricos y los experimentos previos sobre la materia. Los dos efectos principales que se miden en esta tesis, el efecto Josephson y la resonancia ferromagnética, se describen en profundidad. Además, se justifica la elección de los materiales ferromagnéticos y superconductores.

- Capítulo 2: Técnicas experimentales. Se explican las técnicas utilizadas tanto para el crecimiento como para las medidas de las muestras en esta tesis. Es de especial importancia la descripción de los dos sistemas de resonancia ferromagnética que se han establecido desde cero en esta tesis, tanto en el CNRS-Thales como en la Universidad Complutense de Madrid.

- Capítulo 3: Efecto de proximidad en uniones Josephson medio-metal/superconductor. Este es el más importante de los resultados de esta tesis, y en este capítulo se explica la fabricación de dispositivos superconductores/ferromagnéticos y se analizan sus medidas. Se describe el resultado más importante, a saber, el hallazgo de un efecto superconductor de proximidad de largo alcance en una unión Josephson medio metálica a alta temperatura (>50 K). Es la primera vez que se observa un efecto de proximidad de este tipo a una distancia tan larga y a una temperatura tan elevada, y constituye un importante avance en el campo de la espintrónica superconductora.

- Capítulo 4: El efecto de proximidad en las estructuras superconductoras/ferromagnéticas se estudia mediante resonancia ferromagnética. Después de medir el efecto de proximidad mediante la caracterización habitual de magnetotransporte, se realizaron experimentos de resonancia ferromagnética. Se ha encontrado un aumento del *damping* por debajo de la transición superconductora en las estructuras de ferromagneticos/superconductores, confirmando y apoyando la presencia de tripletes de Cooper en nuestros sistemas.

- Capítulo 5: Conclusiones. Se resumen las principales conclusiones de esta tesis y se describe la importancia de los logros alcanzados. El capítulo termina con una serie de observaciones de las perspectivas de futuro.

En esta tesis hemos logrado fabricar microestructuras planares de YBCO/LSMO/YBCO donde los bancos superconductores de YBCO están separados por distancias de micras por un ferromagnético medio metálico LSMO utilizando patrones de alúmina amorfa definidas por litografía de haz de electrones.

Hemos encontrado pruebas convincentes de un efecto de proximidad superconductor de muy largo alcance en el LSMO medio metálico inducidos por los bancos superconductores de YBCO. El acoplamiento de Josephson se ha demostrado sin ambigüedades en las uniones planares que, además de grandes corrientes críticas y, de manera bastante notable, muestran los rasgos distintivos de la física de Josephson: i) oscilaciones de corrientes críticas impulsadas por la cuantificación del flujo magnético; y ii) efectos de fase cuántica bajo excitación de microondas

(pasos de Shapiro). Estos últimos, no reportados en el contexto de la superconductividad inducida de los tripletes, muestran aquí una duplicación anómala de la frecuencia de Josephson predicha por varias teorías. Los patrones de oscilación de largo período de Fraunhofer en la resistencia frente a los barridos de campo magnético han proporcionado fuertes indicios de un efecto Josephson triplete completamente nuevo impulsado por la rotación de la magnetización en una pared de dominio de tipo Bloch en el LSMO. Propuesto teóricamente, esta es, hasta donde sabemos, la primera evidencia experimental de tal efecto.

Además, hemos probado que FMR es una herramienta poderosa para medir el efecto de proximidad en sistemas superconductores/ferromagnéticos. El hecho de que no hay necesidad de muestras de nanoestructuradas, ni de procesos complejos aparte del crecimiento de la muestra, hacen de FMR una técnica relativamente rápida para estudiar la interacción de proximidad en las interfaces.